HAL open science

Simulation numérique de phénomènes d'interaction fluide-structure

Serge Piperno

To cite this version:

Serge Piperno. Simulation numérique de phénomènes d'interaction fluide-structure. Mathématiques [math]. Ecole des Ponts ParisTech, 1995. Français. NNT : . tel-00005618

HAL Id: tel-00005618

https://pastel.hal.science/tel-00005618v1

Submitted on 5 Apr 2004

HAL is a multi-disciplinary open access archive for the deposit and dissemination of scientific research documents, whether they are published or not. The documents may come from teaching and research institutions in France or abroad, or from public or private research centers.

L'archive ouverte pluridisciplinaire **HAL**, est destinée au dépôt et à la diffusion de documents scientifiques de niveau recherche, publiés ou non, émanant des établissements d'enseignement et de recherche français ou étrangers, des laboratoires publics ou privés.

THESE

présentée à

L'ECOLE NATIONALE DES PONTS ET CHAUSSEES

pour obtenir le titre de

DOCTEUR

Spécialité : Mathématiques Appliquées

Simulation numérique de phénomènes d'interaction fluide-structure

par Serge Piperno

Soutenue le 30 Juin 1995 devant la commission composée de MM. :

Alain	DERVIEUX	
Philippe	DESTUYNDER	Rapporteur
Charbel	FARHAT	
Bernard	LARROUTUROU	
Patrick	LE TALLEC	Rapporteur
Yvon	MADAY	
Bruno	STOUFFLET	

REMERCIEMENTS

Je voudrais d'abord remercier avec la plus grande gratitude Monsieur Bernard LARROUTUROU. Après m'avoir guidé dans mes premiers choix scientifiques, il m'a permis d'entreprendre cette thèse en m'accueillant au sein du CERMICS et en me proposant ce thème de recherche très intéressant. Ses conseils attentionnés et ses interventions rapides et avisées m'ont guidé en permanence tout au long de ce travail.

Mes remerciements vont également à Monsieur Charbel FARHAT, qui m'a accueilli si gentiment au CSSC à l'Université du Colorado à Boulder. J'ai pu bénéficier de l'expérience acquise par son équipe et me consacrer à certains aspects théoriques. Je le remercie pour sa disponibilité et son encadrement, souvent electroniques, mais toujours compétents et sympathiques.

J'exprime toute ma reconnaissance à Messieurs Patrick LE TALLEC et Philippe DESTUYNDER qui ont accepté la lourde tâche d'être rapporteur.

Je remercie vivement Monsieur Alain DERVIEUX, responsable du projet SINUS, membre de ce jury, qui a permis une fructueuse collaboration avec son équipe, en mettant à ma disposition l'essentiel des codes de simulation que j'ai utilisés.

J'exprime aussi ma gratitude à Messieurs Bruno STOUFFLET et Yvon MADAY qui me font l'honneur de participer à ce jury.

Je remercie également toutes les personnes dont les avis éclairés ont accompagné cette thèse. Michel LESOINNE m'a donné un angle d'attaque sur ce sujet nouveau. Nathan MAMAN m'a accueilli à bras ouverts aux USA, je n'oublierai pas nos discussions chaleureuses. Stéphane LANTERI s'est montré toujours charmant et disponible, ses compétences ont constamment accompagné cette thèse. Je remercie pour leur gentillesse Katherine MER et Boniface N'KONGA, avec qui la collaboration fut toujours facile et agréable.

Enfin, je remercie les membres de l'équipe "Modélisation et calcul scientifique" du CERMICS à Sophia-Antipolis. Loula FEZOUI, Nathalie GLINSKY-OLIVIER, Armel de LA BOURDONNAYE, Yves D'ANGELO et Robert RIVIERE m'ont apporté leur soutien constant et leur expérience si précieux pour un jeune chercheur. Ce travail n'aurait pas été aussi agréable sans la compagnie de Sophie, Cédric, Didier, Djipé (alias Jean-Pierre), Fredo (alias Frédéric), la Mancha (alias Marco), Pascal, et celle de Christel surtout.

Table des matières

I Introduction **1**

Chapitre 1. Introduction **3**

Chapitre 2. Méthodes numériques pour l'aéroélasticité **9**

2.1 Introduction 9
2.2 Modèles et méthodes pour le fluide 11
2.2.1 Méthodes avec changement de variables 11
2.2.2 Méthodes avec changement de repère 16
2.2.3 Méthodes ALE 21
2.2.4 Méthodes à maillage dynamique 25
2.2.5 Conclusion 31
2.3 Traitement de l'interaction fluide-structure 32
2.3.1 Aspects physiques de l'interaction 32
2.3.2 L'algorithme général 35
2.4 Modèles et méthodes pour la structure. 35
2.4.1 Equations modèles pour la structure 36
2.4.2 Schémas d'intégration 40

II Analyse numérique **43**

Chapitre 3. Analysis and compensation of numerical damping **47**

3.1 Introduction 48
3.2 The physical test case and the global numerical algorithm 49
3.2.1 The model problem 49
3.2.2 Evaluating the system frequency 51
3.2.3 The general integration scheme 53
3.3 Modified equation analysis 54
3.3.1 Modified equation with diffusion 55
3.3.2 Roles of structural schemes and boundary treatments 57
3.4 Coupled eigenvector analysis 59
3.4.1 Presentation of the analysis 60
3.4.2 Analysis with a predicted piston speed 61
3.5 Comparing the two methods 62
3.6 Analyzing other schemes 64

3.6.1 Schemes with predicted pressure and speed 64
3.6.2 Second-order accurate schemes 66
3.6.3 Implicit time integration schemes 67
3.7 Discussion and conclusions 70
3.7.1 Prediction of the numerical damping 70
3.7.2 Compensation of the numerical damping 72

Chapitre 4. Partitioned procedures for aeroelastic simulations 79
4.1 Introduction 80
4.2 A 1D aeroelastic model problem with an Euler flow 82
4.2.1 The piston problem: ALE formulation and linearization 82
4.2.2 Spatial discretization: finite volume formulation and upwinding 84
4.2.3 Transpiration 85
4.2.4 The semi-discrete aeroelastic model problem 85
4.3 Mathematical preliminaries 86
4.3.1 Physical v.s. numerical instabilities 86
4.3.2 Analysis framework 87
4.3.3 Physical stability of the model problem 89
4.3.4 Physical stability in multi-dimensional cases 90
4.4 Implicit/implicit partitioned procedures 91
4.4.1 Unconditionally stable staggered time-integrators 91
4.4.2 Subcycling 94
4.4.3 Examples 97
4.5 Explicit/implicit partitioned procedures 98
4.5.1 A predictor-corrector approach 105
4.5.2 Examples 108
4.6 Parallel staggered strategies, error analysis and CPU distribution . . . 109
4.6.1 Algorithm ALG-0 : the basic staggered scheme 113
4.6.2 Algorithm ALG-1 : subcycling the fluid system 115
4.6.3 Algorithm ALG-2 : improving the accuracy of ALG-1 116
4.6.4 Algorithm ALG-3 : introducing inter-field parallelism 117
4.6.5 Algorithm ALG-4 : improving the accuracy of ALG-3 118
4.6.6 Applications 120
4.7 Aeroelastic response of a flexible panel in transonic nonlinear regime . . 122
4.8 Closure 126

III Résultats 129

Chapitre 5. Staggered methods for a 1D Euler aeroelastic problem 133
5.1 Introduction 134
5.2 The model problems 135
5.2.1 The two one-dimensional problems 135
5.2.2 Equations and boundary conditions 137
5.2.3 Coupled eigenfrequencies 138

5.2.4 Data sets for test cases 140
5.3 Numerical methods 141
5.3.1 Numerical methods used for the structure 141
5.3.2 Numerical methods used for the fluid 143
5.3.3 Coupling numerical methods and subcycling 145
5.4 Volume-continuous methods 148
5.4.1 Description of the algorithm 149
5.4.2 Numerical results 150
5.4.3 Discussion on conservation 151
5.5 Volume-discontinuous methods 156
5.5.1 Description of the algorithm 156
5.5.2 Conservation enhancements 158
5.5.3 Numerical tests 159
5.6 Discussion 172

Chapitre 6. Two-dimensional Euler aeroelastic simulations 177
6.1 Introduction 177
6.2 The physical problems 178
6.2.1 The rigid NACA airfoil in transonic inviscid flow 179
6.2.2 Flat panel under supersonic inviscid flow 183
6.2.3 Comparison with one-dimensional problems 191
6.3 Numerical methods 191
6.3.1 Numerical methods used for the fluid 192
6.3.2 Numerical methods used for the structure 197
6.4 Enhancements of the general coupling scheme 199
6.4.1 Structural time-interpolation 200
6.4.2 Volume-continuous or volume-discontinuous methods 201
6.4.3 Role of the prediction in volume-discontinuous methods 203
6.4.4 Energy conservation 204
6.4.5 Grid motion and subcycling 206
6.4.6 Mesh updating equation 206
6.4.7 Mesh updating algorithm. 209
6.5 Application to the panel flutter simulation 210
6.5.1 Simulations with few degrees of freedom (< 300) 211
6.5.2 Computations with thousands of degrees of freedom 217
6.6 Conclusion 222

IV Conclusion 225

Première partie

Introduction

Chapitre 1

Introduction

La simulation numérique de phénomènes couplés a connu un essor constant ces dernières années. Ce développement est dû en particulier aux succès précédents de la simulation numérique en général, mais aussi à l'accroissement permanent des performances de nos calculateurs.

Parmi ces phénomènes couplés se trouvent les interactions fluide-structure. Elles mettent en jeu une structure toujours mobile, rigide ou déformable, et un fluide liquide ou gazeux, en écoulement autour ou contre une partie de la structure. Ces phénomènes sont dits couplés, parce que l'évolution de chacun des deux éléments dépend de celle de l'autre. Ainsi par exemple, la forme de la voile d'un bateau (en régime permanent) dépend de l'écoulement de l'air autour de celle-ci. Réciproquement, cet écoulement dépend de la forme de la voile.

On pourrait citer un très grand nombre d'exemples du même type. Parmi ceux-ci, on peut exhiber entre autres les phénomènes hydroélastiques (fluide en phase liquide): écoulements autour d'un navire, d'un sous-marin, d'une digue dans un port ou de piles de pont, écoulements liquides à l'intérieur de conduites, mouvements de liquides dans un réservoir, etc... On distingue également les phénomènes aéroélastiques où le fluide est en phase gazeuse: écoulements autour des véhicules aériens (avions, missiles, etc...) et terrestres (trains à grande vitesse, automobiles, etc...), influence du vent sur les constructions souples (ponts suspendus, réfrigérants de centrale nucléaire, etc...).

Les exemples sont très nombreux. Pour certains d'entre eux, des équations simples et/ou linéaires suffisent à représenter précisément l'évolution du fluide. Des théories ont alors permis de réduire à l'interface fluide-structure le domaine qu'il faut discrétiser pour simuler numériquement le phénomène couplé. C'est le cas par exemple des équations intégrales appliquées à des phénomènes de type acoustique en analyse spectrale. Pour d'autres problèmes, ces simplifications sont impossibles. Par exemple, pour un profil d'aile en régime transsonique, certaines parties de l'écoulements sont supersoniques. Comme des effets purement non-linéaires peuvent être prépondérants, une linéarisation globale est insuffisante.

Ainsi, dans le cas général, on se retrouve devant les contraintes suivantes. D'abord, il faut simuler numériquement l'évolution du fluide <u>et</u> de la structure. De plus, il faut utiliser des schémas assez précis en temps et en espace pour ne rien rater du couplage

et disposer simultanément de toutes les inconnues liées au fluide et à la structure. Les progrès récents des performances des super-calculateurs permettent maintenant des simulations numériques utiles de problèmes réels complexes.

Ces simulations sont devenues de véritables enjeux industriels. Par exemple, le phénomène de flottement, bien connu des aérodynamiciens, peut provoquer la ruine d'un avion. Ainsi, il intervient fortement dans la définition des limites du domaine de vol des avions de ligne et sur la manœuvrabilité des avions de chasse. Connaissant mal les mécanismes liés au flottement, les constructeurs préfèrent surdimensionner les structures et réduire les domaines de vol, pour s'épargner des essais réels très coûteux. La simulation numérique, si elle est assez précise et fiable, peut s'avérer une excellente solution. On pourrait multiplier les exemples: le dessin du tablier d'un pont suspendu, le positionnement des réfrigérants d'une centrale nucléaire, etc...

Mais qu'est-ce qu'une simulation fiable? Les questions posées par un constructeur d'avions, par exemple, sont assez simples: dans quels régimes de vol un avion peut-il être instable? Quels sont les modes et les fréquences propres de ces instabilités? La réponse à ces questions permettraient alors de délimiter plus précisément les domaines de vol, voire de les étendre par addition de contrôles actifs.

Cependant, les résultats d'une simulation numérique dépendent fortement du modèle physique choisi et des méthodes employées. Pour satisfaire un industriel, le numéricien doit savoir répondre aux deux questions suivantes: si une simulation prédit un comportement stable de l'avion, l'est-il réellement? Si la simulation prédit une instabilité, dois-je la suivre, et réduire le domaine de vol de l'avion?

* * *

L'objet de cette thèse est la construction et l'analyse de méthodes numériques pour la simulation de phénomènes d'interaction fluide-structure. Ces méthodes étaient encore très peu développées il y a quelques années. Divers travaux consacrés à des cas simples ou particuliers envisageaient des méthodes de résolution couplées (résolution directe des équations concernant toutes les inconnues) ou intégrales (équations acoustiques résultant de la linéarisation des équations d'Euler). Ces méthodes ne sont pas applicables en général sur des problèmes aéroélastiques un peu complexes. Les premières demandent des moyens de calcul dont personne ne dispose, et les secondes s'appliquent à des équations modèles linéaires.

Pour des problèmes aéroélastiques instationnaires un peu complexes, les seules méthodes disponibles étaient des méthodes "décalées" ou "en escalier", ou chaque système - le fluide ou la structure - est intégré dans le temps *à son tour*, en supposant que l'autre système reste fixe. Ces méthodes élémentaires ne donnent de bons résultats que si les pas de temps utilisés pour chaque système sont très petits, ce qui implique de très grands coûts de calcul.

Nous nous intéressons donc plus précisément à la mise au point de nouvelles mé-

thodes décalées, plus efficaces et produisant des résultats fiables.

Nous définissons maintenant le cadre de l'étude. On définit un cas complexe, tel qu'il pourrait être décrit par un industriel. Pour cela, il faut choisir des modèles physiques et des méthodes numériques pour le fluide et la structure. En partant de simplifications de ce problème, et en allant vers le cas "réel", on cherche à mettre au point des algorithmes généraux pour la simulation. Pendant cette construction, on fera en sorte le plus souvent possible que l'algorithme global reste applicable au cas réel.

Notre cas réel est bidimensionnel. Le fluide est régi par les équations d'Euler (non linéaires). La structure est linéaire. Elle possède jusqu'à plusieurs milliers de degrés de liberté. Nous avons choisi ce cadre assez simple, car nous pensons que les extensions à trois dimensions, à un fluide visqueux ou à des structures non-linéaires ne posent pas de problème de couplage particulier.

Nous avons aussi limité notre étude à un certain nombre de méthodes numériques classiques en mécanique des fluides et en dynamique des structures. Nous utilisons des formulations en volumes finis des équations d'Euler écrites sur un maillage mobile non-structuré, avec des flux numériques décentrés de type Roe du second ordre (de type MUSCL). Nous intégrons en temps le fluide à l'aide d'un schéma explicite de type Runge Kutta à trois pas. Cet ensemble de méthodes très classique est reconnu comme efficace, robuste et facilement utilisable. Pour la structure, les matrices symétriques résultant d'une formulation en éléments finis des équations de l'élasticité se prêtent bien aux méthodes implicites de Newmark.

Le problème réel et l'éventail des méthodes numériques auquel nous nous restreignons étant définis, nous entendons construire de nouveaux algorithmes de couplage, fiables et efficaces. Nous cherchons de nouveaux algorithmes dans la famille des méthodes d'intégration en temps décalée. Notre espoir est de construire un algorithme de couplage précis et fiable, sans limite sur les pas de temps autre que celles des schémas numériques utilisés pour chaque sous-système.

* * *

Le plan de cette thèse est le suivant. Dans le reste de cette première partie, l'ensemble des équations mathématiques dérivant d'un problème couplé classique est exposé. Il s'agit bien évidemment des équations régissant chacun des champs, fluide et structure, mais aussi des conditions aux limites pour chacun d'eux. Ces conditions sont déterminantes, puisque l'interface fluide-structure est le siège du couplage aéroélastique.

Les méthodes numériques qui sont utilisées classiquement pour chacun des champs sont également rappelées et détaillées. Outre les méthodes consacrées à chacun des problèmes découplés, les algorithmes de simulation du couplage lui-même utilisés couramment à l'époque du début de cette thèse, sont détaillés et comparés.

Dans la deuxième partie, nous nous intéressons à des aspects théoriques du couplage des méthodes choisies pour chacun des sous-problèmes. Même lorsque ces méthodes sont élémentaires, les caractéristiques de l'algorithme global de résolution sont inconnues. En d'autres termes, l'utilisation de méthodes numériques précises, stables et efficaces pour le fluide et la structure ne nous garantit pas que le schéma soit globalement précis, stable et efficace. En effet, certains points supplémentaires restent à analyser. Les conditions aux limites doivent être traitées précisément (en temps et en espace). La stabilité couplée doit être étudiée – en général, la stabilité des méthodes utilisées pour chaque sous-problème est prouvée lorsque le terme source d'échange est nul, ce qui n'est bien sûr plus le cas). Enfin, la différence entre les temps caractéristiques liés à chaque sous-problème peut diminuer fortement l'efficacité de l'algorithme global.

Pour un problème très simple, mono-dimensionnel et linéaire (linéarisation des équations d'Euler autour d'un état stationnaire inerte), l'influence de l'algorithme de couplage sur les résultats numériques est analysée et prédite. Celle-ci s'avère déterminante, même pour ce cas simple. Cette thèse se trouve ainsi pleinement motivée: il ne suffit pas d'accoller des méthodes existantes. L'algorithme de couplage est essentiel.

Nous montrons ensuite que, dans des cas simples et linéaires, l'utilisation de formulations "énergétiques" permet de prouver si un algorithme global est stable ou non. Aussi, la stabilité de nouveaux schémas couplés est établie. Leur précision et leur efficacité sont aussi étudiées. Ces formulations énergétiques seront également utilisées par la suite pour évaluer de futurs schémas de couplages, pour des problèmes beaucoup plus complexes.

Dans la troisième partie, nous nous tournons vers la simulation numérique de phénomènes aéroélastiques réels. Dans les deux cas considérés, il s'agit du flottement d'une structure dans un écoulement non visqueux. Le but de la simulation est l'étude de la stabilité du système couplé. Pour la structure, on se place dans l'hypothèse des petits déplacements (structure linéaire). Pour ces problèmes, la question est la suivante: sommes-nous capables d'interpréter les résultats obtenus? En d'autres termes, sont-ils le reflet de la réalité (en fait, du modèle utilisé) ou simplement une image déformée par les méthodes de simulation utilisées?

La réponse théorique à ces questions s'est avérée trop difficile. En effet, les équations d'Euler régissant le fluide ne sont plus linéaires et ces écoulements ne sont plus mono-dimensionnels. Pour répondre quand même à ces questions, la méthodologie est assez simple. On comparera les résultats numériques à une solution de référence, obtenue parfois au prix de longues heures de calcul.

Nous étudions d'abord des versions non linéarisées des problèmes modèles vus précédemment. Les formulations énergétiques vues dans la deuxième partie nous permettent de construire de nouvelles méthodes *à double interface*. Ces méthodes sont plus précises, plus stables et plus efficaces.

Elles sont ensuite appliquées au flottement d'une aile d'avion rigide (approche bidimensionnelle) dans un écoulement transsonique et au cas du flottement supersonique d'un panneau metallique (cas également bidimensionnel avec de nombreux degrés de liberté pour la structure). Dans les deux cas, nous sommes parvenus à obtenir d'excel-

lents résultats, en réduisant au strict minimum les coûts de calcul: des artifices liés au sous-cyclage nous ont permis d'utiliser pour le fluide et la structure des pas de temps différents. Ceux-ci sont uniquement limités par la stabilité et la précision de chacune des méthodes numériques utilisées pour les problèmes découplés.

Chapitre 2

Méthodes numériques pour l'aéroélasticité

2.1 Introduction

Comme on l'a dit précédemment, les phénomènes aéroélastiques sont des phénomènes couplés mettant en jeu un gaz et une structure en contact. Les deux milieux sont couplés par le jeu des conditions aux limites à l'interface fluide-structure.

Les aérodynamiciens ont commencé par se limiter à des problèmes purement fluides, en domaine déformable, où le mouvement de l'interface est prédéfini. Ensuite, ils ont fait appel à la dynamique des structures et l'on incluse dans leurs simulations aéroélastiques.

Ces calculs ont d'abord été conçus pour des études de sécurité sur des structures lourdes. Ces études répondent à l'inquiétude des ingénieurs concernant la fatigue des structures sous l'influence couplée de liquides environnants. Par exemple, un gros effort a été produit dans le domaine des réacteurs nucléaires, et plus généralement pour l'ensemble des couplages hydroélastiques [20]. En effet, les cuves des réacteurs nucléaires sont soumises aux mouvements des liquides réfrigérants. Dans le surrégénérateur Super-Phénix, avant correction d'un défaut de conception, un déversement de sodium liquide contenu entre la coque interne déformable et la cuve principale entrait en résonance avec celles-ci. Ainsi, il mettait en danger le réacteur lui-même. D'autres exemples classiques concernent la résistance des sous-marins aux charges immergées et la fatigue des conduites en général.

D'autres études aéroélastiques concernent l'instabilité couplée d'une structure dans un écoulement. Par exemple, les ingénieurs des Ponts et Chaussées Américains ont longtemps médité sur la ruine du pont suspendu de Tacoma Narrows. Dans [68], Scanlan fait un point en 1979 sur l'état général des connaissances sur les trois problèmes principaux des ponts suspendus sous l'action du vent : le détachement périodique de tourbillons, le flottement et le balottement. Sur la Figure 2.1, on comprend comment le vent peut produire un amortissement négatif des mouvements de torsion du tablier d'un pont suspendu, lorsque sa vitesse est suffisamment grande. En effet, on voit sur

la figure qu'une torsion du tablier entraine un déplacement des tourbillons de l'écoulement. La nouvelle distribution des pressions sur le tablier peut alors avoir tendance, lorsque la vitesse du vent est assez grande, à amplifier cette torsion.

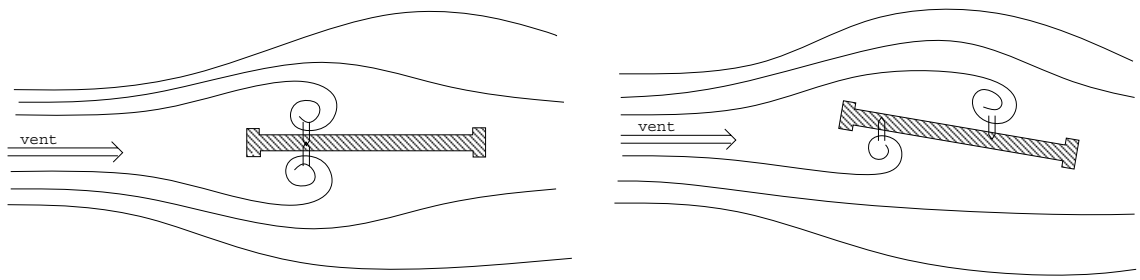

FIG. 2.1 – *Tourbillons autour d'un tablier de pont en torsion.*

En aéronautique, les phénomènes de flottement ont été très étudiés. Par exemple, de très nombreuses simulations ont porté sur le "transonic dip" [31] (domaine transsonique de vol où le flottement des ailes de certains avions fait chuter considérablement leur portance). Comme les limitations du domaine de vol des avions modernes sont principalement dues aux interactions aéroélastiques, de nombreuses études concernent des structures de plus en plus légères et souples [41]. Des éléments de contrôle actif ont été également introduits [32].

Dans ce chapitre, on s'intéresse aux méthodes numériques utilisées couramment (avant le début de ctte thèse) pour des simulations aéroélastiques. En général, ces algorithmes sont applicables à d'autres types d'interactions. Nous n'avons pas l'intention de discuter les modèles utilisés ni la complexité des maillages et des structures considérés (la configuration typique va du profil d'une aile à un avion entier). On pourra trouver dans [31] un résumé et un bref historique du développement des simulations aéroélastiques.

Dans la suite, on se limitera aux équations d'Euler bidimensionnelles pour le fluide et à des modèles linéaires pour la structure. Les méthodes que nous allons présenter s'appliquent aussi à d'autres modèles pour le fluide (théorie du potentiel, équations de Navier-Stokes) ou à des structures dont le comportement est plus complexe.

Comme on l'a dit dans l'introduction, la simulation d'un couplage aéroélastique passe par l'intégration simultanée des équations d'evolution du fluide et de la structure. Le domaine fluide est déformable. C'est pourquoi nous présenterons dans la Section 2.2 des méthodes numériques relevant seulement de la mécanique des fluides en domaine déformable. On verra qu'il est facile d'adapter ces méthodes et de les inclure dans un algorithme général pour la simulation du problème couplé. Nous étudierons l'ensemble de ces algorithmes dans la Section 2.3, en insistant notamment sur la satisfaction du principe d'action et de réaction à l'interface fluide-structure. Pour finir, nous ferons un bref rappel dans la Section 2.4 des méthodes classiques utilisées en dynamique des structures linéaires.

2.2 Modèles et méthodes pour le fluide

Dans cette section, on s'intéresse à la partie fluide du problème. On suppose pour l'instant que les mouvements des limites du domaine fluide sont connus. Dans la section suivante, on insérera les méthodes présentées ici dans l'algorithme général. Il suffira de déduire le mouvement de l'interface fluide-structure de celui de la structure.

Comme le domaine occupé par le fluide est déformable, sa discrétisation – un maillage structuré ou non-structuré – doit être calculée et remise à jour à chaque instant (avant ou après chaque pas de temps). Il est aussi possible d'imaginer des mises à jour moins fréquentes, qui seraient faites après chaque déplacement significatif du bord du domaine fluide.

Cependant, il existe des cas où les calculs successifs du maillage peuvent être simplifiés. Par exemple, si l'on simule un écoulement autour d'un profil d'aile rigidement mobile, on peut changer de référentiel et garder un maillage constant. Ainsi, de nombreuses méthodes particulières sont motivées par la simplification des équations à résoudre ou l'économie du temps de calcul consacré aux mouvements de maillage qu'elles engendrent.

Dans cette section, on s'intéressera d'abord aux méthodes où l'on s'est ramené à un domaine géométrique fixe par un changement de variables ou de repère. Ensuite, nous présentons un ensemble de méthodes fondées sur une formulation arbitrairement Lagrangienne ou Eulérienne (formulation ALE) des équations aux dérivées partielles du modèle physique. Enfin, nous présenterons la famille des méthodes à maillage dynamique, extensions des formulations ALE qui s'adaptent particulièrement bien aux formulations en volumes finis des équations de conservation et à l'utilisation de flux numériques classiques.

2.2.1 Méthodes avec changement de variables

On s'intéresse ici aux méthodes utilisant un changement de coordonnées spatiales. Lorsque le maillage fluide est en mouvement, le calcul des dérivées spatiales intervenant dans les équations d'Euler est assez coûteux. On préfère généralement utiliser un maillage structuré lié à la structure. Si, par exemple, on simule l'écoulement autour d'un profil d'aile rigide, on choisira un maillage en "O" (des lignes concentriques du maillage englobent le profil) ou en "C" (comme précédemment, mais les lignes concentriques ne se referment pas en aval et restent parallèles), parfaitement régulier dans l'espace des nouvelles coordonnées liées à la structure. Lorsque la structure bouge, le maillage bouge aussi, mais les indices des cellules du maillage restent fixes. Le domaine fluide physique varie, mais le domaine fluide fictif dans les nouvelles coordonnées est fixe.

Dès lors, il est plus simple de réécrire les équations modèles dans le nouveau jeu de

coordonnées. Les calculs des différentes dérivées par rapport aux nouvelles coordonnées sont très peu coûteux, puisque le maillage fictif est structuré et régulier.

Dans la suite, on considère un problème bidimensionnel (écoulement autour d'une aile en mouvement rigide) dont les coordonnées physiques sont notées x et y. Les coordonnées curvilignes sont notées ξ et η. Les notations sont résumées sur la Figure 2.2. La coordonnée curviligne ξ varie en tournant autour de l'aile alors que η varie en s'éloignant de l'aile.

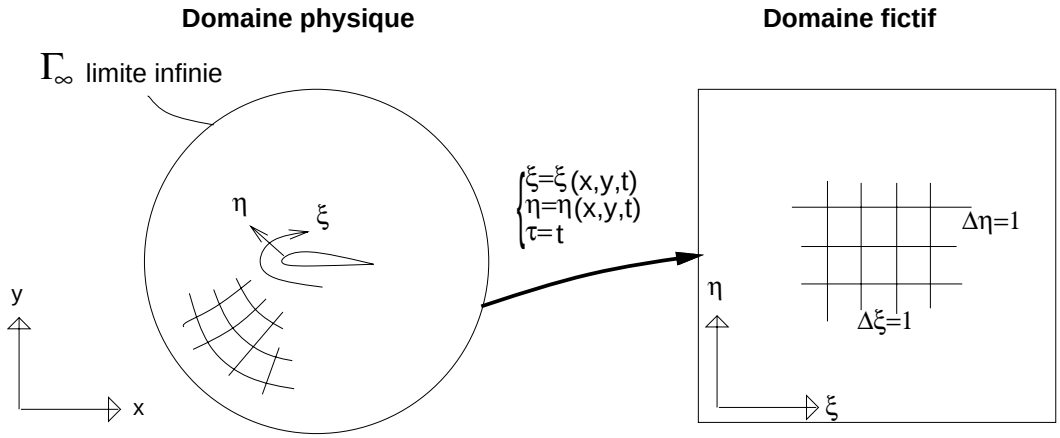

FIG. 2.2 – *Définition des coordonnées curvilignes.*

Formulation [33] :

• La première étape consiste à définir le changement de variable des coordonnées physiques du laboratoire vers les coordonnées curvilignes, par

$$\begin{cases} \tau &= t \\ \xi &= \xi(x,y,t) \\ \eta &= \eta(x,y,t). \end{cases} \tag{2.1}$$

• La transformation précédente est choisie de telle sorte que les conditions aux limites à l'infini mais aussi près du profil puissent être traitées très facilement. Pour un maillage en "O", on fera les choix évidents suivants : le bord de l'aile est défini par $\eta = \eta_0$ et la limite infinie du maillage est définie par $\eta = \eta_\infty$.

• Les équations d'Euler en deux dimensions pour un gaz idéal en coordonnées cartésiennes s'écrivent

$$\boxed{\frac{\partial Q}{\partial t} + \frac{\partial F}{\partial x} + \frac{\partial G}{\partial y} = 0} \tag{2.2}$$

avec

$$Q = \begin{pmatrix} \rho \\ \rho u \\ \rho v \\ E \end{pmatrix}, \qquad F = \begin{pmatrix} \rho u \\ \rho u^2 + P \\ \rho uv \\ (E+P)u \end{pmatrix}, \qquad G = \begin{pmatrix} \rho v \\ \rho uv \\ \rho v^2 + P \\ (E+P)v \end{pmatrix}, \tag{2.3}$$

où ρ, u, v, E et P représentent respectivement la masse volumique, les composantes selon x et y de la vitesse, l'énergie par unité de volume et la pression donnée par la loi d'état des gaz parfaits (γ est un paramètre fixé) :

$$P = (\gamma - 1)[E - \frac{1}{2}\rho(u^2 + v^2)]. \tag{2.4}$$

• Ces équations, dans les nouvelles coordonnées, prennent la forme suivante :

$$\boxed{\frac{\partial \hat{Q}}{\partial \tau} + \frac{\partial \hat{F}}{\partial \xi} + \frac{\partial \hat{G}}{\partial \eta} = 0} \tag{2.5}$$

où les quantités transformées (elles prennent un ' ˆ ') sont données par

$$\begin{gathered} \hat{Q} = J^{-1} \begin{pmatrix} \rho \\ \rho u \\ \rho v \\ E \end{pmatrix}, \\ \hat{F} = J^{-1} \begin{pmatrix} \rho U \\ \rho u U + \xi_x P \\ \rho v U + \xi_y P \\ (E+P)U - \xi_t P \end{pmatrix}, \qquad \hat{G} = J^{-1} \begin{pmatrix} \rho V \\ \rho u V + \eta_x P \\ \rho v V + \eta_y P \\ (E+P)V - \eta_t P \end{pmatrix}. \end{gathered} \tag{2.6}$$

Pour simplifier les équations précédentes, on a écrit par exemple 'ξ_x' à la place de $\partial\xi/\partial x$. J est le déterminant du Jacobien de la transformation des coordonnées physiques vers les coordonnées curvilignes définies par (2.1). Il est donné par

$$J = \begin{vmatrix} \xi_x & \xi_y & \xi_t \\ \eta_x & \eta_y & \eta_t \\ 0 & 0 & 1 \end{vmatrix} = \xi_x \eta_y - \xi_y \eta_x. \tag{2.7}$$

Enfin, les vitesses contravariantes U et V sont définies par

$$\begin{cases} U = \xi_t + \xi_x u + \xi_y v \\ V = \eta_t + \eta_x u + \eta_y v. \end{cases} \tag{2.8}$$

Le maillage fictif est uniforme. Il possède des mailles de longueur unité dans toutes les directions ($\Delta\xi = 1, \Delta\eta = 1$). Comme le maillage est structuré, les dérivées spatiales sont obtenues très simplement par des différences finies. Pour une quantité quelconque g, la dérivée spatiale g_ξ peut être approchée par $g(\xi_{n+1}) - g(\xi_n)$. Enfin, les dérivées

cartésiennes de g s'expriment simplement en fonction des dérivées par rapport aux coordonnées curvilignes grâce à des relations algébriques comme

$$g_x = \xi_x g_\xi + \eta_x g_\eta. \tag{2.9}$$

Les expressions des dérivées cartésiennes des coordonnées curvilignes qui apparaissent dans (2.6), (2.8) et (2.9) sont obtenues à partir de l'équation matricielle

$$\begin{pmatrix} \xi_x & \xi_y & \xi_t \\ \eta_x & \eta_y & \eta_t \\ 0 & 0 & 1 \end{pmatrix} \begin{pmatrix} x_\xi & x_\eta & x_\tau \\ y_\xi & y_\eta & y_\tau \\ 0 & 0 & 1 \end{pmatrix} = \begin{pmatrix} 1 & 0 & 0 \\ 0 & 1 & 0 \\ 0 & 0 & 1 \end{pmatrix}, \tag{2.10}$$

qui se décompose en

$$\begin{aligned} \xi_x &= J y_\eta, & \eta_x &= -J y_\xi, \\ \xi_y &= -J x_\eta, & \eta_y &= J x_\xi, \\ \xi_t &= -x_\tau \xi_x - y_\tau \xi_y, & \eta_t &= -x_\tau \eta_x - y_\tau \eta_y. \end{aligned} \tag{2.11}$$

• Les équations (2.2) et (2.5) définissent toutes deux des systèmes hyperboliques non-linéaires, écrits sous forme conservative. Ainsi, de nombreuses méthodes numériques ont été développées à partir des solveurs les plus populaires des équations d'Euler classiques. Par exemple, la décomposition de flux de Van Leer, en coordonnées curvilignes est présentée dans [2]. D'autres flux décentrés (streamwise flux vector splitting) et le solveur de Riemann approché de Roe peuvent être trouvés dans [58]. L'ensemble de ces transformations existe aussi pour les cas tridimensionnels. Toutes les équations et les variables géométriques sont résumées dans [33].

Algorithme:

• A un instant donné t^n de la simulation, on suppose que l'on connaît les quantités suivantes :

- toutes les grandeurs géométriques dans l'ensemble du maillage, comme les fonctions $x = x(\xi, \eta, t^n)$, $y = y(\xi, \eta, t^n)$ et leurs dérivées x_ξ, x_η, y_ξ, y_η,
- les vitesses de maillage x_τ et y_τ,
- le vecteur des variables conservatives transformé $\hat{Q}$.

• Le système (2.5) est intégré en temps de l'instant t^n à l'instant $t^{n+1} = t^n + \Delta t^n$ en considérant que toutes les grandeurs géométriques ci-dessus sont fixes pendant le pas de temps courant. Les conditions aux limites sont traduites simplement des conditions dans l'espace physique. La vitesse normale du fluide le long des bords mobiles est égale à la vitesse normale du bord. Au-delà de la frontière infinie, le vecteur des variables conservatives est fixé.

• Enfin, toutes les grandeurs géométriques doivent être mises à jour au temps t^{n+1}. De nombreuses méthodes permettent de remplir cette dernière tâche. On peut les regrouper en deux grandes familles.

Dans une première famille de méthodes, les points proches des bords mobiles sont d'abord mis à jour (puisque le mouvement du bord mobile est connu).

Ensuite, les nouvelles positions des points intérieurs peuvent être calculées de plusieurs manières possibles. Entre autres, Guruswamy a présenté dans [33] une formule algébrique de régénération du maillage pour une aile d'avion complète en trois dimensions. Batina propose dans [5] une méthode d'adaptation fondée sur une analogie élastique utilisant des ressorts fictifs placés le long des arêtes du maillage. Enfin, Nakahashi et Deiwert ont présenté dans [55] des principes variationnels (avec contrainte sur la régularité et l'orthogonalité) pour la génération d'un nouveau maillage intérieur.

Finalement, toutes les grandeurs géométriques sont recalculées, et les dérivées temporelles sont elles-mêmes mises à jour suivant les schémas aux différences finies

$$x_\tau^{n+1} = \frac{x^{n+1} - x^n}{\Delta t^n} \quad \text{et} \quad y_\tau^{n+1} = \frac{y^{n+1} - y^n}{\Delta t^n}. \tag{2.12}$$

Dans la seconde famille de méthodes de mise à jour, l'algorithme est le symétrique du précédent. Les nouvelles positions des points intérieurs sont déduites de leur position courante et de leur vitesse par

$$x^{n+1} = x^n + \Delta t^n . x_\tau^n \quad \text{et} \quad y^{n+1} = y^n + \Delta t^n . y_\tau^n. \tag{2.13}$$

Ensuite, il reste à générer de nouvelles vitesses de maillage à l'instant t^{n+1}. Shankar et Ide ont présenté dans [70] un schéma de ce type, avec interpolation linéaire le long des "méridiens" ($\xi = \xi_0$) en allant du profil vers la limite infinie du maillage.

Ces deux méthodes sont à peu près équivalentes. La seule différence notable réside dans le rôle joué par ce qu'on a appelé les vitesses de maillage, dans les équations (2.12) et (2.13).

Remarques :

• Les équations d'Euler en coordonnées curvilignes sont maintenant beaucoup plus complexes. Cependant, la résolution des nouvelles équations est plus rapide.

• Les méthodes présentées ici peuvent rencontrer des difficultés dans certains cas, notamment lorsque les déplacements ne sont pas négligeables. En effet, pour ces méthodes, aucune propriété générale (de stabilité notamment) n'a été démontrée.

• Le fait que le maillage est structuré est fortement utilisé par ces méthodes. L'extension à des maillages non-structurés ne paraît pas simple. De plus, les gains sur les

temps de calcul des dérivées par rapport aux coordonnées curvilignes seraient considérablement réduits. On peut donc mettre en doute l'efficacité de ce type de méthode pour des maillages non-structurés.

• Des instabilités peuvent être produites par certains usages de variables géométriques auxiliaires comme les volumes des cellules, ou le Jacobien de la transformation J^{-1} dans (2.5). Thomas et Lombard ont décrit [72] une loi de conservation géométrique qui doit être respectée par les schémas numériques utilisés. Cette loi est assez simple : elle est équivalente à la conservation du volume de discrétisation. Ainsi, tous les schémas utilisés doivent conserver exactement les volumes. Cette loi s'écrit :

$$\boxed{\frac{\partial J^{-1}}{\partial \tau} + \frac{\partial (J^{-1}\xi_t)}{\partial \xi} + \frac{\partial (J^{-1}\eta_t)}{\partial \eta} = 0.} \tag{2.14}$$

Ainsi, à la fin d'un pas de temps, il serait maladroit de mettre à jour le Jacobien J pour la cellule (i, j) du maillage structuré par la formule suivante :

$$\begin{aligned} 2\Delta\xi\Delta\eta J^{-1} &= [(x_{i+1,j} - x_{i,j})(y_{i+1,j+1} - y_{i,j+1}) \\ &\quad -(x_{i+1,j+1} - x_{i,j+1})(y_{i+1,j} - y_{i,j})] \end{aligned} \tag{2.15}$$

(on rappelle que $\Delta\xi = \Delta\eta = 1$) qui ne conserve pas explicitement les volumes. Il faut par contre utiliser une version scalaire du schéma d'intégration utilisé pour (2.5). En somme, on s'intéresse à des équations de conservation (masse, quantité de mouvement, énergie). Les schémas conservatifs que nous utilisons ont seulement l'apparance de la conservativité. Pour être conservatifs, il faut que le volume lui-même soit conservé (lorsqu'on simule l'intégration en temps d'une grandeur volumique constante et égale à 1).

• Pour toutes les méthodes présentées jusqu'ici, on utilise un changement de variables pour se ramener à un domaine fictif qui ne dépend pas du temps. En contrepartie, toutes les variables géométriques (coordonnées, Jacobien, etc...) doivent être calculées et remises à jour après chaque pas de temps. Ces tâches entrainent des coûts de calcul importants, que l'on n'a pas cherché à éviter grâce à des simplifications globales. On pense par exemple aux cas où le mouvement de la structure est rigide. Pour ceux-ci, on peut se ramener à une géométrie fixe grâce à un changement de repère.

2.2.2 Méthodes avec changement de repère

Comme on l'a déjà dit, les méthodes avec changement de repère sont particulièrement bien adaptées aux écoulements autour d'une structure en mouvement rigide. Les méthodes présentées précédemment s'avèrent parfois inapplicables, en raison de leur caractère plutôt Lagrangien (imaginez ce que donneraient ces méthodes si l'on simule la chute d'un cube rigide en rotation dans un écoulement...).

Un changement de repère peut permettre de garder une approche Lagrangienne en simplifiant considérablement équations et schémas. Par exemple, Kandil et Chuang ont présenté [42] une étude numérique où l'on a utilisé un repère lié à l'aile dont on voulait simuler le mouvement rigide dans un écoulement. Dans ce nouveau repère, l'aile est fixe, le domaine fluide (infini) est fixe. De plus, on peut garder la même discrétisation du domaine fluide pendant tout le calcul. Il faut seulement réécrire les équations physiques en repère mobile.

Formulation [25] :

• Les équations d'Euler classiques (2.2) et (2.3) peuvent être écrites dans un repère différent de celui du laboratoire. De plus, on peut envisager d'utiliser plusieurs référentiels différents, tous mobiles. Le $j^{\text{ième}}$ référentiel est défini par :

- $\vec{r_j}$: position de l'origine,
- T_j : dièdre (ou trièdre) orthonormé direct,
- $\vec{v_j} = d\vec{r_j}/dt$ et $\vec{a_j} = d\vec{v_j}/dt$: vitesse et accélération de l'origine du référentiel,
- $\vec{\omega_j}$ et $\dot{\vec{\omega_j}} = d\vec{\omega_j}/dt$: vitesse et accélération angulaires du référentiel.

Nous allons maintenant écrire les équations d'Euler dans de multiples repères. Le repère dans lequel ces équations seront écrites dépend du point considéré. Il ne sera donc pas étonnant de voir apparaître des dérivées spatiales des éléments définissant le référentiel local. Les équations d'Euler prennent la forme suivante :

$$\boxed{\frac{\partial Q'}{\partial t} + \frac{\partial F'}{\partial x'} + \frac{\partial G'}{\partial y'} = S'} \tag{2.16}$$

où

$$Q' = \begin{pmatrix} \rho \\ \rho u' \\ \rho v' \\ E' \end{pmatrix}, \quad F' = \begin{pmatrix} \rho u' \\ \rho u'^2 + P \\ \rho u' v' \\ (E' + P)' u \end{pmatrix}, \quad G' = \begin{pmatrix} \rho v' \\ \rho u' v' \\ \rho v'^2 + P \\ (E' + P) v' \end{pmatrix} \tag{2.17}$$

avec les dénitions suivantes :

$$\begin{aligned}
S' &= (S'_1, S'_2, S'_3, S'_4)^t \\
S'_1 &= -\rho div(\vec{V_t}) \\
S'_2 &= -\rho a_{t_{x'}} - \rho . div(\vec{V_t}).u' \\
S'_3 &= -\rho a_{t_{y'}} - \rho . div(\vec{V_t}).v' \\
S'_4 &= -\rho \vec{V}.(\vec{a_t} - \vec{\omega_j} \times \vec{V'}) - (E' + P) div(\vec{V_t})
\end{aligned}$$

Le vecteur $\vec{r'} = \vec{r} - \vec{r_j}$ définit la position du point courant dans le repère mobile. La vitesse $\vec{V'} = (u', v')^t$ dans le repère mobile est donnée en fonction de la vitesse absolue (par rapport au laboratoire) $\vec{V} = (u, v)^t$ et de la vitesse d'entrainement $\vec{V_t}$ par

$$\begin{aligned} \vec{V'} &= \vec{V} - \vec{V_t}, \\ \text{avec} \quad \vec{V_t} &= \vec{v_j} + \vec{\omega_j} \times \vec{r'}. \end{aligned}$$

Enfin, la définition de S' ne serait pas complète sans donner les éléments suivants :

$$\begin{aligned} E' &= E + \rho \vec{V}.\vec{V_t} \\ \vec{a_t} &= \vec{a_j} + \dot{\vec{\omega_j}} \times \vec{r'} + \vec{\omega_j} \times (\vec{\omega_j} \times \vec{r'}) + 2\vec{\omega_j} \times \vec{V'}. \end{aligned}$$

Dans les équations précédentes, les dérivations $\partial/\partial t$ sous-entendent que l'on a derivé les grandeurs par rapport au temps en gardant (x', y') constant. Le terme de divergence $div(\vec{V_t})$ représente l'influence de la variation de la vitesse d'entraînement. Il n'est pas uniformément nul, puisque cette vitesse d'entraînement depend du référentiel dans lequel on se trouve, et donc du point considéré.

Toutes ces équations sont valides si toutes les variables utilisées (vecteurs position, vitesses, directions du trièdre, etc...) sont écrites dans le même référentiel. Cependant, quelques simplifications sont susceptibles d'être utilisées pour les termes de divergence, puisque, pour tout champ de vecteur $\vec{K}$, on a

$$\begin{gathered} \vec{K} = K_x \vec{x} + K_y \vec{y} = K_{x'} \vec{x'} + K_{y'} \vec{y'} \\ \Downarrow \\ \frac{\partial K_x}{\partial x} + \frac{\partial K_y}{\partial y} = div_{\vec{x}}(\vec{K}) = div_{\vec{x'}}(\vec{K}) = \frac{\partial K_{x'}}{\partial x'} + \frac{\partial K_{y'}}{\partial y'}. \end{gathered} \tag{2.18}$$

• Remarque : on peut à nouveau utiliser un changement de variable à partir de la formulation précédente. Comme les équations (2.16) et (2.17) sont déjà compliquées, le coût marginal du passage en nouvelles variables est faible. Une nouvelle carte est donnée par

$$\left\{ \begin{array}{lcl} \tau &=& t \\ \xi' &=& \xi'(x', y', t) \\ \eta' &=& \eta'(x', y', t), \end{array} \right. \tag{2.19}$$

et le changement de variable donne pour nouvelle équation

$$\boxed{\frac{\partial \hat{Q}'}{\partial \tau} + \frac{\partial \hat{F}'}{\partial \xi'} + \frac{\partial \hat{G}'}{\partial \eta'} = \hat{S}'} \tag{2.20}$$

où

$$\hat{S}' = J'^{-1} S' \tag{2.21}$$

et $\hat{Q}'$, $\hat{E}'$, $\hat{F}'$ et J' sont donnés par des équations correspondant à (2.6), (2.7), (2.8) et (2.11) – écrites avec les nouvelles variables u', v', e', U', V', ξ', η', x', y'.

Algorithme :

• L'algorithme ressemble beaucoup au précédent. On suppose qu'au début d'un pas de temps, on dispose du champ de vecteurs $\hat{Q}'$, des changements de variables $x' = x'(\xi', \eta', \tau)$, $y' = y'(\xi', \eta', \tau)$, et de leurs dérivées en espace, $x'_{\xi'}$, $x'_{\eta'}$, $y'_{\xi'}$, $y'_{\eta'}$, et en temps, x'_τ et y'_τ. Les données définissant les référentiels sont aussi supposées connues (i.e. $\vec{r_j}$, T_j, $\vec{V_j}$, $\vec{a_j}$, $\vec{\omega_j}$, $\dot{\vec{\omega_j}}$), ainsi que la zone correspondant à chaque référentiel.

• Le système (2.20) est avancé en temps de t^n à $t^{n+1} = t^n + \Delta t^n$ avec les quantités précédentes. Toutes les conditions aux limites sont traduites dans les nouveaux référentiels, avec les nouvelles variables.

• Finalement, toutes les quantités géométriques sont mises à jour avec des schémas ressemblant à (2.12) et (2.13). Les éléments de définition des référentiels doivent aussi être mis à jour. Cette tâche devrait être simple, puisque ces référentiels ont été introduits pour cela (par exemple, dans le cas d'un profil d'aile rigide, il n'y a qu'un seul référentiel lié à l'aile; sa mise à jour se fait en collant au mouvement de l'aile connu à l'avance). L'accélération $\vec{a_j}$ – il en va de même pour l'accélération angulaire $\dot{\vec{\omega_j}}$ – est mise à jour par des schémas du type

$$\vec{a_j}^{\,n+1} = \frac{1}{\Delta t^n}(\vec{V_j}^{\,n+1} - \vec{V_j}^{\,n}) \quad \text{(ordre 1)} \tag{2.22}$$

$$\text{or :} \quad \vec{a_j}^{\,n+1} = \frac{2}{\Delta t^n}(\vec{V_j}^{\,n+1} - \vec{V_j}^{\,n}) - \vec{a_j}^{\,n} \quad \text{(ordre 2).} \tag{2.23}$$

Avantages de ces méthodes :

Jusqu'à maintenant, les avantages éventuels de ces méthodes peuvent paraître submergés par les inconvénients que nous avons déjà mentionnés et par la lourdeur nouvelle des expressions. Nous montrons dans la suite quelques cas où ces formulations dans plusieurs référentiels et avec changement de variables simplifient et allègent la simulation numérique.

Une première famille d'applications regroupe les cas où une ou plusieurs structures sont en mouvement rigide dans un écoulement externe. C'est le cas par exemple du profil d'aile rigide présenté par Kandil et Chuang dans [42]. Pour les cas à deux structures, comme la chute d'un missile rigide sous une aile dans un écoulement, ou l'interaction d'une boîte libre sur le sol et d'un choc, présentés par Löhner [51], deux référentiels au moins sont nécessaires (pour être efficace près de chaque objet). Par contre, lorsqu'une seule structure est présente, un référentiel unique lié à elle permet de se débarasser de

tout problème de mouvement de maillage. De plus, le terme source $\hat{S}'$ dans (2.20) est un peu simplifié, puisque $div(\vec{V}_t) = 0$.

Une deuxième famille d'applications concerne les structures en petites déplacements dans un écoulement. Bien sûr, une changement de référentiel peut être utilisé pour traiter le mouvement rigide de la structure s'il y a lieu. Comme les changements de forme sont assez faibles, le maillage et la métrique doivent être recalculés. Cependant, Lin a montré [25] que la connaissance de la position des points du maillage n'est pas nécessaire pour résoudre (2.20), et que l'on peut utiliser un schéma approché pour la mise à jour des variables géométriques. Dans le cas d'un écoulement autour d'un profil d'aile souple, Lin emploie un référentiel par ligne $\xi = \xi_j$ du maillage (voir Figure 2.3). Chaque référentiel a pour origine le point dont les coordonnées curvilignes sont (ξ_j, η_0), et reste parallèle à la corde du profil. L'idée principale du schéma est simple : les variations des grandeurs géométriques en un point sont déduites par une interpolation linéaire des variations de ces mêmes grandeurs sur le bord de l'aile flexible. Ces dernières sont elles-mêmes calculées à partir des déplacements de la structure (voir [50] pour avoir des détails). On comprend bien que cette approche est optimale pour ce genre de problème. En effet, dans un souci d'efficacité, on a tiré parti de l'aspect des conditions à l'infini pour le fluide (pas de limite définie fixe), de l'utilisation de référentiels multiples et de coordonnées curvilignes pour suivre les déformations de l'aile.

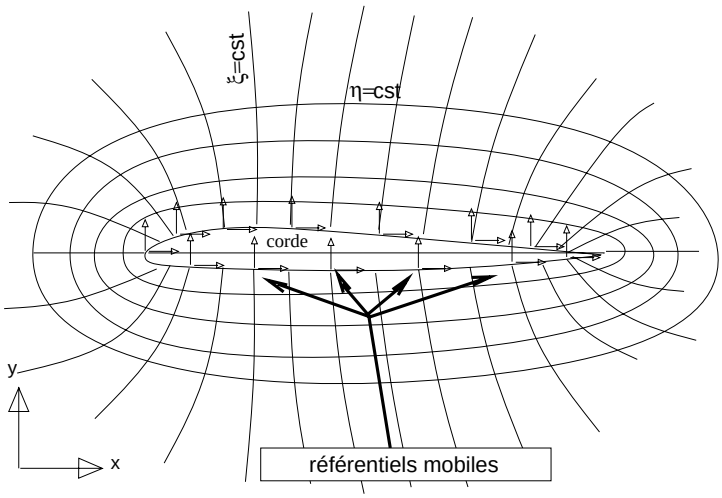

FIG. 2.3 – *Référentiels multiples liés au profil d'aile.*

Bien que ces méthodes permettent de faire de grosses économies en temps et en mémoire lors de certaines simulations numériques bien particulières, elle ne sont pas générales. En outre, certaines astuces, comme les interpolations simples utilisées pour mettre à jour la métrique, doivent être adaptées à chaque simulation. Mais surtout, deux inconvénients semblent inévitables. D'abord, le traitement de grands ou rapides déplacements reste problématique. Ensuite, le changement en variables curvilignes requiert l'utilisation d'un maillage structuré, d'emploi difficile et peu général pour des configurations complexes.

Nous nous tournons maintenant vers un type de formulation, qui évite ces inconvénients. Dans les méthodes précédentes, une portion de l'espace fictif représente une portion de l'espace physique qui se déforme. Dans les méthodes utilisant une formulation arbitrairement Lagrangienne ou Eulérienne (ALE) ou dans les méthodes à maillage mobile, on utilise des cellules déformables et on profite de la forme conservative des équations d'Euler d'origine. Notons au passage que ces cellules déformables peuvent être par exemple issues d'un maillage non-structuré.

2.2.3 Méthodes ALE

La formulation arbitrairement Lagrangienne-Eulérienne (ALE) a été construite pour éviter les inconvénients des deux approches purement Lagrangienne et Eulérienne [20]. D'une part, l'approche Lagrangienne est assez efficace pour la description cinématique du fluide dans certains problèmes hydroélastiques [19], mais se révèle inefficace lorsque l'écoulement devient complexe et impossible à suivre sur une durée assez longue. D'autre part, la formulation purement Eulérienne permet difficilement de suivre avec précision ce qui se passe dans le fluide le long de l'interface fluide-structure. Ainsi, on aimerait réaliser le mélange parfait entre une approche Lagrangienne le long de la structure et une approche Eulérienne à l'intérieur du domaine fluide.

Le principe de base de la formulation ALE consiste à adopter une approche hybride, qui peut revêtir un aspect Lagrangien ou Eulérien à la demande. Dans une approche purement Lagrangienne, notre point de vue est lié à une particule dans l'écoulement. Dans une approche purement Eulérienne, notre point de vue est celui du laboratoire physique. Dans une approche ALE, notre point de vue est lié à un maillage mobile imaginaire du domaine fluide. Appelons $\vec{w}$ la vitesse de ce maillage. Elle n'est pas forcément nulle (comme dans une approche Eulérienne) ni égale à la vitesse du fluide (comme dans une approche Lagrangienne). Elle peut varier arbitrairement et continûment d'une valeur à l'autre.

Dans la suite, nous présentons en détail la formulation ALE d'un problème aéroélastique et l'algorithme le plus couramment utilisé (cf [20]). Nous terminons avec une discussion sur la méthode proposée, qui, rappelons-le, dérive historiquement de problèmes hydroélastiques (où l'approche Lagrangienne est préférée).

Formulation :

• Dans la suite, les coordonnées physiques dans le repère du laboratoire sont notées $\vec{x}$. Nous utiliserons également des coordonnées Lagrangiennes liés au fluide, notées $\vec{a}$. Une dérivation où $\vec{a}$ est fixé correspond à une dérivée particulaire (en suivant une particule fluide dans son mouvement).

• On s'intéresse à un variable physique quelconque "g". Elle sera notée $\tilde{g}$ quand on

la considérera comme une fonction du temps et des coordonnées Lagrangiennes $(\vec{a}, t)$. La notation g sera réservée à l'approche Eulérienne, où l'on verra la grandeur comme une fonction du temps et des coordonnées dans le repère du laboratoire $(\vec{x}, t)$.

• La formulation ALE utilise des coordonnées mixtes. On peut dire qu'elles dépendent des coordonnées Lagrangiennes $(\vec{a}, t)$ et seront notées

$$\overrightarrow{\xi} = \overrightarrow{\xi}(\vec{a}, t) \tag{2.24}$$

Pour simplifier les écritures, on a écrit $\vec{\xi}$ à la place de $\widetilde{\vec{\xi}}$. On définit le Jacobien et la vitesse des variables mixtes par

$$\widetilde{J}(\vec{a}, t) = \det\left(\left.\frac{\partial \vec{\xi}}{\partial \vec{a}}\right|_t (\vec{a}, t)\right) \tag{2.25}$$

$$\widetilde{\vec{w}}(\vec{a}, t) = \left.\frac{\partial \vec{\xi}}{\partial t}\right|_{\vec{a}} (\vec{a}, t), \tag{2.26}$$

où une variable en indice signifie qu'elle a été maintenue constante pour une dérivation. Cette description arbitrairement Lagrangienne-Eulérienne est résumée sur la Figure 2.4.

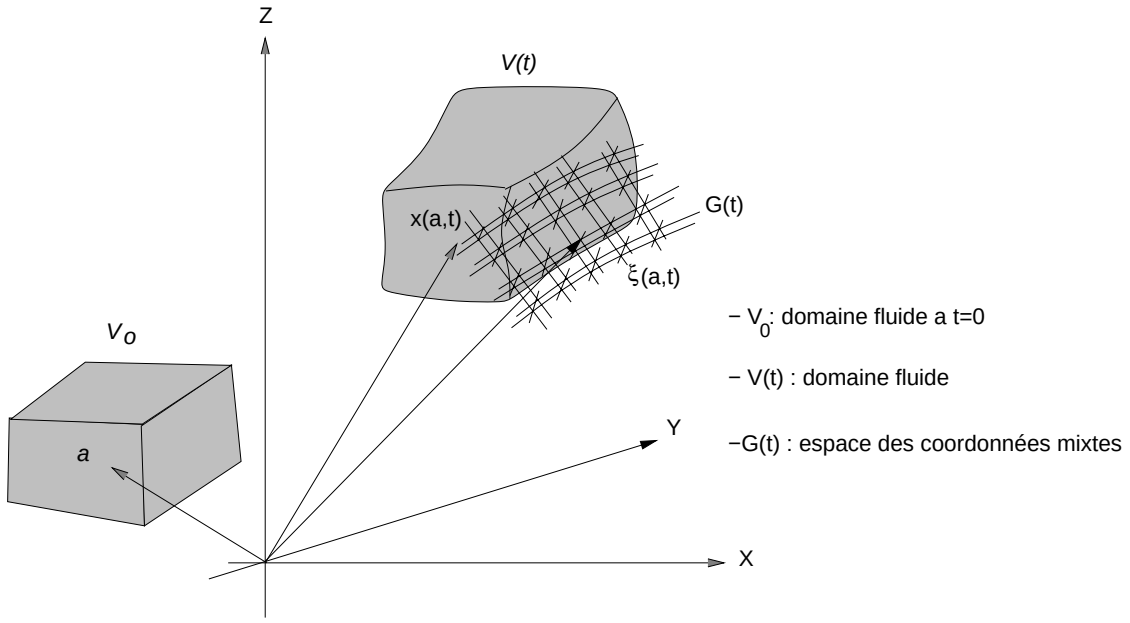

FIG. 2.4 – *Variables Lagrangiennes, Eulériennes et mixtes pour les méthodes ALE.*

• Pour présenter la formulation ALE, nous avons aussi besoin du passage des coordonnées Lagrangiennes aux coordonnées physiques Eulériennes. On definit pour toute fonction $\tilde{g}$ des coordonnées Lagrangiennes, la fonction $\bar{g}$ des coordonnées physiques par :

$$\bar{g}(\vec{x}, t) = \tilde{g}(\vec{a}, t) \text{ où } \vec{a} \text{ est tel que } \vec{x} = \vec{\xi}(\vec{a}, t). \tag{2.27}$$

Réciproquement, pour toute fonction Eulérienne $\bar{g}$, on définit la fonction $\tilde{g}$ des variables Lagrangiennes par :

$$\tilde{g}(\vec{a},t) = \bar{g}(\vec{x},t) \text{ où } \vec{x} \text{ est donné par : } \vec{x} = \vec{\xi}(\vec{a},t). \tag{2.28}$$

Pour ces deux correspondances réciproques, nous avons l'identité

$$\bar{g}(\vec{\xi}(\vec{a},t),t) = \tilde{g}(\vec{a},t). \tag{2.29}$$

• Nous énonçons maintenant deux lemmes généraux assez simples et purement algébriques. On trouvera dans la suite les démonstrations de lemmes similaires (Lemme 3 et Lemme 4). Le premier lemme donne une équation différentielle pour l'évolution du Jacobien mixte $\widetilde{J}$ defini plus haut.

Lemme 1 *$\widetilde{J}$ est solution de l'equation différentielle :*

$$\left.\frac{\partial \widetilde{J}}{\partial t}\right|_{\vec{a}} (\vec{a},t) = \widetilde{J}(\vec{a},t)\, div_{\vec{\xi}}(\bar{\vec{w}}) \left(\vec{\xi}(\vec{a},t),t\right). \tag{2.30}$$

Le deuxième lemme nous donne une relation entre les dérivées temporelles Lagrangiennes (à coordonnées $\vec{a}$ fixées) et Eulériennes (à coordonnées $\vec{x}$ fixées) d'une grandeur scalaire quelconque.

Lemme 2 *Soit g une grandeur scalaire suffisamment régulière, on a*

$$\left.\frac{\partial(\widetilde{J}\widetilde{g})}{\partial t}\right|_{\vec{a}} (\vec{a},t) = \widetilde{J}(\vec{a},t) \left[\left.\frac{\partial \bar{g}}{\partial t}\right|_{\vec{\xi}} + div_{\vec{\xi}}(\bar{g}\bar{\vec{w}})\right] \left(\vec{\xi}(\vec{a},t),t\right) \quad . \tag{2.31}$$

On remarquera que le premier lemme est une application du second avec $g = 1$. Physiquement, le premier lemme correspond à une conservation du volume, alors que le second correspond à la conservation d'une grandeur volumique quelconque g.

• Considérons le vecteur des variables conservatives $\bar{Q}$ défini en (2.3) comme une fonction des variables Eulériennes, et la fonction Lagrangienne correspondante $\tilde{Q}$ définie en (2.28). Le lemme précédent peut être appliqué à chaque composante de $\tilde{Q}$. Comme $\bar{Q}$ est solution des équations d'Euler, on obtient la formulation ALE suivante :

$$\boxed{\left.\frac{\partial(\widetilde{J}\widetilde{Q})}{\partial t}\right|_{\vec{a}} (\vec{a},t) + \widetilde{J}(\vec{a},t)\, div_{\vec{x}} \left[(\bar{F},\bar{G}) - \bar{Q}\otimes\bar{\vec{w}}\right] \left(\vec{\xi}(\vec{a},t),t\right) = 0.} \tag{2.32}$$

qui peut être développée en :

$$\left\{\begin{array}{lll}
\left.\dfrac{\partial(\widetilde{J}\widetilde{\rho})}{\partial t}\right|_{\vec{a}}(\vec{a},t) & +\widetilde{J}(\vec{a},t)\ \left[div_{\vec{x}}\left(\overline{\rho(\vec{v}-\vec{w})}\right)\right]\left(\vec{\xi}(\vec{a},t),t\right) & =0, \\[2ex]
\left.\dfrac{\partial(\widetilde{J}\widetilde{\rho u})}{\partial t}\right|_{\vec{a}}(\vec{a},t) & +\widetilde{J}(\vec{a},t)\ \left[div_{\vec{x}}\left(\overline{\rho u(\vec{v}-\vec{w})}\right)+\bar{P}_x\right]\left(\vec{\xi}(\vec{a},t),t\right) & =0, \\[2ex]
\left.\dfrac{\partial(\widetilde{J}\widetilde{\rho v})}{\partial t}\right|_{\vec{a}}(\vec{a},t) & +\widetilde{J}(\vec{a},t)\ \left[div_{\vec{x}}\left(\overline{\rho v(\vec{v}-\vec{w})}\right)+\bar{P}_y\right]\left(\vec{\xi}(\vec{a},t),t\right) & =0, \\[2ex]
\left.\dfrac{\partial(\widetilde{J}\widetilde{E})}{\partial t}\right|_{\vec{a}}(\vec{a},t) & +\widetilde{J}(\vec{a},t)\ \left[div_{\vec{x}}\left(\overline{E(\vec{v}-\vec{w})+P\vec{V}}\right)\right]\left(\vec{\xi}(\vec{a},t),t\right) & =0.
\end{array}\right. \tag{2.33}$$

On peut facilement vérifier que ces équations prennent la forme des équations de Lagrange pour le fluide, lorsque $\vec{w}=\vec{v}$, et se réduisent aux équations d'Euler classiques pour $\vec{w}=\vec{0}$.

• On peut au passage ontenir une formulation assez intéressante et concise. Si l'on intègre l'équation (2.32) sur un élément de volume matériel (qui suit donc le fluide au cours du temps), les dérivées temporelles peuvent être repoussées à l'extérieur des intégrales, et, après un changement de coordonnées de $\vec{a}$ vers $\vec{\xi}$, on obtient :

$$\boxed{\frac{\partial}{\partial t}\int_{V_{\vec{\xi}}(t)}\bar{Q}\ d\vec{\xi}+\int_{V_{\vec{\xi}}(t)}div_{\vec{x}}\left((F,G)(\bar{Q})-\bar{Q}\otimes\bar{W}\right)d\vec{\xi}=0.} \tag{2.34}$$

On tirera plus tard avantage de cette formulation, d'où les coordonnées matérielles ont presque totalement disparu (néanmoins, il faut se rappeler que les intégrales sont faites sur un domaine matériel bougeant avec le fluide). Cette formulation est en effet utilisée dans les méthodes à maillage dynamique.

Algorithme :

L'algorithme utilisé couramment avec les méthodes purement ALE est vraiment particulier, et assez différent des autres algorithmes utilisés pour simuler une interaction fluide-structure. Même si la formulation générale est proche de celle des méthodes à maillage dynamique, l'intégration en temps se fait en deux temps, dont l'un est plutôt Lagrangien, et empêche l'utilisation d'un schéma global décentré. Ce type de méthode a été historiquement conçu par des mécaniciens des structures, habitués aux équations sous forme Lagrangienne, contrairement aux méthodes à maillage dynamique élaborées par des mécaniciens des fluides, habitués aux formulations Eulériennes. Cette formulation a cependant l'avantage de traiter avec précision l'intégration simultanée des actions mutuelles du fluide et de la structure [20].

• Dans un premier temps, on traite de la partie Lagrangienne de tous les flux. On calcule les vitesses Lagrangiennes près de l'interface fluide-structure, ce qui permet un bon traitement de l'interaction. En supposant que $\vec{w} = \vec{v}$, on calcule la partie Lagrangienne de la seconde intégrale de (2.34). Cette phase peut même être faite avec un schéma implicite et en parallèle avec l'évolution de la structure lors d'une simulation fluide-structure.

• Dans un second temps, on calcule le reste des termes. Connaissant le mouvement de la structure, on met à jour l'ensemble du maillage fluide par un algorithme du type de ceux que l'on a déjà présentés en (2.12) et (2.13). Pour cela, on doit choisir un champ de vitesses $\vec{w}$. On doit également corriger les termes Lagrangiens calculés plus haut et rajouter les termes purement convectifs.

Avantages et inconvénients :

Les méthodes ALE ont clairement plusieurs avantages. D'abord, elles utilisent des équations plutôt simples, lorsqu'on les compare aux méthodes présentés plus haut. La seule complexité ajoutée provient des Jacobiens des coordonnées mixtes. De plus, ces méthodes peuvent être appliquées avec tout type de géométrie, puisqu'aucune forme particulière du maillage n'est requise. Enfin, la séparation en deux sous-pas, dont l'un est purement Lagrangien, permet de faire jouer au fluide et à la structure le même rôle près de leur interface, ce qui devrait respecter avec une très grande précision le principe d'action et de réaction. Cependant, cette formulation n'est pas optimale, puisqu'elle ne s'affranchit pas de certaines difficultés liées aux formulations Lagrangiennes. De plus, la séparation en deux sous-pas nous oblige à utiliser un pas de temps très petit pour obtenir des résultats précis. Enfin, ce genre de méthodes ne permet pas d'utiliser l'ensemble des schémas décentrés dont on dispose.

En somme, la difficulté de la simulation a été transférée du lieu de l'interaction fluide-structure (l'interface) à l'intérieur du fluide, où un splitting entre flux Lagrangiens et Eulériens a été fait. Nous allons maintenant nous intéresser aux méthodes à maillage dynamique, plus proches des approches purement Eulériennes.

2.2.4 Méthodes à maillage dynamique

Les méthodes à maillage dynamique s'appuient sur une discrétisation du domaine fluide qui est mobile. Cependant, la vitesse de chaque nœud du maillage n'est pas considérée comme une vitesse Lagrangienne, mais bien comme une vitesse propre du maillage. Ce type de formulation ne s'appuie ni sur une forme particulière des cellules (triangles, quadrangles, etc...), ni sur l'aspect du maillage (structuré ou non-structuré). Ces méthodes se différencient des méthodes ALE par le fait qu'aucune référence aux coordonnées Lagrangiennes n'est faite.

Formulation :

• Bien que cette nouvelle formulation puisse être déduite de la formulation ALE générale vue plus haut, nous choisissons de l'obtenir complètement sans faire appel à aucune variable Lagrangienne. Nous utilisons de nouveau des coordonnées mixtes $\vec{\xi}$ dont les courbes de niveau peuvent être vue comme les lignes du maillage. Les deux systèmes de coordonnées $\vec{x}$ et $\vec{\xi}$ dépendent du temps, et l'un de l'autre. Ceci s'exprime par :

$$\vec{\xi} = \vec{\xi}(\vec{x}, t) \qquad \text{et} \qquad \vec{x} = \vec{x}(\vec{\xi}, t). \tag{2.35}$$

On introduit aussi le Jacobien J de la transformation et la vitesse de maillage $\vec{w}$ par

$$J = \det\left(\left.\frac{\partial \vec{x}}{\partial \vec{\xi}}\right|_t\right) \qquad \text{et} \qquad \vec{w} = \left.\frac{\partial \vec{x}}{\partial t}\right|_{\vec{\xi}} \quad . \tag{2.36}$$

Comme précédemment, les indices attachés aux dérivations signifient que les variables sont maintenues constantes. On utilise aussi les notations suivantes :

$$\vec{\nabla}_{\vec{x}} g = (\frac{\partial g}{\partial x_1}, \ldots, \frac{\partial g}{\partial x_D})^t \qquad \text{et} \qquad div_{\vec{x}}(\vec{g}) = \sum_i \frac{\partial g_i}{\partial x_i}.$$

Nous commençons par établir un lemme algébrique classique :

Lemme 3 *Le Jacobien J est solution de l'équation différentielle suivante :*

$$\left.\frac{\partial J}{\partial t}\right|_{\vec{\xi}} = J \; div_{\vec{x}}(\vec{w}) \tag{2.37}$$

Démonstrations :

Nous donnons une première démonstration un peu originale. Notant Tr pour l'opérateur de trace, on a :

$$div_{\vec{x}}(\vec{w}) = \sum_i \frac{\partial w_i}{\partial x_i} = \sum_i \sum_j \frac{\partial w_i}{\partial \xi_j} \frac{\partial \xi_j}{\partial x_i} = Tr(\left[\frac{\partial \vec{w}}{\partial \vec{\xi}}\right] \left[\frac{\partial \vec{\xi}}{\partial \vec{x}}\right]). \tag{2.38}$$

Si l'on écrit $\mathcal{J}$ à la place de $\partial \vec{x}/\partial \vec{\xi}$, et si l'on note que $\partial \vec{w}/\partial \vec{\xi} = \partial \mathcal{J}/\partial t \stackrel{\text{def}}{=} \mathcal{J}'$, on déduit de (2.38) que

$$div_{\vec{x}}(\vec{w}) = Tr(\mathcal{J}' \mathcal{J}^{-1}). \tag{2.39}$$

Pour s assez petit, on a :

$$\mathcal{J}(t+s) = \mathcal{J}(t)\left(Id + s\mathcal{J}(t)^{-1}\mathcal{J}'(t) + o(s)\right) = \mathcal{J}\exp(s\mathcal{J}^{-1}\mathcal{J}') + o(s).$$

Comme le déterminant est une fonction continue, en utilisant les identités classiques $Tr(AB) = Tr(BA)$ et $det(\exp(sA)) = \exp(s\; Tr(A))$, on trouve

$$J(t+s) = J(t)\exp(s\; Tr(\mathcal{J}'\mathcal{J}^{-1})) + o(s) = J(t) + s\; J(t) Tr(\mathcal{J}'\mathcal{J}^{-1}) + o(s),$$

et donc

$$J' = J\ Tr(\mathcal{J}'\mathcal{J}^{-1}), \tag{2.40}$$

ce qui conclut la première démonstration. □

Nous donnons maintenant une démonstration plus classique. En developpant la dérivée d'un déterminant comme la somme des déterminants où chaque ligne successivement a été dérivée, on obtient :

$$\left.\frac{\partial J}{\partial t}\right|_{\vec{\xi}} = \sum_i \begin{vmatrix} \frac{\partial \vec{x}_1}{\partial \vec{\xi}_1} & \cdots & \frac{\partial \vec{x}_1}{\partial \vec{\xi}_N} \\ \vdots & & \vdots \\ \frac{\partial \vec{w}_i}{\partial \vec{\xi}_1} & \cdots & \frac{\partial \vec{w}_i}{\partial \vec{\xi}_N} \\ \vdots & & \vdots \\ \frac{\partial \vec{x}_N}{\partial \vec{\xi}_1} & \cdots & \frac{\partial \vec{x}_N}{\partial \vec{\xi}_N} \end{vmatrix} = \sum_i \begin{vmatrix} \frac{\partial \vec{x}_1}{\partial \vec{\xi}_1} & \cdots & \frac{\partial \vec{x}_1}{\partial \vec{\xi}_N} \\ \vdots & & \vdots \\ \sum_j \frac{\partial \vec{w}_i}{\partial \vec{x}_j}\frac{\partial \vec{x}_j}{\partial \vec{\xi}_1} & \cdots & \sum_j \frac{\partial \vec{w}_i}{\partial \vec{x}_j}\frac{\partial \vec{x}_j}{\partial \vec{\xi}_N} \\ \vdots & & \vdots \\ \frac{\partial \vec{x}_N}{\partial \vec{\xi}_1} & \cdots & \frac{\partial \vec{x}_N}{\partial \vec{\xi}_N} \end{vmatrix}.$$

Dans le $i$ème déterminant écrit ci-dessus, la $i$ème ligne s'écrit quasiment comme une combinaison linéaire des $N-1$ autres lignes. Elle s'écrit en fait comme $\partial \vec{w}_i/\partial \vec{x}_1$ fois la première, plus $\partial \vec{w}_i/\partial \vec{x}_2$ fois la deuxième, etc... Ainsi, en retranchant justement les lignes du déterminant, on arrive à réduire la $i$ème ligne aux termes suivants :

$$\left.\frac{\partial J}{\partial t}\right|_{\vec{\xi}} = \sum_i \frac{\partial \vec{w}_i}{\partial \vec{x}_i} \begin{vmatrix} \frac{\partial \vec{x}_1}{\partial \vec{\xi}_1} & \cdots & \frac{\partial \vec{x}_1}{\partial \vec{\xi}_N} \\ \vdots & & \vdots \\ \frac{\partial \vec{x}_i}{\partial \vec{\xi}_1} & \cdots & \frac{\partial \vec{x}_i}{\partial \vec{\xi}_N} \\ \vdots & & \vdots \\ \frac{\partial \vec{x}_N}{\partial \vec{\xi}_1} & \cdots & \frac{\partial \vec{x}_N}{\partial \vec{\xi}_N} \end{vmatrix} = J\ div_{\vec{x}}(\vec{w}).$$

Ceci conclut cette deuxième démonstration. □

Du lemme précédent, on déduit le

Lemme 4 *Pour toute quantité scalaire g (suffisamment régulière), on a :*

$$\left.\frac{\partial (Jg)}{\partial t}\right|_{\vec{\xi}} = J\ \left(\left.\frac{\partial g}{\partial t}\right|_{\vec{x}} + div_{\vec{x}}(g\vec{w}) \right) \quad . \tag{2.41}$$

Démonstration :
On peut utiliser la relation classique entre les dérivées temporelles à $\vec{\xi}$ et à x constants suivante :

$$\left.\frac{\partial g}{\partial t}\right|_{\vec{\xi}} = \left.\frac{\partial g}{\partial t}\right|_{\vec{x}} + \vec{\nabla}_{\vec{x}} g . \left.\frac{\partial \vec{x}}{\partial t}\right|_{\vec{\xi}}. \tag{2.42}$$

En multipliant par J et en utilisant la définition de $\vec{w}$, on obtient :

$$J \left.\frac{\partial g}{\partial t}\right|_{\vec{\xi}} = J \left.\frac{\partial g}{\partial t}\right|_{\vec{x}} + J \overrightarrow{\nabla}_{\vec{x}} g.\vec{w} \quad . \tag{2.43}$$

Si on multiplie les deux membres de (2.37) par g et si on l'ajoute à (2.43), on obtient le résultat (2.41), puisque on a

$$div_{\vec{x}}(g\vec{w}) = g\ div_{\vec{x}}(\vec{w}) + \overrightarrow{\nabla}_{\vec{x}} g.\vec{w} \quad \square$$

Si l'on applique le lemme précédent aux variables conservatives ρ, ρu, ρv et E, on obtient une nouvelle forme des équations d'Euler :

$$\boxed{\left.\frac{\partial (JQ)}{\partial t}\right|_{\vec{\xi}} + J\ div_{\vec{x}} \vec{\bar{F}} = 0} \tag{2.44}$$

où

$$\bar{F}_x = \begin{pmatrix} \rho\bar{u} \\ \rho u\bar{u} + P \\ \rho v\bar{u} \\ E\bar{u} + Pu \end{pmatrix}, \quad \bar{F}_y = \begin{pmatrix} \rho\bar{v} \\ \rho u\bar{v} \\ \rho v\bar{v} + P \\ E\bar{v} + Pv \end{pmatrix} \quad \text{et} \quad \left| \begin{array}{l} \bar{u} = u - w_x \\ \bar{v} = v - w_y \end{array} \right. \quad . \tag{2.45}$$

Il est intéressant de remarquer que l'on retrouve à nouveau des équations pleines de sens pour certains choix particuliers des coordonnées mixtes $\vec{\xi}$. Lorsque $\vec{\xi}(\vec{x}, t) = \vec{x}$, on retrouve en (2.44) et (2.45) les équations d'Euler classiques puisque $\vec{w} = \vec{0}$. Lorsqu'on choisit $\vec{\xi}(\vec{x}, t) = \vec{a}(\vec{x}, t)$ (coordonnées Lagrangiennes), on obtient la formulation Lagrangienne de la dynamique des gaz.

• On peut obtenir une formulation intégrale de (2.44) qui est la même que celle utilisée par Batina dans [5]. Soit C une cellule de la discrétisation. Elle occupe en fait le domaine $C_{\vec{x}}$ dans les coordonnées du laboratoire et le domaine $C_{\vec{\xi}}$ dans l'espace des coordonnées mixtes. On fait l'hypothèse forte que le domaine $C_{\vec{\xi}}$ ne dépend pas du temps. En intégrant (2.44) sur $C_{\vec{\xi}}$, on trouve :

$$\int_{C_{\vec{\xi}}} \left.\frac{\partial (JQ)}{\partial t}\right|_{\vec{\xi}} d\vec{\xi} + \int_{C_{\vec{\xi}}} J\ div_{\vec{x}} \vec{\bar{F}}\ d\vec{\xi} = 0.$$

Comme la dérivée en temps est prise à $\vec{\xi}$ constant, et comme justement le domaine $C_{\vec{\xi}}$ est indépendant du temps, on peut faire sortir la dérivation en temps de l'intégrale. De plus, on peut faire le changement de variables $\vec{\xi} = \vec{\xi}(\vec{x}, t)$ (avec le changement de mesure $d\vec{x} = J\, d\vec{\xi}$), on obtient finalement :

$$\boxed{\frac{d}{dt}\left[\int_{C_{\vec{x}}} Q\, d\vec{x}\right] + \int_{C_{\vec{x}}} div_{\vec{x}} \vec{\bar{F}}\, d\vec{x} = 0.} \tag{2.46}$$

Rappelons quand même que cette formule n'est valable que si le domaine $C_{\vec{x}}$ correspond à une cellule fixe dans l'espace des coordonnées mixtes. Cette formule se prète bien à une méthode de volumes finis. En utilisant des moyennes par cellule, on écrit :

$$A_i^{n+1}Q_i^{n+1} - A_i^n Q_i^n + \Delta t \sum_{j=1}^{n(i)} \|\widetilde{\partial C_{ij}}\|.\bar{\Phi}(Q_i, Q_j, \widetilde{\vec{\eta_{ij}}}) = 0, \tag{2.47}$$

où Q_i^n est la moyenne de Q dans la cellule C_i à l'instant t^n, A_i^n est l'aire de la cellule C_i à t^n, $\Delta t = t^{n+1} - t^n$ est le pas de temps, $n(i)$ est le nombre de cellules voisines de C_i, $\widetilde{\partial C_{ij}}$ est une moyenne temporelle de la position de l'interface entre les cellules C_i et C_j (dont la longueur est $\|\widetilde{\partial C_{ij}}\|$ et la normale orientée de C_i vers C_j est $\widetilde{\vec{\eta_{ij}}}$), et finalement $\bar{\Phi}$ est un flux numérique tel que

$$\Delta t \ \|\widetilde{\partial C_{ij}}\| \ \bar{\Phi}(Q_i, Q_j, \widetilde{\vec{\eta_{ij}}}) \simeq \int_{t^n}^{t^n+\Delta t} \left[\int_{\partial C_{ij}} \vec{\vec{F}}.\vec{\eta_{ij}} \, d\sigma \right] d\tau \ . \tag{2.48}$$

On trouvera dans [35] une formulation générale des schémas de type Godunov pour les équations hyperboliques mono-dimensionnelles écrits en maillage dynamique. Pour la résolution de (2.44), on peut faire appel au large éventail de méthodes décentrées déjà écrites pour les maillages fixes. Par exemple, on peut déduire de (2.48) une méthode de type Roe en maillage dynamique [35]. En deux dimensions, un flux numérique de Roe prend la forme suivante :

$$\bar{\Phi}(Q_i, Q_j, \vec{\eta}) = \frac{1}{2} \left[\left(\vec{\vec{F}}_i + \vec{\vec{F}}_j \right) .\vec{\eta} - \left| \tilde{A} - (\vec{w}.\vec{\eta}) \, I \right| (Q_i - Q_j) \right], \tag{2.49}$$

où $\tilde{A}$ est la matrice de Roe pour le flux $\vec{\vec{F}}.\vec{\eta}$ et le signe $|\ |$ signifie que l'on prend les valeurs absolues des valeurs propres dans la diagonalisation.

Le flux de type Roe défini ci-dessus appelle deux remarques. D'abord, on peut montrer facilement que ce flux numérique ne depend du champ de vitesse de maillage $\vec{w}$ que par sa composante normale $\vec{w}.\vec{\eta}$. Ensuite, il fait garder à l'esprit que le champ des vitesses de maillage varie au cours du temps. Il faut donc utiliser des moyennes temporelles $\widetilde{\vec{w}}$, $\widetilde{\partial C_{ij}}$ et $\widetilde{\vec{w}}.\widetilde{\vec{\eta_{ij}}}$ dans (2.49) et les choisir au mieux.

Des expressions identiques à (2.49) peuvent être obtenues à partir d'une approche spatio-temporelle des équations d'Euler. Dans [56], N'Konga et Guillard considèrent des volumes de contrôle dans l'espace-temps, qui sont générés par le balayage d'une cellule C_i au cours d'un pas de temps. En intégrant les équations d'Euler sur ces volumes, ils obtiennent la formulation (2.47). Par contre, ils donnent une justification de choix géométriques naturels pour $\widetilde{\partial C_{ij}}$ et $\widetilde{\vec{w}}.\widetilde{\vec{\eta_{ij}}}$. En appelant P_{ij1} et P_{ij2} les extrémités du segment ∂C_{ij}, on prend pour $\widetilde{\partial C_{ij}}$ le segment dont les extremités sont les positions moyennes (au cours du pas de temps courant) des points P_{ij1} et P_{ij2}. Ils choisissent en outre

$$\widetilde{\vec{w}}.\widetilde{\vec{\eta_{ij}}} = \frac{1}{2} \left(\vec{w}(P_{ij1}) + \vec{w}(p_{ij2}) \right) .\widetilde{\vec{\eta_{ij}}}. \tag{2.50}$$

Nous verrons plus tard que ces choix très importants peuvent être justifiés par des considérations sur la conservation du volume.

L'extension aux maillages dynamiques pour différentes méthodes classiques a déjà été faite. Les plus populaires sont probablement les solveurs de Riemann approchés de type Roe et leurs extensions aux ordres supérieurs [43], ainsi que le "flux-vector splitting" de Van Leer [6].

Algorithme:

• Au début de chaque pas de temps, on intègre (2.44) avec la méthode définie par (2.47), (2.48) et (2.49).

• Dans un deuxième temps, on doit mettre à jour toutes les variables géométriques utilisées. Le schéma de mise à jour du champ de vecteurs $\vec{w}$ peut prendre une forme proche de (2.12) ou (2.13). De plus, l'algorithme très simple ainsi défini peut être agrémenté de multiples améliorations particulières, comme le raffinement de maillage [51] (qui s'adapte aussi assez bien aux méthodes ALE)) ou les méthodes multigrilles [54].

Cependant, la mise à jour des aires des cellules doit être faite en respectant une loi de conservation géométrique [72]. Comme on utilise généralement des schémas conservatifs, cette conservativité n'est effective que si les volumes eux-mêmes sont conservés. Ainsi, les aires des cellules utilisées dans (2.47) doivent être mises à jour selon un schéma particulier. Comme pour l'équation (2.14) dans les méthodes avec changement de variables, les aires des cellules doivent être mises à jour en appliquant le schéma (2.47) à un champ scalaire uniforme à la place de Q. Ceci évite des instabilités légères qui peuvent apparaître lorsque la conservation du volume n'est pas exacte [72]. Ainsi, ce schéma prend la forme :

$$A_i^{n+1} - A_i^n + \Delta t \sum_{j=1}^{n(i)} \|\widetilde{\partial C_{ij}}\|.(-\widetilde{\vec{w}}.\widetilde{\vec{\eta_{ij}}}) = 0. \tag{2.51}$$

Les variables $\widetilde{\partial C_{ij}}$ et $\widetilde{\vec{w}}.\widetilde{\vec{\eta_{ij}}}$ sont alors choisies de telle sorte que l'aire $\mathcal{S}$ balayée par ∂C_{ij} pendant le pas de temps Δt soit approchée au mieux par

$$\mathcal{S} \simeq \Delta t \, \|\widetilde{\partial C_{ij}}\| \left(\widetilde{\vec{w}}.\widetilde{\vec{\eta_{ij}}}\right). \tag{2.52}$$

Les formules donnés par N'Konga et Guillard [56] sont construites pour obtenir la plus petite erreur possible dans l'équation précédente.

Discussion sur la méthode:

Cette méthode comporte de nombreux avantages. D'abord, des schémas décentrés classiques peuvent être utilisés globalement, ce qui n'était pas le cas des formulations ALE. Les seules variables géométriques supplémentaires sont les vitesses de maillage, ce qui est optimal. Par contre, toutes les variables géométriques annexes doivent être

mises à jour à chaque pas de temps, mais on a vu que le schéma utilisé (2.51) est simple, conserve les volumes et évite des instabilités purement géométriques. Le seul inconvénient est le besoin de bouger le maillage après chaque pas de temps.

Bien que la méthode puisse s'avérer moins performante dans certains cas particuliers [25], elle est très certainement plus générale. De plus, des algorithmes assez simples [5] permettent de réduire les coûts de calcul induits par les mouvements du maillage.

2.2.5 Conclusion

Dans cette partie, nous avons présenté plusieurs méthodes numériques pour la simulation d'écoulements gazeux en domaine déformable. Nos équations modèles, les équations d'Euler (2.2–2.3), point de départ de toutes les formulations, ont pris des formes différentes. Elles furent écrites successivement en coordonnées curvilignes (2.5–2.6), puis dans des repères mobiles multiples (2.20) et finalement sous forme intégrale dans les méthodes ALE puis à maillage dynamique (2.34)-(2.46).

On peut noter que ces dernières sont relativement proches : les coordonnées matérielles ont disparu et des dérivées où les coordonnées physiques sont maintenues constantes sont toujours présentes. On peut d'ailleurs faire deux remarques. D'abord, la formulation ALE n'est clairement pas optimale, puisqu'elle fait référence à trois systèmes de coordonnées différents. On aurait pu se limiter aux coordonnées mixtes et matérielles, ou bien aux coordonnées mixtes et physiques (comme dans la formulation en maillage dynamique). Ensuite, les méthodes ALE et les formulations en maillage mobile ne diffèrent que par l'usage qui est fait d'une formulation intégrale. Pour les méthodes ALE, deux phases distinctes, l'une Lagrangienne et l'autre Eulérienne, sont séparées. Ceci leur permet d'être facilement utilisées pour des études hydroélastiques [20]. Par contre, l'utilisation de schémas décentrés populaires en "CFD" est plus facile en maillage dynamique.

Les méthodes que nous avons présentées sont également assez générales pour être appliquées aux formulations potentielles (théorie tridimensionnelle des petites perturbations pour des écoulements instationnaires non-visqueux [14] et équation tridimensionnelle instationnaire du potentiel [70]) ou équations de Navier-Stokes (version instationnaire tridimensionnelle en coordonnées curvilignes [34]).

Pour toutes les méthodes présentées, nous ne nous sommes pas attardés sur le traitement des conditions aux limites. En fait, elles n'apportent pas de difficultés particulières. Il faut simplement traduire leur contenu physique dans chaque reformulation particulière. Par exemple, pour un écoulement à l'infini, les variables conservatives doivent garder une valeur fixée.

Jusqu'à maintenant, on a supposé que les mouvements et les déformations de la structure, et donc des limites du domaine fluide, étaient connus. Ils sont d'ailleurs utilisés dans l'expression des conditions aux limites et dans tous les schémas de mise à jour des variables géométriques (changement de référentiel, ou mise à jour du maillage dynamique, etc...) Cela ne sera plus le cas pour de véritables simulations aéroélastiques.

2.3 Traitement de l'interaction fluide-structure

Dans cette partie, nous considérons le traitement effectif du couplage entre le fluide et la structure. Ce couplage a les mêmes caractéristiques, qu'il s'agisse d'un problème aéroélastique, hydroélastique, ou toute autre interaction fluide-structure. Nous reviendrons d'abord sur les aspects physiques de ce couplage, puis nous présenterons l'ensemble des méthodes numériques disponibles. Enfin, un algorithme simple et général sera présenté en détail.

2.3.1 Aspects physiques de l'interaction

Le couplage peut être vu comme un cycle d'interaction ou d'échanges entre le fluide et la structure. Ces échanges de quantité de mouvement et d'énergie ont lieu à chaque instant et sans délai. Les déplacements de l'interface fluide-structure induisent immédiatement une modification de l'écoulement. Réciproquement, une variation de la pression du fluide entraîne une variation dans les forces appliquées à la structure, ce qui modifie sont mouvement. On dit que le fluide et la structure sont couplés. On comprend aussi que ce couplage est particulier, car il intervient au bord des deux sous-sytèmes. Ce n'est pas le cas par exemple de l'écoulement d'un mélange de gaz (non réactifs) : dans ce cas, les champs de fraction massique des deux gaz sont couplés dans l'ensemble de l'écoulement.

Presque toutes les méthodes utilisées en aéroélasticité utilisent la notion de cycle d'interaction. L'idée sous-jacente est en fait l'intégration temporelle décalée des deux sous-systèmes. On comprend d'ailleurs que l'intégration simultanée du fluide et de la structure est très difficile en général, puisque la position du maillage du domaine fluide (et toutes les grandeurs géométriques) deviennent alors des inconnues du problème. Les coûts de calculs induits sont rapidement prohibitifs [60]. Les méthodes ALE peuvent permettre une intégration simultanée (grâce à la séparation entre flux Lagrangiens et termes convectifs) au prix d'une faible précision qui nécessite l'emploi de faibles pas de temps. Les autres algorithmes peuvent être résumés ainsi :

$$P^n \overset{1}{\Longrightarrow} S^{n+1} \overset{2}{\longrightarrow} I^{n+1} \overset{3}{\Longrightarrow} M^{n+1} \overset{4}{\Longrightarrow} F^{n+1} \overset{5}{\longrightarrow} P^{n+1} \overset{6}{\Longrightarrow} S^{n+2} \cdots$$

Dans le schéma précédent, les exposants sont relatifs au numéro du pas de temps courant (cette convention vaut pour l'ensemble de cette thèse). Respectivement, P, S, I, M et F représentent la distribution des pressions exercées par le fluide sur la structure, l'état de la structure, la position de l'interface fluide-structure, le maillage du domaine fluide et le champ de vecteurs des variables conservatives dans le fluide. D'une part, les flèches épaisses "$\Longrightarrow$" représentent des calculs plutôt lourds. C'est

le cas de l'intégration de la structure du temps t^n au temps t^{n+1} ($\overset{1}{\Longrightarrow}$), du calcul d'un nouveau maillage fluide M^{n+1} lorsque la position I^{n+1} de l'interface est connue ($\overset{3}{\Longrightarrow}$) ou de l'intégration du fluide sur le pas de temps ($\overset{4}{\Longrightarrow}$). D'autre part, les flèches simples "$\longrightarrow$" représentent des calculs très légers, comme l'obtention de l'interface fluide-structure lorsqu'on connaît la position de la structure ($\overset{2}{\Longrightarrow}$) ou l'obtention des forces de pression P^{n+1} lorsque l'écoulement est connu ($\overset{5}{\Longrightarrow}$).

Le schéma précédent est applicable à de nombreux systèmes physiques [70], et notamment à tous les problèmes aérodynamiques. Mais il est assez universel. Pour des configurations où la structure est fixée, seule la phase 4 est exécutée. L'algorithme donne alors la solution stationnaire de l'écoulement autour de la structure. Pour des calculs où la structure est animée d'un mouvement rigide, la phase 1 est très allégée, puisque le nombre de degrés de liberté est faible. Enfin, cette méthode s'applique exactement de la même manière aux problèmes stationnaires d'interaction fluide-structure, pour lesquels des schémas implicites utilisant de grands pas de temps peuvent être employés. C'est la cas par exemple de la détermination de la déformation d'un panneau flexible dans un écoulement permanent. Les versions pour une structure rigide puis déformable d'un même problème stationnaire sont présentées sur la Figure 2.5.

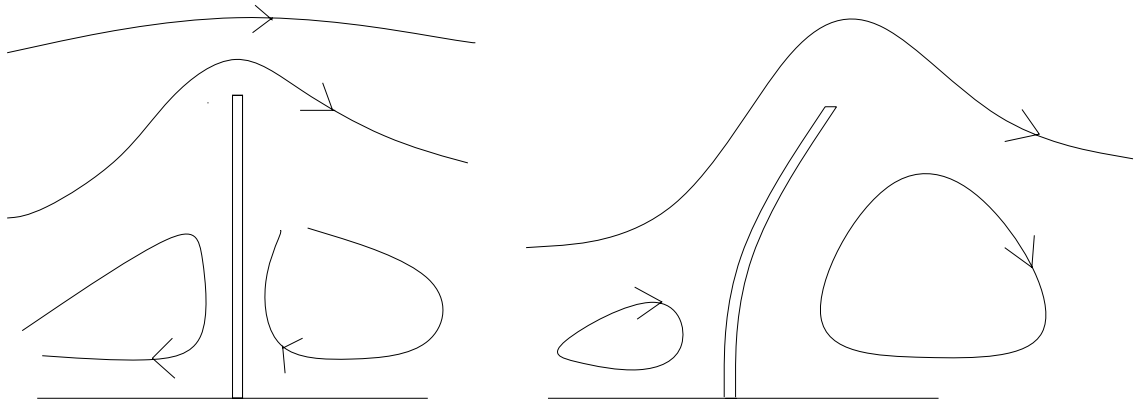

FIG. 2.5 – *Solutions stationnaires de l'écoulement autour d'un panneau rigide et d'un panneau flexible.*

On peut remarquer que, dans chaque phase du schéma présenté, le système qui n'est pas concerné est supposé constant. Ainsi, on intègre la structure d'abord, puis le fluide. Ils sont donc très certainement un peu décalés. Il n'est d'ailleurs pas évident de comprendre dans quel sens ce fait ce décalage. La structure, intégrée en premier, semble être en avance sur le fluide. Par contre, comme elle est intégrée sous l'action de forces de pression qui datent un peu, on peut penser qu'elle est en retard.

De manière générale, ces considérations sont mises de côté, car des pas de temps très faibles sont utilisés. Un autre choix possible consiste à intégrer le fluide avant la structure, ce qui est plutôt plus populaire chez les aérodynamiciens. Cet autre algorithme a l'allure suivante :

$$M^n \overset{1}{\Longrightarrow} F^{n+1} \overset{2}{\longrightarrow} P^{n+1} \overset{3}{\Longrightarrow} S^{n+1} \overset{4}{\longrightarrow} I^{n+1} \overset{5}{\Longrightarrow} M^{n+1} \overset{6}{\Longrightarrow} F^{n+2} \cdots \tag{2.53}$$

La différence entre cet algorithme et le premier ne se limite pas à un changement d'indice. Il ya un changement dans l'ordre de mise à jour des variables. Nous verrons dans la prochaine partie, que cet ordre peut être déterminant.

Deux remarques pour terminer. D'abord, il peut paraître surprenant que l'on ne dispose que de ces algorithmes décalés, qui permettent l'intégration en "boîte noire" du fluide et de la structure par des méthodes qui ont déjà fait leurs preuves dans les domaines séparés de la mécanique des fluides et de la dynamique des structures. On a vu que les méthodes ALE permettent une prise en compte très précise du couplage à l'interface, mais que ceci ce fait au détriment de la précision ou du temps de calcul.

Ensuite, on a déjà remarqué que l'intégration simultanée des deux champs est en général irréalisable. Il faudrait en effet disposer de fonctions particulièrement complexes donnant explicitement l'influence d'une structure sur un écoulement, ou réciproquement le champ de pression d'un fluide autour d'une forme. Dans certains cas, ces fonctions (ou des approximations de ces fonctions) sont disponibles. Elles permettent de réduire un problème couplé à un problème simple avec terme source explicite.

Par exemple, Lottati [52], dans une étude sur l'influence des amortissements aérodynamique et structurel sur le comportement aéroélastique d'ailes d'avion, utilise une formule approchée qui donne les forces de pression exercées sur les parois en fonction de la fréquence d'oscillation de l'aile. Dans [49], Lin et al. ont étudié le flottement de plaques en utilisant un modèle potentiel linéarisé (dérivé de la théorie de la surface portante et de la méthode des doublets [17]) pour des écoulements subsoniques. Ainsi, ils obtiennent une équation du type

$$\frac{v(\vec{x})}{u_\infty} = \frac{1}{8\pi}\int_{surf} \Delta C_p(\vec{x_s}).K(\vec{x}-\vec{x_s})d\vec{x_s}, \tag{2.54}$$

qui donne l'expression de la vitesse verticale du fluide autour d'une aile en fonction du champ de pression (K est un noyau donnant la vitesse verticale en $\vec{x}$ induite par une impulsion donnée en $\vec{x_s}$).

Sarma et Varadan ont [67] ont étudié le flottement non-linéaire d'un panneau sous un écoulement supersonique, en utilisant la théorie quasistatique des écoulements supersoniques [11]. Ils se sont servi d'une expression réciproque de (2.54), comme la suivante (où M_∞ est le nombre de Mach à l'infini) :

$$\Delta C_p = \left(\frac{-2}{\sqrt{M_\infty^2-1}}\right)\left[\frac{\partial v}{\partial x} + \frac{1}{u_\infty}\left(\frac{M_\infty^2-2}{M_\infty^2-1}\right)\frac{\partial v}{\partial t}\right]. \tag{2.55}$$

Ces artifices permettent d'éviter de véritables simulations numériques de couplages. Ils ne s'appliquent que dans des cas très particuliers, bien loin des configurations complexes que nous voudrions simuler, comme, par exemple, le flottement d'une structure dans un écoulement transsonique (les phénomènes non-linéaires sont alors prépondérants).

En somme, on a vu que toutes les méthodes utilisées sont assez rudimentaires. Dans la pratique, seules les méthodes décalées sont utilisées. De plus, l'emploi d'un

pas de temps très réduit est rendu nécessaire par la faible précision des méthodes en général. Ces limitations ont été étudiées théoriquement dans certains cas [60]. On peut remarquer aussi qu'aucun algorithme à notre connaissance ne propose (c'était le cas avant cette thèse) d'utiliser des pas de temps différents (et donc du sous-cyclage) pour le fluide et la structure. La compréhension détaillée des erreurs numériques dues au décalage entre les intégrations temporelles du fluide et de la structure se révèle être primordiale.

2.3.2 L'algorithme général

Nous décrivons ici en détail l'algorithme résumé en (2.53). Nous utilisons les mêmes notations. En outre, la vitesse et l'accélération de la structure sont notées respectivement $\dot{S}$ et $\ddot{S}$. Dans la Table 2.1, les calculs se font du haut vers le bas. On a supposé que l'on dispose initialement de toutes les grandeurs concernant le fluide (et son maillage) et la structure.

La Table 2.1 est bien sûr cyclique. Six tâches sont effectuées à chaque pas de temps. Les calculs de type mécanique des fluides en domaine déformable sont faits à la ligne 3, sur la base de la reformulation utilisée. Elle peut être (2.5) si des coordonnées curvilignes sont utilisées, ou (2.16) si l'on utilise des référentiels mobiles, ou (2.20) si l'on utilise les deux. Les formulations en maillage dynamique sont aussi possibles (2.44 ou 2.46). L'intégration de la structure est faite à la ligne 5. Les vitesses de maillage sont calculées à la ligne 1 par des formules proches de (2.12) ou (2.13). Toutes les grandeurs géométriques sont aussi mises à jour à la première étape, suivant par exemple (2.11) si l'on utilise des coordonnées curvilignes. Pour des référentiels mobiles liés à la structure, on a besoin de la position et de la vitesse de la structure.

En somme, les algorithmes présentés dans cette section sont assez peu nombreux. Dans la pratique, on n'utilise que les méthodes d'intégration décalées. Cependant, de nombreux choix sont possibles, non seulement sur la formulation des équations physiques, mais aussi sur l'ensemble des prédictions et corrections faites sur chaque élément du calcul.

2.4 Modèles et méthodes pour la structure.

Après avoir étudié la simulation numérique d'écoulements en domaine déformable et le traitement effectif de l'interaction fluide-structure, nous nous intéressons maintenant à l'autre partie du système couplé : la structure. Dans cette section, on s'intésse aux méthodes numériques couramment employées dans les simulations d'interactions fluide-structure. Nous n'avons pas l'intention de présenter toutes les méthodes relevant de la dynamique des structures en général. Nous nous limitons ici à des structures linéaires élastiques. Nous présentons dans la suite les modèles et les discrétisations

Variables calculées	Variables utilisées
vitesses de maillage de t^n à t^{n+1}	S^n, $\dot{S}^n$
conditions aux limites B^n	S^n, $\dot{S}^n$
nouvel état du fluide F^{n+1}	F^n, B^n, M^n
champ de pression P^{n+1}	F^{n+1}
S^{n+1}, $\dot{S}^{n+1}$, $\ddot{S}^{n+1}$	P^{n+1}, S^n, $\dot{S}^n$, $\ddot{S}^n$
nouveau maillage M^{n+1}	S^{n+1}
$\vdots$	$\vdots$

TAB. 2.1 – *La forme générale des schémas décalés.*

utilisés, ainsi que les méthodes employées pour intégrer en temps la structure.

2.4.1 Equations modèles pour la structure

La structure est au départ continue, et le champ des déplacements décrit donc un espace de dimension infinie. On utilise en général une discrétisation en éléments finis, qui ramène les déplacements dans un espace de dimension finie. Ensuite, nous utilisons l'équation de Lagrange pour obtenir l'équation d'évolution de la structure, sous l'action des forces aérodynamiques.

Discrétisation :

• Nous utilisons une discrétisation en éléments finis (voir par exemple [17]). On suppose que les déplacements de la structure continue peuvent être représentés par leur valeurs

en un ensemble fini de points de contrôle. Le déplacement r prend alors la forme

$$r = \sum_{i=1}^{n} q_i \, . \left(\frac{\partial r}{\partial q_i} \right) , \tag{2.56}$$

où n est la dimension finie de la discrétisation, les fonctions $\partial r / \partial q_i$ sont les fonctions de base et les q_i sont appelés les coordonnées généralisées.

• En notant d'un point les dérivations en temps et en utilisant la définition précédente, on peut donner des expressions pour les énergies cinétique, potentielle élastique et dissipée.

- L'énergie cinétique T est donnée par :

$$T = \frac{1}{2} \int \rho \, \dot{r}^t \, . \, \dot{r} = \frac{1}{2} \, \dot{q}^t M \dot{q} \ , \tag{2.57}$$

où ρ est la densité de la structure et M est la matrice $(n \times n)$ de masse généralisée. Le terme (i, j) de cette matrice est donné par :

$$M_{i,j} = \int \rho \left(\frac{\partial r}{\partial q_i} \right)^t \left(\frac{\partial r}{\partial q_j} \right) \ . \tag{2.58}$$

- L'énergie potentielle élastique U est donnée par :

$$U = \frac{1}{2} \int \bar{\bar{\sigma}} : \bar{\bar{\varepsilon}} \ = \frac{1}{2} \, q^t K q \ , \tag{2.59}$$

où $\bar{\bar{\sigma}}$ et $\bar{\bar{\varepsilon}}$ désignent respectivement les tenseurs de contrainte et de déformation (les deux points représentent un produit tensoriel contracté) et K est la matrice $(n \times n)$ de raideur généralisée. On peut donner l'expression des termes de la matrice K en fonction des tenseurs $\bar{\bar{\sigma}}_k$ et $\bar{\bar{\varepsilon}}_k$ de contrainte et de déformation dans le déplacement $\partial r / \partial q_k$. Le terme (i, j) de la matrice K est donné par :

$$K_{i,j} = \int \bar{\bar{\sigma}}_i : \bar{\bar{\varepsilon}}_j \ . \tag{2.60}$$

- L'énergie dissipée D est donnée par :

$$D = \frac{1}{2} \int f_{dis} \, . \, \dot{r} \ , \tag{2.61}$$

où f_{dis} est le champ de force de dissipation. Dans la plupart des cas, on suppose que cette force est de type visqueux, c'est-à-dire que c'est une fonction linéaire de $\dot{q}$. Elle est définie par :

$$f_{dis} = \sum_{i=1}^{n} \left(\frac{\partial f_{dis}}{\partial \dot{q}_k} \right) \dot{q}_k \ . \tag{2.62}$$

Sous cette hypothèse, l'énergie dissipée D peut s'écrire sous la forme suivante :

$$D = \frac{1}{2}\, \dot{q}^t B \dot{q} \ , \tag{2.63}$$

où la matrice de dissipation généralisée B a pour terme (i, j) :

$$B_{i,j} = \int \left(\frac{\partial f_{dis}}{\partial \dot{q}_k}\right)\left(\frac{\partial r}{\partial q_l}\right) \ . \tag{2.64}$$

- La matrice M, symétrique et positive, est aussi supposée définie. K est symétrique et positive. Enfin, on peut montrer qu'en général, la partie symétrique de B (elle seule importe dans (2.63) visiblement) est aussi positive.

• Enfin, si l'on considère le champ de forces surfaciques f exercées sur la surface Σ de la structure, leur travail dans un champ de déplacement r est donné par :

$$W = \int_\Sigma r^t \,.\, f = q^t \,.\, Q \tag{2.65}$$

où Q est le vecteur des forces généraliseés défini par

$$Q_k = \int_\Sigma \left(\frac{\partial r}{\partial q_k}\right)^t . f \ . \tag{2.66}$$

Equations modèles :

• A partir des équations (2.57), (2.59), (2.61) et (2.65), on obtient l'équation de Lagrange pour notre système en appliquant le principe des travaux virtuels. Elle s'écrit :

$$\frac{d}{dt}\left(\frac{\partial T}{\partial \dot{r}}\right) - \frac{\partial T}{\partial r} + \frac{\partial D}{\partial \dot{r}} + \frac{\partial U}{\partial r} = Q. \tag{2.67}$$

Comme T, D, U et Q ont une forme quadratique, on déduit notre équation modèle en coordonnées généralisées :

$$\boxed{M\ddot{q} + B\dot{q} + Kq = Q.} \tag{2.68}$$

• Cette équation modèle du mouvement fait intervenir tous les n degrés de liberté que possède la structure. Elle permet de faire apparaître n modes propres (n est le nombre de degrés de liberté). Il est parfois intéressant de ne pas considérer tous les modes propres de la structure discrète. On se limite alors à un nombre réduit de modes propres importants (en général les premiers). Dans [31], Guruswamy présente la forme des premiers modes propres pour une aile simple rectangulaire ou pour une configuration beaucoup plus complexe (cellule et aile).

• Un mode propre de la structure associé à une pulsation ω_i est un champ de déplacement U_i tel que

$$q_i = U_i \cos(\omega_i t) \quad \text{est solution de} \quad M\ddot{q} + Kq = 0,$$

ce qui est équivalent à

$$\left(K - {\omega_i}^2 M\right) U_i = 0. \tag{2.69}$$

Chaque U_i est un vecteur propre de la matrice $M^{-1}K$ pour la valeur propre ${\omega_i}^2$. Lorsque les modes propres U_i sont indépendants (il suffit pour cela que les pulsations propres soient toutes distinctes, ce qui est généralement le cas), on peut les utiliser eux mêmes comme vecteurs de base de déplacement $\partial r/\partial q_i$. On peut alors réécrire les équations (2.56) à (2.68) où les coordonnées $\tilde{q}_i$ sont maintenant les coordonnées modales. On obtient :

$$\tilde{M}\ddot{\tilde{q}} + \tilde{B}\dot{\tilde{q}} + \tilde{K}\tilde{q} = \tilde{Q}. \tag{2.70}$$

Les matrices $\tilde{M}$ et $\tilde{K}$ sont toutes deux diagonales. Leurs termes génériques sont d'ailleurs données par

$$\left\{ \begin{array}{lcl} \tilde{M}_{i,i} & = & U_i^t \; M \; U_i \\ \tilde{K}_{i,i} & = & U_i^t \; K \; U_i \end{array} \right. . \tag{2.71}$$

Les termes non-diagonaux sont nuls, car les modes propres U_i sont M-orthogonaux et K-orthogonaux deux à deux. On écrira respectivement (μ) et (γ) à la place de $\tilde{M}$ et $\tilde{K}$. La matrice $\tilde{B}$ n'a aucune raison a priori d'être diagonale. Dans la plupart des cas, on suppose que B est une combinaison linéaire de M et K (hypothèse de Rayleigh) ou plus simplement que $\tilde{B}$ est diagonale (hypothèse de Basile), ce qui est un peu plus faible. Cependant, il a été montré [17] que l'hypothèse de Basile est valide pour les structures faiblement dissipatives. Cette hypothèse est utilisée par exemple par Borland et Rizzetta [14] avec des coefficients d'amortissement spécifiques pour chaque mode propre.

Grâce à cette nouvelle formulation, sous l'hypothèse de Basile (on écrit maintenant (β) à la place de $\tilde{B}$), on obtient un ensemble d'équations scalaires modales qui sont maintenant découplées :

$$\boxed{(\mu)\; \ddot{\tilde{q}} + (\beta)\; \dot{\tilde{q}} + (\gamma)\; \tilde{q} = \tilde{Q}.} \tag{2.72}$$

Cette approche modale a été utilisée dans la plupart des études disponibles (il existe quand même des exceptions [25]). Elle permet de manipuler un nombre de variables fixé par l'utilisateur, qui sont les coordonnées du champ de déplacement sur ces modes. Si l'on utilise très peu de modes, l'équation différentielle (2.72) peut être résolue exactement.

Cette approche a cependant l'inconvénient de tout rapporter aux modes propres de la structure seule. Pour des modes propres de couplage aéroélastique différents des modes structurels, cette approche peut être insuffisante. Il faut donc faire appel à des schémas d'intégration en temps, qui ne seront pas nécessairement appliqués aux équations scalaires (2.72)

2.4.2 Schémas d'intégration

A partir de (2.68) et en utilisant des coordonnées généralisées, nous accomplissons la tâche correspondant à la cinquième ligne de la Table 2.1. Les pressions P^{n+1}, la position, la vitesse et l'accélération de la structure ($\ddot{S}^n$, $\dot{S}^n$, S^n) sont connues. Elles sont transformées respectivement en forces généralisées Q^{n+1} et coordonnées généralisées (et leurs dérivées) $\ddot{q}^n$, $\dot{q}^n$, q^n. Nous devons calculer les mêmes grandeurs généralisées à la fin du pas de temps courant : $\ddot{q}^{n+1}$, $\dot{q}^{n+1}$, q^{n+1}. Ces grandeurs nous permettront facilement d'obtenir $\ddot{S}^{n+1}$, $\dot{S}^{n+1}$ et S^{n+1}.

Les méthodes les plus couramment utilisées sont les méthodes de Newmark. Elles s'écrivent :

$$\begin{aligned}
\dot{q}^{n+1} &= \dot{q}^n + \Delta t \left((1-\alpha)\ddot{q}^n + \alpha\ddot{q}^{n+1}\right) \\
q^{n+1} &= q^n + \Delta t\dot{q}^n + \frac{\Delta t^2}{2}\left((1-\beta)\ddot{q}^n + \beta\ddot{q}^{n+1}\right) \\
M\ddot{q}^{n+1} &+ B\dot{q}^{n+1} + Kq^{n+1} = Q^{n+1}.
\end{aligned} \tag{2.73}$$

On peut commenter ce schéma en quelques mots. Connaissant la valeur de Q^{n+1}, on connaît grâce à (2.68) une relation entre les grandeurs généralisées au temps t^{n+1}. On choisit de donner un rôle prépondérant à l'accélération (les erreurs sur $\ddot{q}_{n+1}$ seront réduites après multiplication par un facteur Δt^2). On exprime alors la position et la vitesse (q^{n+1}, $\dot{q}^{n+1}$) à l'aide de prédictions simples dépendant des deux coefficients α et β en fonction de $\ddot{q}_{n+1}$. La méthode de Newmark est égale à la règle du trapèze quand $\alpha = \beta = 1/2$ (la plus couramment utilisée) et à la méthode de l'accélération linéaire quand $\alpha = 1/2$ et $\beta = 1/3$ [25].

La méthode d'intégration en temps (règle du trapèze) est implémentée de la manière suivante :

- $$\dot{q}^* = \dot{q}^n + \frac{\Delta t}{2}\ddot{q}^n \tag{2.74}$$
- $$q^* = q^n + \Delta t\,\dot{q}^n + \frac{\Delta t^2}{4}\ddot{q}^n \tag{2.75}$$
- $$\ddot{q}^{n+1} = \left[M + \frac{\Delta t}{2}B + \frac{\Delta t^2}{4}K\right]^{-1}\left(Q^{n+1} - B\dot{q}^* - Kq^*\right) \tag{2.76}$$
- $$\dot{q}^{n+1} = \dot{q}^* + \frac{\Delta t}{2}\ddot{q}^{n+1} \tag{2.77}$$
- $$q^{n+1} = q^* + \frac{\Delta t^2}{4}\ddot{q}^{n+1} \tag{2.78}$$

Cet algorithme est assez général. Il est également applicable aux formulations modales (et dans ce cas, il est encore plus simple puisque les matrices sont diagonales).

On peut remarquer que le calcul le plus coûteux (2.76), et notamment la factorisation de la matrice à inverser, peut être fait une fois pour toutes si le pas de temps utilisé reste constant pendant toute la simulation.

On voit aussi le grand intérèt de la formulation modale. Les calculs des modes propres et des matrices modales généralisées peuvent être faits une fois pour toutes. L'intégration en temps est ensuite très légère, puisqu'il s'agit d'équations scalaires découplées. Pour une simulation aéroélastique, après chaque pas de temps, il faut recomposer les grandeurs physiques S^{n+1} et $\dot{S}^{n+1}$ à partir des variables généralisées. Elles peuvent être obtenues à l'aide de matrices de passage de la base des $\partial r/\partial q_i$ à celle des U_i. Ces matrices sont également fixes pendant tout le calcul.

En somme, nous avons vu que le coût de l'intégration en temps de la partie structure d'une simulation aéroélastique dépend fortement du nombre de degrés de liberté utilisé. L'emploi d'une approche modale permet de réduire considérablement le temps de calcul nécessaire. Cependant, elle pourrait être insuffisante pour certains problèmes où les modes propres couplés sont très différents des modes propres de la structure.

On peut rappeler que l'emploi de grandeurs généralisées n'est pas très coûteux, puisque les matrices de masse, d'amortissement et de raideur peuvent être calculées une fois pour toutes au début du calcul. De même, l'emploi d'un pas de temps constant pour l'intégration de la structure (lorsqu'elle est linéaire) permet de factoriser une seule fois la matrice d'évolution écrite en (2.76).

Deuxième partie

Analyse numérique

Dans cette partie, nous nous intéressons au couplage des méthodes numériques utilisées séparément dans chacun des champs. Pour le fluide, nous disposons d'un large éventail de méthodes numériques, parmi lesquelles nous avons privilégié les méthodes en volumes finis. Pour la structure, la nature symétrique des matrices découlant des formulations en éléments finis nous permet d'utiliser une panoplie de méthodes classiques. Comme nous l'avons expliqué dans la partie précédente, seules les méthodes d'intégration décalée sont envisageables, dans la mesure où l'intégration globale de tous les champs (fluide, maillage du domaine fluide et structure) est encore beaucoup trop coûteuse pour les calculateurs actuels.

Pour chacune de ces deux familles de méthodes, classiques pour les spécialistes de mécanique des fluides et de dynamique des structures, l'inventaire des propriétés a été fait plus haut: leur précision, leur stabilité et leur efficacité sont connues. Par contre, le couplage de ces méthodes, et les propriétés heritées par ces "schémas couplés" sont au cœur du sujet de cette thèse.

Il est important de comprendre, même intuitivement, pourquoi les propriétés des méthodes couplées peuvent différer de celles des méthodes-mères utilisées. D'abord, la précision spatiale se transporte généralement, à condition que les traitements des conditions aux bords soient adaptés. De même, l'efficacité globale est limitée par celles des méthodes-mères. Cependant, nous verrons dans cette partie que diverses techniques, comme le sous-cyclage et le calcul parallèle permettent de l'augmenter. Enfin, la stabilité est *la* propriété qui ne se transmet pas en général. En effet, les études de stabilité sont faites sur la version homogène *sans terme source* des équations qu'elles résolvent. Dans un système couplé, chaque champ intervient dans un terme source pour l'autre champ. Des analyses de stabilité séparées occultent ces termes sources, donc le couplage, et par là-même, se montrent complètement inadaptées aux problèmes couplés, et fausses a priori. Le problème qui se pose est donc double: mettre au point des méthodes numériques d'intégration pour ces systèmes couplés d'une part, et des méthodes d'analyse de leurs propriétés.

L'abord direct et général de cette problématique est trop complexe. Nous nous limiterons dans l'ensemble de cette partie à des problemes simples, pour lesquels on peut exhiber des solutions exactes – et parfois analyser exactement le comportement de certaines méthodes numériques couplées. Ces problèmes seront mono-dimensionnels et linéaires. Si cette première approche peut paraître simpliste, elle nous permettra de comprendre, sur ces problèmes élémentaires, comment les propriétés des schémas d'intégration couplée se déduisent de celles de leurs méthodes-mères.

Dans le Chapitre 3, nous étudions un problème mono-dimensionnel linéaire, avec un seul degré de liberté pour la structure: le problème du piston.

Nous présentons une analyse dont le but est double: identifier les erreurs d'origine numérique liées au couplage entre fluide et structure, et donner un moyen d'éliminer ces effets purement numériques.

Nous introduisons deux méthodes d'analyse: la première est fondée sur la théorie des équations équivalentes, et la seconde est une analyse de modes propres pour le problème couplé. Ces deux méthodes fournissent des corrections des schémas d'intégration du système couplé qui éliminent les effets purements numériques quand la réponse physique du système est connue. D'autres méthodes sont présentées pour les cas où cette réponse est inconnue.

Dans le Chapitre 4, on passe à une autre méthode d'analyse numérique, fondée sur des formulations énergétiques. Cette analyse peut donc porter sur des cas où les modes propres couplés sont inconnus.

Nous présentons plusieurs algorithmes d'intégration en temps pour le problème du piston, nous étudions leur précision, leur stabilité et leur efficacité, en considérant également les apports possibles du calcul parallèle et hétérogène et du sous-cyclage.

Bien que l'étude théorique de ces algorithmes soit menée pour le problème à une dimension du piston, certaines conclusions tirées de cette étude seront confirmées dans la partie suivante par la simulation numérique plus complexe de la réponse aéroélastique d'un panneau flexible dans un écoulement bidimensionnel en régime transsonique non-linéaire.

Chapitre 3

Analysis and compensation of numerical damping in a 1D aeroelastic problem

Réalisé avec † Bernard Larrouturou et ‡ Michel Lesoinne.

† CERMICS
INRIA, BP 93, 06902 Sophia-Antipolis Cedex, France

‡ Department of Aerospace Engineering Sciences
and Center for Aerospace Structures
University of Colorado at Boulder
Boulder, CO 80309-0429, U. S. A.

Ce chapitre est paru sous la forme d'un rapport de recherche CERMICS (N° 93-17), accepté pour publication à l' *International Journal of Computational Fluid Dynamics*.

3.1 Introduction

In aerospace engineering and in the particular field of fluid-structure interaction, it is important to accurately investigate the physical stability of complex coupled systems such as flows around three-dimensional structures [11, 31, 70]. These investigations are performed through numerical simulations [61], in order to better predict the general behaviour of these coupled systems and to prevent unstable phenomena such as flutter or buffetting [14, 41, 68]. Using their own space and time schemes, these simulations naturally have their own stability characteristics [35, 43, 60]. Thus, the results of these simulations give a combination of two responses, the physical one and the numerical one. Of course, it is desirable that the numerical simulation predicts a stable response (respectively: an unstable response) of a physical system only if this system is actually stable (resp.: unstable). Hence, controling the influence of the numerical schemes and in particular of the numerical damping on the numerical results is the only way to reach accuracy, in terms of stability of our numerical simulations.

The ultimate objective of this study is to obtain better integration schemes for fluid-structure interaction problems. For example, the well-known phenomenon of wing flutter corresponds to an unstable behavior of a wing (or a wing-body configuration), which occurs in three-dimensional geometries, with a non-ideal viscous fluid and complex three-dimensional structures. The first step towards better numerical simulations of such phenomena is to analyze simpler fluid-structure problems. This is why we consider in this section numerical simulations of a simple model problem, which we present in Section 3.2: we deal with a plane piston subjected to the one-dimensional flow of a compressible fluid, in the linear acoustic regime. We use a fixed uniform mesh and take the motion of the piston into account by a boundary mass flux. This formulation allows us to consider a linear problem, which is a necessary first step towards a more complete understanding of fluid-structure interaction. This means also that we have separated here fluid-structure interactions and fluid-mesh interactions (we intend to analyze the latter, which occur in moving meshes methods or ALE-type formulations [5, 20, 25, 35], in a forthcoming work).

Then, the goal of our study is two-fold. Our first goal is to derive methods for obtaining accurate analytical predictions of the general damping of the numerical simulation. Once the first goal is achieved for a large family of schemes, we use these analytical results in order to achieve our second goal, namely modifying the numerical schemes in order to accurately simulate the exact physical damping of the system.

We also present in Section 3.2 the family of numerical schemes we use: since most engineering coupled applications are simulated with *staggered* schemes (which allow to integrate the structural and the fluid parts separately during each time step), we consider this algorithmic approach. Therefore we use simple schemes for the integration of the fluid and the structure equations. For the boundary conditions, in particular at the fluid-structure boundary, we use different formulations which are commonly used by aeroelasticians; this discrete treatment of the coupling between fluid and structure will appear to have a very strong influence on the numerical results.

In Section 3.3, we introduce a first method based on the modified equation theory

[75] for the numerical analysis of this problem. This method is very simple, and gives good qualitative results provided that the treatment of the boundary conditions is precisely taken into account. These results give useful informations for more general aeroelastic simulations.

In Section 3.4, we present a more accurate and powerful method for the analysis of the numerical results. This method is based on the analysis of eigenvalues and eigenvectors of the amplification matrix for the coupled numerical system. Although this method may be uneasily extendable to multi-dimensional cases, it gives in our case very interesting results: it confirms some principles of the common know-how in numerical aeroelasticity, it confirms the results obtained with the modified equation analysis, and it predicts accurately the numerical damping for all linear schemes. The two methods are compared in Section 3.5.

In Section 3.6, we discuss applications of both previous methods to different families of schemes. Finally, in Section 3.7, we show how the results of our analyses can be used more generally for aeroelastic simulations. The presented methods allow us to exactly control the final damping in the numerical simulation when the fundamental frequency of the system is known (which is often the case in aerospatial applications, since flutter pulsations of wing-body configurations are close or equal to eigen-pulsations of the structure). In such a case, we show that we can derive corrections of the numerical schemes in order to compensate the numerical damping. We also propose other general methods for achieving this goal in cases where there is no available prediction for the system frequency.

3.2 The physical test case and the global numerical algorithm

In this section, we present the physical experiment under consideration: since actual aerospace engineering problems are too complex to be analyzed, we consider a simple one-dimensional model problem. We also present the type of staggered schemes we will use to perform the temporal integration of the coupled fluid-structure system.

3.2.1 The model problem

We consider the one-dimensional flow of a perfect gas in a chamber closed by a moving piston. The equilibrium state of the system is defined by a uniform pressure P_0 inside and out of the chamber, a uniform gas density ρ_0 in the chamber, where the gas is still ($u_0 = 0$), and by a stationnary chamber length L (in our experiment, we take standard values: $P_0 = 1$ atm, $\rho_0 = 1.3$ kg/m^3, $\gamma = 1.4$). The chamber is described on Figure 3.1.

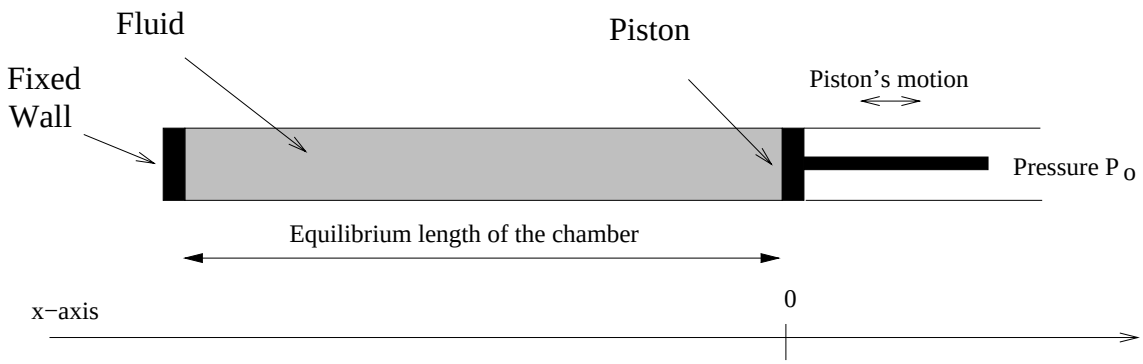

FIG. 3.1 – *The piston and the fluid-filled one-dimensional chamber.*

The one-dimensional flow in the chamber is supposed to be governed by the compressible Euler equations, which we write with usual notations as:

$$\begin{cases} \rho_t + (\rho u)_x = 0 \ , \\ (\rho u)_t + (\rho u^2 + P)_x = 0 \ , \\ E_t + [u(E+P)]_x = 0 \ . \end{cases} \tag{3.1}$$

Here, ρ is the density, u is the velocity, P is the pressure and E is the total energy per unit volume. The position, speed and acceleration of the piston are respectively denoted by $L + x$ (i.e. x denotes the deviation of the piston from its equilibrium position), $\dot{x}$ and $\ddot{x}$. Calling m, d and k the mass, the internal damping d and the stiffness of the piston respectively, we write the piston governing equation as:

$$m\ddot{x} + d\dot{x} + kx = P(x+L) - P_0 \ ; \tag{3.2}$$

here, $P(x+L)$ is the internal pressure at the piston, and we assume that the outer pressure remains constant and equal to P_0.

The boundary conditions for the fluid are:

$$\rho u(0) = 0 \tag{3.3}$$

at the fixed wall, and:

$$u(x+L) = \dot{x} \tag{3.4}$$

at the piston, which expresses that the fluid velocity is there equal to the piston speed.

Assuming furthermore that the system undergoes only small perturbations around the equilibrium state, we linearize the above equations. Thus, we assume that:

$$\Delta\rho = \rho - \rho_0 \ \ll \ \rho_0 \ , \tag{3.5}$$

$$\Delta P = P - P_0 \ \ll \ P_0 \ , \tag{3.6}$$

$$u \ \ll \ c_0 \ , \tag{3.7}$$

and, as usual in the linear acoustic regime, we have:

$$\Delta P = c^2 \Delta\rho \ , \tag{3.8}$$

which means that the gas variations are isentropic (we simply denote by c instead of c_0 the unperturbed sound speed). We then write the governing equations using the vector

$$W = \begin{pmatrix} \Delta\rho \\ \Delta(\rho u) \end{pmatrix} = \begin{pmatrix} \Delta\rho \\ \rho_0 \Delta u \end{pmatrix}$$

as:

$$W_t + \begin{pmatrix} 0 & 1 \\ c^2 & 0 \end{pmatrix} W_x = 0 \ . \tag{3.9}$$

The linearized boundary conditions take the form:

$$\Delta u(0) = 0 \ , \tag{3.10}$$

$$\Delta u(L) = \dot{x} \ , \tag{3.11}$$

and the piston equation now can be written as:

$$m\ddot{x} + d\dot{x} + kx = \Delta P(L) = c^2 \Delta\rho(L) \ . \tag{3.12}$$

3.2.2 Evaluating the system frequency

In the following, the reader will assume that d and k are equal to 0, if no other explicit statement is made. The piston equation then reduces to:

$$m\ddot{x} = \Delta P(L) = c^2 \Delta\rho(L) \ . \tag{3.13}$$

Since d is equal to 0, the physical system is undamped and should undergo infinite oscillations of constant amplitude. We now present two different ways of evaluating the frequency of these oscillations.

The first crude estimate can be obtained in a very simple and rapid way by assuming that, in addition to being isentropic, the gas flow is isobaric. In other words, one assumes that the pressure is spatially constant in the chamber (an assumption which is consistent with the highly subsonic character of the flow). Using this approximation (which differs from the acoustic approximation described above), we can write:

$$m\,\ddot{x} = P - P_0, \tag{3.14}$$

where $P = P(t)$ is the spatially constant pressure. It is given by:

$$P\rho^{-\gamma} = P_0 {\rho_0}^{-\gamma} \ , \tag{3.15}$$

where ρ is the gas density (also spatially constant). Writing the mass conservation for the system, we have:

$$(L + x)\,\rho = L\,\rho_0. \tag{3.16}$$

The position x then satisfies the following equation:

$$m\,\ddot{x} = P_0 \left[\left(\frac{L+x}{L} \right)^{-\gamma} - 1 \right]. \tag{3.17}$$

For small enough initial perturbations (in piston speed and location), we can linearize the preceding equation for $x \ll L$. We get:

$$m\,\ddot{x} = -\frac{\gamma P_0}{L} x. \tag{3.18}$$

Hence, the "isobaric pulsation" ω_i of the system is given by:

$${\omega_i}^2 = \frac{\gamma P_0}{mL}. \tag{3.19}$$

This formula can be rewritten with non-dimensional quantities as

$$\boxed{\left(\frac{\omega_i L}{c} \right)^2 = \frac{\rho_0 L}{m}.} \tag{3.20}$$

Now, a second more instructive way of evaluating the system frequency consists in solving the linear system (3.9)-(3.13). Indeed, a major interest of this one-dimensional acoustic physical experiment is that we can exhibit an exact solution of the linear system (3.9)-(3.13). This exact solution will be used later for more complex predictions. We have the following:

Lemma 1 *A solution of equation (3.9) with the boundary condition (3.10) is given by:*

$$W = \begin{pmatrix} 1 \\ +c \end{pmatrix} \cos[\omega(t - \frac{x}{c})] + \begin{pmatrix} 1 \\ -c \end{pmatrix} \cos[\omega(t + \frac{x}{c})] \quad (\text{with } \omega \in I\!R). \tag{3.21}$$

The proof is elementary and will be omitted. □

In order to solve the complete system (3.9)-(3.13), it remains to take into account the piston boundary condition (3.11) and the equation (3.13) for the piston dynamics. Using (3.21), we then have:

$$u(L) = \frac{2c}{\rho_0} \sin(\frac{\omega L}{c}) \sin(\omega t) \ , \tag{3.22}$$

$$m\dot{u}(L) = \frac{2mc\omega}{\rho_0} \sin(\frac{\omega L}{c}) \cos(\omega t) \ , \tag{3.23}$$

$$\Delta P(L) = 2c^2 \cos(\frac{\omega L}{c}) \cos(\omega t) \ . \tag{3.24}$$

Hence, the piston equation (3.13) is satisfied if and only if:

$$\frac{2mc\omega}{\rho_0}\sin(\frac{\omega L}{c}) = 2c^2\cos(\frac{\omega L}{c}) \ , \tag{3.25}$$

which can be written as

$$\boxed{\left(\frac{\omega L}{c}\right)\tan\left(\frac{\omega L}{c}\right) = \frac{\rho_0 L}{m}.} \tag{3.26}$$

This formula deserves several comments. First, this relation is consistent with the previous "isobaric estimate" (3.20): in the limit of c going to $+\infty$, then $\tan(\omega L/c) \simeq \omega L/c$ and ω tends to ω_i.

Also, two interesting limits can be observed for relation (3.26). If m tends to $+\infty$, then $\omega L/c = k\pi$: the infinite-mass piston behaves as a fixed wall, and we have a classical acoustic regime with a velocity node at each end of the chamber. On the other hand, if m tends to 0, then $\omega L/c = \pi/2 + k\pi$: the boundary condition at the piston becomes $\Delta P(L) = 0$ from (3.13), and we now have an acoustic regime with a velocity node at the fixed wall and a pressure node a the piston.

Beside this, since $\tan(z) > z, \forall z \in]0, \pi/2[$, we see that the fundamental pulsation given by (3.26) is smaller than ω_i. Thus, the period of the system is greater than the "isobaric period", which is also coherent with the hypothesis of finite wave speed.

3.2.3 The general integration scheme

We conclude this section by briefly presenting the general type of schemes used in our simulations below. The algorithm is derived from general aeroelasticity know-how [60, 61] and uses so-called staggered schemes, where the fluid and the structure are integrated separately during each time step.

Thus, the algorithm is the following: at each time level t^n, we:

- predict the piston speed for the next time step $[t_n, t_{n+1}]$,
- compute wall fluxes for the fluid during this time step,
- integrate the fluid from t_n to t_{n+1},
- compute an average pressure at the piston for the time step $[t_n, t_{n+1}]$,
- integrate the piston (submitted to this pressure) from t_n to t_{n+1}.

We notice here that we could have used other staggered schemes, where the structure is integrated first. But in fact, these algorithms differ only by indices translations.

In the following, we consider only explicit time integration schemes (except in section 3.6.3 below).

Although we postpone till the end of this section the presentation of our numerical results for the oscillating piston, it is worth saying here that the clearest feature of these result lies in the inability of the numerical schemes to reproduce the constant-amplitude system oscillations: the amplitude of the computed oscillations decreases with time (see e.g. Figure 3.2 below). Moreover, we sometimes also observe a deviation between the computed frequency and the known analytical frequency. Analyzing these numerical effects, and in particular the numerical damping, is the object of the next sections.

3.3 Modified equation analysis

In this section, we use the modified equation theory [75] to obtain analytical predictions of our numerical results. Referring to [1, 75] for the details, we simply recall here that, for the numerical solution of a linear hyperbolic or parabolic equation, the modified equation is the differential equation which is exactly satisfied by the computational values; it is obtained through Taylor expansions, and it is an adequate way to express the main properties of the numerical schemes, in terms of error analysis.

Let us recall the following example, which will be useful later on. Consider the numerical solution of the advection equation $u_t + cu_x = 0$, with $c > 0$, with the simple explicit upwind scheme:

$$\frac{u_j^{n+1} - u_j^n}{\Delta t} + c\frac{u_j^n - u_{j-1}^n}{\Delta x} = 0 \ . \tag{3.27}$$

Then, the modified equation of this scheme is, up to second-order accuracy (see e.g. [1]):

$$u_t + cu_x = \mu u_{xx} + c\lambda u_{xxx} \ , \tag{3.28}$$

with:

$$\mu = \frac{c\Delta x}{2}\left(1 - \nu\right) \ , \tag{3.29}$$

$$\lambda = -\frac{\Delta x^2}{6}\left(1 - 3\nu + 2\nu^2\right) \ , \tag{3.30}$$

where the Courant number ν is given by $\nu = \dfrac{c\Delta t}{\Delta x}$.

Recalling that our goal is to analyze the numerical errors for the fluid-structure coupled system, we are going to use the modified equation in order to represent the numerical errors related to the simulation of the fluid (more precisely, of the linear acoustic waves in the fluid). We will therefore have to couple the modified equation with the discrete piston equation, and we will see that not only the numerical approximation in the fluid (taken into account through the modified equation), but also the time integration scheme for the structure and the discrete treatment of boundary conditions have important influences on the numerical results.

3.3.1 Modified equation with diffusion

Let us assume that we use an explicit first-order accurate upwind scheme for the integration of system (3.9). Restricting our attention to the main error term in the fluid approximation, we will consider that our numerical solution satisfies:

$$W_t + \begin{pmatrix} 0 & 1 \\ c^2 & 0 \end{pmatrix} W_x = \mu W_{xx} \ , \tag{3.31}$$

where the positive diffusion coefficient μ is given in (3.29).

Since this equation differs from (3.9), we are now interested in appreciating the influence of μ on the system pulsation. We will use the same method as in the undamped case. The essential difference lies in finding elementary solutions of (3.31). The first natural idea consists in taking temporally damped oscillations. With this kind of solution, it is not possible to fulfill both the fixed wall boundary condition (3.10) and the fundamental equation of dynamics for the piston. Thus, we will consider temporally and spatially damped oscillations:

Lemma 2 *A solution of equation (3.31) with the boundary condition (3.10) is given by:*

$$W = e^{z(\mu z - c)t} \left[\begin{pmatrix} 1 \\ +c \end{pmatrix} e^{zx} + \begin{pmatrix} 1 \\ -c \end{pmatrix} e^{-zx} \right] \quad (\text{with } z \in \mathcal{C}). \tag{3.32}$$

We leave the proof to the reader. □

As previously, we can write:

$$u(L) = \frac{2c}{\rho_0} \sinh(zL) e^{z(\mu z - c)t} \ , \tag{3.33}$$

$$m\dot{u}(L) = \frac{2mc}{\rho_0} \sinh(zL) z(\mu z - c) e^{z(\mu z - c)t} \ , \tag{3.34}$$

$$\Delta P(L) = 2c^2 \cosh(zL) e^{z(\mu z - c)t} \ . \tag{3.35}$$

Hence, the fundamental equation (3.13) is satisfied if and only if:

$$\frac{2mc}{\rho_0} \sinh(zL) z(\mu z - c) = 2c^2 \cosh(zL) \ , \tag{3.36}$$

which can be written as:

$$z(\mu z - c) \tanh(zL) = \frac{\rho_0 c}{m} \ , \tag{3.37}$$

or:

$$\boxed{(-izL) \left(1 - \frac{\mu z}{c}\right) \tan(-izL) = \frac{\rho_0 L}{m} \ .} \tag{3.38}$$

Equation (3.38) has conjugate solutions. It is consistent with (3.26): indeed, if we take $\mu = 0$ in (3.38), it can be proved that $z = \pm i\omega/c$, with ω given by (3.26) (the reader may check that a complex number r such that $r\tan(r) \in I\!R^+$ is necessarily on the imaginary axis).

Remark 1: Before analyzing the relation (3.38), let us come back to (3.31), and investigate whether it was valid to keep only the diffusion error term. If we add the dispersion term, we write, up to second order in Δx and Δt:

$$W_t + \begin{pmatrix} 0 & 1 \\ c^2 & 0 \end{pmatrix} W_x = \mu W_{xx} + \lambda \begin{pmatrix} 0 & 1 \\ c^2 & 0 \end{pmatrix} W_{xxx} \ , \tag{3.39}$$

where the dispersion coefficient λ is given by (3.30). As above for Lemma 2, we can show that the elementary solutions of equation (3.39) with the boundary condition (3.10) are given by:

$$W = e^{z(\mu z - c + \lambda c z^2)t} \left[\begin{pmatrix} 1 \\ +c \end{pmatrix} e^{zx} + \begin{pmatrix} 1 \\ -c \end{pmatrix} e^{-zx} \right] \quad (\text{for } z \in \mathcal{C}). \tag{3.40}$$

Then, the equation (3.38) for z becomes:

$$\frac{2mc}{\rho_0} \sinh(zL) z(\mu z - c + \lambda c z^2) = 2c^2 \cosh(zL) \ . \tag{3.41}$$

Of course, the preceding equation reduces to (3.38) when $\lambda = 0$. But we see also that the influence of the dispersion term is much weaker than the one of the diffusion term, since the ratio $\lambda c z^2/(\mu z)$ is small (when μ and λ are small, i.e. for $z \approx \pm i\omega/c$):

$$\frac{|\lambda c z^2|}{|\mu z|} = \left(\frac{1-2\nu}{3}\right) \frac{\omega \Delta x}{c} \ . \tag{3.42}$$

Therefore, we will actually neglect the dispersion error in the sequel, and analyze equation (3.38) instead of (3.41). •

It is also interesting to analyze the dependence on the solution z of (3.38) of the diffusion parameter μ. We can linearize the equation for z around $\mu = 0$, knowing that for $\mu = 0$, $z = \pm i\omega/c$. We obtain (the details are omitted):

$$\left. \frac{\partial \mathcal{I}m\,(z(\mu z - c))}{\partial \mu} \right|_{\substack{\mu=0 \\ z=\pm i\omega/c}} = 0 \ , \tag{3.43}$$

$$\left. \frac{\partial \mathcal{R}e\,(z(\mu z - c))}{\partial \mu} \right|_{\substack{\mu=0 \\ z=\pm i\omega/c}} = -\frac{\omega^2}{c^2} \left[1 - \left[1 + \frac{\rho_0 L}{m} \left(1 + \frac{m^2\omega^2}{\rho_0^2 c^2} \right) \right]^{-1} \right] \ . \tag{3.44}$$

Thus, from (3.43), it follows that the temporal pulsation of the elementary waves are changed only at the second order when μ is small (recall from Lemma 2 that $z(\mu z - c)$ is precisely the coefficient of the time variable t in the solution (3.32)).

The interpretation of (3.44) is less obvious. For the sake of convenience, we have considered so far complex variables, but we should now come back to the actual (real) variables, and observe the piston motion. With our complex solution, we have $\dot{x} = \dfrac{2c}{\rho_0}\sinh(zL)e^{z(\mu z - c)t}$, whence $x = \dfrac{2c}{a\rho_0}\sinh(zL)e^{at}$, with $a = z(\mu z - c)$. Then, it is easy to check that we can write an equation of the form:

$$m\ddot{x} = \alpha x + \beta \dot{x} \tag{3.45}$$

for the piston, with α and β real, by taking:

$$\alpha = -m|a|^2 = -m|z(\mu z - c)|^2 \ , \quad \beta = 2m\mathcal{R}e(a) = 2m\mathcal{R}e\left(z(\mu z - c)\right) \ . \tag{3.46}$$

Thus, we are now able to know the stiffness and the damping induced by the fluid on the piston. For $\mu = 0$, we find of course $\alpha = -m\omega^2$ and $\beta = 0$. For a small diffusion μ, we get from (3.43) and (3.44):

$$\beta = -\frac{2m\omega^2}{c^2}\left[1 - \left[1 + \frac{\rho_0 L}{m}\left(1 + \frac{m^2\omega^2}{\rho_0^2 c^2}\right)\right]^{-1}\right] \mu + O(\mu^2) \ , \tag{3.47}$$

$$\alpha = -m\omega^2 + O(\mu^2) \ . \tag{3.48}$$

Remark 2: We achieved the same study with retaining the second-order terms (but still neglecting the dispersion term in the modified equation). It shows that no second-order term is introduced in the expansion of the damping β by the diffusion μ. The influence of the dispersion error will be analyzed with second-order accurate schemes in Section 3.6.2 below. •

3.3.2 Roles of structural schemes and boundary treatments

Through α and β, the above analysis predicts analytical values for the numerically observed pulsation and damping of the piston oscillations. For the pulsation of the coupled system, the prediction (3.26) reveals to compare very well with numerical simulations: it gives a predicted pulsation with a relative error less than one percent. This great accuracy is partly explained by (3.48). But the analytically predicted damping factor β is not so accurate and is even sometimes quite far from the numerical results.

In the following, we give explanations for this inaccuracy of the above analysis. We will derive a new formula for the numerical damping β of the system, and we will check the validity of the preceding prediction for α.

Sources of numerical damping

In the physical problem, we did not introduce any dissipation which could produce damping ($d = 0$ in (3.12)). The whole damping is therefore of numerical origin. The first origin lies in the numerical scheme for the fluid, and was taken into account through the modified equation. But there is a second origin of numerical dissipation, which is related to the temporal integration of the piston's motion.

Indeed, in the above analysis, we considered that the numerical solution W in the fluid is no longer discrete, but continuous in space and time: it is the solution (3.32) of the modified equation (3.31), and we considered that all spatial and temporal errors of the fluid approximation are dealt with through the modified equation. However, we also used a time-continuous representation for the piston, since we coupled the solution (3.32) with the differential piston equation (3.13). In practice, in the numerical simulations, we use a discrete form of the fundamental equation, and the numerical errors related to this approximation have been neglected in the above analysis, since they are not taken into account in the modified equation of the fluid.

For instance, if the speed of the piston is computed with the scheme:

$$m\frac{\dot{x}^{n+1} - \dot{x}^n}{\Delta t} = \Delta P^n(L) \ , \tag{3.49}$$

then the argument used in the preceding section to obtain equations (3.36) and (3.38) is no longer valid. We then have to introduce the discrete temporal scheme in our reasoning.

New predictions for the numerical damping

Let us therefore come back to (3.32), and search a new equation for z, assuming that the scheme (3.49) is used for the piston. From (3.33) and (3.35), we deduce (still denoting $a = z(\mu z - c)$):

$$m\frac{e^{a\Delta t} - 1}{\Delta t}\frac{2c}{\rho_0}\sinh(zL) = 2c^2\cosh(zL) \ , \tag{3.50}$$

which can be rewritten as:

$$z(\mu z - c)\tanh(zL) = \frac{\rho_0 c}{m}\frac{a\Delta t}{e^{a\Delta t} - 1} \ , \tag{3.51}$$

which now replaces (3.37).

The expansion of z around the value $z_0 = \pm i\omega/c$ (where ω is given by (3.26)) in terms of μ and Δt (which are assumed to be small with respect to c^2/ω and $1/\omega$ respectively) takes the form:

$$z = \pm\frac{i\omega}{c} - \left[1 + \frac{\rho_0 L}{m}\left(1 + \frac{m^2\omega^2}{\rho_0^2 c^2}\right)\right]^{-1}\left[\frac{\omega^2}{c^3}\mu + \frac{\omega^2}{2c}\Delta t\right] , \tag{3.52}$$

hence:

$$\boxed{\begin{aligned}\beta \;=\; & -\frac{2m\omega^2}{c^2}\left[1-\left[1+\frac{\rho_0 L}{m}\left(1+\frac{m^2\omega^2}{\rho_0^2c^2}\right)\right]^{-1}\right]\mu \\ & +m\omega^2\left[1+\frac{\rho_0 L}{m}\left(1+\frac{m^2\omega^2}{\rho_0^2c^2}\right)\right]^{-1}\Delta t \\ & +O(\mu^2,\Delta t^2)\ .\end{aligned}} \tag{3.53}$$

The preceding formula appears to give a very good prediction of the total numerical damping. For example, we simulated the motion of a 0.8kg piston with a one meter chamber, and tried several values of the Courant number (with 50 mesh points). With $\nu = 0.045$, we numerically found $\beta = -1.87$, whereas our formula (3.53) predicts $\beta = -1.80$. For $\nu = 0.45$, we found $\beta = -1.33$ and the analytical prediction is $\beta = -1.32$. The average error is then less than 4% in the first case, less than 1% in the latter.

3.4 Coupled eigenvector analysis

In the previous section, we were only able to take partially into account the influence of the discrete treatment of the boundary conditions on the numerical simulations. We now have to be more specific about these conditions, and analyze in details their overall effect on the numerical damping of the piston oscillations.

To be more specific, let us write down the boundary conditions for the family of schemes considered in this section. We call N the number of computational cells in the chamber $[0, L]$ (i.e. $N\Delta x = L$), and write the explicit scheme under the following form, for $1 \leq i \leq N$:

$$\frac{W_i^{n+1} - W_i^n}{\Delta t} + \frac{\Phi_{i+1/2}^n - \Phi_{i-1/2}^n}{\Delta x} = 0\ . \tag{3.54}$$

Outside the boundaries, the numerical flux $\Phi_{i+1/2}^n$ is based on first-order upwinding. For $\Phi_{1/2}^n$, at the fixed wall, we use upwinding with a "mirror" cell, i.e. a fictitious cell with the same density as in the first cell and the opposite momentum of the first true cell. At the other end of the chamber, we have to evaluate a flux through the moving piston; we take:

$$\Phi_{N+1/2}^n = \begin{pmatrix} \rho_0 V_p^* \\ c^2\Delta\rho_N^n \end{pmatrix}\ . \tag{3.55}$$

Here, V_p^* is a prediction of the piston speed, evaluated as a weighted average of the nth and $n+1^{st}$ computational speeds by the formulas:

$$m\frac{V_p^{n+1} - V_p^n}{\Delta t} = c^2\Delta\rho_N^n\ , \tag{3.56}$$

$$V_p^* = (1-\theta)V_p^n + \theta V_p^{n+1} \ , \tag{3.57}$$

where θ is a fixed parameter. Such conditions are commonly used in aeroelasticity simulations (see e.g. [31]).

At first sight, we are not able to really take these conditions into acount in the modified equation analysis of the previous section. This is why we now introduce a second method, which we call the "coupled eigenvector analysis".

3.4.1 Presentation of the analysis

The analysis which we now present is an eigenvector and eigenvalues analysis. We consider the set of all computational values at a certain time step, for both the fluid and the piston, and we see it as an unknown vector which is changing during time integration. We still denote by W the vector of the conserved variables for the fluid and by V_p the speed of the piston. Let us also add that we still consider the physically undamped and free (i.e. with no spring) piston ($d = k = 0$ in (3.12)).

Writing the complete scheme under the form:

$$\begin{pmatrix} W \\ V_p \end{pmatrix}^{n+1} = \begin{pmatrix} W \\ V_p \end{pmatrix}^{n} + \Delta t \mathcal{F} \begin{pmatrix} W \\ V_p \end{pmatrix}^{n}, \tag{3.58}$$

we are going to search the eigenvectors and eigenvalues of the linear operator $\mathcal{F}$, which in particular takes into account the detailed formulation of the discrete coupling between fluid and structure.

From our knowledge of the exact solution (3.21) and of the modified solution (3.32), we may make a good guess for the eigenvectors of the coupled operator $\mathcal{F}$. We set:

$$\left\{ \begin{array}{lllllll} W_1^n & = & & A^n W^+ e^{zx_1} & + & k_l & B^n W^- e^{-zx_1} \ , \\ W_i^n & = & & A^n W^+ e^{zx_i} & + & & B^n W^- e^{-zx_i} \ \text{ for } 1 < i < N \ , \\ W_N^n & = & k_r & A^n W^+ e^{zx_N} & + & & B^n W^- e^{-zx_N} \ , \end{array} \right. \tag{3.59}$$

where $x_i = (i - 1/2)\Delta x$ is the center of the ith cell, $z \in \mathcal{C}$ is a spatial pulsation, $W^\pm = (1 \quad \pm c)^t$ are the eigenvectors of the acoustic matrix appearing in (3.9), A^n and B^n are the amplitudes of the forward and backward waves, k_l and k_r are correction coefficients at both ends of the chamber.

Our goal is to find A^n, B^n, k_l, k_r and z such that:

1. the solution at time $t^{n+1} = t^n + \Delta t$ has the form:

$$\left\{ \begin{array}{lllllll} W_1^{n+1} & = & & A^{n+1} W^+ e^{zx_1} & + & k_l & B^{n+1} W^- e^{-zx_1} \ , \\ W_i^{n+1} & = & & A^{n+1} W^+ e^{zx_i} & + & & B^{n+1} W^- e^{-zx_i} \ \text{ for } 1 < i < N \ , \\ W_N^{n+1} & = & k_r & A^{n+1} W^+ e^{zx_N} & + & & B^{n+1} W^- e^{-zx_N} \ ; \end{array} \right. \tag{3.60}$$

2. there exists a complex number λ such that:

$$\frac{A^{n+1}}{A^n} = \frac{B^{n+1}}{B^n} = \frac{V_p^{n+1}}{V_p^n} = \lambda \ . \tag{3.61}$$

3.4.2 Analysis with a predicted piston speed

Let us conduct the coupled eigenvector analysis, for the scheme detailed in equations (3.54)–(3.57). We give the main outlines of the whole computation. First we write the evolution equation for the fluid in a medium cell (including cells 2 and $N-1$, because the upwind fluxes for these cells do not involve neither k_l nor k_r). Writing $x = x_i$, for $2 \leq i \leq N-1$, we have:

$$W_i^{n+1} = W_i^n + \frac{c\Delta t}{\Delta x}\left[A^n W^+ e^{z(x-\Delta x)} - B^n W^- e^{-zx} - A^n W^+ e^{zx} + B^n W^- e^{-z(x+\Delta x)}\right] \ . \tag{3.62}$$

Identifying with (3.61), we get:

$$\frac{A^{n+1}}{A^n} = \frac{B^{n+1}}{B^n} = 1 + \frac{c\Delta t}{\Delta x}\left(e^{-z\Delta x} - 1\right) = \lambda \ . \tag{3.63}$$

If we write the same equation for the first cell, we obtain:

$$W_1^{n+1} = W_1^n + \frac{c\Delta t}{\Delta x}\left[\left(W^+ - W^-\right) k_l B^n e^{-zx_1} - A^n W^+ e^{zx_1} + B^n W^- e^{-z(x_1+\Delta x)}\right] \ , \tag{3.64}$$

and the identification implies:

$$k_l = 1 \ , \tag{3.65}$$

$$B^n = A^n \ . \tag{3.66}$$

The equation for the last cell writes:

$$\begin{aligned} W_N^{n+1} = W_N^n + \frac{\Delta t}{\Delta x}[\ & cA^n W^+ e^{z(x_N-\Delta x)} - cB^n W^- e^{-zx_N} \\ & -\frac{\rho_0 V_p^*}{2}\left(W^+ + W^-\right) - \frac{c\Delta\rho_N^n}{2}\left(W^+ - W^-\right) \ ] \ . \end{aligned} \tag{3.67}$$

Introducing the expressions of V_p^* and $\Delta\rho_N^n$, the preceding equation implies:

$$k_r = 1 + \left(1 - e^{z\Delta x}\right) e^{-2zx_N} \ , \tag{3.68}$$

$$\begin{aligned} \frac{V_p^n}{A^n} = & -\frac{c^2\theta\Delta t}{m}\left[2\cosh zx_N + \left(1 - e^{z\Delta x}\right) e^{-zx_N}\right] \\ & -\frac{2c}{\rho_0}\left[e^{-zx_N}\left(e^{-z\Delta x} - 1\right) - \frac{1}{2}\left(e^{zx_N} - e^{-zx_N} e^{z\Delta x}\right)\right] \ . \end{aligned} \tag{3.69}$$

Lastly, writing the last relation (3.61), we find an additional equation which determines z (and therefore λ from (3.63)):

$$\boxed{\begin{aligned}&\left[\frac{\Delta x}{(e^{-z\Delta x}-1)}+\theta c\Delta t\right]\left[2\cosh zx_N+\left(1-e^{z\Delta x}\right)e^{-zx_N}\right]=\\&\frac{-2m}{\rho_0}\left[e^{-zx_N}\left(e^{-z\Delta x}-1\right)-\sinh zx_N+\frac{1}{2}e^{-zx_N}\left(e^{z\Delta x}-1\right)\right]\ .\end{aligned}} \tag{3.70}$$

We recall that, in this equation, x_N is given by $x_N = L - \Delta x/2$. Notice also that, as expected, the amplitudes A_n, B_n are determined only up to a multiplicative constant.

Equation (3.70) is very interesting. For example, *if we assume that* $\theta = 0$ and if we take the limit when Δt and Δx tend to 0, we find exactly equation (3.26).

Assuming that Δx and Δt are very small (compared with c/ω and $1/\omega$ respectively), we can obtain the following expansion of z around the value $z_0 = \pm i\omega/c$ given by (3.26):

$$z = z_0 - \frac{\omega^2}{2c^2}\left[1+\frac{\rho_0 L}{m}\left(1+\frac{m^2\omega^2}{\rho_0^2c^2}\right)\right]^{-1}\left[\Delta x - 2\theta c\Delta t\right]\ . \tag{3.71}$$

Defining the coefficient a by setting $\lambda = \exp(a\Delta t)$, we can again define the stiffness coefficient α and the continuous damping β as in (3.46). Then α can be shown to be equal to its previous value $\alpha = -m\omega^2$ up to second-order accuracy, whereas, using (3.63) and (3.71), we find:

$$\boxed{\frac{\beta}{2m} = \frac{\omega^2(\nu-1)\Delta x}{2c} - \frac{\omega^2(2\theta\nu-1)\Delta x}{2c\left[1+\frac{\rho_0 L}{m}\left(1+\frac{m^2\omega^2}{\rho_0^2c^2}\right)\right]}\ .} \tag{3.72}$$

Thus, we now have a precise analytical prediction of the numerical damping effect, which takes into account in full detail the numerical formulation (3.54)-(3.57). The question is then to compare this prediction with the prediction (3.53) obtained with the modified equation analysis.

3.5 Comparing the two methods

The first remark to be pointed out about equation (3.72) is the following one: if we take $\theta = 0$, corresponding to the choice $V_p^* = V_p^n$ in (3.57), we find exactly the same prediction for β as in (3.53) (with μ in (3.53) given by (3.29)). This is the reason why our previous prediction (3.53) turned out to be valid when we took $V_p^* = V_p^n$, as in the simulations whose results are reported at the very end of Section 3.3.

Now, if we take $\theta \neq 0$ in (3.72), we find a different prediction. Again, this analytical prediction revealed to be very accurate when compared with the actually observed

damping of the piston in a numerical simulation: for the same physical parameters as before but with $\theta = 1$, the simulation gave $\beta = -2.73$, whereas (3.72) predicts $\beta = -2.82$, i.e. the error in the prediction is again less than 4%.

It is also worth noticing that, when $\theta > 0$, $\beta < \beta_{\theta=0}$. Taking a positive value for θ gives more damping and more stable numerical simulations. This explains the usual choice of aeroelasticians.

At this point, we may wonder whether the modified equation analysis is really restricted to cases where $\theta = 0$: is it really impossible to analyze the schemes operating with $\theta \neq 0$ using the modified equation analysis? This question leads us to revisit our first analysis, and will also allow us to better understand the equations (3.56)-(3.57).

Indeed, for the modified equation analysis, we did not explicitly describe the discrete boundary condition at the piston. Of course, the treatment of the boundary has no influence on the modified equation itself, which concerns only the internal part of the flow. But, in practice, the formulation of the boundary condition with the parameter θ induces a certain time shift between the fluid and the structure, and this acts as a modified boundary condition for the modified equation.

Let us be more specific, and show how we can handle the dependence on θ within the modified equation analysis. To make the boundary flux (3.55) consistent with the other numerical fluxes, we have to consider that V_p^* is an approximation of the piston speed at time $n\Delta t$. But then, from (3.57), the nth computational piston speed V_p^n represents the speed of the piston at time $(n-\theta)\Delta t$! In other words, for the scheme (3.54)-(3.57) with the parameter θ, we should replace equation (3.49) in the modified equation analysis by:

$$m\frac{\dot{x}[(n+1-\theta)\Delta t] - \dot{x}[(n-\theta)\Delta t]}{\Delta t} = \Delta P(L, n\Delta t) \ . \tag{3.73}$$

Instead of (3.50), we then find:

$$m\ e^{-a\theta\Delta t}\ \frac{e^{a\Delta t}-1}{\Delta t}\ \frac{2c}{\rho_0}\ \sinh(zL) = 2c^2\cosh(zL)\ , \tag{3.74}$$

and the final result for β, which replaces (3.53), becomes:

$$\boxed{\beta = -\frac{2m\omega^2\mu}{c^2} + \frac{m\omega^2\left(\frac{2\mu}{c^2} + (1-2\theta)\Delta t\right)}{\left[1 + \frac{\rho_0 L}{m}\left(1 + \frac{m^2\omega^2}{\rho_0^2 c^2}\right)\right]} + +O(\mu^2, \Delta t^2)\ .} \tag{3.75}$$

It is straightforward to see that this prediction exactly coincides with (3.72) (again with the value (3.29) of μ). We have therefore extended the modified equation analysis to the above family of schemes, for any value of the parameter θ, and we have also learnt how to interprete the role of this parameter: V_p^* is an approximation of the piston speed at time $n\Delta t$, and V_p^n must be seen as an evaluation of the piston speed at time $(n-\theta)\Delta t$.

Remark 3: Since the modified equation analysis is easier to conduct than the eigenvector analysis, the preceding remarks about the extension of the former make it possible to analyze situations where the eigenvector analysis would be very complex or would even fail, because finding the analytical form of the eigenvectors is impossible. For example, we simulated a slightly different problem, with acoustic waves propagating in a chamber of fixed length L (without a piston), but moving on tracks without friction. The coupled eigenvector analysis is feasible but complex. On the contrary, it is easy to solve the modified equation; we find that:

$$W = \left[W^+ e^{zx} - W^- e^{z(L-x)}\right] e^{z(\mu z - c)t} \ . \tag{3.76}$$

For the "θ-scheme" (i.e. with discrete equations similar to (3.56)-(3.57) for the chamber velocity), the complex pulsation z is solution of:

$$e^{-a\theta\Delta t}\frac{e^{a\Delta t}-1}{\Delta t} = \tanh(\frac{zL}{2})\frac{2c\rho_0}{m} \ . \tag{3.77}$$

Then, the new pulsation $\bar{\omega}$ and the new damping $\bar{\beta}$ are given by:

$$\tan(\frac{\bar{\omega}L}{2c}) = -\frac{m}{\rho_0 L}\frac{\bar{\omega}L}{2c} \ , \tag{3.78}$$

and:

$$\boxed{\frac{\bar{\beta}}{2m} = \frac{\bar{\omega}^2(\nu-1)\Delta x}{2c} - \frac{\bar{\omega}^2(2\theta\nu-1)\Delta x}{2c\left[1+\frac{\rho_0 L}{m}\left(1+\frac{m^2\bar{\omega}^2}{4\rho_0^2c^2}\right)\right]} \ .} \tag{3.79}$$

These predictions were numerically tested and we again found an error less than 3%. Moreover, we also performed artificially undamped solutions of the physical problem with an adequate value of θ (see Section 3.7.2 below). •

3.6 Analyzing other schemes

We now use the two previous methods in order to analyze some other schemes for our model fluid-structure problem.

3.6.1 Schemes with predicted pressure and speed

In this part, we conduct the coupled eigenvector analysis for other schemes which are also commonly used by aeroelasticians, where a predicted pressure at the piston is used. Instead of (3.55), we now use a wall flux given by:

$$\Phi^n_{N+1/2} = \begin{pmatrix} \rho_0 V_p^* \\ c^2\Delta\rho^* \end{pmatrix} \ , \tag{3.80}$$

with:

$$\Delta\rho^* = (1-\phi)\,\Delta\rho_N^n + \phi\Delta\rho_N^{n+1} \ , \tag{3.81}$$

where $\Delta\rho_N^{n+1}$ is predicted with the first component of (3.67). The predicted piston speed V_p^* is still given by (3.56)-(3.57).

The computation follows the same lines as above. Equations (3.63), (3.65) and (3.66) still hold, and the evolution equations for the solution in the last cell gives:

$$\Delta\rho_N^{n+1} = \Delta\rho_N^n + \frac{\Delta t}{\Delta x}\left[cA^n e^{z(x_N-\Delta x)} - cB^n e^{-zx_N} - \rho_0 V^*\right] \ , \tag{3.82}$$

$$\Delta(\rho u)_N^{n+1} = \Delta(\rho u)_N^n + \frac{c\Delta t}{\Delta x}\left[cA^n e^{z(x_N-\Delta x)} + cB^n e^{-zx_N} - c\Delta\rho_N^*\right] \ . \tag{3.83}$$

Introducing the expressions of V^* and $\Delta\rho^*$, we deduce from the preceding equations (after a quite heavy computation) that:

$$k_r = \frac{1 + e^{-2zx_N}\left(1-e^{z\Delta x}\right)\left(1-\dfrac{c\phi\Delta t}{\Delta x}\right)}{1+\left(1-e^{z\Delta x}\right)\dfrac{c\phi\Delta t}{\Delta x}} \ , \tag{3.84}$$

$$\frac{V_p^n}{A^n} = -\frac{c}{\rho_0}\left[\left(e^{-z\Delta x} - 1 + \frac{\rho_0 c\theta\Delta t}{m}\right)\left(k_r e^{zx_N} + e^{-zx_N}\right) + e^{-zx_N} - e^{z(x_N-\Delta x)}\right] \ . \tag{3.85}$$

Using (3.56) and the last equality in (3.61), we finally obtain the following relation fixing z:

$$\boxed{\left[\frac{\rho_0\Delta x}{m\left(e^{-z\Delta x}-1\right)} + e^{-z\Delta x} - 1 + \frac{\rho_0 c\theta\Delta t}{m}\right]\left[k_r e^{zx_N} + e^{-zx_N}\right] = e^{z(x_N-\Delta x)} - e^{-zx_N} \ .} \tag{3.86}$$

Assuming again that Δx and Δt are very small (respectively compared with c/ω and $1/\omega$), we can obtain the new expansion of z around the value $z_0 = \pm i\omega/c$. We first find:

$$k_r = 1 + z_0\left(1+e^{-2Lz_0}\right)(c\phi\Delta t - \Delta x) \ , \tag{3.87}$$

whence:

$$z = z_0 - \frac{\omega^2}{2c^2}\left[1 + \frac{\rho_0 L}{m}\left(1+\frac{m^2\omega^2}{\rho_0^2 c^2}\right)\right]^{-1}\left[\Delta x - 2(\theta-\phi)c\Delta t\right] \ . \tag{3.88}$$

Using the value (3.63) of λ, we find again that α has only a second-order variation, and we obtain a new value of the "continuous damping" β:

$$\boxed{\frac{\beta}{2m} = \frac{\omega^2(\nu-1)\Delta x}{2c} - \frac{\omega^2[2(\theta-\phi)\nu-1]\Delta x}{2c\left[1+\dfrac{\rho_0 L}{m}\left(1+\dfrac{m^2\omega^2}{\rho_0^2c^2}\right)\right]} \ .} \tag{3.89}$$

This equation is again very close to (3.72). Naturally, it coincides with (3.72) if we take $\phi = 0$, but it gives a different prediction for β if $\phi \neq 0$. In order to test this

expression, we performed four numerical simulations, with $\theta = 0$ or 1 and $\phi = 0$ or 1 (and $\nu = 0.45$). The results are presented in the following table:

(θ, ϕ)	$(0,0)$	$(0,1)$	$(1,0)$	$(1,1)$
Numerical damping	- 1.326	+ 0.250	- 2.917	- 1.318
Predicted damping	- 1.321	+ 0.181	- 2.823	- 1.321

Table 1: Numerically observed and analytically predicted values of the damping factor β for the (θ, ϕ)-scheme.

We again have a very good agreement between the prediction and the results of the simulations. Relative errors between the analytically predicted and the numerically observed damping are less than 3%, except in the case $(\theta, \phi) = (0, 1)$ (in this case, the absolute error between the prediction and the numerical value of β remains small, but the relative error is larger because β itself is rather small). Thus, the analytical prediction (3.89) of the numerical damping appears to be quite satisfactory for the class of schemes under consideration.

Remark 4: Notice also on Table 1 that the simulation with $(\theta, \phi) = (0, 1)$ ran unstable: $\beta > 0$. We see here that the method for the *coupled* system might be unstable, although the fluid scheme in itself operates under stable conditions ($\nu < 1$). This point is investigated in our next chapter [63]. •

3.6.2 Second-order accurate schemes

So far, we have restricted our attention to first-order accurate schemes for the fluid approximation. In this section, we turn to a second-order accurate explicit scheme and analyze the influence of this modification on our analytical predictions of the stiffness and damping parameters α and β. We are going to use the modified equation analysis.

Let us therefore assume that we use for the integration of (3.9) a scheme which is second-order accurate in both time and space (such as the Lax-Wendroff, or second-order upwind, or leap-frog schemes...). Then, the modified equation writes, up to second-order accuracy:

$$W_t + \begin{pmatrix} 0 & 1 \\ c^2 & 0 \end{pmatrix} W_x = \lambda \begin{pmatrix} 0 & 1 \\ c^2 & 0 \end{pmatrix} W_{xxx} \ , \tag{3.90}$$

with $\lambda = O(\Delta x^2)$ (for instance, $\lambda = \dfrac{\Delta x^2}{6}(\nu^2 - 1)$ for the leap-frog and Lax-Wendroff schemes; see [1]).

In order to reach also second-order accuracy for the structure, we use the scheme (3.55)-(3.57) with $\theta = 1/2$. Indeed, when $\theta = 1/2$, in full agreement with our previous

observations on the meaning of θ and the interpretation of V_p^n (see Section 3.5), we can rewrite (3.55)-(3.57) as:

$$\Phi_{N+1/2}^n = \begin{pmatrix} \rho_0 V_p^* \\ c^2 \Delta \rho_N^n \end{pmatrix} , \tag{3.91}$$

$$V_p^* = \frac{V_p^{n-1/2} + V_p^{n+1/2}}{2} , \quad m \frac{V_p^{n+1/2} - V_p^{n-1/2}}{\Delta t} = c^2 \Delta \rho_N^n , \tag{3.92}$$

and this scheme is obviously second-order accurate.

Then, we can easily conduct the modified equation analysis. Using (3.40), we can show that the equation for z still takes the form (3.74), with $a = cz(\lambda z^2 - 1)$. The asymptotic expansions then give:

$$\boxed{\alpha = -m\omega^2 - 2m \frac{\omega^5 c^3 L}{\dfrac{\omega L}{c} + \dfrac{\rho_0 m c \omega}{\rho_0^2 c^2 + m^2 \omega^2}} \lambda + O(\lambda^2) ,} \tag{3.93}$$

$$\boxed{\frac{\beta}{2m} = O(\lambda^2) .} \tag{3.94}$$

We see that the dispersion parameter λ produces a perturbation of the second order in Δx in the pulsation (like the diffusion μ) and a negligible fourth-order perturbation on the damping.

3.6.3 Implicit time integration schemes

In this section, we consider the temporal integration of our acoustic model with implicit schemes. We will still use the coupled eigenvector analysis to predict the spatial and temporal pulsations.

Presentation of the schemes

We now present a staggered implicit scheme for the solution of our model problem. For the time step from t^n to t^{n+1}, we first compute the evolution of the fluid, and then the evolution of the structure in a second step. For the fluid integration, we use predictions of the evolution of the structure based on its state at time t^n (but the state of the structure at t^{n+1} is not available in this fluid step); on the other hand, for the structural integration, we can use the state of the fluid at time t^{n+1}.

In the preceding sections (except in Section 3.6.2), we used a classical first-order accurate explicit upwind scheme. The flux at the cell interfaces in the fluid was given by:

$$\Phi_{i+1/2}^n = A^+ W_i^n + A^- W_{i+1}^n , \tag{3.95}$$

where $A^{\pm} = \frac{1}{2}\begin{pmatrix} \pm c & 1 \\ c^2 & \pm c \end{pmatrix}$, and the boundary fluxes were given as:

$$\Phi^n_{1/2} = \begin{pmatrix} 0 \\ c^2\Delta\rho^n_1 - c\Delta(\rho u)^n_1 \end{pmatrix} \ , \quad \Phi^n_{N+1/2} = \begin{pmatrix} \rho_0 V^*_p \\ c^2\Delta\rho^* \end{pmatrix} \ , \tag{3.96}$$

with (from (3.81)):

$$V^*_p = V^n_p + \frac{c^2\theta\Delta t}{m}\Delta\rho^n \ , \tag{3.97}$$

$$\Delta\rho^* = \Delta\rho_N{}^n + \frac{\phi\Delta t}{\Delta x}\left(A^+W^n_{N-1} + A^-W^n_N - \rho_0 V^*_p\right) \ . \tag{3.98}$$

All fluxes we just wrote are basically explicit. We consider from now on that, as far as the fluid is concerned, we use hybrid explicit-implicit fluxes obtained by substituting:

$$F^n \longrightarrow (1-\chi)F^n + \chi F^{n+1} \ . \tag{3.99}$$

Moreover, in order to consider all implicit possibilities since the fluid's state F^{n+1} is already known, we introduce a new updating scheme for the piston. Instead of (3.56), we will write:

$$m\frac{V^{n+1}_p - V^n_p}{\Delta t} = c^2\left((1-\psi)\Delta\rho^n + \psi\Delta\rho^{n+1}\right) \ . \tag{3.100}$$

For the fluid alone, this scheme is unconditionally stable when $\chi \geq 1/2$. If $\chi < 1/2$, the hybrid scheme is stable under the condition:

$$\nu \leq \frac{1}{1-2\chi} \ . \tag{3.101}$$

Coupled eigenvector analysis

We present again the main outlines of the computation. Writing implicit fluxes instead of explicit ones in the conservation equations for a standard cell gives instead of (3.63) the new relation:

$$\frac{A^{n+1}}{A^n} = \frac{B^{n+1}}{B^n} = \frac{1 + (\chi-1)\frac{c\Delta t}{\Delta x}\left(1 - e^{-z\Delta x}\right)}{1 + \chi\frac{c\Delta t}{\Delta x}\left(1 - e^{-z\Delta x}\right)} = \lambda \ . \tag{3.102}$$

The conservation equation for the first cell again gives equations (3.65) and (3.66). Lastly, the conservation equation for the last cell gives back (after some long calculations) equations (3.84) and (3.85). Then, using the new equations (3.100) and (3.102), we find a new equation for z:

$$\boxed{\frac{\rho_0\Delta x}{m\left(e^{-z\Delta x} - 1\right)} + e^{-z\Delta x} - 1 + \frac{\rho_0 c\Delta t}{m}(\theta + \psi - 1) = \frac{k_r e^{zx_N} + e^{-zx_N}}{e^{z(x_N - \Delta x)} - e^{-zx_N}} \ .} \tag{3.103}$$

Now, we want to study this equation when Δx is considered as very small (compared with c/ω). But we can no longer consider Δt as small since the time step Δt is not limited by any CFL-like condition (if we choose $\chi \geq 1/2$).

First we must notice that the expansion (3.87) for k_r is no longer valid, since Δt may be not small. In order to avoid any boundary artefact at spatial convergence, we would like to have:

$$\lim_{\Delta x \to 0} k_r = 1 \ . \tag{3.104}$$

This condition was automatically met for explicit schemes. For implicit schemes, the condition (3.104) will be satisfied if we take:

$$\boxed{\phi = 0 \ .} \tag{3.105}$$

With some easy computations, we find that z tends towards a limit z_1 when Δx tends to 0, with z_1 solution of:

$$z_1 \tanh(z_1 L) = -\frac{\rho_0}{m}\left(1 - z_1 c \Delta t(\theta + \psi - 1)\right) \ . \tag{3.106}$$

Thus, if we want the spatial and temporal pulsation to take a value independent of the time step, we have to take:

$$\boxed{\theta + \psi = 1 \ .} \tag{3.107}$$

If (3.107) holds, then $z_1 = z_0 = \pm i\omega/c$ with ω given by (3.26). We can now write the expansion of the solution z of (3.103) around z_0 in terms of Δx:

$$z = z_0 - \frac{\omega^2}{2c^2}\left[1 + \frac{\rho_0 L}{m}\left(1 + \frac{m^2\omega^2}{\rho_0^2 c^2}\right)\right]^{-1} \Delta x \ , \tag{3.108}$$

and we deduce the expansion of λ:

$$\lambda = \frac{1 + i(\chi - 1)\omega\Delta t}{1 + i\chi\omega\Delta t} - \frac{\omega^2 \Delta t}{2c} \frac{\left(1 - \left[1 + \frac{\rho_0 L}{m}\left(1 + \frac{m^2\omega^2}{\rho_0^2 c^2}\right)\right]^{-1}\right)}{(1 + i\chi\omega\Delta t)^2} \Delta x \ . \tag{3.109}$$

We have chosen here $z_0 = +i\omega/c$. If we had chosen the conjugate value for z_0, we would have found the conjugate value of λ. We see also that:

$$\lim_{\Delta x \to 0} \lambda = \frac{1 + i(\chi - 1)\omega\Delta t}{1 + i\chi\omega\Delta t} \ . \tag{3.110}$$

Recalling that the stiffness coefficient α is defined by $\alpha = -m|a|^2$, where a is chosen such that $\lambda = \exp(a\Delta t)$, we see that α will have a second-order variation from its unperturbed value $-m\omega^2$ if $\lambda = exp(\pm i\omega\Delta t) + O(\Delta t^2)$ (in the limit of Δx going to 0). From (3.110), this can be realized if we choose:

$$\boxed{\chi = \frac{1}{2} \ .} \tag{3.111}$$

With this choice, the stiffness and damping coefficients α and β have the following expansions:

$$\boxed{\alpha = -m\omega^2 \left(1 - \frac{\omega^2 \Delta t^2}{6} + O\left(\omega^3 \Delta t^3\right) + O(\Delta x^2)\right) \ ,} \tag{3.112}$$

$$\boxed{\frac{\beta}{2m} = \frac{-\omega^2}{2c\left(1 + \dfrac{\omega^2 \Delta t^2}{4}\right)} \left(1 - \left[1 + \frac{\rho_0 L}{m}\left(1 + \frac{m^2\omega^2}{\rho_0^2 c^2}\right)\right]^{-1}\right) \Delta x + O(\Delta x^2) \ .} \tag{3.113}$$

Let us make a few remarks on this last prediction. First, we see that β is always negative (and this point is clearly related with the unconditional stability of the hybrid explicit-implicit scheme when $\chi = 1/2$). Notice also that the free parameters θ and ψ (on which we have imposed the relation (3.107)) are not involved in the preceding analytical prediction for β.

The unconditional global stability of these coupled schemes makes it possible to choose the time step according to accuracy requirements. For instance, for $\Delta t = T/25$, $T = 2\pi/\omega$ being the period of the system, the relation (3.112) predicts only a one percent error on the system pulsation α. However, numerical tests tend to show that the preceding predictions are not as accurate as expected. A possible explanation is that terms of higher order in Δx in (3.112) and (3.113) may not be negligible.

Remark 5: We see on (3.113) that the damping does depend on the time step, and more precisely that increasing Δt (with Δx small and fixed) decreases the damping (i.e. increases β towards 0). This is a somewhat surprising conclusion, since the dissipation error of implicit scheme usually increases with the time step. But we should keep in mind here that the dissipation error of our implicit scheme (which is given by $2\mu = c\Delta x \ (1 + (2\chi - 1)\nu)$ is independent of Δt when $\chi = 1/2$. •

3.7 Discussion and conclusions

In this section, we gather the conclusions of the preceding analyses, and show how their results can be used in order to reduce the overall numerical damping in the simulations of the model problem. Since our objective is to improve the numerical simulations of fluid-structure interactions in more general situations, we will try to extend our conclusions to more complex cases.

3.7.1 Prediction of the numerical damping

As a first general conclusion, we have recovered on our model problem some features of the numerical schemes which are commonly used in aeroelasticity. First, for schemes

like (3.55)-(3.57), where a prediction of the speed of the structure is used for the time integration of the fluid, we found that the resulting numerical damping increases with the time lag θ between the fluid and the structure (i.e., $|\beta|$ increases with θ). On the contrary, for schemes like (3.80)-(3.81), where the pressure is predicted at the fluid-structure boundary, we proved that the numerical damping decreases with the delay in the prediction of the pressure (i.e., $|\beta|$ decreases with ϕ). Both results are illustrated on Figure 3.2, where we have presented the speed of the piston as function of time for four choices of the parameters θ and ϕ: the solid line, the dashed line and the dotted line were respectively obtained with $(\theta, \phi) = (0, 0)$ and $(1, 1)$, with $(\theta, \phi) = (1, 0)$ and with $(\theta, \phi) = (0, 1)$. In full agreement with our analyses, we also notice on Figure 3.2 that changing the parameters θ and ϕ has a very little effect on the numerically observed pulsation.

We have then achieved our first goal: an accurate prediction of the global numerical damping. We have also explained why both predictions have opposite effects on the global damping. Moreover, the fact that this observation fully agrees with the general aeroelasticity know-how [60, 61] shows that analyzing our linear model problem can be useful for understanding more general situations in aeroealsticity.

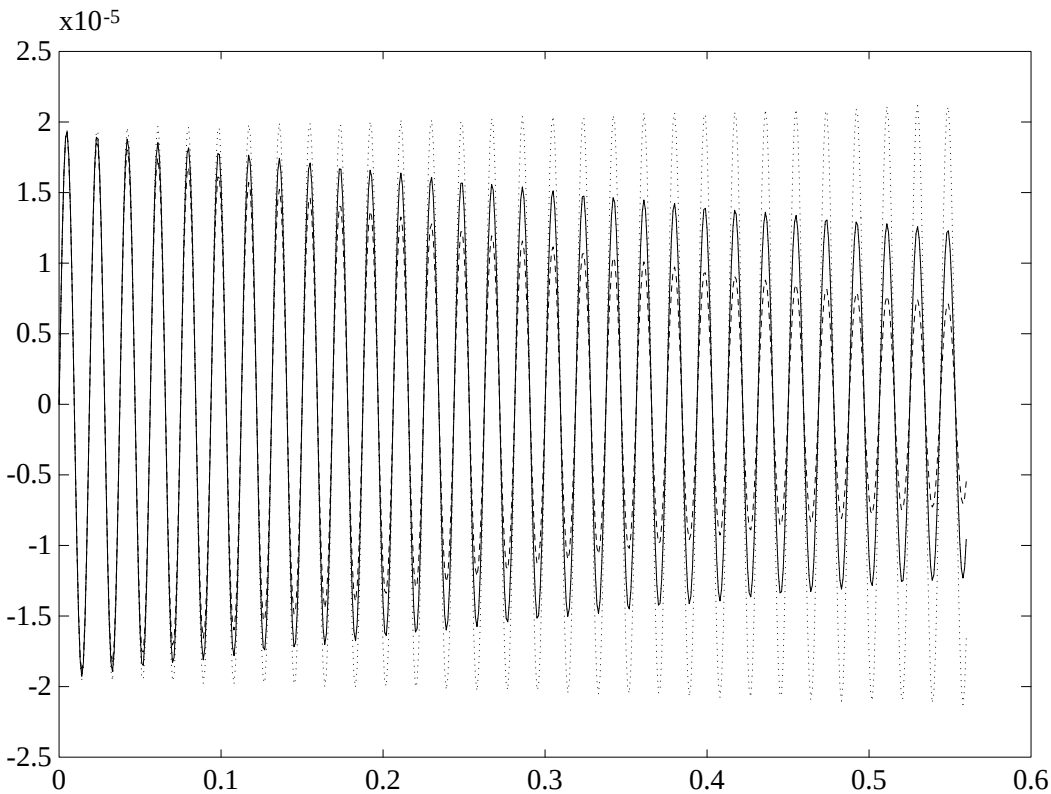

FIG. 3.2 – *Piston speed as a function of time with different predictions using the* (θ, ϕ) *scheme.*

3.7.2 Compensation of the numerical damping

Now, as said in the introduction, we want to use our analytical predictions of the numerical results in order to reduce the numerical damping.

We will have to distinguish between two situations. Fluid-structure simulations can indeed be made in one of the two following opposite conditions: either one knows *a priori* a prediction of the pulsation and of the exact damping of the physical system, or no such prediction is available. In fact, an intermediate case could be considered, where upper and/or lower bounds for these values are known. In the following, we successively consider these cases and show which conclusions can be drawn from the previous analyses.

Simulations with available predictions

Let us come back for a moment to our model acoustic problem, and perform some other numerical experiments, using the (θ, ϕ)-schemes of Section 3.6.1. Then, we can use our analytical prediction (3.89) to perform simulations where β is as small as possible: evaluating all terms in (3.89), we find that, for $\nu = 0.45$, β vanishes if $\phi - \theta = 0.88$. This was realized with the couples (0.12, 1.00) and (-0.88,0.00) for (θ, ϕ), and we actually obtained piston oscillations of fixed amplitude !

Therefore, when the pulsation and the damping of the physical system are known *a priori*, a correction of the scheme can be derived from our analytical predictions in order to recover the correct damping. For more general situations, this objective may be reached only approximately, by taking average values for the physical parameters (such as L, ρ_0..) involved in the analytical expression (3.89).

For our model problem, we also found an additional way of correcting the numerical scheme (but extending this second type of modification to multi-dimensional problem may be uneasy). We used a very simple scheme (with $\theta = 0$ and $\phi = 0$), but modified the piston time integration scheme as follows:

$$m\frac{V_p^{n+1} - V_p^n}{\Delta t} = c^2 \Delta\rho^n - \delta d\, V_p^n \ , \tag{3.114}$$

where δd is a small adaptable negative damping factor. Using either the modified equation or the coupled eigenvector analyses, it can be shown that the overall damping β vanishes if the artificial negative damping δd is taken equal to:

$$\delta d = -\frac{L\rho_0\omega^2\mu}{c^2}\left(1 + \frac{m^2\omega^2}{\rho_0^2 c^2}\right) \ , \tag{3.115}$$

where μ is given by (3.29). The efficiency of this modification is illustrated on Figure 3.3, where we observe a nearly perfectly undamped numerical simulation.

Let us also emphasize that all methods presented above can be applied to cases where the piston is physically damped and/or linked to a spring, that is with non-zero coefficients d or k in (3.12). The major difference is that the exact pulsation ω is no

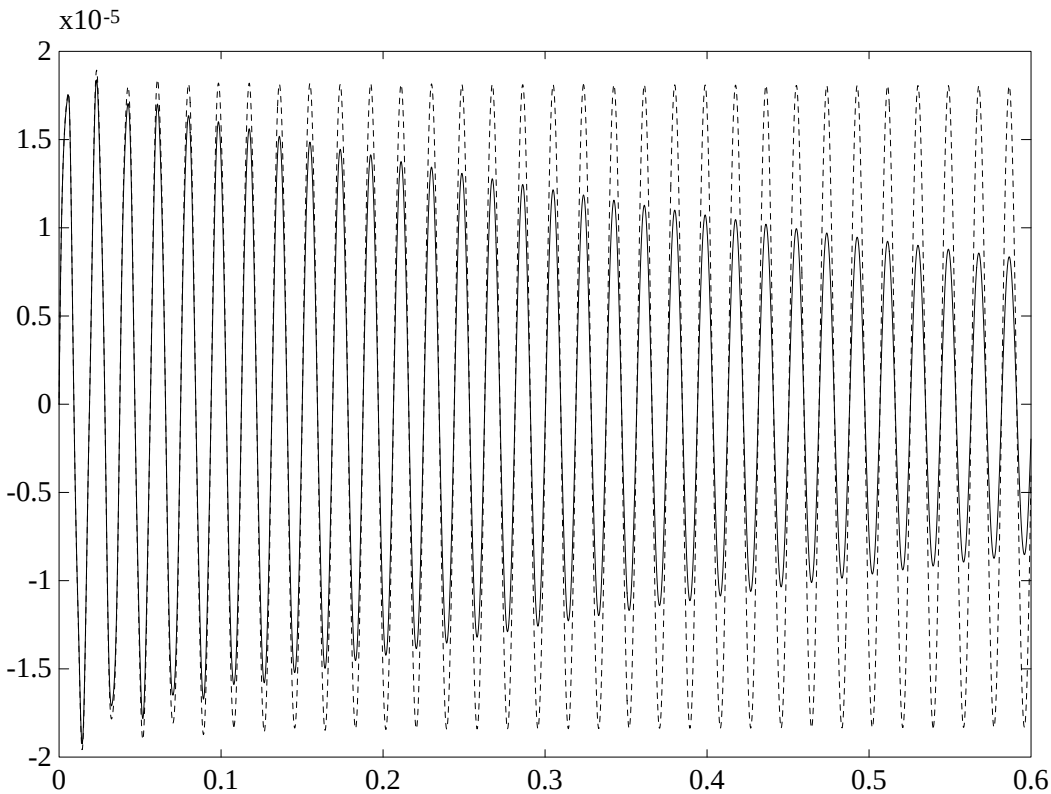

FIG. 3.3 – *Piston's speed for two simulations : the undamped one is obtained with compensation via negative damping δd of the piston.*

longer given by (3.26), but is obtained from the complex solution z of:

$$\left(mcz + d + \frac{k}{zc}\right) \tanh(zL) = -\rho_0 c \ . \tag{3.116}$$

Remark 6: Following the same approach as above for the explicit (θ, ϕ)-scheme, when we used equation (3.89) in order to perform simulations with no global damping, let us now examine if we can eliminate the first-order damping term written in (3.113) for the implicit scheme of Section 3.6.3. Ideally, we would like to do this without losing the second-order accuracy on α shown in (3.112). Thus, we will relax the conditions (3.107) and (3.111) and set instead:

$$\chi = \frac{1}{2} + \gamma \ , \quad \theta + \psi = 1 + \delta \ , \tag{3.117}$$

where γ and δ have to be chosen. Assuming that $c\delta\Delta t$ is small in (3.106), we obtain the following first-order expansions:

$$z = z_0 + D^{-1}\left[-\frac{\omega^2}{2c^2}\Delta x + \frac{\omega^2 \Delta t}{c}\delta\right] \ , \tag{3.118}$$

where $D = 1 + \dfrac{\rho_0 L}{m}\left(1 + \dfrac{m^2\omega^2}{\rho_0^2 c^2}\right)$, and:

$$\lambda = \left[\frac{1 - i\omega\Delta t/2}{1 + i\omega\Delta t/2}\right]\left[\frac{1 + \omega^2\Delta t^2\left(\frac{1}{4} - \gamma\right) - D^{-1}\Delta t\left(\frac{\omega^2\Delta x}{2c}(D-1) + \omega^2\Delta t\delta\right)}{1 + \frac{\omega^2\Delta t^2}{4}}\right] . \tag{3.119}$$

We can now obtain the desired result:

$$\alpha = -m\omega^2\left(1 - \frac{\omega^2\Delta t^2}{6} + O\left((\omega\Delta t)^3\right) + O(\Delta x^2)\right) \ , \quad \beta = O(\Delta x^2) \ , \tag{3.120}$$

provided that we take:

$$\gamma = \delta = -\frac{\Delta x}{2c\Delta t} \ . \tag{3.121}$$

This result raises a problem: since γ is negative, we will have $\chi < 1/2$ from (3.117) and we may loose the unconditional stability of the scheme for the fluid; but this does not happen, since (3.117) and (3.121) imply that $\nu = 1/(1 - 2\chi)$: in view of (3.101), we obtain an unconditionally (marginally) stable scheme. It seems therefore that we have found a close connection between our desire to suppress the global damping for the coupled system and the stability limit for the hybrid explicit-implicit scheme used in the fluid. •

Simulations with unavailable (accurate) prediction

In this part of the discussion, we assume that we do not dispose of predictions for the fundamental pulsation and damping of the physical system (this can be for instance the case for configurations where the masses of the fluid and of the structure are close to each other).

In such a case, most of the predictions presented in the preceding sections cannot be used. For our model problem with the physically undamped piston, we can however notice that the global damping factor β given by (3.72) can be made equal to zero (without using any information on the pulsation ω) by taking $\nu = 1$ and $\theta = 1/2$, which respectively produce no numerical damping in the fluid and in the structure. For the implicit scheme also, we can obtain zero damping, since no information on ω is used to choose γ and δ in (3.121). But in these two cases, these conclusions lead to use numerical schemes operating exactly at their stability limit, which cannot be useful for more general (nonlinear, multi-dimensional) situations. We therefore have to find some other methods for reducing the numerical damping.

In the case where the pulsation of the system can be bounded, the method (3.114) which introduces an artificial negative damping in the piston equation can provide help in decreasing the numerical damping in the simulation. Let us indeed call $\delta d(\omega)$ the right-hand side of (3.115) (notice that δd is a monotone decreasing function of ω). If we know *a priori* a lower bound $\omega \geq \Omega$ on the system pulsation ω, then we can use

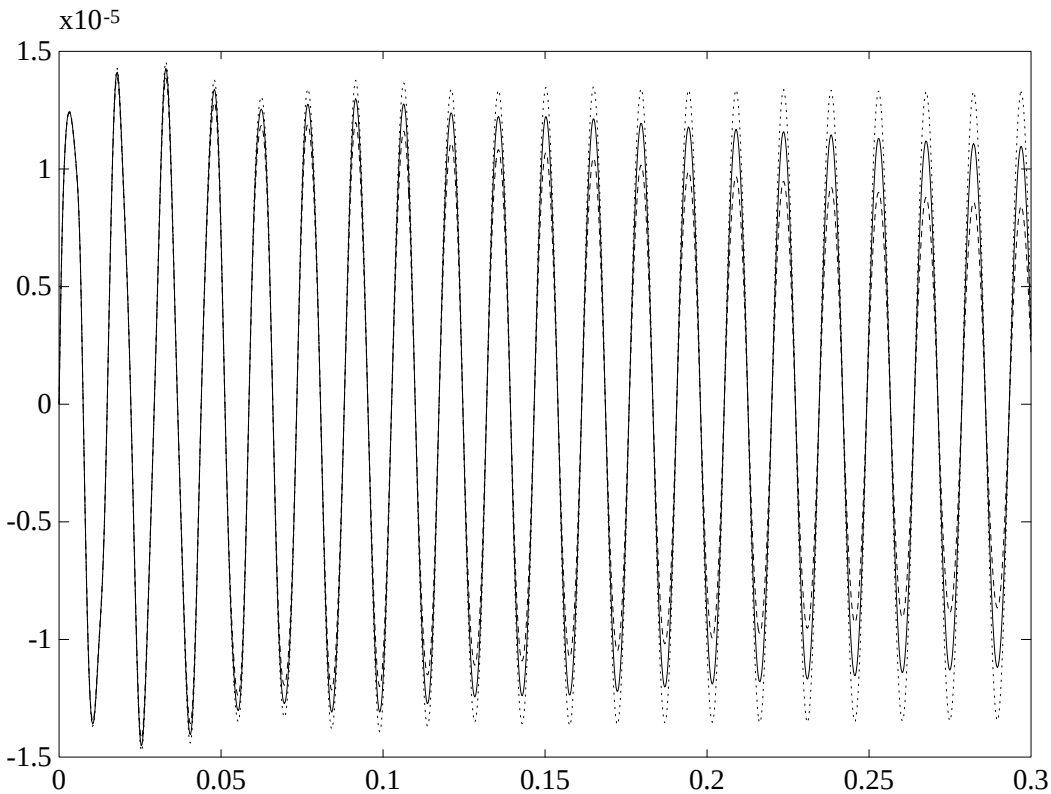

FIG. 3.4 – *Piston speed for three compensation modes: no compensation (dashed line), compensation via negative damping δd based on the spring pulsation ω_s (solid line) or on the coupled system pulsation ω (dotted line).*

the equation (3.114) for the piston, with $\delta d = \delta d(\Omega)$: this is a safe way to obtain a better (less damped) simulation, with no risk of instability.

As an example, consider the undamped piston with a spring (i.e., take $d = 0$ but $k > 0$ in (3.12)). The pulsation of the coupled system is then given by:

$$\left(\omega^2 - \omega_s^2\right) \tan(\frac{\omega L}{c}) = \frac{\omega \rho_0 c}{m} \ , \tag{3.122}$$

where $\omega_s = \sqrt{k/m}$ is the spring pulsation. In a case where the system pulsation ω is larger than the spring pulsation ω_s, we tried the above method, with $\delta d(\omega_s)$. The results are shown on Figure 3.4, where the improvement clearly appears.

Remark 7: Finally, other procedures based on energetic formulations can also be imagined (but their extensions to multiple dimensions are really not obvious). However, they can give interesting results for our model problem. Starting from the expression of the fluid energy per unit volum $\left(P/(\gamma - 1) + \rho u^2/2\right)$, assuming that the evolution of the fluid is isentropic and using the expansions of P, u and ρ in terms of the

perturbations $\Delta\rho$ and Δu, we find that the total energy in the system is given by:

$$E = \frac{1}{2\rho_0}\left(\int_0^L c^2\Delta\rho^2 + \rho_0^2\Delta u^2\right) + \frac{1}{2}m\dot{x}^2 \ . \tag{3.123}$$

The (constant) equilibrium energy has been omitted in the preceding equation. The reader will also notice that all first-order terms have disappeared in the expression of the total energy (these terms exactly cancel because the perturbations $\Delta\rho$, Δu and x are solutions of the linear system (3.9)-(3.12).

For a given spatial scheme in the fluid and given time integration schemes for the fluid and the piston, we can evaluate the variation of the total energy in terms of all computational values. For instance, for the first-order accurate explicit upwind scheme coupled with the explicit scheme (3.56), we obtain:

$$E^{n+1} = E^n - \frac{c\Delta t}{2\rho_0}\left(1 - \frac{c\Delta t}{\Delta x}\right)\sum_i \left(W_{i+1} - W_i\right)^t B\left(W_{i+1} - W_i\right) + O(\Delta t^2) \ , \tag{3.124}$$

where the symmetric positive definite matrix B is such that W^tBW is the discrete form of the integral term of (3.123).

Then, as we did in (3.114), we can add in the piston equation a negative damping δd evaluated at each time step in order to give back to the system the amount of energy dissipated during the current time step. This procedure has shown very interesting results in the one-dimensional model problem with an explicit time-integration scheme (see Figure 3.5). However, the negative damping had to switched off when the piston speed was too small (this term is basically given by the relation $\delta d\dot{x}^2 = \delta E$, where δE is the dissipated energy). Perturbations on the momentum balance of the system were also observed. Moreover, if the structure had not been reduced to a single point, a remaining question would have been to know where – on the structure – and how give back to the system the dissipated energy. •

Conclusions

The coupled problems which are to be investigated in realistic fluid-structure interactions problems are so complex that we need to examine simplified model problems in order to analyze in detail the behaviour of the numerical solution for the coupled system. For the one-dimensional model problem proposed in this section, we have derived efficient ways of analyzing the overall effect of the numerical schemes on the pulsation and the amplitude of the system oscillations, and of compensating these effects by modifying the discrete formulations, for a wide class of numerical methods. There is good hope that several of these techniques can be useful for more general problems (although this conjecture still needs to be supported by more general numerical simulations).

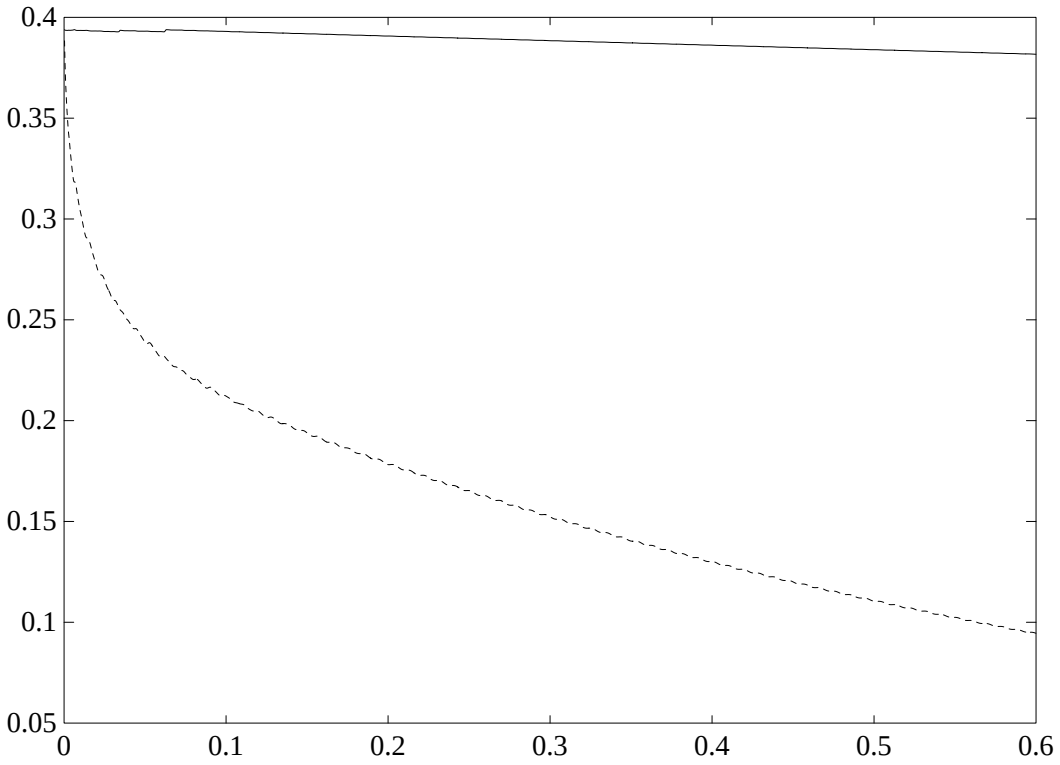

FIG. 3.5 – *Total energy of the system during the simulation: the upper curve is obtained with a negative damping based on energy compensation, as in Remark 7.*

Chapitre 4

Partitioned procedures for aeroelastic simulations

Réalisé avec † Charbel Farhat et ‡ Bernard Larrouturou.

† Department of Aerospace Engineering Sciences
and Center for Aerospace Structures
University of Colorado at Boulder
Boulder, CO 80309-0429, U. S. A.

‡ CERMICS
INRIA, BP 93, 06902 Sophia-Antipolis Cedex, France

Ce chapitre est une version étendue du rapport de recherche (CU-CAS-94-06, University of Colorado at Boulder, Colorado, 80309 USA), accepté pour publication à *Computer Methods in Applied Mechanics and Engineering* sous le titre "Partitioned procedures for the transient solution of coupled aeroelastic problems. Part I: model problem, theory and two-dimensional application".

4.1 Introduction

In order to predict the dynamic response of a flexible structure in a fluid flow, the equations of motion of the structure and the fluid must be solved simultaneously. One difficulty in handling numerically the fluid-structure coupling stems from the fact that the structural equations are usually formulated with material (Lagrangian) coordinates, while the fluid equations are typically written using spatial (Eulerian) coordinates. Therefore, a straightforward approach to the solution of the coupled fluid-structure dynamic equations requires moving at each time-step at least the portions of the fluid grid that are close to the moving structure. This can be appropriate for small displacements of the structure but may lead to severe grid distorsions when the structure undergoes large motion. Several different approaches have emerged as an alternative to partial re-gridding in transient aeroelastic computations, among which we note the arbitrary Lagrangian-Eulerian (ALE) formulation [20, 40, 9], the co-rotational approach [42, 25], and dynamic meshes [5] (see also [61] for a review). All of these approaches treat a computational aeroelastic problem as a coupled two-field problem.

However, the moving mesh itself can be formulated as a pseudo-structural system with its own dynamics [48], and therefore, the coupled transient aeroelastic problem can be formulated as a three- rather than two-field problem: the fluid, the structure, and the dynamic mesh. The semi-discrete equations governing this three-way coupled problem can be written as follows:

$$\begin{aligned} \frac{\partial}{\partial t}(A(x,t)W(x,t)) + \tilde{F}_c^c(W(x,t),x,\dot{x}) &= \tilde{F}^d(W(x,t)) \\ M\frac{\partial^2 q}{\partial t^2} + f^{int}(q) &= f^{ext}(W(x,t)) \\ \tilde{M}\frac{\partial^2 x}{\partial t^2} + \tilde{D}\frac{\partial x}{\partial t} + \tilde{K}x &= K_c q \end{aligned} \tag{4.1}$$

where x is the position of a moving fluid grid point, W is the fluid state vector, A results from the finite element/volume discretization of the fluid equations, $\tilde{F}_c^c$ is the convected vector of convective fluxes [48], $\tilde{F}^d$ is the vector of diffusive fluxes, q is the structural displacement vector, f^{int} denotes the vector of internal forces in the structure, f^{ext} the vector of external forces, M is the finite element mass matrix of the structure, $\tilde{M}$, $\tilde{D}$, and $\tilde{K}$ are fictitious mass, damping, and stiffness matrices associated with the fluid moving grid and constructed to avoid any parasitic interaction between the fluid and its grid, or the structure and the moving fluid grid [48], and K_c is a transfer matrix that describes the action of the motion of the structural side of the fluid-structure interface on the fluid dynamic mesh. For example, $\tilde{M} = \tilde{D} = 0$, and $\tilde{K} = R$ where R is a rotation matrix corresponds to a rigid mesh motion of the fluid grid around an oscillating airfoil, and $\tilde{M} = \tilde{D} = 0$ corresponds to the spring-based mesh motion scheme introduced in [5].

Each of the three components of the coupled problem described by equations (4.1) has different mathematical and numerical properties, and distinct software implementa-

tion requirements. For Euler and Navier-Stokes flows, the fluid equations are nonlinear. The structural equations may be linear or nonlinear. The semi-discrete equations governing the pseudo-structural fluid grid system are linear. The matrices resulting from a linearization procedure are in general symmetric for the structural problem, but they are typically unsymmetric for the fluid problem. Moreover, the nature of the coupling in (4.1) is implicit rather than explicit, even when the fluid mesh motion is ignored. The fluid and the structure interact only at their interface, via the pressure and the motion of the physical interface. However, the pressure variable cannot be easily isolated neither from the fluid equations nor from the fluid state vector W. Consequently, the numerical solution of (4.1) via a fully coupled monolithic scheme is computationally challenging and software-wise unmanageable.

Alternatively, equations (4.1) can be solved via partitioned procedures [59]. This approach offers several appealing features including the ability to use well established discretization and solution methods within each discipline, simplification of software development efforts, and preservation of software modularity. Traditionally, transient aeroelastic problems have been solved via the simplest possible partitioned procedure whose cycle can be described as follows: a) advance the structural system under a given pressure load, b) update the fluid mesh accordingly, and c) advance the fluid system and compute a new pressure load (see [14, 70] as well as [66, 12]). Occasionally, some investigators have advocated the introduction of a few predictor-corrector iterations within each cycle of this three-step staggered integrator in order to improve accuracy [71], especially when the fluid equations are nonlinear and treated implicitly [65].

The objective of this chapter is the investigation of a broader range of partitioned procedures for the transient solution of coupled aeroelastic problems, with particular attention to accuracy and stability issues, subcycling schemes, accuracy v.s. speed trade-offs, implementation on heterogeneous computing platforms, and inter-field as well as intra-field parallel processing. The complete three-dimensional aeroelastic problem is difficult to analyze because it mixes linear and nonlinear operators, symmetric and unsymmetric matrices, explicit and implicit coupling, and can become physically unstable. Therefore, we begin our investigation with the design and analysis of partitioned integrators for the same simplified one-dimensional aeroelastic problem as in Chapter 3. It turned out to be a good model problem for the more complex aeroelastic systems that we wish to gain some intuition about. For instance, we found in the preceding chapter the possible influence of any prediction used in the coupling staggered algorithm on the results of the simulation. We still focus on implicit time-integration schemes for the structural field, because the aeroelastic response of a structure is often dominated by low frequency dynamics. However, we consider both implicit/implicit and explicit/implicit fluid-structure partitioned procedures, with and without non-trivial prediction schemes. We discuss the computational and implementation aspects of each procedure and contrast their respective merits and shortcomings. Finally, we validate all the conclusions drawn from the investigation of the model problem with the simulation of the two-dimensional transient aeroelastic response of a flexible panel in a transonic nonlinear Euler flow.

4.2 A 1D aeroelastic model problem with an Euler flow

4.2.1 The piston problem: ALE formulation and linearization

As a model problem, we consider the one-dimensional piston depicted in Figure 4.1. The equilibrium state of this coupled system is defined by a uniform pressure p_0 inside and outside the piston chamber, a uniform gas density ρ_0, a zero flow velocity $u_0 = 0$, and a chamber length equal to l_0. The gas is assumed to be perfect, and the flow isentropic. Hence, the pressure p is function of the density ρ only and obeys:

$$\frac{dp}{d\rho} = c^2 \tag{4.2}$$

where c denotes the sound speed. The cross sectional area of the chamber is assumed to be constant and equal to one.

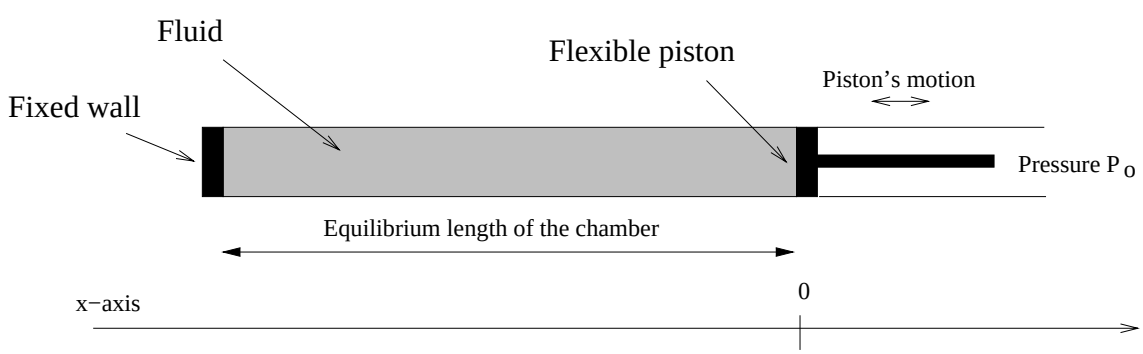

FIG. 4.1 – *The one-dimensional piston problem*

For this model aeroelastic problem, the one-dimensional mass and momentum conservation equations for the fluid are:

$$\begin{aligned} \frac{\partial \rho}{\partial t} + \frac{\partial}{\partial x}(\rho u) &= 0 \\ \frac{\partial}{\partial t}(\rho u) + \frac{\partial}{\partial x}((\rho u^2 + p)) &= 0 \end{aligned} \tag{4.3}$$

The linear dynamic equilibrium of the piston is governed by:

$$m\ddot{q} + d\dot{q} + kq = p(l_0 + q) - p_0 \tag{4.4}$$

where m, d, k, and q denote respectively the piston mass, damping, stiffness and displacement. A dot superscript designates a derivative with respect to time.

The boundary conditions for this coupled fluid-structure problem are given by:

$$\begin{aligned} \rho u(0) &= 0 \\ u(l_0 + q) &= \dot{q} \end{aligned} \tag{4.5}$$

Equations (4.5) above state that the fluid velocity is zero at the fixed wall, and equal to the piston speed at the other end of the chamber.

Clearly, the fluid flow has one moving boundary. Therefore, it is convenient to re-write (4.3) with respect to a moving frame characterized by a velocity $\dot{\xi}$ that may be different from the fluid velocity u and from zero. Let $\mathcal{J} = det(\partial x/\partial \xi)$ denote the jacobian of the frame transformation $\xi \to x$. The ALE form of (4.3) goes as follows:

$$\begin{aligned} \frac{1}{\mathcal{J}}\frac{\partial}{\partial t}(\mathcal{J}\rho) + \frac{\partial}{\partial x}(\rho(u - \dot{\xi})) &= 0 \\ \frac{1}{\mathcal{J}}\frac{\partial}{\partial t}(\mathcal{J}\rho u) + \frac{\partial}{\partial x}((\rho u(u - \dot{\xi}) + p)) &= 0 \end{aligned} \tag{4.6}$$

The above equations can be re-written in vector form as:

$$\frac{1}{\mathcal{J}}\frac{\partial}{\partial t}(\mathcal{J}W) + \frac{\partial}{\partial x}(F^c(W)) = 0 \tag{4.7}$$

where W and F^c are respectively the fluid state and fluid convected flux vectors:

$$\begin{aligned} W &= \begin{pmatrix} \rho \\ \rho u \end{pmatrix} \\ F^c &= \begin{pmatrix} \rho(u - \dot{\xi}) \\ (\rho u(u - \dot{\xi}) + p) \end{pmatrix} \end{aligned} \tag{4.8}$$

The convection matrix associated with the above convected flux vector is:

$$J(\dot{\xi}) = \frac{\partial F^c}{\partial W} = \begin{pmatrix} -\dot{\xi} & 1 \\ -u^2 + c^2 & 2u - \dot{\xi} \end{pmatrix} \tag{4.9}$$

We consider the response of the aeroelastic coupled system to small perturbations around the equilibrium position (ρ_0, $u_0 = 0$, p_0, c_0). First, we note that the fluid state vector at equilibrium $W_0 = (\rho_0 \; 0)^t$ satisfies[1]:

$$\frac{1}{\mathcal{J}}\frac{\partial}{\partial t}(\mathcal{J}W_0) + \frac{\partial}{\partial x}(F^c(W_0)) = 0 \tag{4.10}$$

and the convection matrix at equilibrium is:

$$J_0(0) = \begin{pmatrix} 0 & 1 \\ c_0^2 & 0 \end{pmatrix} \tag{4.11}$$

Then, we linearize the convected flux vector around W_0:

$$F^c(W) = F^c(W_0) + J_0(0)\delta W - \delta\dot{\xi}W_0 \tag{4.12}$$

Finally, from equations (4.7-4.12) it follows that the linearized fluid flow equations are:

$$\frac{1}{\mathcal{J}}\frac{\partial}{\partial t}(\mathcal{J}\delta W) + \frac{\partial}{\partial x}(J_0(0)\delta W - \delta\dot{\xi}W_0) = 0 \tag{4.13}$$

1. Here, the superscript t designates the transpose operation.

4.2.2 Spatial discretization: finite volume formulation and upwinding

The one-dimensional chamber region is discretized into N grid points and N cells (Figure 4.2). Integrating (4.13) between $x_{j-\frac{1}{2}}$ and $x_{j+\frac{1}{2}}$ and using a finite volume formulation with upwinding leads to:

$$\Delta x_j \; \delta\dot{W} + (\widetilde{F}^c_{j+\frac{1}{2}} - \widetilde{F}^c_{j-\frac{1}{2}}) \quad = \quad 0 \tag{4.14}$$

where

$$\Delta x_j \;=\; \frac{x_{j+1} - x_{j-1}}{2}.$$

Here, $\widetilde{F}^c_{j+\frac{1}{2}}$ and $\widetilde{F}^c_{j-\frac{1}{2}}$ are the convected numerical fluxes [48] associated with the classical linear flux splitting:

$$\begin{aligned} \widetilde{F}^c_{j+\frac{1}{2}} &= J_0^+(0)\delta W_j + J_0^-(0)\delta W_{j+1} - \delta\dot{\xi}_{j+\frac{1}{2}} \frac{(W_{0_j} + W_{0_{j+1}})}{2} \\ \widetilde{F}^c_{j-\frac{1}{2}} &= J_0^+(0)\delta W_{j-1} + J_0^-(0)\delta W_j - \delta\dot{\xi}_{j-\frac{1}{2}} \frac{(W_{0_{j-1}} + W_{0_j})}{2} \end{aligned} \tag{4.15}$$

and $J_0^+(0)$ and $J_0^-(0)$ satisfy $J_0(0) = J_0^+(0) + J_0^-(0)$ and are given by:

$$\begin{aligned} J_0^+(0) &= \tfrac{1}{2}\begin{pmatrix} c_0 & 1 \\ c_0^2 & c_0 \end{pmatrix} \\ J_0^-(0) &= \tfrac{1}{2}\begin{pmatrix} -c_0 & 1 \\ c_0^2 & -c_0 \end{pmatrix} \end{aligned} \tag{4.16}$$

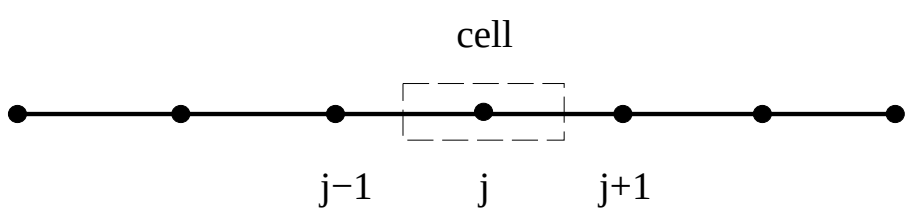

FIG. 4.2 – *Discretization of the one-dimensional flow*

Substituting equations (4.15) into equations (4.14) gives:

$$\begin{aligned} &\Delta x_j \; \delta\dot{W} = \\ &\quad J_0^+(0)\delta W_{j-1} + (J_0^-(0) - J_0^+(0))\delta W_j - J_0^-(0)\delta W_{j+1} + \\ &\quad \delta\dot{\xi}_{j+\frac{1}{2}} \frac{(W_{0_j} + W_{0_{j+1}})}{2} + \delta\dot{\xi}_{j-\frac{1}{2}} \frac{(W_{0_{j-1}} + W_{0_j})}{2} \end{aligned} \tag{4.17}$$

4.2.3 Transpiration

From Figure 4.2 and the second equation of (4.5), it follows that:

$$\delta\dot{\xi}_{N+\frac{1}{2}} \;=\; \dot{q} \tag{4.18}$$

All other ALE grid velocity perturbations $\delta\dot{\xi}_j$, $j = 1, ..., N$ are arbitrary. In order to simplify the piston problem from a three- to a two-field coupled problem, we assume that these velocity perturbations are small compared to the unperturbed sound speed c_0. Consequently, equations (4.17) become:

$$\begin{array}{lllll} \Delta x_j\ \delta\dot{W} & -J_0^+(0)\delta W_{j-1} & +(J_0^+(0) - J_0^-(0))\delta W_j & +J_0^-(0)\delta W_{j+1} & = 0 \quad (j \neq N) \\ \Delta x_N\ \delta\dot{W} & -J_0^+(0)\delta W_{N-1} & +(J_0^+(0) - J_0^-(0))\delta W_N & -\dot{q}W_{0_N} & = 0 \end{array} \tag{4.19}$$

The quantity $\dot{q}W_{0_N}^t = (\rho_0\dot{q} \;\; 0)^t$ corresponds to a "transpiration" flux. The reader can check that except for the presence of this transpiration flux, equations (4.19) are identical to the semi-discrete linearized equations governing a one-dimensional fluid flow with fixed boundaries.

4.2.4 The semi-discrete aeroelastic model problem

We define the structure state vector as:

$$Q \;=\begin{pmatrix} q \\ \dot{q} \end{pmatrix} \tag{4.20}$$

Using Q, the structural equation (4.4) can be re-written as:

$$\dot{Q} \;=\begin{pmatrix} 0 & 1 \\ -\dfrac{k}{m} & -\dfrac{d}{m} \end{pmatrix} Q + \begin{pmatrix} 0 \\ \dfrac{p(l_0+q) - p_0}{m} \end{pmatrix} \tag{4.21}$$

For the linearized piston problem, the forcing term of (4.21) also writes

$$\begin{pmatrix} 0 \\ \dfrac{p(l_0+q) - p_0}{m} \end{pmatrix} = \frac{c_0^2}{m}\begin{pmatrix} 0 \\ \delta\rho_N \end{pmatrix}.$$

It is a linear function of the fluid state vector $\delta W = (\delta\rho \quad \delta(\rho u))^t$. Hence, (4.21) can be re-written as:

$$\dot{Q} = \; DQ + C\delta W, \tag{4.22}$$

where the structural matrix D is given by

$$D = \begin{pmatrix} 0 & 1 \\ -\dfrac{k}{m} & -\dfrac{d}{m} \end{pmatrix} \tag{4.23}$$

Also, the fluid equations (4.19) can be re-arranged in matrix form as follows:

$$\delta\dot{W} \;=\; A\delta W + BQ \tag{4.24}$$

where B is the matrix induced by the transpiration flux $\dot{q}W_{0_N}$. The explicit expression of the coupling matrices B and C is discretization dependent. An example is given in (4.36).

In summary, the semi-discrete coupled system associated with the one-dimensional aeroelastic model problem is completely defined by:

$$\boxed{\begin{aligned} \begin{pmatrix} \delta\dot{W} \\ \dot{Q} \end{pmatrix} &= \begin{pmatrix} A & B \\ C & D \end{pmatrix} \begin{pmatrix} \delta W \\ Q \end{pmatrix} \\ \begin{pmatrix} \delta W \\ Q \end{pmatrix}_{(t=0)} &= \begin{pmatrix} \delta W \\ Q \end{pmatrix}_0 \end{aligned}} \tag{4.25}$$

In the remainder of this chapter, we focus on developing, analyzing, and validating partitioned procedures for solving equations (4.25). Because the aeroelastic response of a structure is often dominated by low frequency dynamics, we consider only implicit schemes for time-integrating the structural field. However, we consider both explicit and implicit time-integrators for advancing the fluid field, as both approaches are popular in computational fluid dynamics. Elegant methods for analyzing the stability of partitioned integrators with and without subcycling can be found in [39, 10]. However, both of these references deal with symmetric fields only. We have found that the extension of these analysis methods to mixed symmetric/unsymmetric problems such as those described by equations (4.25) is difficult — if not impossible — which has also motivated us to investigate first a simplified aeroelastic model problem.

Remark 1. The validity of equations (4.25) for both 2D and 3D linearized aeroelastic problems will be discussed later.

4.3 Mathematical preliminaries

4.3.1 Physical v.s. numerical instabilities

Transient fluid-structure (gas-structure) interaction problems have one particularity: they possess a wide variety of self-excited vibrations and instabilities. For example, at speeds of flow somewhat above the *critical flutter speed* [30], the structural system extracts energy from the flow system and a small accidental disturbance of the airfoil can serve as a trigger to initiate an oscillation of great violence. Physical instabilities can also occur in the linear regime. An example of a linear dynamic instability is vibrations due to von Kármán vortices [69]. If the frequency of the structure loading caused by the vortices is close or equal to the natural frequency of the body, then a resonance effect is present and large amplitudes of vibrations result. Therefore, when it comes to analyzing the numerical stability of a proposed algorithm for time-integrating

fluid-structure interaction problems, it is essential to consider the case where the coupled system is physically stable — that is, when (4.1) or even (4.25) have a solution that does not grow indefinitely in time.

The objectives of this section are to present a mathematical framework for the stability analysis of the solution of the semi-discrete equations (4.25), and to show that for the aeroelastic model problem introduced and discretized in Section 4.2, these equations have always a stable solution. Hence, the fluid-structure interaction model problem presented in this chapter is also a good problem for analyzing partitioned time-integrators with particular reference to numerical stability.

Remark 2. Intuitively, one can expect equations (4.25) to admit a stable solution for the aeroelastic model problem, because the fluid flow is confined inside a closed chamber and therefore has a limited amount of energy to exchange with the piston, and the piston is not excited by any other external and time-dependent force. However, the analysis framework presented in Section 4.3.2 is interesting because it also reveals a numerical property of the coupled model problem that turns out to be important for the design of an unconditionally stable partitioned procedure for solving (4.25).

4.3.2 Analysis framework

Let X, M, and $Sp(M)$ denote respectively a real vector, a real matrix that is diagonalizable in the complex space $\mathcal{C}$, and its set of complex eigenvalues[2]. We focus our attention on the linear system of ordinary differential equations (ODE):

$$\dot{X} \;=\; MX \tag{4.26}$$

First, we introduce two definitions.

Definition 1 *We will say that M is "stable" if and only if:*

a) M is diagonalizable in $\mathcal{C}$

b) $\forall \lambda \in Sp(M),\ \Re(\lambda) \;\leq\; 0$

Definition 2 *We will say that the real symmetric positive definite (RSPD) matrix E_M is an "energy matrix" for M if and only if $E_M M$ is non-positive, that is:*

$$\forall X, \quad X^t E_M M X \;\leq\; 0 \tag{4.27}$$

2. In the following, $\Re(\lambda)$ and $\Im(\lambda)$ designate respectively the real and imaginary parts of a complex eigenvalue λ.

Next, we state and prove four theorems.

Theorem 1 *An RSPD matrix E_M is an energy matrix for M if and only if:*

$$\forall X \text{ solution of } \dot{X} = MX, \quad \frac{d}{dt}(\frac{1}{2}X^t E_M X) \ \leq \ 0 \tag{4.28}$$

Proof. From (4.26), it follows that $\frac{d}{dt}(\frac{1}{2}X^t E_M X) = X^t E_M M X$. Hence, $\frac{d}{dt}(\frac{1}{2}X^t E_M X) \leq 0$ if and only if E_M is an energy matrix for M. □

Theorem 2 *If $M = P^{-1}\Omega P$ denotes the diagonalization of a stable matrix M, then an energy matrix for M is given by:*

$$E_M \ = \ \overline{P}^t P \ + \ P^t \overline{P} \tag{4.29}$$

where $\overline{P}$ is the complex conjugate matrix of P.

Proof. Clearly, $E_M = \overline{P}^t P + P^t \overline{P}$ is real symmetric. For all real vectors X, $X^t E_M X = 2|PX|^2$ is positive and equal to zero only if $X = 0$ because P is non singular. Finally since $\overline{M} = M$, we have:

$$\begin{aligned} X^t E_M M X &= X^t \bar{P}^t \Omega P X + X^t P^t \bar{P} P^{-1} \Omega P X \\ &= 2\Re\left(X^t \bar{P}^t \Omega P X\right) = 2\sum_i |(PX)_i|^2 \Re(\Omega_i) \ \leq \ 0 \end{aligned}$$

which completes the proof of Theorem 2. □

Theorem 3 (Reciprocal of Theorem 2) *Let M be a real matrix that is diagonalizable in $\mathcal{C}$. If there exists an energy matrix E_M for M, then M is stable.*

Proof. Let $X = R + iI \ \neq \ 0$, where $i^2 = -1$, denote a complex eigenvector of M associated with an eigenvalue λ. If E_M is an energy matrix for M, we have:

$$\begin{aligned} 0 \ \geq \ R^t E_M M R &= R^t E_M \Re(MX) \\ &= R^t E_M \Re(\lambda X) \quad = \quad R^t E_M [\Re(\lambda) R - \Im(\lambda) I] \\ 0 \ \geq \ I^t E_M M I &= I^t E_M \Im(MX) \\ &= I^t E_M \Im(\lambda X) \quad = \quad I^t E_M [\Re(\lambda) I + \Im(\lambda) R] \end{aligned} \tag{4.30}$$

Adding the two inequalities in (4.30) and exploiting the symmetry of E_M leads to the statement $\Re(\lambda)[R^t E_M R + I^t E_M I] \leq 0$. Since E_M is RSPD and $X \ \neq \ 0$, it follows that $\Re(\lambda) \leq 0$, which completes the proof of Theorem 3. □

Theorem 4 *If A and D are two real stable matrices with energy matrices E_A and E_D, then:*

$$E_A B \ + \ (E_D C)^t \ = \ 0 \ \Longrightarrow \ M \ = \ \begin{pmatrix} A & B \\ C & D \end{pmatrix} \text{ is a stable matrix} \tag{4.31}$$

Proof. The matrix $E_M = \begin{pmatrix} E_A & 0 \\ 0 & E_D \end{pmatrix}$ is RSPD. If $X = \begin{pmatrix} \delta W \\ Q \end{pmatrix}$ is a real vector satisfying $\dot{X} = MX$, we have:

$$\begin{aligned} \frac{d}{dt}(\frac{1}{2}X^t E_M X) &= \delta W^t E_A A \delta W + \delta W^t E_A B Q + Q^t E_D C \delta W + Q^t E_D D Q \\ &= \delta W^t E_A A \delta W + \delta W^t \left[E_A B + (E_D C)^t\right] Q + Q^t E_D D Q \\ &= \delta W^t E_A A \delta W + Q^t E_D D Q \ \leq \ 0 \end{aligned}$$

which in view of Theorem 1 implies that E_M is an energy matrix for M. From Theorem 3, it follows that M is stable. □

Theorems 1-3 set the stage to Theorem 4 which has a nice physical interpretation. An uncoupled fluid system is physically stable: it does not produce energy. If D is non-negative, an uncoupled structural system is also stable. For a coupled fluid-structure system, $E_A B + (E_D C)^t = 0$ simply expresses that the energy extracted from one system is equal to that injected into the other one. Hence, Theorem 4 merely states that a coupled system where the energy is exactly conserved is a physically stable system.

4.3.3 Physical stability of the model problem

Consider again the aeroelastic model problem introduced in Section 4.2. After linearization, we have found that the energy of the fluid (with omission of a constant) does not have any first-order term in its expansion (other than the predictable $p_0 q$ term[3]) . Moreover, second order terms derive from a quadratic form. Assuming a constant mesh size Δx, the energy $\mathcal{E}_{fluid}$ of the discretized fluid system can be written as:

$$\mathcal{E}_{fluid} \ = \ \Delta x \sum_{j=1}^{j=N} (\frac{c_0^2 \delta \rho_j^2}{2\rho_0} + \frac{\rho_0 \delta u_j^2}{2}) \tag{4.32}$$

and its perturbed state vector is $\delta W = (\delta\rho_1, \delta(\rho_0 u_1), \ldots, \delta\rho_N, \delta(\rho_0 u_N))^t$. Therefore, E_A can be constructed for this system as follows:

$$E_A \ = \ \begin{pmatrix} \begin{pmatrix} \frac{\Delta x c_0^2}{\rho_0} & 0 \\ 0 & \frac{\Delta x}{\rho_0} \end{pmatrix} & & 0 \\ & \ddots & \\ 0 & & \begin{pmatrix} \frac{\Delta x c_0^2}{\rho_0} & 0 \\ 0 & \frac{\Delta x}{\rho_0} \end{pmatrix} \end{pmatrix} \tag{4.33}$$

Using (4.19), the reader can verify through tedious but elementary calculations that E_A is an energy matrix for A induced by the spatial flux splitting.

3. Since the structure has also a potential energy equal to $-p_0 q$, both these terms will be omitted in the sequel.

For the piston, the state vector is $Q = \begin{pmatrix} q \\ \dot{q} \end{pmatrix}$ and the energy is simply given by

$$\mathcal{E}_{piston} = \frac{1}{2}kq^2 + \frac{1}{2}m\dot{q}^2. \tag{4.34}$$

Hence, for this structural system E_D can be written as:

$$E_D = \begin{pmatrix} k & 0 \\ 0 & m \end{pmatrix} \tag{4.35}$$

Proving that E_D is an energy matrix for D is straightforward. Using the second equation of (4.23), we have:

$$E_D D = \begin{pmatrix} k & 0 \\ 0 & m \end{pmatrix} \begin{pmatrix} 0 & 1 \\ \frac{-k}{m} & \frac{-d}{m} \end{pmatrix} = \begin{pmatrix} 0 & k \\ -k & -d \end{pmatrix}$$

which shows that $E_D D$ is negative when the damping d is non-negative, and therefore proves that E_D is an energy matrix for D.

The transpiration term in the last grid cell and the pressure force on the piston generate respectively the matrices:

$$B = \begin{pmatrix} 0 & 0 & \cdots & 0 & 0 \\ 0 & 0 & \cdots & \frac{-\rho_0}{\Delta x} & 0 \end{pmatrix}^t \text{ and } C = \begin{pmatrix} 0 & 0 & \cdots & 0 & 0 \\ 0 & 0 & \cdots & \frac{c_0^2}{m} & 0 \end{pmatrix} \tag{4.36}$$

From equations (4.33-4.36) and after some algebraic manipulations, it follows that we have $E_A B + (E_D C)^t = 0$, which shows that the semi-discrete aeroelastic model problem introduced in Section 4.2 admits a stable solution. Therefore, staggered algorithms for time-integrating the system (4.25) can be analyzed for unconditional stability.

4.3.4 Physical stability in multi-dimensional cases

In Section 4.7, we shall deal with two-dimensional and three-dimensional linearized aeroelastic problems. The algorithms presented are only deduced from the procedures that are built in the next section under the only assumption that $E_A B + (E_D C)^t = 0$ holds.

The treatment of multi-dimensional cases is not as simple as our one-dimensional problem because the equality $E_A B + (E_D C)^t = 0$ is not preserved. Lesoinne has shown in [47] that this relation cannot be generally true, even for a simple uniform inert two-dimensional flow aroud a structure.

For instance, let us consider perturbations around the uniform two-dimensional flow given by $W_0 = (\rho_0 \;\; 0 \;\; 0)^t$. Along the fluid-structure interface, we denote by $\vec{n}$ the normal (from the fluid into the structure). We could use the same methodology for this new case. We would obtain the same equations with two additional terms. These terms derive from the pressure fluxes at the boundary. In one dimension, the forcing term in (4.21) was derived from

$$F_{F \to S} = p - p_0 = c_0^2 \delta \rho_N.$$

In two dimensions, after linearization, we get

$$F_{F\to S} = p\vec{n} - p_0\vec{n_0} = c_0^2\delta\rho_N.\vec{n}_0 + p_0\delta\vec{n}. \tag{4.37}$$

If the last term of (4.37) is not omitted, it is easy to check that the equality $E_AB + (E_DC)^t = 0$ cannot simply be preserved. We reach the limits of this analysis. Maybe some extensions – like system energies that are not decoupled (including terms of the form $(\delta(\rho u)_N - \rho_0 q_{\to N})^2$), as well as a precise study on the two-dimensional boundary fluxes in the finite-volume formulation – might allow a similar analysis.

If the omission of the last term in (4.37) is possible, the previous analysis holds. It is easy to check, that, if a certain duality between the outgoing flux of pressure at the fluid-structure interface and the incoming transpiration flux is respected, the relationship $E_AB + (E_DC)^t = 0$ also holds – if the same upwinding schemes are used on a regular orthogonal structured grid, and with the new fluid energy given by

$$\mathcal{E}_{fluid} \;=\; \Delta x \sum_{j=1}^{j=N} (\frac{c_0^2\delta\rho_j^2}{2\rho_0} + \frac{\rho_0\delta u_j^2}{2} + \frac{\rho_0\delta v_j^2}{2}).$$

In that case, the staggered time-integrator described in (4.41) is also unconditionally stable. For example, if the pressure flux at an interface cell C_i made of triangles T_j is evaluated as

$$F_P(C_i) = c^2\rho_i \frac{\sum\limits_{T_j\in C_i} \vec{n}_{T_j}}{\sum\limits_{T_j\in C_i} 1}, \tag{4.38}$$

the relationship $E_AB + (E_DC)^t = 0$ holds if the transpiration flux is computed as

$$F_T(C_i) = \rho_0\vec{U}_i.\frac{\sum\limits_{T_j\in C_i} \vec{n}_{T_j}}{\sum\limits_{T_j\in C_i} 1}, \tag{4.39}$$

where $\vec{n}$ and $\vec{U}$ stand respectively for the normal to the fluid-structure interface and the velocity vector.

4.4 Implicit/implicit partitioned procedures

4.4.1 Unconditionally stable staggered time-integrators

Here, we present a family of unconditionally stable implicit/implicit staggered algorithms for solving the model equations (4.25) whose "design" is based on the following 4-step methodology. In this section, the characters "II" stand for "implicit/implicit" (implicit schemes for the fluid and the structure).

Step II1. Predict the structural field using the value computed at $t_n = n\Delta t$:

$$Q^p = Q^n$$

Step II2. Advance the fluid system using the trapezoidal rule:

$$\begin{aligned} \overline{\delta W^{n+1}} &= \delta W^n + \Delta t\ A\ \overline{\delta W^{n+\frac{1}{2}}} + \Delta t\ B\ Q^p \\ \text{where} \quad \overline{\delta W^{n+\frac{1}{2}}} &= \frac{\delta W^n + \overline{\delta W^{n+1}}}{2} \end{aligned}$$

Step II3. Advance the structural system using an implicit time-integrator selected from the so-called *generalized trapezoidal family of methods* [38], and a midpoint value of the previously updated fluid state $\delta W^{n+\frac{1}{2}}$:

$$\begin{aligned} \overline{Q^{n+1}} &= Q^n + \Delta t\ D\ \overline{Q^{n+\alpha}} + \Delta t\ C\ \overline{\delta W^{n+\frac{1}{2}}} \\ \text{where} \quad \overline{Q^{n+\alpha}} &= (1-\alpha)Q^n + \alpha\overline{Q^{n+1}} \qquad \alpha\ \in\ ]0,\ 1] \end{aligned}$$

Step II4. Correct the equations giving $\overline{\delta W^{n+1}}$ and $\overline{Q^{n+1}}$ to enforce unconditional stability of the implicit/implicit staggered procedure:

$$\begin{aligned} \delta W^{n+1} &= \delta W^n + \Delta t\ A\ \delta W^{n+\frac{1}{2}} + \Delta t\ B\ Q^p + \left[\delta W^{n+1^c}\right] \\ Q^{n+1} &= Q^n + \Delta t\ D\ Q^{n+\alpha} + \Delta t\ C\ \delta W^{n+\frac{1}{2}} + \left[Q^{n+1^c}\right] \end{aligned}$$

It should be emphasized that the above steps describe the design process of a solution methodology and not the computer implementation of a time-integration algorithm. In particular, neither the fluid nor the structural fields should be solved until the correction terms $[\delta W^{n+1^c}]$ and $[Q^{n+1^c}]$ are first specified.

The trapezoidal rule is unconditionally stable and second-order accurate when applied to the solution of the uncoupled linearized fluid system (4.17). For $\alpha \geq 1/2$, the generalized trapezoidal family of methods is unconditionally stable when applied to time-integrate the uncoupled structural problem. For $\alpha\ \in\ ]0,\ 1]$, these methods are first-order accurate, except for $\alpha = 1/2$, in which case the corresponding scheme is second-order accurate. The correction terms $[\delta W^{n+1^c}]$ and $[Q^{n+1^c}]$ should be computed to ensure the unconditional stability of the resulting implicit/implicit staggered solution procedure.

Theorem 5 *For $\alpha \geq 1/2$, and for the two following correction terms*

$$\begin{aligned} \left[\delta W^{n+1^c}\right] &= \tfrac{1}{2}\Delta t^2\ BC\ \delta W^{n+\frac{1}{2}} \\ \left[Q^{n+1^c}\right] &= (1-\alpha)\Delta t^2\ DC\ \delta W^{n+\frac{1}{2}} \end{aligned} \tag{4.40}$$

the implicit/implicit staggered time-integrator defined by Steps II1-II4 above is unconditionally stable[4].

4. Note that the preceding corrections seem unique.

Proof. For $[\delta W^{n+1^c}] = \frac{1}{2}\Delta t^2\ BC\ \delta W^{n+\frac{1}{2}}$ and $[Q^{n+1^c}] = (1-\alpha)\Delta t^2\ DC\ \delta W^{n+\frac{1}{2}}$, the proposed implicit/implicit staggered solution algorithm for solving (4.25) becomes:

$$\boxed{\begin{array}{rcl} \delta W^{n+1} & = & \delta W^n + \Delta t\ A\ \delta W^{n+\frac{1}{2}} + \Delta t\ B\ Q^n + \frac{1}{2}\Delta t^2\ BC\ \delta W^{n+\frac{1}{2}} \\ Q^{n+1} & = & Q^n + \Delta t\ D\ Q^{n+\alpha} + \Delta t\ C\ \delta W^{n+\frac{1}{2}} + (1-\alpha)\Delta t^2\ D\ C\delta W^{n+\frac{1}{2}} \\ \alpha & \in & [\frac{1}{2},\ 1] \end{array}} \tag{4.41}$$

The above partitioned procedure can also be written as:

$$\left\{\begin{array}{rcl} Q^* & = & Q^n + \frac{\Delta t}{2} C\delta W^{n+\frac{1}{2}} \\ Q^{**} & = & Q^n + \Delta t C\delta W^{n+\frac{1}{2}} \\ \dfrac{\delta W^{n+1} - \delta W^n}{\Delta t} & = & A\delta W^{n+\frac{1}{2}} + BQ^* \\ \dfrac{Q^{n+1} - Q^{**}}{\Delta t} & = & D((1-\alpha)Q^{**} + \alpha Q^{n+1}) \end{array}\right. \tag{4.42}$$

Using the energy matrices E_A and E_D, we define the system energy as:

$$\mathcal{E}_{\delta W,Q} \ = \ \frac{1}{2}\delta W^t E_A \delta W + \frac{1}{2} Q^t E_D Q \tag{4.43}$$

From equations (4.41-4.43) and Definition 2, we deduce (writing $Q^{**\alpha}$ instead of $(1-\alpha)Q^{**} + \alpha Q^{n+1}$):

$$\begin{array}{rcl} \mathcal{E}_{\delta W^{n+1},Q^n} & = & \mathcal{E}_{\delta W^n,Q^n} + \Delta t \delta W^{n+\frac{1}{2}^t} E_A A \delta W^{n+\frac{1}{2}} + \Delta t Q^{*^t} B^t E_A \delta W^{n+\frac{1}{2}} \\ & \Rightarrow & \mathcal{E}_{\delta W^{n+1},Q^n} \ \leq \ \mathcal{E}_{\delta W^n,Q^n} + \Delta t Q^{*^t} B^t E_A \delta W^{n+\frac{1}{2}} \end{array} \tag{4.44a}$$

$$\begin{array}{rcl} \mathcal{E}_{\delta W^{n+1},Q^{**}} & = & \mathcal{E}_{\delta W^{n+1},Q^n} + \Delta t \delta W^{n+\frac{1}{2}^t} C^t E_D Q^n + \dfrac{\Delta t^2}{2} \delta W^{n+\frac{1}{2}^t} C^t E_D C \delta W^{n+\frac{1}{2}} \\ & \Rightarrow & \mathcal{E}_{\delta W^{n+1},Q^{**}} \ = \ \mathcal{E}_{\delta W^{n+1},Q^n} + \Delta t \delta W^{n+\frac{1}{2}^t} C^t E_D Q^* \end{array} \tag{4.44b}$$

$$\begin{array}{rcl} \mathcal{E}_{\delta W^{n+1},Q^{n+1}} & = & \mathcal{E}_{\delta W^{n+1},Q^{**}} + \Delta t Q^{**\alpha^t}\ E_D D\ Q^{**\alpha} \\ & + & (1-2\alpha)\dfrac{\Delta t^2}{2} Q^{**\alpha^t}\ D^t E_D D\ Q^{**\alpha} \\ & \Rightarrow & \text{For } \alpha \ \geq \ \dfrac{1}{2},\ \mathcal{E}_{\delta W^{n+1},Q^{n+1}} \ \leq \ \mathcal{E}_{\delta W^{n+1},Q^{**}} \end{array} \tag{4.44c}$$

which also implies (by addition of 4.44c, 4.44b and 4.44c) that:

$$\mathcal{E}_{\delta W^{n+1},Q^{n+1}} \ \leq \ \mathcal{E}_{\delta W^n,Q^n} + \Delta t Q^{*^t} B^t E_A \delta W^{n+\frac{1}{2}} + \Delta t \delta W^{n+\frac{1}{2}^t} C^t E_D Q^*$$

and we have (if $\alpha \geq \frac{1}{2}$),

$$\mathcal{E}_{\delta W^{n+1},Q^{n+1}} \ \leq \ \mathcal{E}_{\delta W^n,Q^n} + \Delta t \delta W^{n+\frac{1}{2}^t} [E_A B + (E_D C)^t] Q^* \tag{4.45}$$

Finally, since the aeroelastic model problem satisfies $E_A B + (E_D C)^t = 0$, it follows that:

$$\mathcal{E}_{\delta W^{n+1}, Q^{n+1}} \quad \leq \quad \mathcal{E}_{\delta W^n, Q^n} \tag{4.46}$$

which shows that the numerical energy of the system does not increase in time, and therefore the partitioned solution procedure (4.41) is unconditionally stable. □

Theorem 6 *The implicit/implicit unconditionally stable partitioned procedure defined by (4.41) is first-order accurate.*

Proof. Expanding the various terms in (4.41) around the time $t_n = n\Delta t$ leads to:

$$\begin{aligned} \delta \dot{W}^n &= A\delta W^n + BQ^n + O\ (\Delta t) \\ \dot{Q}^n &= C\delta W^n + DQ^n + O\ (\Delta t) \end{aligned}$$

Comparing the above equations with (4.25) completes the proof. □

Clearly, second-order accuracy would require a more sophisticated predictor in Step II1. It is interesting to note that with the partitioned solution methodology described in Steps II1-II4, we are able to achieve unconditional stability without resorting to an augmentation technique [59, 27]. Augmentation based schemes are often expensive and cumbersome to implement because they require forming and factoring the product of the independent field and coupling matrices. The staggered time-integrator described in equations (4.41) requires only one additional sparse matrix-matrix product to form BC.

4.4.2 Subcycling

The fluid and structure fields have often different time scales. For problems in aeroelasticity, the fluid flow usually requires a smaller temporal resolution than the structural vibration. Therefore, if the unconditionally stable staggered algorithm (4.41) is used to solve a coupled fluid-structure problem, the coupling time-step Δt_c will be typically dictated by the time-step Δt_F that guarantees a certain accuracy in the flow solution, rather than the time-step $\Delta t_S > \Delta t_F$ that meets the accuracy requirements of the structural field.

Using the same time-step Δt_c in both fluid and structure computational kernels presents only minor implementational advantages. On the other hand, subcycling the fluid computations with a factor $n_{S/F} = \Delta t_S / \Delta t_F$ can offer substantial computational advantages, including:

- savings in the overall simulation CPU time, because in that case the structural field will be advanced fewer times.
- savings in I/O transfers and/or communication costs when computing on a heterogeneous platform, because in that case the fluid and structure kernels will exchange information fewer times.

However, the computational advantages highlighted above are effective only if subcycling does not restrict the stability region of the staggered algorithm to values of the coupling time-step Δt that are small enough to offset these advantages. For example, consider the following fluid-subcycled version of the unconditionally stable staggered time-integrator given in (4.41):

$$
\begin{aligned}
&\delta W^{n+1^{(0)}} = \delta W^n \\
&\{ \\
&\quad For\ k = 0,\ ...,\ n_{S/F} - 1 \\
&\quad \delta W^{n+1^{(k+1)}} = \delta W^{n+1^{(k)}} + (\Delta t A + \tfrac{\Delta t^2}{2} BC)\ \delta W^{n+1^{(k+\frac{1}{2})}} + \Delta t B Q^n \\
&\} \\
&\delta W^{n+1} = \delta W^{n+1^{(n_{S/F})}} \\
&Q^{n+1} = Q^n + \Delta t D Q^{n+\alpha} + \Delta t C \delta W^{n+\frac{1}{2}} + (1-\alpha)\Delta t^2 DC\delta W^{n+\frac{1}{2}}
\end{aligned}
\tag{4.47}
$$

This algorithm implements the simplest possible subcycling scheme and is often used in many applications. Unfortunately, the reader can easily check that the above fluid-subcycled partitioned procedure (4.47) is no longer unconditionally stable. Next, we present an improved subcycling approach that preserves the unconditional stability of the partitioned procedure (4.41).

Theorem 7 *For $1/2 \leq \alpha \leq 1$, the following fluid-subcycled version of the staggered time-integrator given in (4.41) is unconditionally stable:*

$$
\boxed{
\begin{aligned}
&\delta W^{n+1^{(0)}} = \delta W^n \\
&X^{(0)} = Q^n \\
&\{ \\
&\quad For\ k = 0,\ ...,\ n_{S/F} - 1 \\
&\quad \delta W^{n+1^{(k+1)}} = \delta W^{n+1^{(k)}} + (\Delta t A + \tfrac{\Delta t^2}{2} BC)\ \delta W^{n+1^{(k+\frac{1}{2})}} + \Delta t B X^{(k)} \\
&\quad X^{(k+1)} = X^{(k)} + \Delta t\ C\delta W^{n+1^{(k+\frac{1}{2})}} \\
&\} \\
&\delta W^{n+1} = \delta W^{n+1^{(n_{S/F})}} \\
&Q^{n+1} = X^{(n_{S/F})} + n_{S/F}\Delta t D\left((1-\alpha)X^{(n_{S/F})} + \alpha Q^{n+1}\right)
\end{aligned}
}
\tag{4.48}
$$

Proof. The proof of this theorem is similar to that of Theorem 5 and uses the system energy defined in (4.43). Using equations (4.43) to (4.48) and Definition 2, one obtains:

$$
\begin{aligned}
&\mathcal{E}_{\delta W^{n+1^{(0)}}, X^{(0)}} = \mathcal{E}_{\delta W^n, Q^n} \\
&\mathcal{E}_{\delta W^{n+1^{(k+1)}}, X^{(k)}} \leq \mathcal{E}_{\delta W^{n+1^{(k)}}, X^{(k)}} + \Delta t \delta W^{n+1^{(k+\frac{1}{2})}{}^t} E_A B(X^{(k)} + \tfrac{\Delta t}{2} C\delta W^{n+1^{(k+\frac{1}{2})}}) \\
&\Rightarrow \mathcal{E}_{\delta W^{n+1^{(k+1)}}, X^{(k)}} \leq \mathcal{E}_{\delta W^{n+1(k)}, X^{(k)}} + \Delta t \delta W^{n+1^{(k+\frac{1}{2})}{}^t} E_A B X^{(k+\frac{1}{2})} \\
&\mathcal{E}_{\delta W^{n+1^{(k+1)}}, X^{(k+1)}} = \mathcal{E}_{\delta W^{n+1^{(k+1)}}, X^{(k)}} + \Delta t \delta W^{n+1^{(k+\frac{1}{2})}{}^t} C^t E_D(X^{(k)} + \tfrac{\Delta t}{2} C\delta W^{n+1^{(k+\frac{1}{2})}}) \\
&\Rightarrow \mathcal{E}_{\delta W^{n+1^{(k+1)}}, X^{(k+1)}} = \mathcal{E}_{\delta W^{n+1^{(k+1)}}, X^{(k)}} + \Delta t \delta W^{n+1^{(k+\frac{1}{2})}{}^t} C^t E_D X^{(k+\frac{1}{2})}
\end{aligned}
$$

We then have for each fluid time step

$$\mathcal{E}_{\delta W^{n+1(k+1)},X^{(k+1)}} \leq \mathcal{E}_{\delta W^{n+1(k)},X^{(k)}} + \Delta t \delta W^{n+1^{(k+\frac{1}{2})^t}} \left[E_A B + (E_D C)^t\right] X^{(k+\frac{1}{2})} \quad (4.49)$$

If we add these inequalities over all subcycles, we find

$$\mathcal{E}_{\delta W^{n+1},X^{(n_{S/F})}} \leq \mathcal{E}_{\delta W^n,Q^n} + \Delta t \sum_{k=0}^{n_{S/F}-1} \left(\delta W^{n+1^{(k+\frac{1}{2})^t}} \left[E_A B + (E_D C)^t\right] X^{(k+\frac{1}{2})}\right) \quad (4.50)$$

On the structural side, we have (writing $Q^{n+\alpha}$ for $(1-\alpha)X^{(n_{S/F})} + \alpha Q^{n+1}$):

$$\begin{aligned}\mathcal{E}_{\delta W^{n+1},Q^{n+1}} &= \mathcal{E}_{\delta W^{n+1^{(n_{S/F})}},X^{n+1^{(n_{S/F})}}} \\ &+ n_{S/F}\Delta t Q^{n+\alpha^t} E_D D\, Q^{n+\alpha} + (1-2\alpha)\frac{{n_{S/F}}^2 \Delta t^2}{2} Q^{n+\alpha^t} D^t E_D D\, Q^{n+\alpha}.\end{aligned}$$

Since $E_D D$ is negative and since $1/2 \leq \alpha \leq 1$, we have for the structural time step:

$$\mathcal{E}_{\delta W^{n+1},Q^{n+1}} \leq \mathcal{E}_{\delta W^{n+1},X^{(n_{S/F})}} \quad (4.51)$$

The above inequalities (4.50) and (4.51) imply that:

$$\mathcal{E}_{\delta W^{n+1},Q^{n+1}} \leq \mathcal{E}_{\delta W^n,Q^n} + \Delta t \sum_{k=0}^{n_{S/F}-1} \delta W^{n+1^{(k+\frac{1}{2})^t}} \left[E_A B + (E_D C)^t\right] X^{(k+\frac{1}{2})} \quad (4.52)$$

Finally, since the aeroelastic model problem satisfies $E_A B + (E_D C)^t = 0$, it follows that:

$$\mathcal{E}_{\delta W^{n+1},Q^{n+1}} \leq \mathcal{E}_{\delta W^n,Q^n} \quad (4.53)$$

which shows that the numerical energy of the system does not increase in time, and therefore the partitioned and fluid-subcycled solution procedure (4.48) is unconditionally stable. □

Theorem 8 *The implicit/implicit unconditionally stable partitioned and fluid-subcycled procedure defined by (4.48) is first-order accurate.*

Proof. The proof of this theorem is similar to that of Theorem 6. □

The subcycling approach advocated in equations (4.48) preserves the computational advantages of subcycling. At each stage, the evaluation by the fluid solver of the correction term $X^{(k+1)}$ does not require neither advancing the structural state vector, nor exchanging information with the structural solver. Moreover, updating $X^{(k+1)}$ and $BX^{(k)}$ requires only two sparse matrix-vector products and therefore is relatively inexpensive.

The interpretation of the role of the correction term $X^{(k+1)}$ goes as follows. In order to solve $\dot{Q} = DQ + C\delta W$ between t_n and t_{n+1}, the structure kernel must receive from

the fluid module the best possible approximation of the coupling quantity $\int_{t_n}^{t_{n+1}} C\delta W dt$. In the fluid-subcycled partitioned procedure (4.47), this integral is approximated by $\Delta t C\delta W^{n+\frac{1}{2}}$, which guarantees a certain accuracy but does not warrant unconditional stability. On the other hand, the strategy consisting in approximating $\int_{t_n}^{t_{n+1}} C\delta W dt$ via updating $X^{(k+1)} = X^{(k)} + \Delta t C\delta W^{n+1^{(k+\frac{1}{2})}}$ and replacing in the procedure (4.47) the "frozen" $\Delta t B Q^n$ by the updated quantity $\Delta t B X^{(k)}$ not only provides a better coupling accuracy, but also preserves the unconditional stability of the original non subcycled partitioned procedure (4.41).

The implications of the above results and discussion on the staggered and subcycled solution of more complex aeroelastic problems can be formulated as follows. When the fluid field is subcycled and updated ahead of the structural field, then:

- the motion of the moving fluid boundary induced by the structural deformation should not be completely absorbed during the first fluid subcycle and "frozen" during the remaining ones. Rather, this induced motion should be distributed among all subcycle stages via a careful interpolation scheme.

- after all fluid subcycles are completed, the mean value rather than the final value of the pressure field must be transmitted to the structure.

4.4.3 Examples

Here, we illustrate the numerical properties of the family of implicit/implicit staggered procedures presented in Sections 4.4.1-4.4.2 with the solution of the aeroelastic model problem (4.25). We consider the case where $\alpha = 1/2$ and the structure is undamped ($d = 0$). First, we introduce the non-dimensional variables:

$$\begin{array}{rclrcl} \bar{t} & = & \dfrac{c_0}{l_0}\, t & \bar{\rho} & = & \dfrac{\rho}{\rho_0} \\ \bar{x} & = & \dfrac{x}{l_0} & \overline{\rho u} & = & \dfrac{\rho u}{\rho_0 c_0} \\ \bar{q} & = & \dfrac{q}{l_0} & \delta\overline{W} & = & \begin{pmatrix} \delta\bar{\rho} \\ \delta\overline{\rho u} \end{pmatrix} \end{array} \tag{4.54}$$

and rewrite equations (4.19) and (4.4) in non-dimensional form as follows:

$$\begin{array}{l} \Delta\bar{x}_j\ \delta W'_j - \overline{J}_0^+(0)\delta\overline{W}_{j-1} + (\overline{J}_0^+(0) - \overline{J}_0^-(0))\delta\overline{W}_j + \overline{J}_0^-(0)\delta\overline{W}_{j+1} \ = \ 0 \quad (j \neq N) \\ \Delta\bar{x}_N\ \delta W'_N - \overline{J}_0^+(0)\delta\overline{W}_{N-1} + (\overline{J}_0^+(0) - \overline{J}_0^-(0))\delta\overline{W}_N - \begin{pmatrix} \bar{q}' \\ 0 \end{pmatrix} \ = \ 0 \\ \bar{q}'' + \bar{\omega}_s^2\bar{q} \ = \ \frac{1}{\bar{m}}(\delta\bar{\rho}_N - 1) \end{array} \tag{4.55}$$

where a the character ' means a derivation with respect to $\bar{t}$ and

$$\begin{aligned}
\overline{J}_0^+(0) &= \tfrac{1}{2}\begin{pmatrix} 1 & 1 \\ 1 & 1 \end{pmatrix} \\
\overline{J}_0^-(0) &= \tfrac{1}{2}\begin{pmatrix} -1 & 1 \\ 1 & -1 \end{pmatrix} \\
\bar{\omega}_s^2 &= \frac{l_0^2}{c_0^2}\frac{k}{m} \\
\bar{m} &= \frac{m}{\rho_0 l_0}
\end{aligned} \tag{4.56}$$

Next, we discretize the piston chamber into 21 grid points and $N = 20$ finite volume cells, and set the non-dimensional parameters to $\bar{\omega}_s^2 = 3.03 \times 10^{-4}$ and $\bar{m} = 30.77$. We consider the following initial conditions:

$$\begin{aligned}
\delta\bar{\rho}(\bar{t}=0) &= 0 \qquad & \delta\overline{\rho u}(\bar{t}=0) &= 0 \\
\bar{q}(\bar{t}=0) &= 0 \qquad & \dot{\bar{q}}(\bar{t}=0) &= 1
\end{aligned}$$

and solve the coupled equations (4.55)-(4.56) using eight time-steps varying between $\Delta t = 1\times$CFL and $\Delta t = 128\times$CFL, where CFL $= l_0/(Nc_0)$ is computed with respect to the uncoupled fluid problem (this abusive notation means that, for $\Delta t =$CFL, the maximum Courant number in the fluid is equal to 1). The obtained non-dimensional piston displacement $\bar{q}/l_0$ and fluid pressure in the cell in contact with the piston $(p/\rho_0 c_0^2)_{20}$ are depicted in Figures 4.3-4.4 for the case without subcycling.

Clearly, the results reported in Figures 4.3-4.4 highlight the unconditional stability of the family of implicit/implicit staggered procedures presented in Sections 4.4.1-4.4.2. Stable responses are observed for all time-steps, and accurate results are obtained for both the piston displacement and fluid pressure for time-steps as large as $\Delta t = 32\times$CFL.

The previous computations are repeated using the fluid-subcycled staggered time integrator described in (4.48), $2\times\text{CFL} \leq \Delta t_F \leq 4\times\text{CFL}$, and several subcycling factors $1 \leq n_{S/F} \leq 32$. The corresponding results (see Figures 4.5 to 4.8) confirm numerically the unconditional stability proved mathematically in Theorem 7. Note however that large subcycling factors $n_{S/F}$ introduce a spurious phase shift in the initial stages of the coupled computations that can ruin the accuracy of the response history. Both amplitude and phase errors can also be observed in that case. This suggests that an adaptive time-stepping strategy is needed in order to resolve better the initial response of the coupled system.

4.5 Explicit/implicit partitioned procedures

Next, we consider the case where an explicit scheme is desired for advancing the fluid field. We know how to design an unconditionally stable staggered algorithm for that case also, however, such an algorithm would be only conditionally consistent [28].

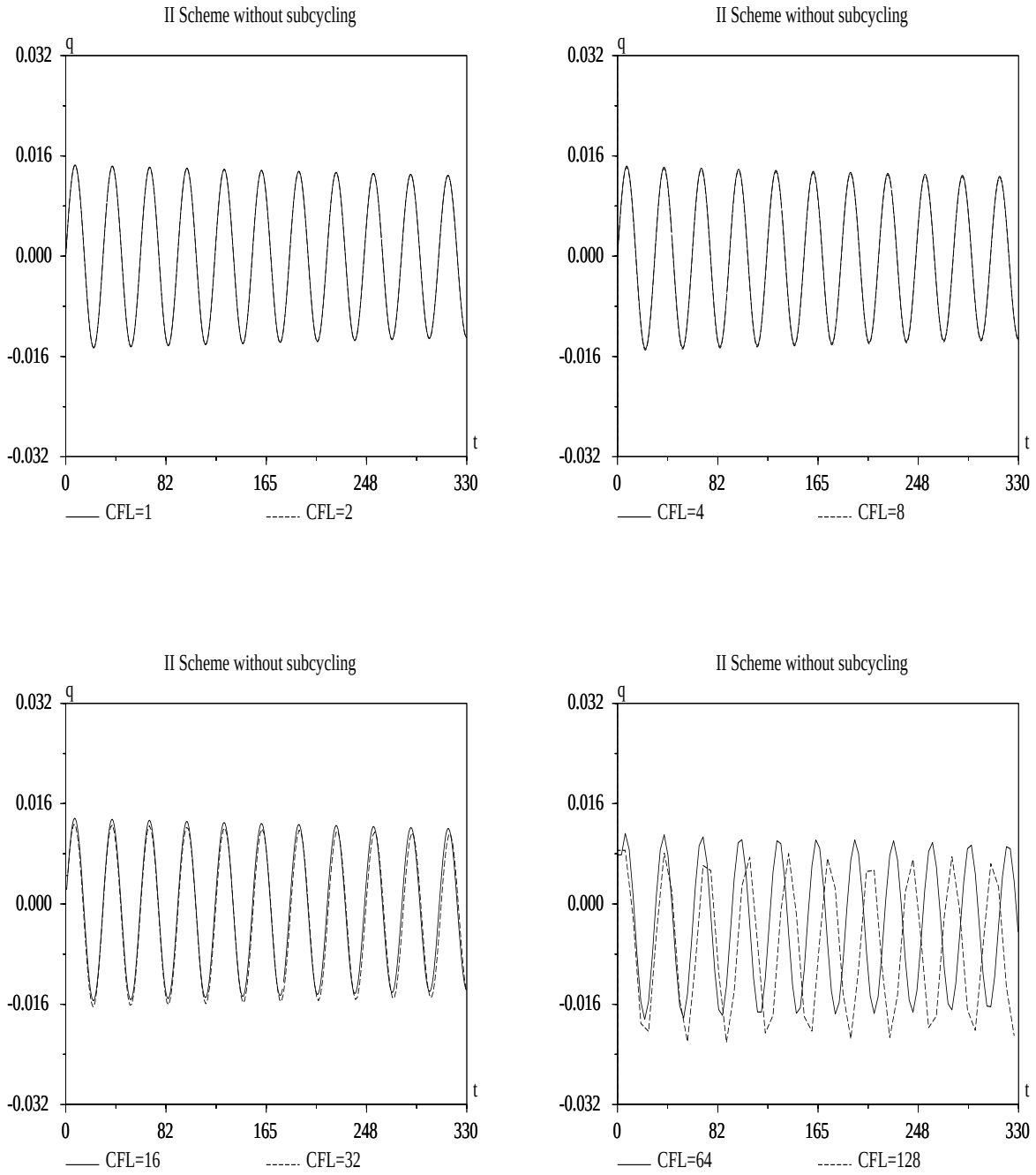

FIG. 4.3 – *Computed non-dimensional piston displacement (without subcycling)*

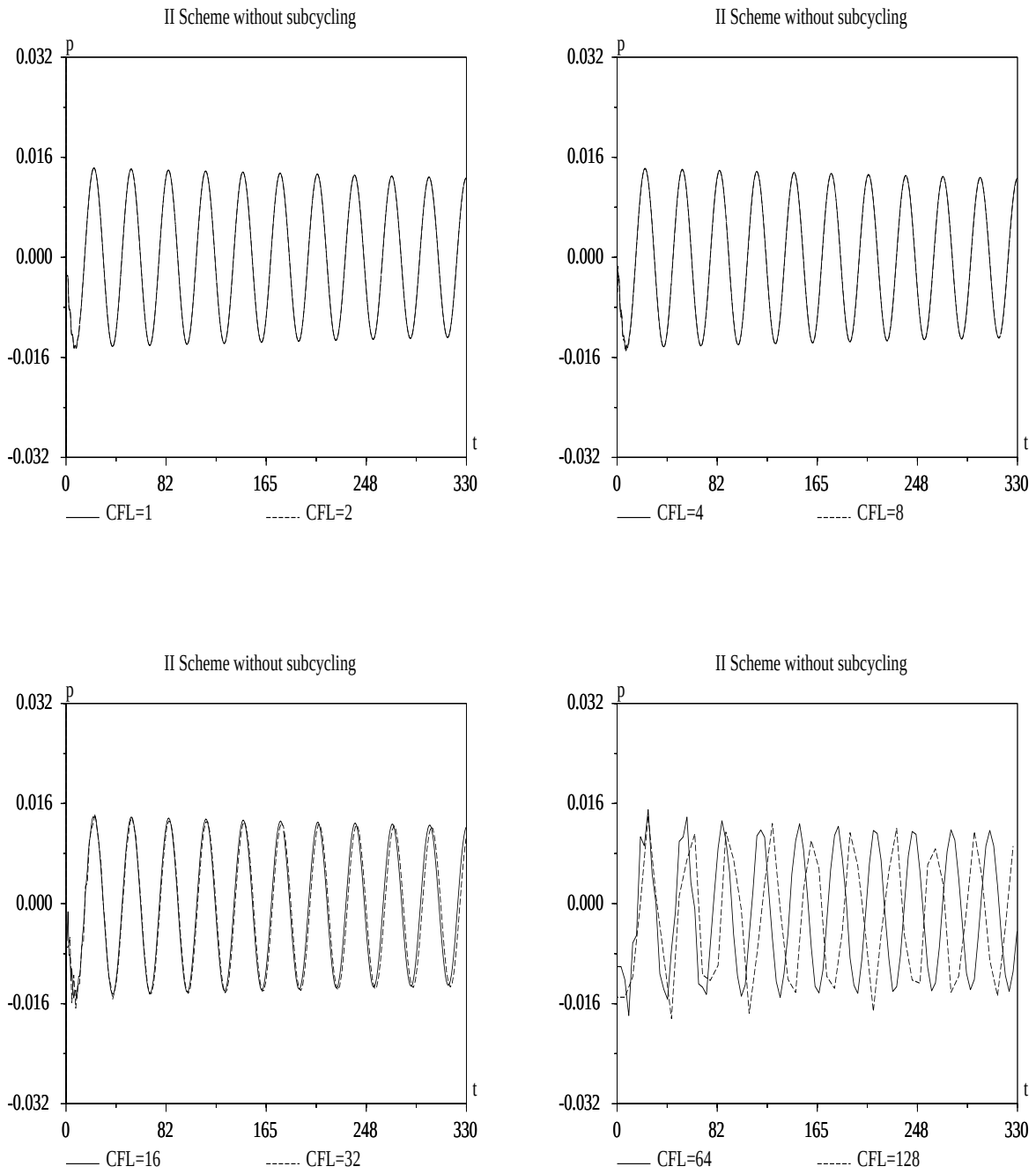

FIG. 4.4 – *Computed non-dimensional fluid pressure (without subcycling)*

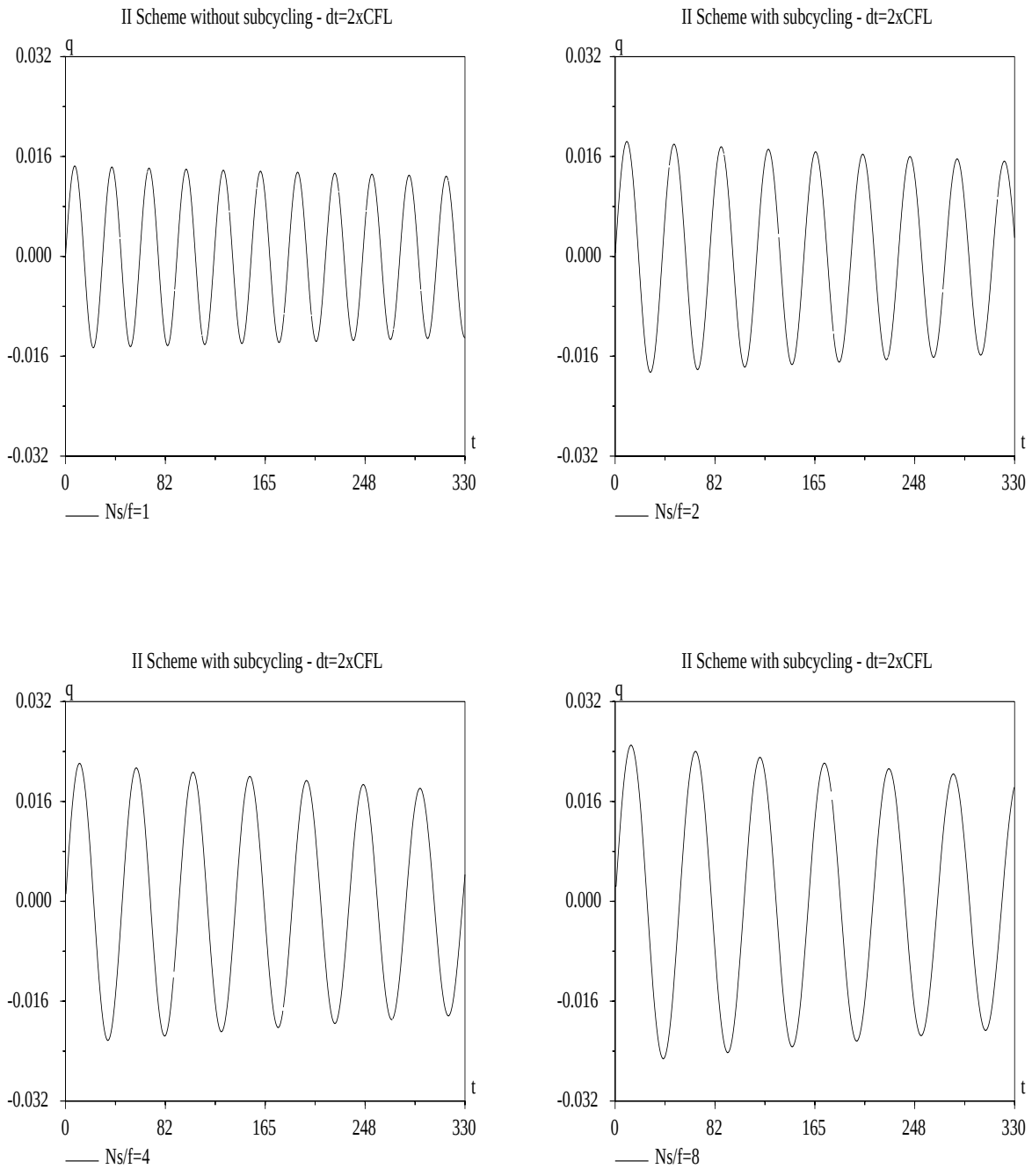

FIG. 4.5 – *Computed non-dimensional piston displacement ($\Delta t = 2\times CFL$ and with several subcycling factors $n_{S/F}$)*

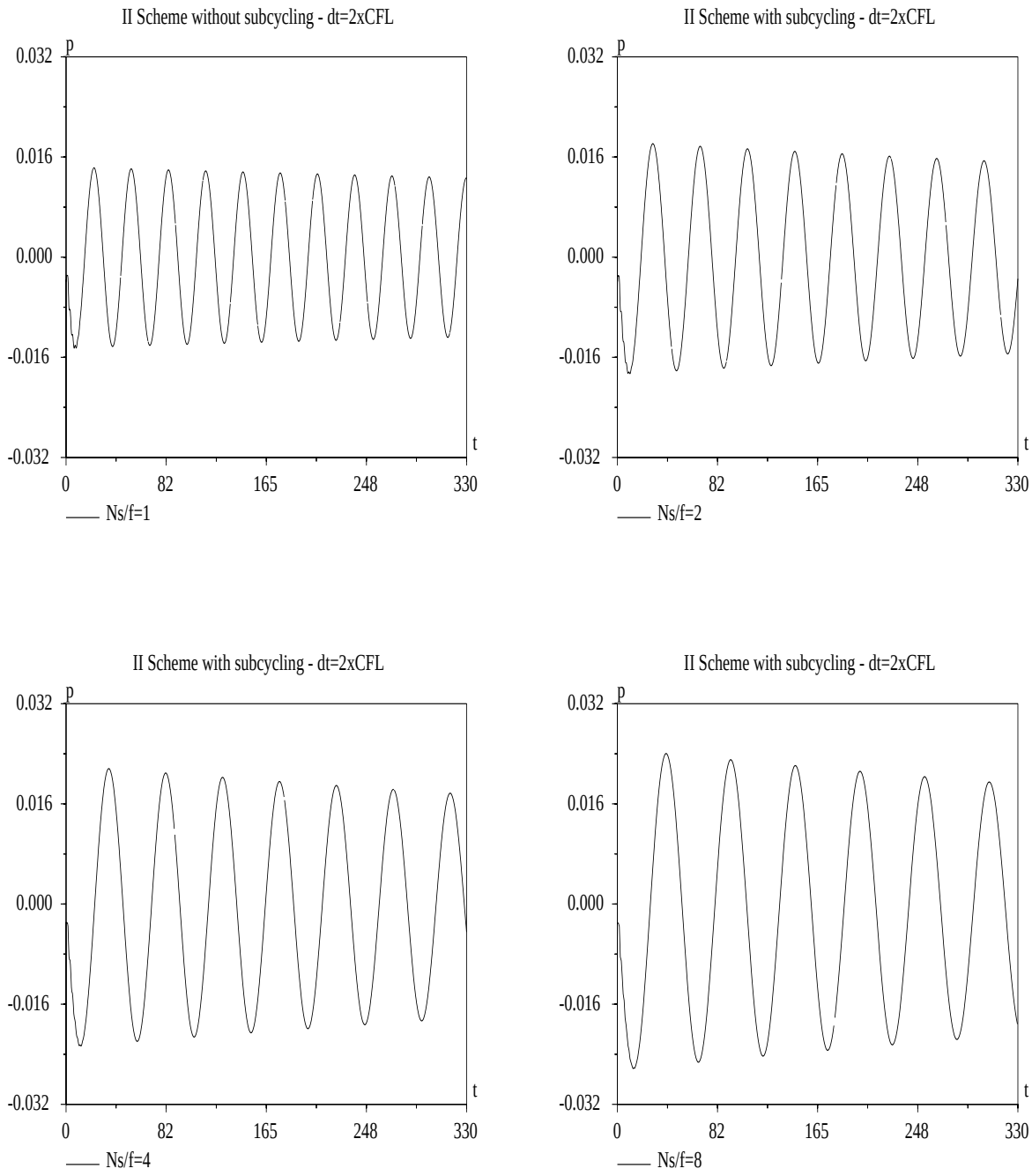

FIG. 4.6 – *Computed non-dimensional fluid pressure ($\Delta t = 2\times CFL$ and with several subcycling factors $n_{S/F}$)*

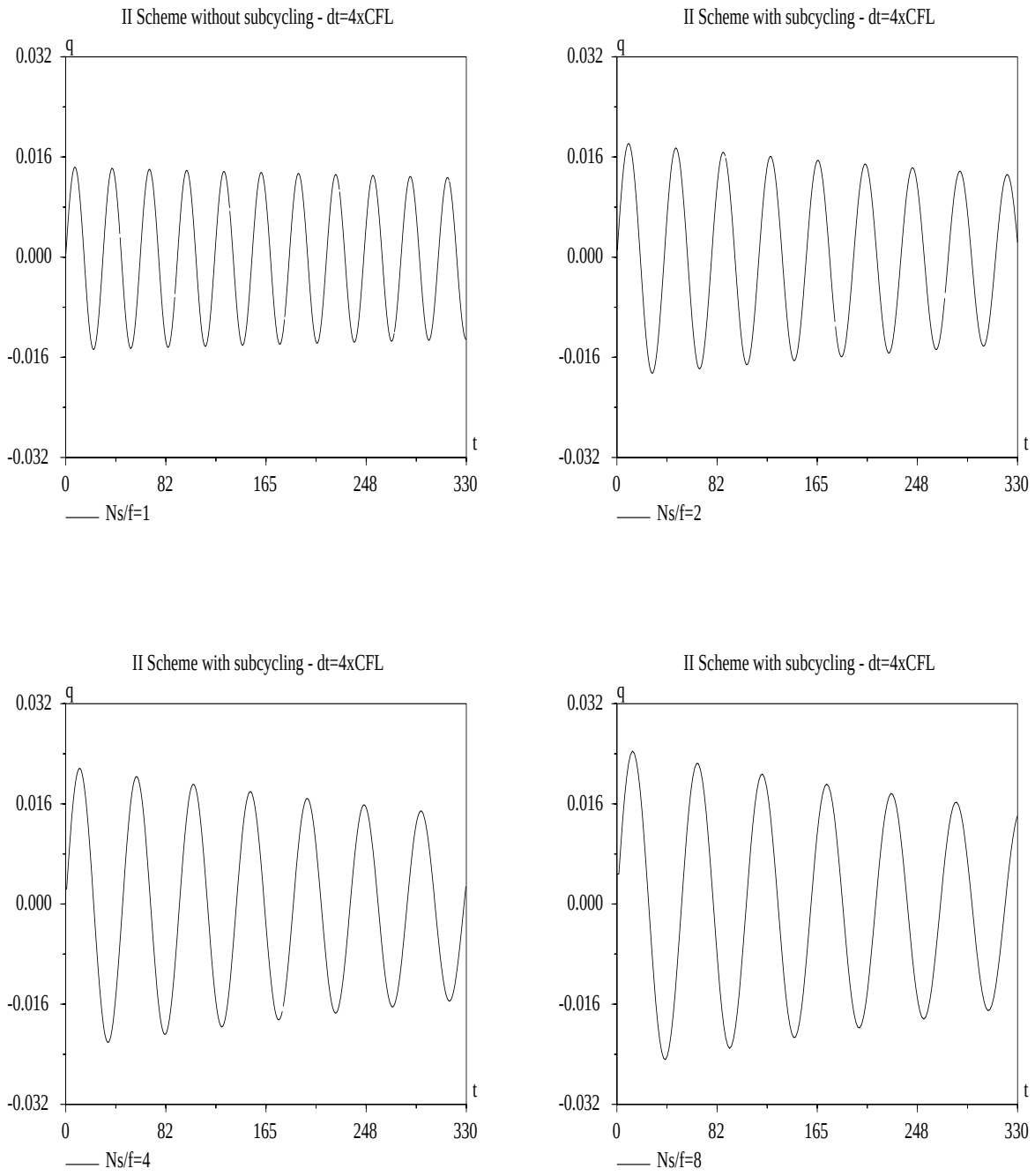

FIG. 4.7 – *Computed non-dimensional piston displacement ($\Delta t = 4\times CFL$ and with several subcycling factors $n_{S/F}$)*

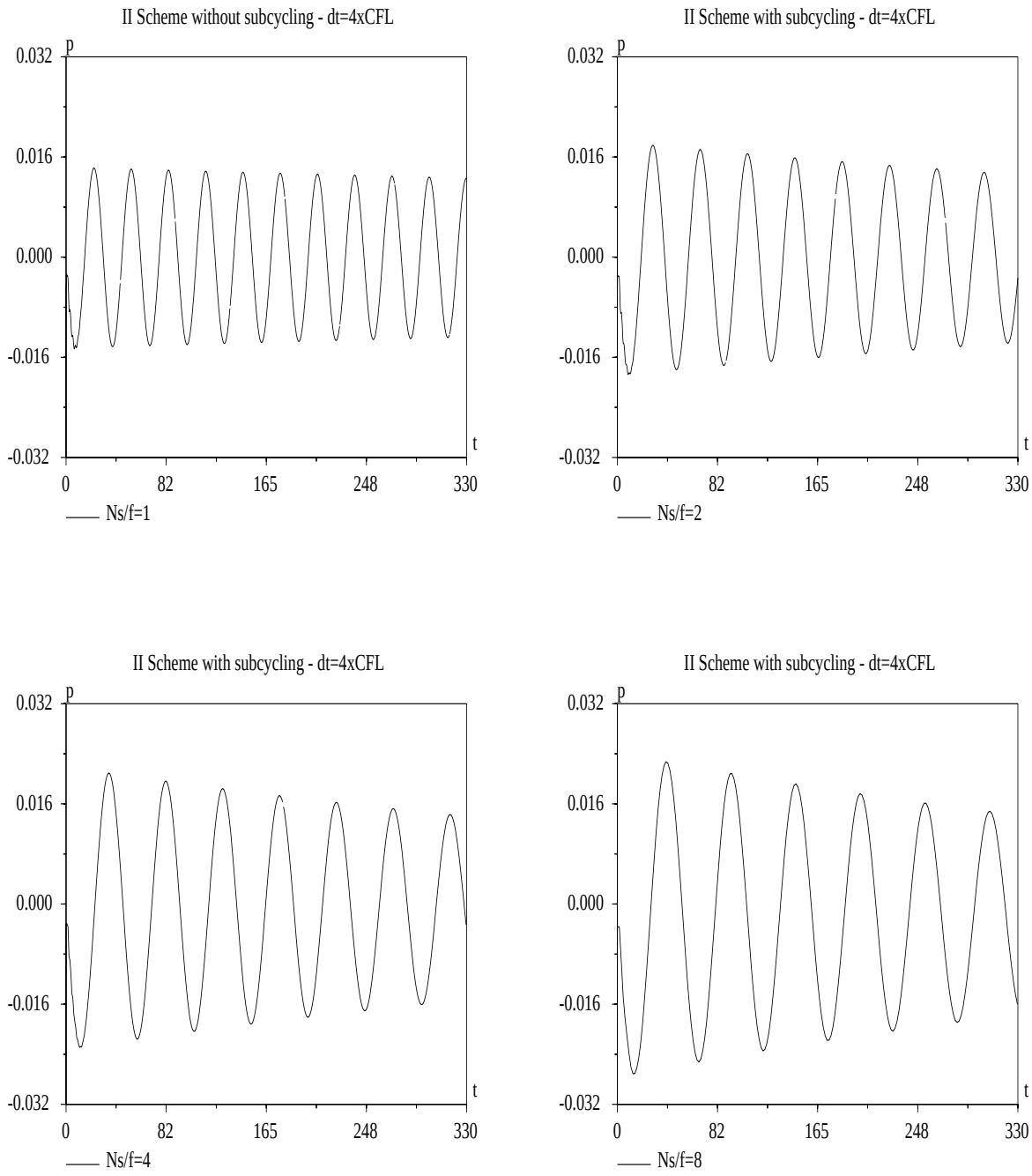

FIG. 4.8 – *Computed non-dimensional fluid pressure ($\Delta t = 4\times CFL$ and with several subcycling factors $n_{S/F}$)*

Rather, we focus on developing a family of partitioned procedures whose stability limit is governed by the critical time-step of the fluid solver. In other words, we wish to design a staggered solution algorithm for the coupled problem whose stability limit is not worse than that of the underlying fluid explicit time-integrator. This is not necessarily a trivial task because coupling effects can restrict the stability limits of the independent field time-integrators.

4.5.1 A predictor-corrector approach

Here, we present a family of explicit/implicit staggered algorithms for solving the fluid-structure equations (4.25) that is based on similar ideas to those presented in Section 4.4. The methodology now reads:

Step EI1. Predict the structural field using the value computed at $t_n = n\Delta t$:

$$Q^p = Q^n$$

Step EI2. Predict the fluid system using the forward Euler explicit scheme:

$$\delta W^p \;=\; \delta W^n + \Delta t\; A\; \delta W^n + \Delta t\; B\; Q^p$$

Step EI3. Improve the structural field using an implicit generalized trapezoidal method and the predicted fluid state δW^p:

$$\overline{Q^{n+1}} \;=\; Q^n + \Delta t\; D\; \overline{Q^{n+\alpha}} + \Delta t\; C\; \delta W^p \qquad \alpha \;\in\;]0,\; 1]$$

Step EI4. Correct the expressions yielding the fluid and structural fields to enhance the stability of the explicit/implicit staggered procedure:

$$\begin{aligned} \delta W^{n+1} &= \delta W^n + \Delta t\; A\; \delta W^n + \Delta t\; B\; Q^p + \left[\delta W^{n+1^c}\right] \\ Q^{n+1} &= Q^n + \Delta t\; D\; Q^{n+\alpha} + \Delta t\; C\; \delta W^p + \left[Q^{n+1^c}\right] \end{aligned}$$

When applied to the solution of the uncoupled linearized fluid system (4.17), the forward Euler algorithm is first-order accurate and stable for CFL ≤ 1. For $\alpha \geq 1/2$, the generalized trapezoidal family of methods is unconditionally stable when applied to time-integrate the uncoupled structural problem. For $\alpha \;\in\;]0,\; 1]$, these methods are first-order accurate, except for $\alpha = 1/2$, in which case the corresponding scheme is second-order accurate. The correction terms $[\delta W^{n+1^c}]$ and $[Q^{n+1^c}]$ should be computed to enhance the stability of the resulting explicit/implicit staggered solution procedure.

In order to present simple proofs, we now give a simple theorem concerning the energy variation of a structure through an implicit time-integration step with source term.

Theorem 9 *Let D be a RSDP matrix, and E_D an associated energy matrix. Let us define $\mathcal{E}^n = 1/2\ {Q^n}^t E_D Q^n$. If Q^{n+1} is given by:*

$$Q^{n+1} = Q^n + \Delta t\ D\ Q^{n+\alpha} + X$$
$$\textit{with} \quad \alpha \in [\tfrac{1}{2}, 1] \quad \textit{and} \quad Q^{n+\alpha} = (1-\alpha)\, Q^n + \alpha Q^{n+1}$$

then we have the following relation on the "successive" energies

$$\mathcal{E}^{n+1} \leq \mathcal{E}^n + X^t\ E_D\ Q^{n+\alpha}. \tag{4.57}$$

Proof. We have the following equalities:

$$\begin{aligned}
(1-\alpha)\, Q^{n+1} &= (1-\alpha)\, Q^n + (1-\alpha)\, \Delta t\ D\ Q^{n+\alpha} + (1-\alpha)\, X \\
\alpha Q^{n+1} &= \alpha Q^{n+1} \\
Q^{n+1} &= Q^{n+\alpha} + (1-\alpha)\, \Delta t\ D\ Q^{n+\alpha} + (1-\alpha)\, X.
\end{aligned} \tag{4.58}$$

Following the same, simple methodology, we find also that

$$\begin{aligned}
\alpha Q^{n+1} &= \alpha Q^n + \alpha \Delta t\ D\ Q^{n+\alpha} + \alpha X \\
(1-\alpha)\, Q^n &= (1-\alpha)\, Q^n \\
Q^n &= Q^{n+\alpha} - \alpha \Delta t\ D\ Q^{n+\alpha} - \alpha X.
\end{aligned} \tag{4.59}$$

Using (4.58) and (4.59), we find

$$\begin{aligned}
\mathcal{E}^{n+1} - \mathcal{E}^n &= \left(\frac{Q^n + Q^{n+1}}{2}\right)^t E_D \left(Q^{n+1} - Q^n\right) \\
&= \left(Q^{n+\alpha} + \left(\frac{1}{2} - \alpha\right) \Delta t\ D\ Q^{n+\alpha} + \left(\frac{1}{2} - \alpha\right) X\right)^t E_D \left(\Delta t\ D\ Q^{n+\alpha} + X\right) \\
&= {Q^{n+\alpha}}^t E_D X + \ \Delta t {Q^{n+\alpha}}^t E_D D Q^{n+\alpha} \\
&+ \left(\frac{1}{2} - \alpha\right) \left(\Delta t\ D\ Q^{n+\alpha} + X\right)^t E_D \left(\Delta t\ D\ Q^{n+\alpha} + X\right)
\end{aligned}$$

Since $1/2 \leq \alpha$, E_D is positive and $E_D D$ is non-positive in the sense of (4.27), the conclusion of the proof is straightforward. □

We now introduce an explicit/implicit stable time-integrator.

Theorem 10 *For $\alpha \geq 1/2$, and for the two following correction terms*

$$\begin{aligned}
\left[\delta W^{n+1^c}\right] &= \alpha \Delta t\ B\ (Q^{n+1} - Q^n) \\
\left[Q^{n+1^c}\right] &= -\frac{\Delta t}{2}\ C\ (\Delta t\ B\ Q^n + \delta W^{n+1^c})
\end{aligned} \tag{4.60}$$

the stability of the explicit/implicit staggered time-integrator defined by Steps EI1-EI4 above is governed by the stability of the explicit time-integrator of the uncoupled fluid problem.

Proof. For $[\delta W^{n+1^c}] = \alpha\Delta t\ B(Q^{n+1} - Q^n)$ and $[Q^{n+1^c}] = -\Delta t/2\ C(\Delta t\ B\ Q^n + \delta W^{n+1^c})$, the proposed explicit/implicit staggered solution algorithm for solving equations (4.25) becomes:

$$\boxed{\begin{array}{rcl} Q^{n+1} & = & Q^n + \Delta t D Q^{n+\alpha} + \Delta t\ C\ \left(\delta W^n + \Delta t A \delta W^n + \dfrac{\Delta t}{2} B Q^{n+\alpha}\right) \\ \delta W^{n+1} & = & \delta W^n + \Delta t A \delta W^n + \Delta t B Q^{n+\alpha} \end{array}} \tag{4.61}$$

Let the structural energy E_s^n be defined as follows:

$$\mathcal{E}_s^n = \frac{1}{2} Q^{n^t} E_D Q^n.$$

Applying Theorem 9 with

$$X = \Delta t\ C\ (\delta W^n + \Delta t A \delta W^n + \frac{\Delta t}{2} B Q^{n+\alpha}), \tag{4.62}$$

it follows that for $\alpha \geq \frac{1}{2}$ we have:

$$\mathcal{E}_s^{n+1} \ \leq\ \mathcal{E}_s^n + Q^{n+\alpha^t} E_D X. \tag{4.63}$$

For the fluid part, we define as well a fluid energy by:

$$\mathcal{E}_f^n = \frac{1}{2} \delta W^{n^t} E_A \delta W^n.$$

We then have

$$\begin{aligned} \mathcal{E}_f^{n+1} &= \mathcal{E}_f^n + \Delta t \Big(A\ \delta W^n + B\ Q^{n+\alpha}\Big)^t E_A \left(\delta W^n + \frac{\Delta t}{2}\ A\ \delta W^n + \frac{\Delta t}{2} B\ Q^{n+\alpha}\right) \\ \mathcal{E}_f^{n+1} &= \mathcal{E}_f^n && (4.64a) \\ &+ \Delta t\ \delta W^{n^t}\ A^t\ E_A \left(\delta W^n + \frac{\Delta t}{2} A\ \delta W^n\right) && (4.64b) \\ &+ \Delta t\ Q^{n+\alpha^t}\ B^t\ E_A \left(\delta W^n + \Delta t\ A\ \delta W^n + \frac{\Delta t}{2} B\ Q^{n+\alpha}\right). && (4.64c) \end{aligned}$$

The sign of the term in (4.64b) is governed by the stability of the explicit scheme applied to the uncoupled fluid problem. Actually, if the structure is omitted, these terms give the energy variation through one explicit fluid time step. In general, there is a limit time step, under which the explicit time-integrator is stable <u>and</u> gives a negative energy variation for the fluid. For example, for the fluid energy matrix given in (4.33) and for the matrix A induced by the spatial flux splitting, tedious calculations show that the fluid energy decreases as long as a CFL-like condition ($\text{CFL} \leq \text{CFL}_c$) holds.[5]

5. We point out here that have found some influences of boundary fluxes on the number CFL_c. For the simple pressure flux $(\rho_0 \dot{q} \quad c_0^2 \delta \rho^N)^t$, we found a disappointing $\text{CFL}_c = 0.5$. But for the mirror flux $(\rho_0 \dot{q} \quad c_0^2 \delta \rho_N + c_0 \rho_0 \dot{q} - c_0 \delta(\rho u))^t$, we found a satisfying $\text{CFL}_c = 1$.

Finally, under the assumptions that CFL ≤ 1 and $\alpha \geq \frac{1}{2}$, defining the total system energy as

$$\mathcal{E}^n = \mathcal{E}_s^n + \mathcal{E}_f^n,$$

we deduce from (4.62-4.63) and from (4.64a-4.64c) that

$$\mathcal{E}^{n+1} \leq \mathcal{E}^n + \Delta t\ Q^{n+\alpha^t} \left(B^t E_A + E_D C\right) \left(\delta W^n + \Delta t\ A\ \delta W^n + \frac{\Delta t}{2} B\ Q^{n+\alpha}\right).$$

Since the aeroelastic model problem satisfies $E_A B + (E_D C)^t = 0$, it follows that:

$$\mathcal{E}^{n+1} \quad \leq \quad \mathcal{E}^n \tag{4.65}$$

which shows that the numerical energy of the system does not increase in time, and therefore the partitioned solution procedure (4.61) is unconditionally stable. □

The construction of the correction terms in Theorem 10 might seem mysterious. The reader could also wonder if these corrections are the only ones which have this property. We would like to explain shortly how these corrections were built, and why they are unique.

The goal of the preceding energetic demonstration is to prove that, under the assumptions that both schemes used separately for the fluid and the structure are stable, the total energy of the system is non-increasing. Then we have to get rid of all coupled terms of the form $W^t <> Q$. The coupled terms produced by the integration of the fluid are written on (4.64c). A term of the form $Q^{n+\alpha^t} <> (\delta W^n + \Delta t A \delta W^n)$ can only disappear if a similar term appears in X in (4.62), which explains the construction of the corrections. Also, the quadratic term $Q^t <> Q$ of (4.64c) is compensated via the last term of X in (4.62).

Theorem 11 *The explicit/implicit partitioned procedure defined by equations (4.61) is first-order accurate.*

Proof. The proof of this theorem is similar to that of Theorem 6. □

Remark 3. Note that while the family of implicit/implicit partitioned procedures (4.41) and its fluid-subcycled version (4.48) require updating the fluid flow ahead of the structural field, the family of explicit/implicit staggered algorithms (4.61) require updating the structural system first.

4.5.2 Examples

Here, we illustrate the numerical properties of the family of explicit/implicit staggered procedures presented in Section 4.5.1 with the solution of the non-dimensional coupled equations (4.55). We consider the case $\alpha = 1/2$, and use the same non-dimensional parameters and finite volume mesh as in Section 4.4.3.

First, we solve the coupled problem for $0.5\times\text{CFL} \leq \Delta t \leq 1.0\times\text{CFL}$, where the CFL is with respect to the uncoupled fluid problem. The obtained non-dimensional piston displacement $\bar{q}/l_0$ and fluid pressure in the cell in contact with the piston $(p/\rho_0 c_0^2)_{20}$ are reported in Figures 4.9-4.10 for the case without subcycling. Clearly, these results demonstrate numerical stability for $\Delta t \leq 1.0\times\text{CFL}$. However, they also show that at time-steps close to the uncoupled fluid CFL condition, the errors introduced in the initial stages of the computations propagate throughout the entire history response of the fluid pressure, but do not affect significantly the evaluation of the structural displacement.

Next, we repeat the previous explicit/implicit computations and subcycle the fluid system. We use a subcycling scheme similar to that introduced in equations (4.48) in order to maximize the coupled stability time-step. In that case, the numerical results reported in Figure 4.11 for the non-dimensional piston displacement $\bar{q}/l_0$ indicate that there exists a maximum subcycling factor beyond which the explicit/implicit time-integrator (4.61) with subcycling becomes numerically unstable.

Remark 4. An explicit/implicit subcycled partitioned procedure, whose stability would be limited by the stability of the explicit fluid time integrator is still to be found. Numerically, for all explicit/implicit subcycled procedures we have imagined, we were not able to prove that a total energy was decreasing. We also found that the stability of the coupled scheme was of the form $n_{S/F} * \text{CFL} \leq \text{C}$, which makes these subcycled procedures useless.

4.6 Parallel staggered strategies, error analysis and CPU distribution

The family of partitioned procedures presented in Sections 4.4 and 4.5 are inherently sequential: in the implicit/implicit case, the fluid state vector must be updated before the structural system can be advanced, and in the explicit/implicit case, the new structural displacements and velocities must be computed before the new fluid state vector can be evaluated. For aeroelastic simulations where the structural component is modeled as a spring system with two or three degrees of freedom (i.e., two-dimensional airfoil flutter), or as a simple plate with a few hundred degrees of freedom (i.e., three-dimensional wing flutter), the computational cost of the coupled aeroelastic simulation is dominated by the cost of the fluid computations. In such cases, and with the advent of parallel processors and distributed computing platforms, a significant performance enhancement can be accomplished by parallelizing the fluid kernel only, even if the fluid-structure staggering is performed in a serial manner. However, for aeroelastic problems involving full-scale structural systems such as a complete aircraft with several hundred thousand degrees of freedom, it becomes interesting not only to parallelize each field computations, but also to design staggered time-integration algorithms that promote inter-field parallelism — that is, that allow advancing simultaneously the fluid and structural systems. Moreover, it is shown in [23] that inter-field parallelism allows an overlapping between the fluid-structure communication and each

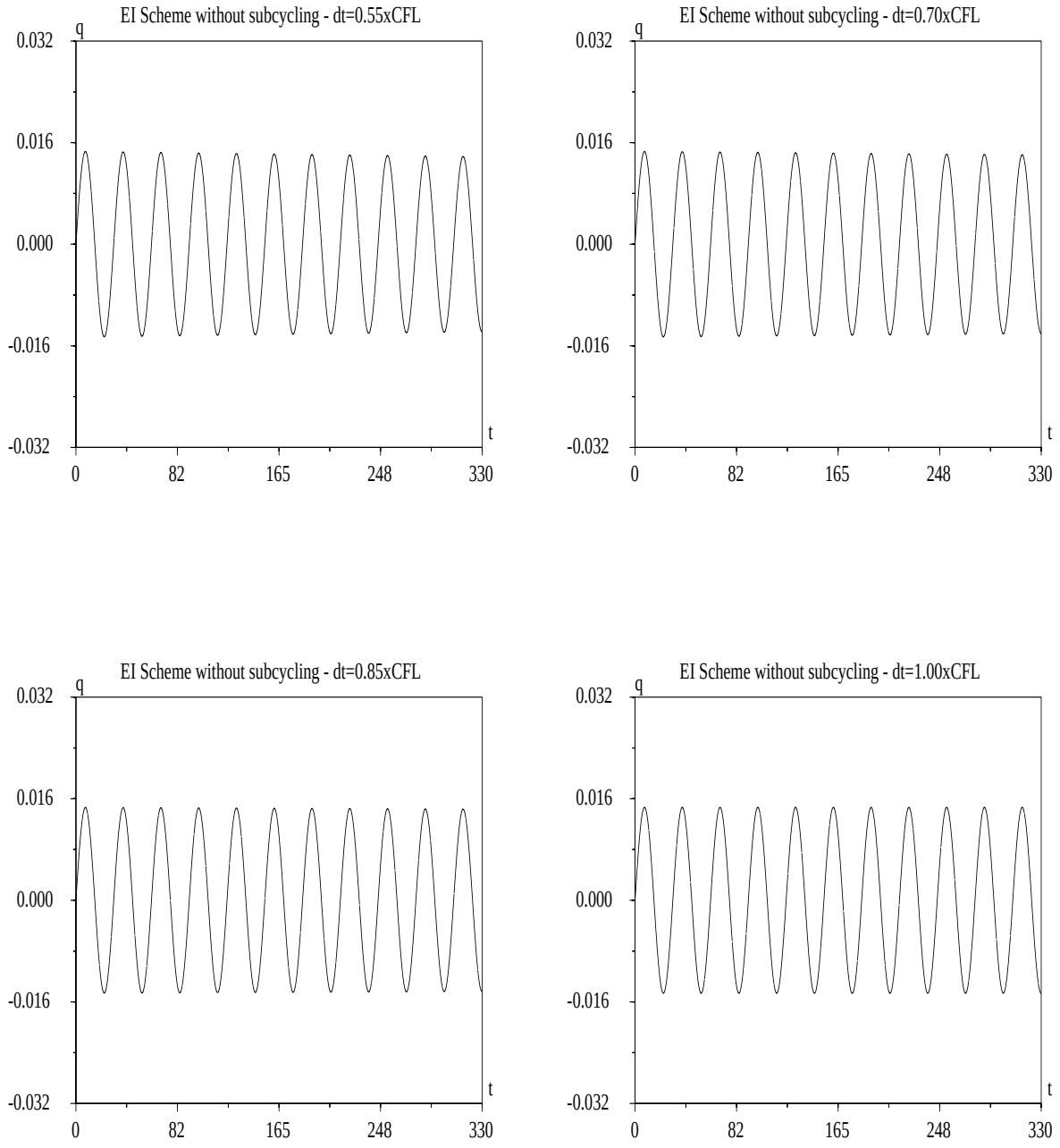

FIG. 4.9 – *Computed non-dimensional piston displacement (without subcycling)*

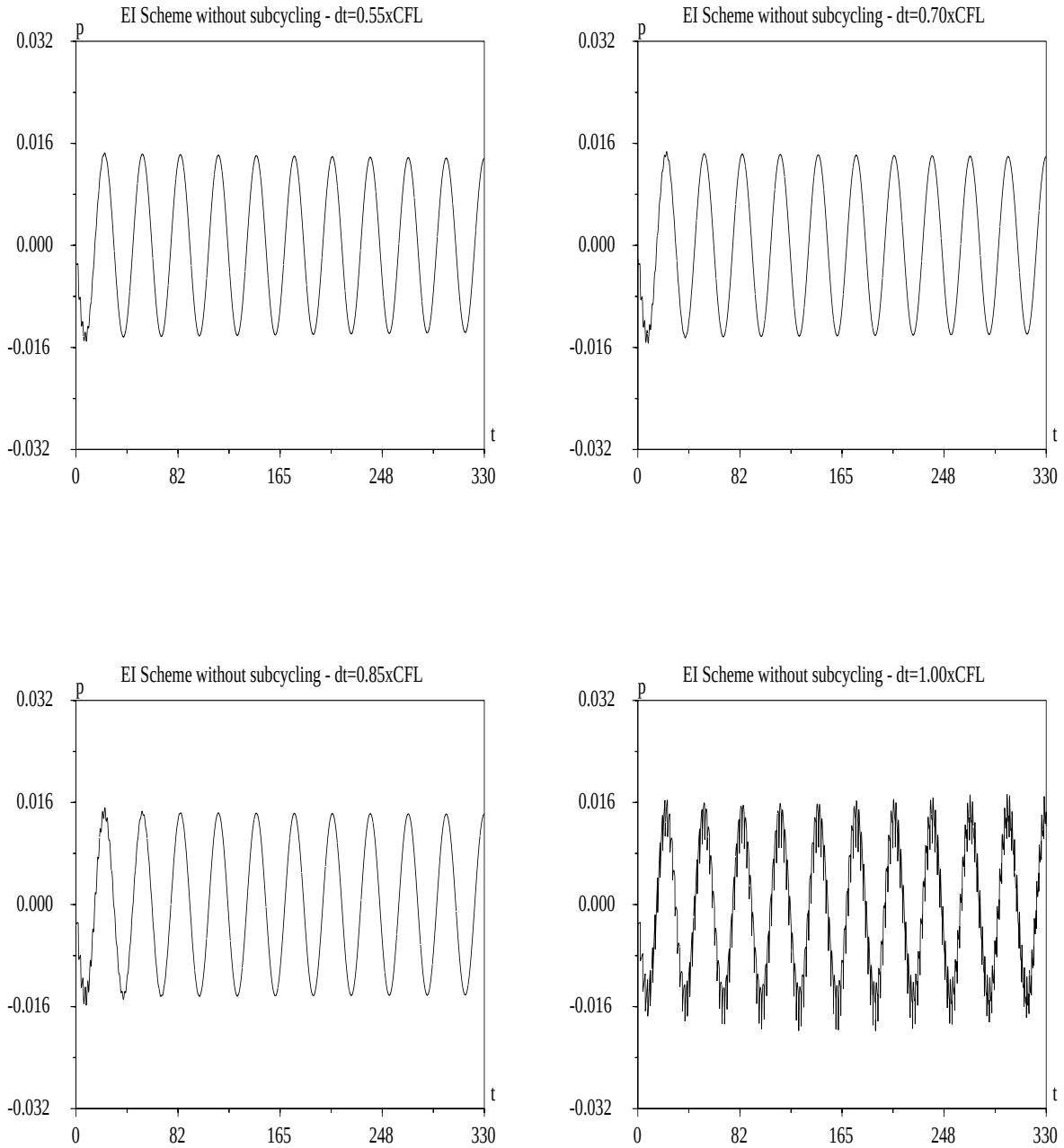

FIG. 4.10 – *Computed non-dimensional fluid pressure (without subcycling)*

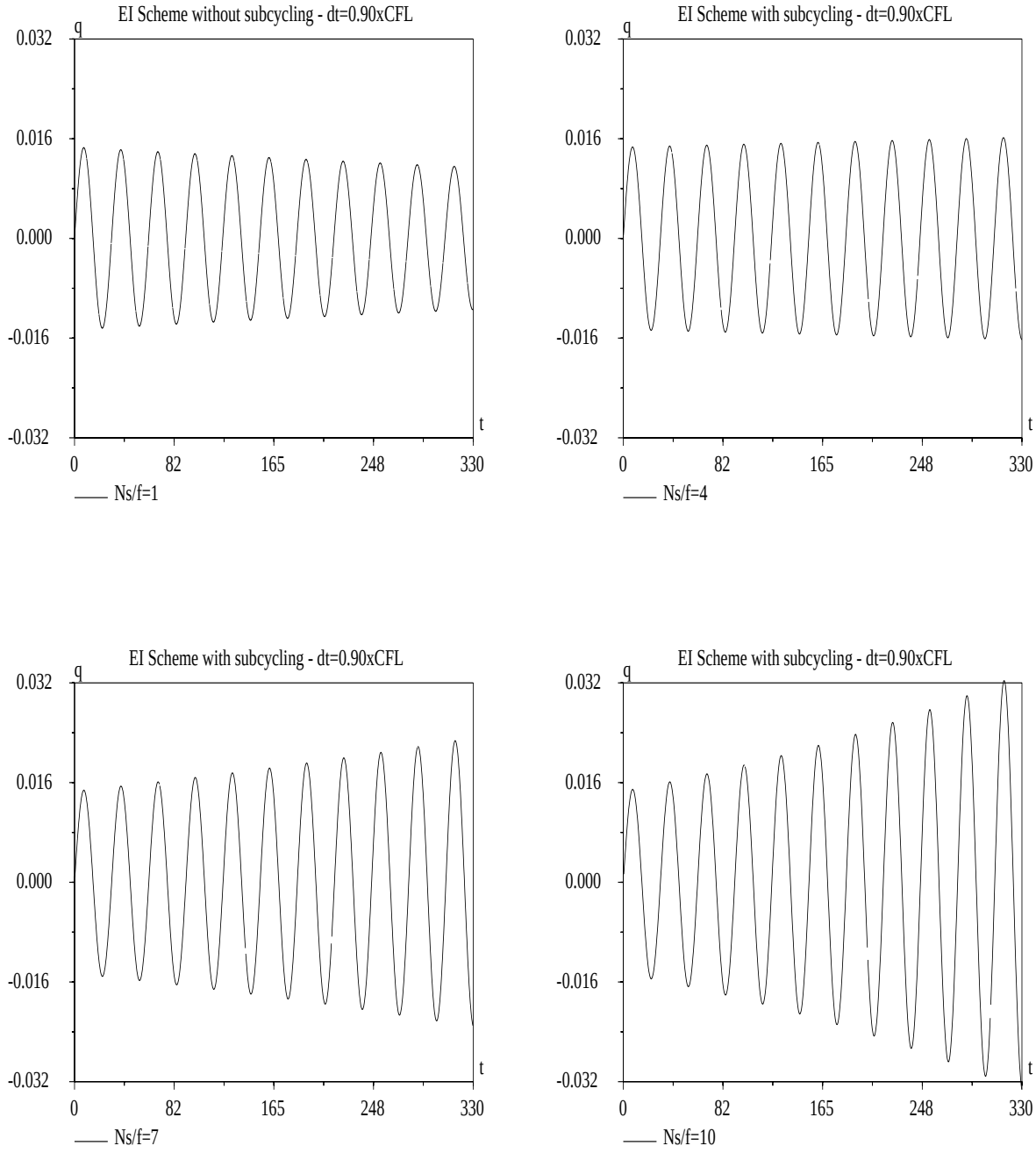

FIG. 4.11 – *Computed non-dimensional piston displacement ($\Delta t = 0.9 \times CFL$ and with several subcycling factors $n_{S/F}$)*

of the fluid and structure computations, which reduces the overall simulation time.

In this section, we present partitioning procedures with inter-field parallelism, and discuss their accuracy v.s. speed trade-offs. We consider only explicit/implicit algorithms. More specifically, we focus on the case where the fluid is advanced using the first-order accurate forward Euler scheme and the structure is advanced using the second-order accurate midpoint rule, because these algorithms are already available in our large-scale simulation parallel software. We use the family of time-integrators (4.61) as reference, and therefore begin with their error analysis.

We introduce the following nomenclature:

O_F : number of floating-point operations in one fluid time-step

O_S : number of floating-point operations in one structural time-step

T_F : fluid-to-structure single pass transfer time

T_S : structure-to-fluid single pass transfer time

CPU_F : CPU resource allocated to the fluid kernel

CPU_S : CPU resource allocated to the structure kernel

For every partitioned procedure, we give the resource distribution between the fluid and structure kernels for simulations on heterogeneous platforms.

4.6.1 Algorithm ALG-0 : the basic staggered scheme

In the sequel, we refer to the explicit/implicit time-integrator (4.61) as the basic staggered algorithm ALG-0. Let Z be defined as follows:

$$Z = \begin{pmatrix} Q \\ \delta W \end{pmatrix}. \tag{4.66}$$

Considering the time-interval $[t_n, t_{n+n_{S/F}}]$ (where we have assumed $t_n = n\,\Delta t,\ \forall n$), it follows from equations (4.61-4.66) that:

$$\begin{aligned} Z^{n+n_{S/F}} = \Bigg[I &+ n_{S/F}\Delta t \begin{pmatrix} D & C \\ B & A \end{pmatrix} \\ &+ n_{S/F}^2 \frac{\Delta t^2}{2} \begin{pmatrix} D^2 + BC & DC + CA \\ BD + AB & BC + A^2 \end{pmatrix} \\ &+ n_{S/F} \frac{\Delta t^2}{2} \begin{pmatrix} 0 & CA \\ -AB & A^2 \end{pmatrix} + O\left(\Delta t^3\right) \Bigg] Z^n \end{aligned} \tag{4.67}$$

If $ER_{\delta W}$ and ER_Q denote respectively the errors in the fluid and structural responses after $n_{S/F}$ time-steps, it follows from (4.67) that:

$$\boxed{\begin{aligned} ER_{\delta W}^{ALG-0} &= -n_{S/F}\frac{\Delta t^2}{2}A\delta\dot{W}^n + O(\Delta t^3) \\ ER_{Q}^{ALG-0} &= n_{S/F}\frac{\Delta t^2}{2}CAQ^n + O(\Delta t^3) \end{aligned}} \tag{4.68}$$

which shows that ALG-0 is first-order accurate. Hence, the accuracy of the structural computation is first-order even though the midpoint rule applied to the uncoupled structural problem is second-order accurate.

The basic steps of ALG-0 are graphically depicted in Figure 4.12. The CPU time needed to advanced the coupled solution $n_{S/F}\Delta t$ is equal to:

$$T_{coupled} = n_{S/F}(T_F + T_S + \frac{O_F}{CPU_F} + \frac{O_S}{CPU_S})$$

If the total amount of CPU resources $CPU = CPU_F + CPU_S$ is assumed to be fixed, $T_{coupled}$ is minimum for:

$$\frac{CPU_F}{CPU_S} = \sqrt{\frac{O_F}{O_S}}$$

which gives:

$$\boxed{T_{coupled}^{ALG-0} = n_{S/F}(T_F + T_S + \frac{O_F + O_S + 2\sqrt{O_F O_S}}{CPU})} \tag{4.69}$$

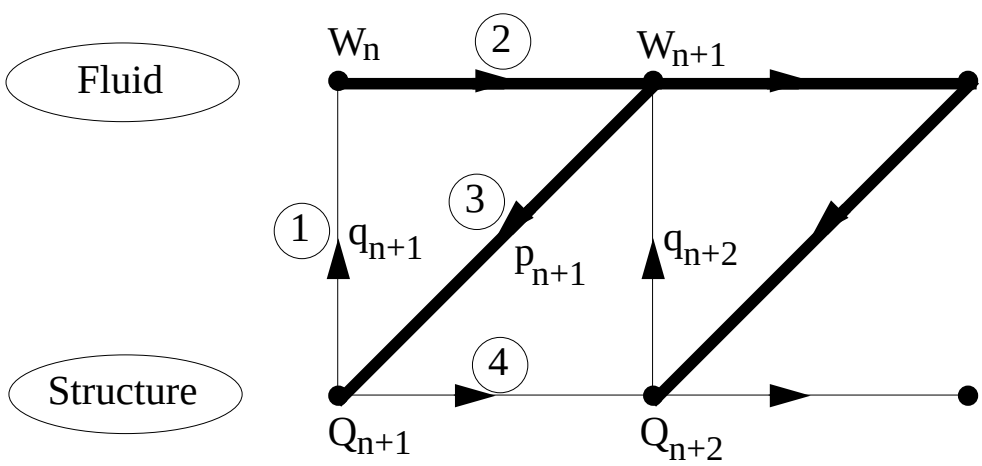

FIG. 4.12 – *ALG-0: the basic staggered algorithm*

4.6.2 Algorithm ALG-1 : subcycling the fluid system

A fluid-subcycled version of a slightly modified ALG-0 where the subcycling scheme follows the guidelines of Theorem 7 is referred to as ALG-1 in the sequel and is given by:

$$\boxed{\begin{array}{l}
\delta W^{n+1^{(0)}} \;=\; \delta W^n \\
X^{(0)} \;=\; Q^n \\
\{ \\
\quad For\ k \;=\; 0,\ ...,\ n_{S/F}-1 \\
\quad \delta W^{n+1^{(k+1)}} \;=\; \delta W^{n+1^{(k)}} + \Delta t\ A\ \delta W^{n+1^{(k)}} + \Delta t\ B\ Q^n \\
\quad X^{(k+1)} \;=\; X^{(k)} + \Delta t\ C\ \delta W^{n+1^{(k+\frac{1}{2})}} \\
\} \\
\delta W^{n+1} \;=\; \delta W^{n+1^{(n_{S/F})}} \\
Q^{n+1} \;=\; X^{(n_{S/F})} + n_{S/F}\Delta t\ D\left(\dfrac{X^{(n_{S/F})}+Q^{n+1}}{2}\right)
\end{array}} \tag{4.70}$$

Essentially, the fluid system is subcycled during $n_{S/F}$ time-steps Δt, and the structural field is advanced in one shot a large time-step equal to $n_{S/F}\Delta t$ using the average fluid pressure between t_n and $t_{n+1} = t_n + n_{S/F}\Delta t$.

Expanding the various terms in (4.70) around t_n leads to:

$$\boxed{\begin{array}{lcl}
ER_{\delta W}^{ALG-1} & = & -n_{S/F}^2\dfrac{\Delta t^2}{2}B\delta\dot{W}^n + O(\Delta t^3,\ n_{S/F}\Delta t^2) \\
ER_{Q}^{ALG-1} & = & n_{S/F}^3\dfrac{\Delta t^3}{12}(D^3Q^n + 2C\delta\ddot{W}^n - 2CB\dot{Q}^n) + O(\Delta t^4,\ n_{S/F}^2\Delta t^3)
\end{array}} \tag{4.71}$$

which shows that ALG-1 is also first-order accurate. However, from (4.68) and (4.71), it follows that subcycling amplifies the fluid errors by the subcycling factor $n_{S/F}$. Measuring the effect of subcycling on the structural errors of ALG-0 is less trivial: in order to keep its computer implementation simple, we have designed ALG-1 as a fluid-subcycled version of a "slightly modified" rather than the "original" ALG-0. Consequently, the structural errors grow as $O(n_{S/F}\Delta t^2)$ in ALG-0, and as $O(n_{S/F}^3\Delta t^3)$ in ALG-1.

The basic steps of ALG-1 are graphically depicted in Figure 4.13. The CPU time needed to advanced the coupled solution of $n_{S/F}\Delta t$ is equal to:

$$T_{coupled} \;=\; T_F + T_S + \frac{n_{S/F}O_F}{CPU_F} + \frac{O_S}{CPU_S}$$

For a fixed total amount of CPU resources $CPU = CPU_F + CPU_S$, the CPU time $T_{coupled}$ is minimum for:

$$\frac{CPU_F}{CPU_S} \;=\; \sqrt{\frac{n_{S/F}O_F}{O_S}}$$

which gives:

$$\boxed{T^{ALG1}_{coupled} \;=\; T_F + T_S + \frac{n_{S/F}O_F + O_S + 2\sqrt{n_{S/F}O_F O_S}}{CPU}} \tag{4.72}$$

The comparison of $T^{ALG-0}_{coupled}$ and $T^{ALG-1}_{coupled}$ highlights the computational advantages of subcycling.

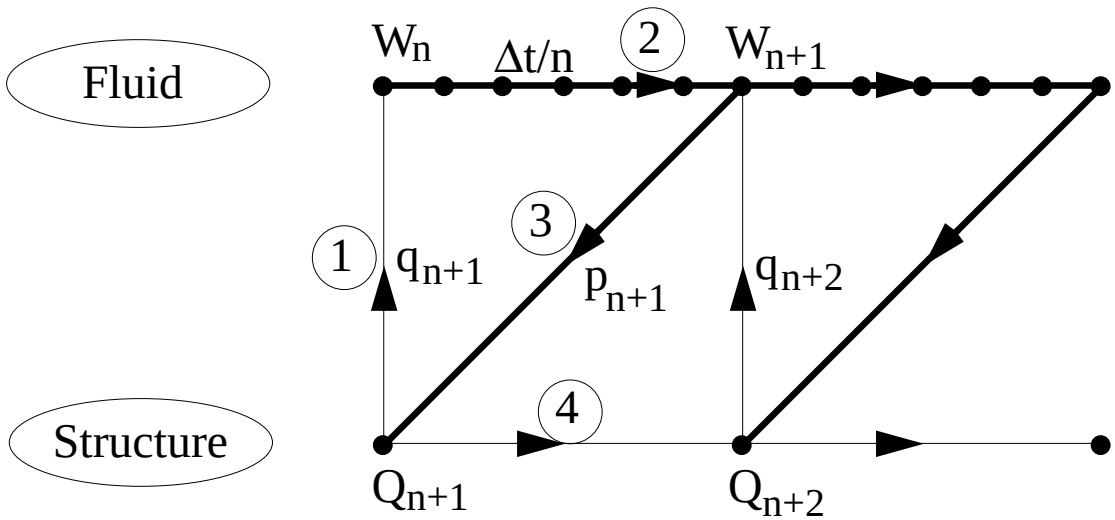

FIG. 4.13 – *The fluid-subcycled ALG1 staggered algorithm*

4.6.3 Algorithm ALG-2 : improving the accuracy of ALG-1

In order to improve the accuracy of the fluid solution in ALG-1, we introduce a computational phase shift between the fluid and structure kernels equal to $n_{S/F}\Delta t/2$. Assuming that δW^n and $Q^{n+\frac{1}{2}}$ are available, the improved subcycled explicit/implicit algorithm ALG-2 computes δW^{n+1} and $Q^{n+\frac{3}{2}}$ as follows:

$$\boxed{\begin{array}{l}
\delta W^{n+1^{(0)}} \;=\; \delta W^n \\
X^{(0)} \;=\; Q^{n+\frac{1}{2}} \\
\{ \\
\quad For\ k \;=\; 0,\ ...,\ n_{S/F}-1 \\
\quad \delta W^{n+1^{(k+1)}} \;=\; \delta W^{n+1^{(k)}} + \Delta t\ A\ \delta W^{n+1^{(k)}} + \Delta t\ B\ Q^{n+\frac{1}{2}} \\
\quad X^{(k+1)} \;=\; X^{(k)} + \Delta t\ C\ \delta W^{n+1^{(k+\frac{1}{2})}} \\
\} \\
\delta W^{n+1} \;=\; \delta W^{n+1^{(n_{S/F})}} \\
Q^{n+\frac{3}{2}} \;=\; X^{(n_{S/F})} + n_{S/F}\Delta t\ D\left(\dfrac{X^{(n_{S/F})} + Q^{n+\frac{3}{2}}}{2}\right)
\end{array}} \tag{4.73}$$

Algorithm ALG-2 has the same computational and I/O transfer requirements as ALG-1. The only computational difference consists of the treatment of the initial fluid and structural states (actually, these initial states must be provided at different times). Therefore, ALG-2 has the same stability limits as ALG-1. However, the error analysis of ALG-2 is different. It leads to:

$$\boxed{\begin{aligned} ER_{\delta W}^{ALG-2} &= -n_{S/F}\frac{\Delta t^2}{2} A\ \delta\dot{W}^n + O(\Delta t^3) \\ ER_{Q}^{ALG-2} &= O(\Delta t^4,\ n_{S/F}^3 \Delta t^3) \end{aligned}} \tag{4.74}$$

A direct comparison of (4.68), (4.71) and (4.74) shows that ALG-2 offers the computational advantages of ALG-1, and the higher accuracy of ALG-0.

4.6.4 Algorithm ALG-3 : introducing inter-field parallelism

ALG-0, ALG-1 and ALG-2 are inherently sequential. In all three algorithms, the fluid system must be updated before the structural system can be advanced. The following explicit/implicit fluid-subcycled time-integrator ALG-3 introduces inter-field parallelism in the solution of the system (4.25):

$$\boxed{\begin{aligned} &\delta W^{n+1^{(0)}} = \delta W^n \\ &\{ \\ &\quad For\ k = 0,\ ...,\ n_{S/F} - 1 \\ &\quad \delta W^{n+1^{(k+1)}} = \delta W^{n+1^{(k)}} + \Delta t\ A\ \delta W^{n+1^{(k)}} + \Delta t\ B\ Q^n \\ &\} \\ &\delta W^{n+1} = \delta W^{n+1^{(n_{S/F})}} \\ &Q^{n+1} = Q^n + n_{S/F}\Delta t\ C\ \delta W^n + n_{S/F}\Delta t\ D\ Q^{n+\frac{1}{2}} \end{aligned}} \tag{4.75}$$

Clearly, the fluid and structure kernels can run in parallel during the time-interval $[t_n,\ t_{n+1}]$ (with $t_{n+1} = t_n + n_{S/F}\Delta t$). Inter-field communication or I/O transfer is needed only at the beginning of a time-interval. Expanding the various terms in (4.75) around t_n leads to:

$$\boxed{\begin{aligned} ER_{\delta W}^{ALG-3} &= O(n_{S/F}^2 \Delta t^2) \\ ER_{Q}^{ALG-3} &= O(n_{S/F}^2 \Delta t^2) \end{aligned}} \tag{4.76}$$

which demonstrates that ALG-3 is first-order accurate. However, the above error analysis also shows that parallelism in ALG-3 is achieved at the expense of amplified errors in both the fluid (a factor equal to $n_{S/F}$ with respect to ALG-2) and structural (a factor equal to $1/(n_{S/F}\Delta t)$ with respect to ALG-2) systems.

The basic steps of ALG-3 are graphically depicted in Figure 4.14. The parallel CPU time needed to advanced the coupled solution of $n_{S/F}\Delta t$ is equal to:

$$T_{coupled} \;=\; T_F + T_S + max(\frac{n_{S/F}O_F}{CPU_F},\; \frac{O_S}{CPU_S}).$$

For a fixed total amount of CPU resources — for example, a fixed number of processors in a parallel machine — $T_{coupled}$ is minimum when the two arguments of the maximum above are equal, which happens for:

$$\frac{CPU_F}{CPU_S} \;=\; \frac{n_{S/F}O_F}{O_S}.$$

Hence, the parallel CPU time associated with ALG-3 is:

$$\boxed{T_{coupled}^{ALG-3} = T_F + T_S + \frac{n_{S/F}O_F + O_s}{CPU}} \tag{4.77}$$

which demonstrates the computational advantages of this parallel scheme.

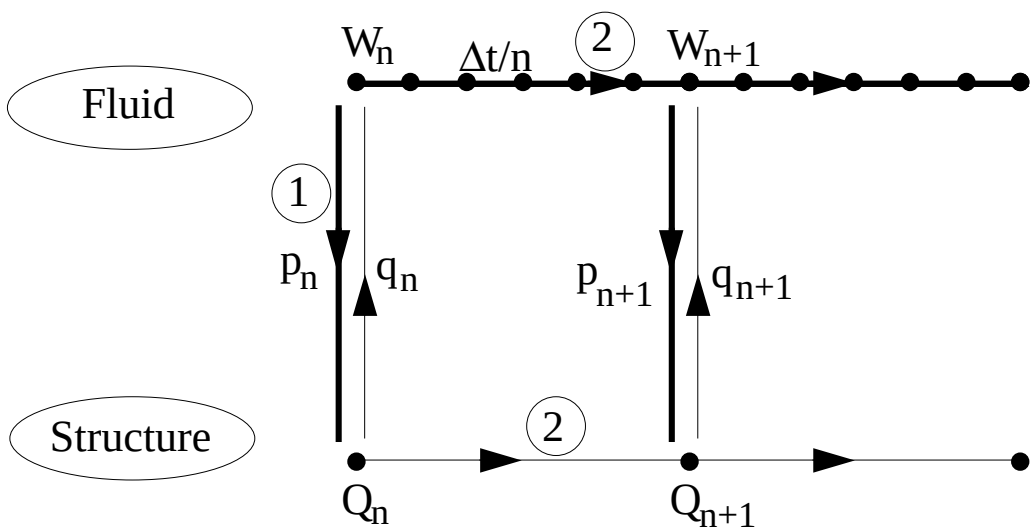

FIG. 4.14 – *The basic parallel subcycled ALG-3 algorithm*

4.6.5 Algorithm ALG-4 : improving the accuracy of ALG-3

In order to improve the accuracy of the basic parallel time-integrator ALG-3, we propose to exchange information between the fluid and structure kernels at half-step in the following specific manner (ALG-4):

$$
\boxed{
\begin{array}{l}
\delta W^{n+1^{(0)}} \;=\; \delta W^{n} \\
\{ \\
\quad For\ k \;=\; 0,\ ...,\ \frac{n_{S/F}}{2} - 1 \\
\quad \delta W^{n+1^{(k+1)}} \;=\; \delta W^{n+1^{(k)}} + \Delta t\ A\ \delta W^{n+1^{(k)}} + \Delta t\ B\ Q^{n} \\
\} \\
\delta W^{n+\frac{1}{2}} \;=\; \delta W^{n+1^{(\frac{n_{S/F}}{2})}} \\
\overline{Q^{n+1}} \;=\; Q^{n} + n_{S/F}\Delta t\ C\ \delta W^{n} + n_{S/F}\Delta t\ D \left(\dfrac{Q^{n} + \overline{Q^{n+1}}}{2} \right) \\
\{ \\
\quad For\ k \;=\; \frac{n_{S/F}}{2},\ ...,\ n_{S/F} - 1 \\
\quad \delta W^{n+1^{(k+1)}} \;=\; \delta W^{n+1^{(k)}} + \Delta t\ A\ \delta W^{n+1^{(k)}} + \Delta t\ B\ \overline{Q^{n+1}} \\
\} \\
\delta W^{n+1} \;=\; \delta W^{n+1^{(n_{S/F})}} \\
Q^{n+1} \;=\; Q^{n} + n_{S/F}\Delta t\ C\ \delta W^{n+\frac{1}{2}} + n_{S/F}\Delta t\ D \left(\dfrac{Q^{n} + Q^{n+1}}{2} \right)
\end{array}
}
\tag{4.78}
$$

The above algorithm ALG-4 is illustrated in Figure 4.15. The first-half of the computations is identical to that of ALG-3, except that the fluid system is subcycled only up to $t_n + \frac{n_{S/F}}{2}\Delta t$, while the structure is advanced in one shot up to $t_n + n_{S/F}\Delta t$. At $t_n + \frac{n_{S/F}}{2}\Delta t$, the fluid and structure kernels exchange pressure, displacement and velocity informations. In the second-half of the computations, the fluid system is subcycled from $t_n + \frac{n_{S/F}}{2}\Delta t$ to $t_n + n_{S/F}\Delta t$ using the new structural information, and the structural behavior is re-computed in parallel using the newly received pressure distribution. Note that the first evaluation of the structural state vector $\overline{Q^{n+1}}$ can be interpreted as a predictor.

An error analysis of ALG-4 reveals that:

$$
\boxed{
\begin{array}{lcl}
ER_{\delta W}^{ALG-4} & = & O(n_{S/F}\Delta t^{2}) \\
ER_{Q}^{ALG-4} & = & O(n_{S/F}^{3}\Delta t^{3})
\end{array}
}
\tag{4.79}
$$

which definitely shows that this parallel algorithm has the same accuracy as the improved ALG-2.

The parallel CPU time needed to advance the coupled solution of $n_{S/F}\Delta t$ using ALG-4 is equal to:

$$
T_{coupled} \;=\; 2\ (T_F + T_S + max(\frac{\frac{n_{S/F}}{2}O_F}{CPU_F},\ \frac{O_S}{CPU_S}))
$$

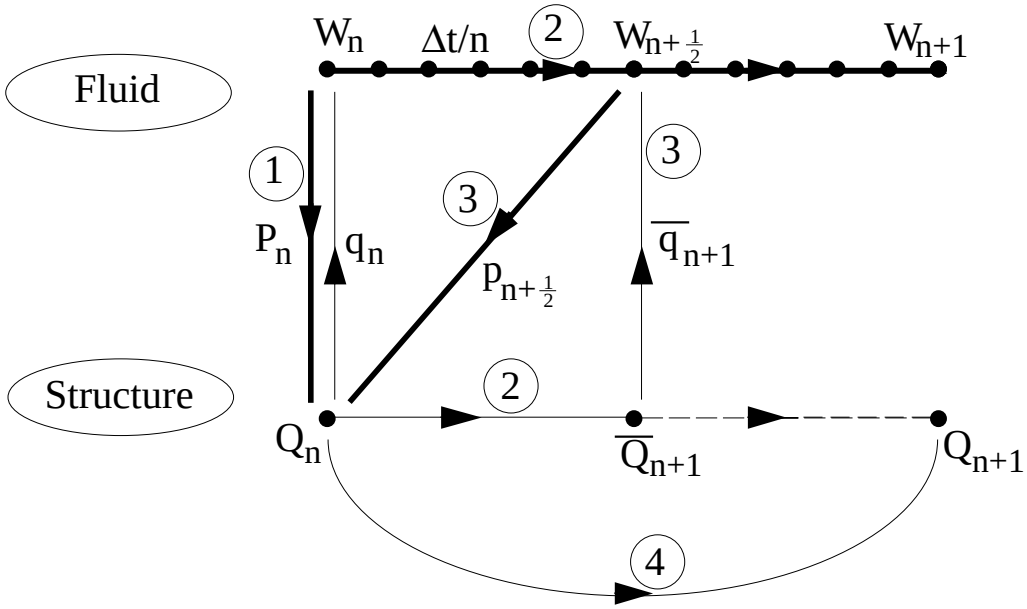

FIG. 4.15 – *The improved parallel subcycled ALG4 algorithm*

For a fixed total amount of CPU resources, this parallel time is minimum for:

$$\frac{CPU_F}{CPU_S} = \frac{n_{S/F} O_F}{2 O_S}$$

Hence, the parallel CPU time corresponding to ALG-4 is:

$$\boxed{T_{coupled}^{ALG-4} = 2\,(T_F + T_S) + \frac{n_{S/F} O_F + 2O_s}{CPU}} \tag{4.80}$$

In summary, the accuracy of the basic parallel algorithm ALG-3 is improved at the expense of an additional communication step or I/O transfer during each coupled cycle.

4.6.6 Applications

Some advantages and limitations of ALG-0 – ALG-4 are illustrated in Figure 4.16 which contrasts the various computed solutions $\bar{q}/l_0$ of the non-dimensional equations (4.55), using the same non-dimensional parameters and finite volume mesh as in Section 4.4.3, and with $\Delta t = 0.9\times$CFL.

If the ALG-0 solution is used as reference, the reader can observe that ALG-1 and ALG-2 are at the stability limit when $n_{S/F} = 5$. The accuracy of ALG-3 is comparable to that of ALG-1, but its stability is restricted to $n_{S/F} = 2$. On the other hand, the parallel algorithm ALG-4 is shown to have the same accuracy as ALG-0 even for $n_{S/F} = 20$, which highlights the merits of this improved parallel algorithm.

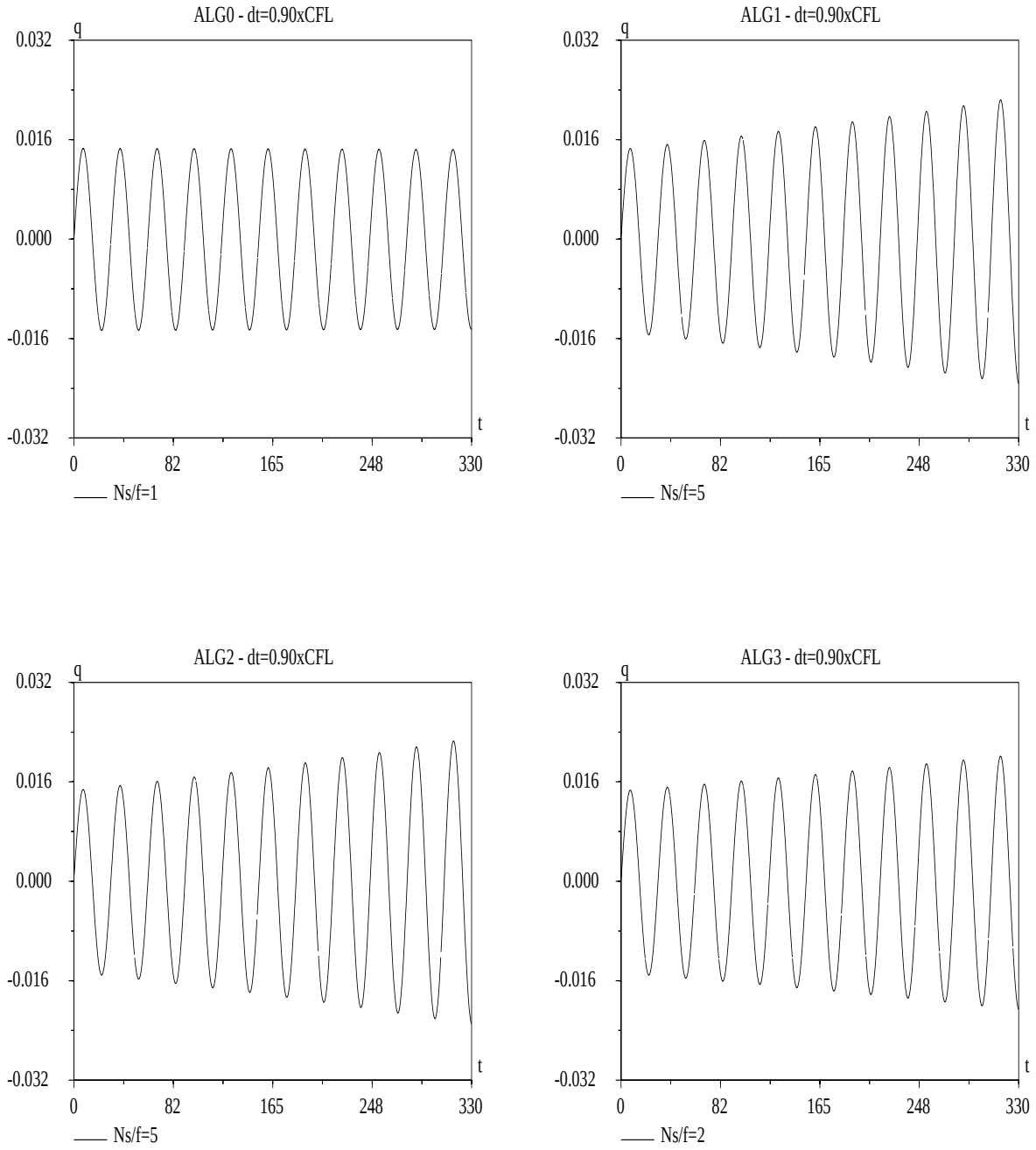

FIG. 4.16 – *Computed non-dimensional piston displacement (ALG-0 – ALG-4)*

4.7 Aeroelastic response of a flexible panel in transonic nonlinear regime

Based on the insight gained from the analysis and solution of the coupled piston problem, we have extended the algorithms presented in this chapter to the solution of the three-field coupled formulations summarized in (4.1), and complex aeroelastic problems. The generalization of ALG-0 – ALG-4, their implementation on heterogeneous parallel processors, and the analysis of their performance results are discussed in details in a companion paper [23]. Here, we focus on validating qualitatively the conclusions drawn from the mathematical and numerical investigations of the model problem with the simulation of the two-dimensional transient aeroelastic response of a flexible panel in transonic nonlinear regime.

For a two-dimensional simulation, the panel is represented by its cross section that is assumed to have a unit length $L = 1$, a uniform thickness $h = 10^{-2} \times L$, and to be clamped at both ends. This rectangular cross section is discretized into 300×3 plane strain 4-node elements with perfect aspect ratio to avoid mesh locking. This fine discretization — which generates 1204 nodes — is not needed for accuracy; we have designed this structural mesh only because we were also interested in assessing some computational and I/O performance issues. The two-dimensional flow domain around the panel is discretized into 2880 triangles and 1504 vertices. The free stream Mach number is set to $M_\infty = 0.8$, and a slip condition is imposed at the fluid-structure boundary. Because the fluid and structural meshes are not compatible at their interfaces (Figure 4.17), the MATCHER software [53] is used to transfer the pressure load to the structure, and to transmit the structural deformations at the surfaces of the panel to the fluid.

Initially, a steady-state flow is computed around the panel at $M_\infty = 0.8$ (see Figure 4.18). Next, this flow is perturbed via an initial displacement of the panel that is proportional to its second fundamental mode (Figure 4.19), and the subsequent panel motion and flow evolution are computed using the ALG-0 – ALG-4 explicit/implicit fluid-structure time-integrators (see Figures 4.20 and 4.21).

More specifically, the dynamic equations of equilibrium of the structure are solved via the parallel implicit transient FETI method [16], with the improvements proposed in [21] for the efficient iterative solution of systems with repeated right hand sides. The Euler flow equations are solved with a parallel algorithm that combines a second-order accurate Monotonic Upwinding Scheme for Conservation Laws for spatial approximation, and a second-order low-storage explicit Runge-Kutta scheme for time-integration [22].

All computations are carried out on an iPSC-860 parallel processor. Four processors are allocated to the fluid code, and two processors to the structural program. The fluid and structural computations are implemented in a heterogeneous manner using the intercube communication procedures described in [4].

For the uncoupled fluid problem, the CFL stability time-step is $\Delta t = 1 \times \text{CFL}$

$= 6.25 \times 10^{-6}$. The lift solutions computed by

$$\begin{array}{lll} & \text{ALG-0} & (\Delta t_c = \Delta t_F = \Delta t_S = 3.9 \times 10^{-6}), \\ & \text{ALG-1} & (\Delta t_F = 3.9 \times 10^{-6}, \quad \Delta t_S = 1.17 \times 10^{-4}, \quad n_{S/F} = 30), \\ & \text{ALG-3} & (\Delta t_F = 3.9 \times 10^{-6}, \quad \Delta t_S = 1.17 \times 10^{-4}, \quad n_{S/F} = 30), \\ \text{and} & \text{ALG-4} & (\Delta t_F = 3.9 \times 10^{-6}, \quad \Delta t_S = 1.17 \times 10^{-4}, \quad n_{S/F} = 30) \end{array}$$

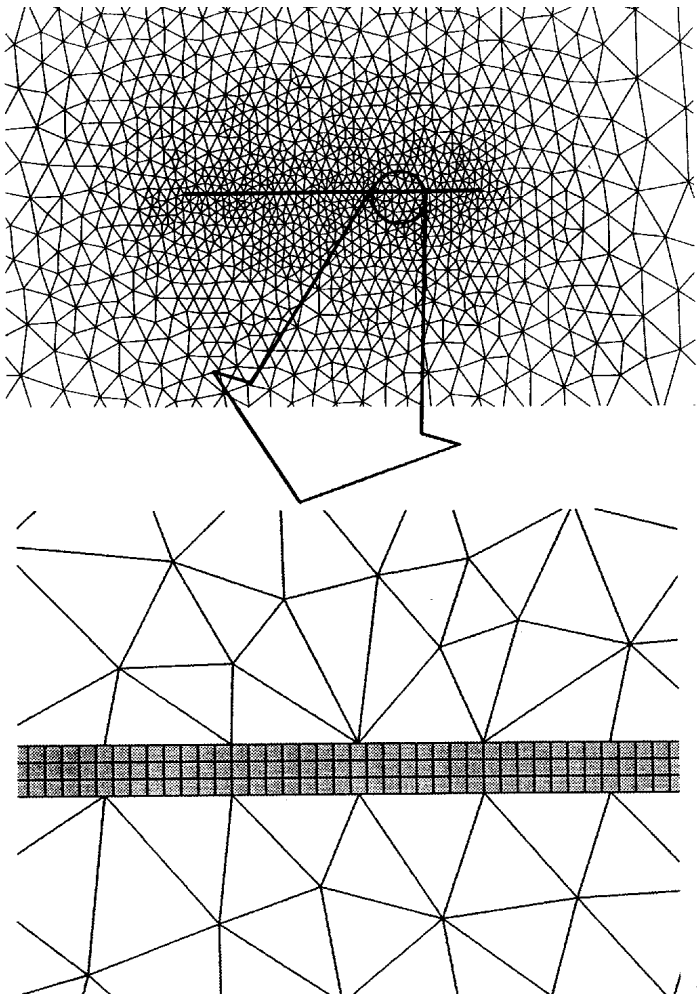

FIG. 4.17 – *A partial view of the structure and fluid discretizations*

are depicted in Figure 4.22. Clearly, as predicted by the theory presented in this chapter, all proposed explicit/implicit time-integrators are shown to be numerically stable at $\Delta t_F = 1\times$CFL and $n_{S/F} = 30$, For $n_{S/F} = 30$, ALG1 and ALG4 exhibit essentially the same accuracy. In the long run, their amplitude and phase errors are less important than those of ALG3. Clearly, this highlights the superiority of ALG4 which, despites its inter-field parallelism and unlike ALG3, is capable of delivering the same accuracy as the sequential algorithm ALG1.

Next, the relative speed of the focus partitioned solution procedures is assessed by comparing their CPU performance for a certain level of accuracy dictated by ALG0. It

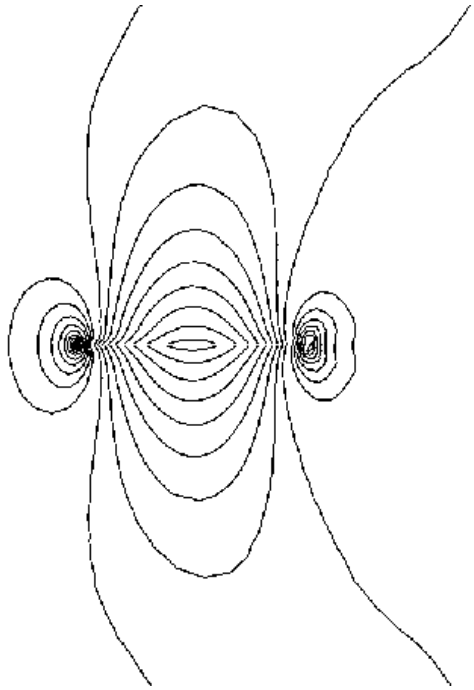

FIG. 4.18 – *Pressure isovalues of the steady-state flow solution*

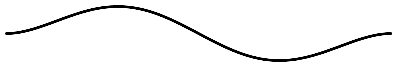

FIG. 4.19 – *Initial perturbation of the panel displacement field*

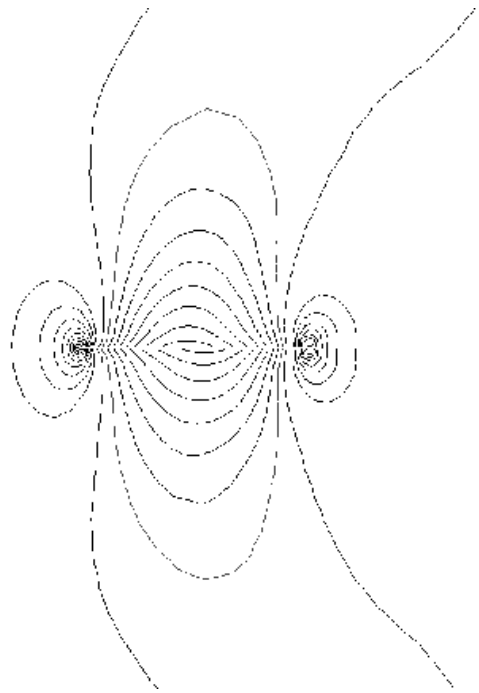

FIG. 4.20 – *Pressure isovalues at* $t = 8.75 \times 10^{-5}$

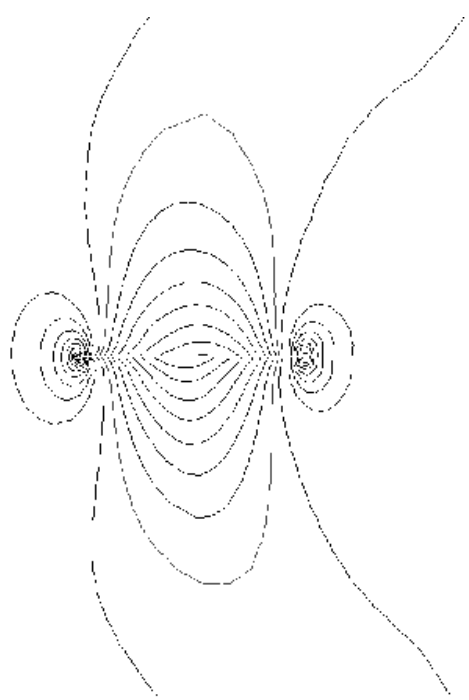

FIG. 4.21 – *Pressure isovalues at* $t = 1.25 \times 10^{-4}$

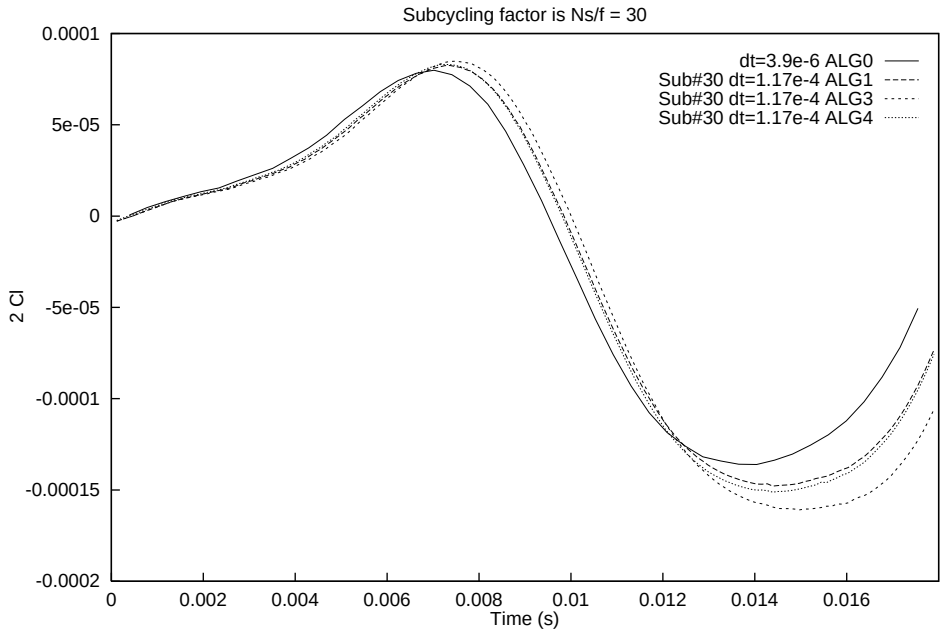

FIG. 4.22 – *Lift coefficient history for* $n_{S/F} = 30$ *(ALG1, ALG3, ALG4)*

turns out that in order to meet the accuracy requirements of ALG0, ALG1 and ALG4 can use a subcycling factor as large as $n_{S/F} = 10$, but ALG3 can subcycle only up to $n_{S/F} = 5$ (see Figure 4.23).

4.8 Closure

In this chapter, we have presented several partitioned procedures for time-integrating the transient coupled aeroelastic problem, and have discussed their merits in terms of accuracy, stability, heterogeneous computing, I/O transfers, subcycling, and parallel processing. All theoretical results have been derived for a one-dimensional piston model problem with a compressible flow, because the complete three-dimensional aeroelastic problem is difficult to analyze mathematically. However, the insight gained from the analysis of the coupled piston problem and the conclusions drawn from its numerical investigation have been confirmed with the numerical simulation of the two-dimensional transient aeroelastic response of a flexible panel in a transonic nonlinear Euler flow regime. In a future paper, we will extend these procedures to the three-dimensional case, and apply them to the solution of large-scale three-dimensional aeroelastic problems. In particular, we will focus on implementing the unconditionally stable implicit-implicit staggered procedure presented herein, and validating the developed aeroelastic simulation capability by comparing the computed results for test problems with experimental ones.

Acknowledgments

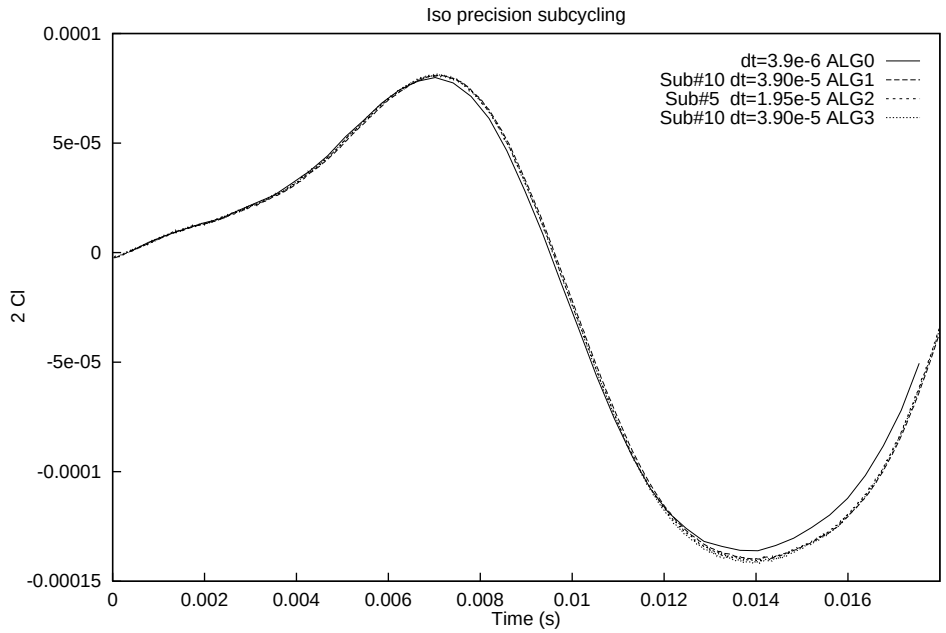

FIG. 4.23 – *Iso-precision on computed lifts (ALG0, ALG1, ALG3, ALG4)*

The second author acknowledges partial support by NASA Lewis Research Center under Grant NAG3-1273, partial support by the National Science Foundation under Grant ASC-9217394, and partial support by Dassault Aviation, Saint Cloud, France. The authors would like to thank Po-Shu Chen, Luis Crivelli, Stephane Lanteri, and Nathan Maman for the parallel implementations on the iPSC-860.

Troisième partie

Résultats

Dans cette dernière partie, nous nous tournons vers des problèmes de couplage fluide-structure plus réalistes. Ces problèmes aéroélastiques (où le fluide intervient donc à l'état gazeux) sont désormais non-linéaires. En fait, on se limitera à des structures linéaires dans l'hypothèse des petits déplacements pour des raisons de simplicité. Par contre, les équations d'Euler régissant l'écoulement ne sont plus linéarisées.

Pour chacun des problèmes modèles considérés, nous essaierons de disposer d'une solution exacte ou d'un élément de comparaison. Notre but est d'obtenir par une simulation numérique (si possible peu coûteuse) des résultats précis sur les caractéristiques globales du système, comme sa première fréquence et sa stabilité. Pour cela, nous allons étendre aux cas non-linéaires les méthodes et les conclusions tirées de l'analyse faite précédemment sur des problèmes modèles linéaires.

Malheureusement, l'extension théorique de ces méthodes s'est avérée trop difficile. C'est sur la base d'idées générales que ces méthodes ont été étendues.

Le passage à des configurations concrètes nécessite la résolution de quelques problèmes intermédiaires nouveaux.

D'une part, les théorèmes démontrés dans la partie précédente ne pourront pas s'appliquer, puisqu'ils concernent exclusivement des problèmes linéaires (pour la structure et le fluide, linéarisé autour d'un écoulement uniforme). Forts de notre expérience linéaire, nous essaierons d'étendre certains principe généraux aux cas plus complexes traités maintenant. Par exemple, l'utilisation d'intégrales temporelles de la pression plutôt que de valeurs courantes peut permettre d'augmenter la précision. Ou encore, l'influence du mouvement du bord du maillage à partir d'une prédiction de l'état de la structure sur le résultat de la simulation peut s'avérer déterminante.

D'autre part, nous devrons tôt ou tard sortir du cadre mono-dimensionnel. Le passage essentiel est celui qui nous conduira à des problémes en deux dimensions. En effet, les algorithmes de mouvements de maillage ne sont plus évidents. De plus, le lieu de l'interface n'est plus localisé en un seul point matériel, mais en une courbe ou une surface, qui doit elle-même être discrétisée. Enfin, le principe d'action et de réaction en tout point de l'interface ne peut être qu'approché, avec une précision qui dépend des choix d'interpolation ou d'extrapolation qui seront faits de part et d'autre de l'interface.

Dans le Chapitre 5, nous présentons deux problèmes modèles aéroélastiques à une dimension. L'un est la version non linéarisée du problème du piston du Chapitre 3, et l'autre en est une variante. Nous étudions la stabilité de méthodes d'intégration temporelle décalée pour ces problèmes couplés. Ces méthodes sont inspirées des méthodes de résolution déjà introduites pour les problèmes couplés linéaires. Comme précédemment, leur modularité permet l'emploi de schémas décentrés explicites (éventuellement sous-cyclés) pour le fluide et implicites pour la structure dont les stabilités découplées sont connues. La stabilité du schéma couplé est cependant inconnue. En effet, une analyse linéaire de stabilité de ces algorithmes se révèle bien plus complexe que pour les cas vus à la partie précédente. Comme l'ensemble du maillage fluide est maintenant

susceptible de bouger, il s'agirait alors d'une étude de stabilité à trois champs (fluide, maillage du fluide et structure). De plus, par souci de généralité, on ne se limite plus à des écoulements uniformes. Nous présentons d'abord la méthode avec interface simple. Nous montrons que cette méthode très populaire viole le principe d'action et de réaction à l'interface fluide-structure. Ce défaut est corrigé dans la nouvelle méthode avec interface double. Nous montrons que cette dernière est plus souple et plus stable. Pour finir, l'extension de cette nouvelle méthode à des cas multi-dimensionnels est envisagée.

Dans le Chapitre 6, cette extension est réalisée. D'abord, nous considérons un écoulement non visqueux autour d'un profile d'aile en mouvement rigide. Nous présentons un schéma général de couplage. Des méthodes classiques sont employées pour chaque champ et nous proposons des extensions de procédures de couplage utilisèes pour des problèmes mono-dimensionnels. Nous présentons et évaluons des améliorations possibles de l'algorithme de couplage, notamment en ce qui concerne la précision et la stabilité du sous-cyclage. Ces améliorations sont ensuite testées sur des problèmes avec de très grands nombres de degrés de liberté. Finalement, nous décrivons en détail un algorithme de couplage "optimal".

Chapitre 5

Staggered time-integration methods for a one-dimensional Euler aeroelastic problem

Ce chapitre est paru sous la forme d'un rapport de recherche CERMICS (N° 94-33)

5.1 Introduction

We present in this chapter some numerical methods that have been constructed for the numerical simulation of fluid-structure interactions. This class of coupled problems and some classical methods used for their simulations have been reviewed in [61]. Shortly, numerical methods used for the simulation of aeroelastic problems should have the following qualities: accuracy, efficiency and modularity. The accuracy of the methods used allows the interpretation of numerical results, where numerical errors (numerical damping and diffusion, dispersion) were added to the exact solution. For example, the Euler flutter analysis of an airfoil [66] can be done if the numerical diffusion does not make flutter disappear. Efficiency allows accurate computations with limited costs. In some cases, the characteristic times of the fluid part and the structural part of the coupled system are very different. Their time-integrations might require very different time steps. Efficiency can be enhanced with the use of subcycling [63]. Finally, by the use of staggered schemes [60], modularity is achieved. Most popular existing modules for the separate resolutions of fluid and structural parts can be coupled. Each part can be dealt with separately, and even computed on separate heterogeneous machines [63]. As a consequence, some particular coupling methods are required.

The aim of this chapter is to present some numerical methods constructed for the numerical simulation of a one-dimensional Euler aeroelastic model problem. Alhough the problem is very simple, we intend to only consider methods that could be extended to multi-dimensional, complex cases. We use in this chapter the insights gained from the study in Chapter 3 on the linearization of the same model problem, and some proved stability results of Chapter 4 on numerical methods used for the simulation of linear aeroelastic problems. Since the problem considered is not linear, the main results of Chapter 4 cannot be used. However, some similar considerations on energy and momentum conservations will allow us to build some staggered schemes with similar properties. We will only consider explicit schemes for the fluid part of the problem, since no implicit procedure was at our disposal.

The content of this chapter is as follows. In Section 5.2, we present the aeroelastic problems considered. These two very similar problems are one-dimensional. The structure is linear with a single degree of freedom. The fluid satisfies one-dimensional Euler equations (perfect fluid). They differ by some boundary conditions for the fluid. These problems were chosen because they are simple, and have the same characteristics as some other aeroelastic problems: the piston problem is mainly internal and acoustic, while the box problem is rather external (close to the flutter case analyzed in [25, 66]).

In Section 5.3, we present the global algorithm. We use staggered schemes, which allow modularity. We then have to present the set of numerical methods used separately in the fluid part (finite volume method, Van Leer flux splitting) and the structural (generalized-α method) part of the problem. We also present the methodology for the coupling of the previous methods, and the necessity of subcycling.

In Sections 5.4, we show and analyze volume-continuous methods, which is currently used in most industrial codes. Both fluid and structural mesh boundaries are matching (at least the continuous interfaces are matching before separate spatial dis-

cretizations). We explain why this kind of method does not respect the action/reaction principle (and the conservation of the momentum), which might be the cause of its poor subcycling stability properties.

In Section 5.5, we present volume-discontinuous methods. The boundaries of the fluid and structural meshes are different. We show that this method can allow the conservation of the momentum. The flexibility of the method is used with multiple prediction algorithms, in order to enhance the stability and the accuracy of the method.

Finally, we discuss in Section 5.6 the use of more complex time-interpolation schemes, and the possibilities of extension to multi-dimensional cases.

5.2 The model problems

In this section, we set the physical problems which will be studied in this chapter. These two problems were needed because of their different relations with well-known aeroelastic test-cases. In the following, we first present the model problems. Then we set the corresponding mathematical problems. Finally, we explain our choice, based on eigenfrequencies considerations and similarities with cases of external flows and flows with strong compressibility effects.

5.2.1 The two one-dimensional problems

In this chapter, we consider two one-dimensional problems which are quite close indeed. The first one, which will be called the "piston" problem, is shown on Figure 5.1. A perfect gas flow is contained in a chamber closed by a moving piston. The other end of the chamber is fixed. The structural part of this problem - the piston - closes the fluid domain, which produces the fluid-structure interaction. The problem will be set in more details in the following.

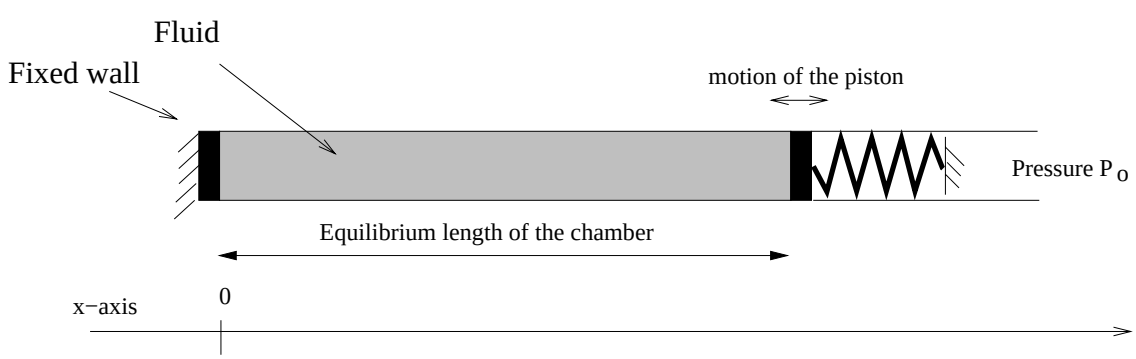

FIG. 5.1 – *The "piston" problem (fluid-filled one-dimensional flexible chamber with one moving end)*

The second problem we shall consider is shown on Figure 5.2. In the "box" problem, both ends of the chamber are moving. However, the length of the box remains constant (both ends speeds are equal). Again, there is an interaction between the fluid and the box - the structural part of the problem - because the box contains the fluid, which reciprocally exerts a pressure force at both ends.

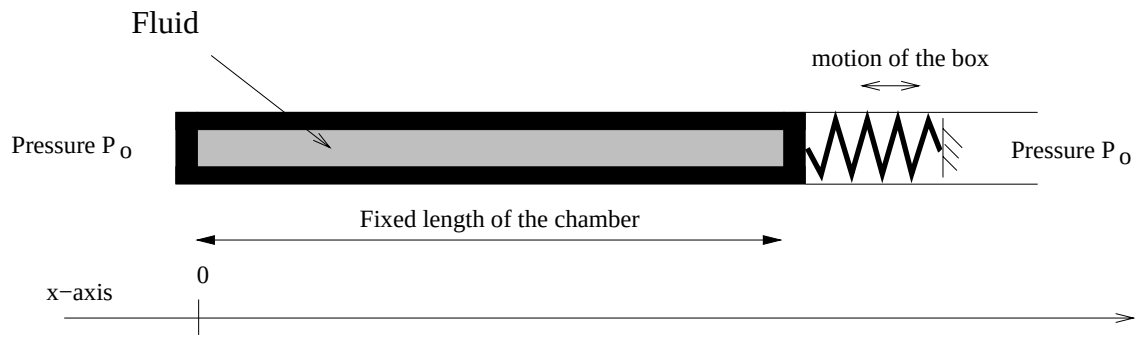

FIG. 5.2 – *The "box" problem (rigid fluid-filled one-dimensional moving box)*

In both problems, we assume no point of the flow is transonic and structural speeds are small compared to the average fluid sound speed. We shall denote by X the displacement of the right end of the chamber. We shall write x_L and x_R for the abscissae of the left and right ends. The origin of the X-axis is set at the left end of the chamber at equilibrium. The equilibrium length of the chamber for the piston problem is set to L, which also is the fixed length of the box in the box problem. We have $x_R = L + X$ and $x_L = 0$ (resp. $x_L = X$) for the piston (resp. box) problem. We assume the one-dimensional flow inside the chamber is governed by the compressible Euler equations and that the external pressure is constant and equal to P_0. In both cases, we shall refer to the equilibrium state of the system as the state where:

1. the flow is uniform, with no velocity and the pressure is equal to P_0,

2. the right end has no speed, and is at the equilibrium position.

These problems have different characteristics. In the piston problem, the length of the chamber is variable. Then strong compressibility effects occur. The behaviour of the flow is close to a very rigid spring. As a matter of fact, this case is not far from an internal fluid-structure interaction problem. Paradoxally, the problem of the box is close to an external flow case. The fluid is not globally compressed since the length of the box is fixed. The fluid is just displaced, like the flow around an airfoil in subsonic flight. These aspects will be verified by the determination of first acoustic coupled eigenfrequencies.

5.2.2 Equations and boundary conditions

Mathematically, the problem is the following:

– Euler equations for the fluid in the domain $[x_L; x_R]$

$$\begin{cases} \rho_t + (\rho u)_x = 0 \ , \\ (\rho u)_t + (\rho u^2 + P)_x = 0 \ , \\ E_t + [u(E+P)]_x = 0 \ . \end{cases} \tag{5.1}$$

Here, ρ is the density, u is the velocity, P is the pressure and E is the total energy per unit volume. The fluid is assumed to be perfect and the pressure is given by

$$P = (\gamma - 1)(E - \frac{1}{2}\rho u^2) \tag{5.2}$$

where γ is set to 1.4.

– boundary conditions for the fluid are the following:

$$\left| \begin{array}{lcl} u(x_L) & = & \dot{x_L} \\ u(x_R) & = & \dot{x_R} \end{array} \right. \tag{5.3}$$

where dotted variables stand for corresponding time derivatives. They reduce to

$$\begin{array}{ll} \text{Piston problem:} & \left\{ \begin{array}{rcl} u(0) & = & 0 \\ u(L+X) & = & \dot{X} \end{array} \right. \\ \text{Box problem:} & \left\{ \begin{array}{rcl} u(X) & = & \dot{X} \\ u(L+X) & = & \dot{X} \end{array} \right. \end{array} \tag{5.4}$$

– the motion of the structure is given by

$$m\ddot{X} + d\dot{X} + kX = F \tag{5.5}$$

where m, d and k are respectively the mass, the internal damping and the stiffness of the structure. The external force F is given by

$$\begin{array}{rcccl} \text{piston problem:} & F & = & P(x_R) - P_0 & = & P(L+X) - P_0 \\ \text{box problem:} & F & = & P(x_R) - P(x_L) & = & P(L+X) - P(X) \end{array} \tag{5.6}$$

5.2.3 Coupled eigenfrequencies

We are interested in the numerical simulation of the two problems we just set. In both cases, the unique source of energy dissipation is the damping in the structural part. Then, we control the damping of the coupled system. For example, if we choose $d = 0$, we know that some global energy is conserved. Like aircraft designers, we would like to know the discrepancies between numerical simulations and physical experiments in the stability simulated for the coupled system. In our cases, we shall just have to test if our numerical results are rather stable or unstable, and to know what damping or amplification rates are numerically produced. We shall also be interested in phase errors, and we need an estimation of the coupled frequencies of our problem.

In this chapter, we shall only consider small perturbations of the equilibrium states defined previously. Thus we intend to perform a linear stability analysis around these equilibrium states. We shall use linearizations of our equations around these equilibrium states to obtain coupled eigenfrequencies of the problems. However, we shall solve non-linearized problems with classical non-linear methods.

The linear stability analysis around equilibrium states can be found in details in [64]. We give here a sketch of main parts of these analyses.

In the following, ρ_0 is the uniform density at equilibrium and c is the sound speed (given by $\gamma P_0 = \rho_0 c^2$). We add a perturbation to all variables: a density perturbation $\delta\rho$ ($\delta\rho \ll \rho_0$), a velocity perturbation δu ($\delta u \ll c$). The pressure perturbation is given by

$$\delta P = c^2 \delta\rho \ , \tag{5.7}$$

which is derived from the isentropic hypothesis we make. Finally, the energy perturbation can be derived from the other perturbations. More, the linearization of the energy conservation equation (third Euler equation) reduces to an equation which is always verified (when the linearized forms of mass and momentum conservation equations are verified). Then, we get rid of this equation under the isentropic hypothesis.

Using the notation $W = (\delta\rho, \quad \rho_0 \delta u)^t$, both problems reduce to the following:

– acoustic fluid equations written

$$W_t + \begin{pmatrix} 0 & 1 \\ c^2 & 0 \end{pmatrix} W_x = 0, \text{ on } [0; L] \text{ for both problems,} \tag{5.8}$$

– with boundary conditions given by

$$\begin{aligned} \text{piston problem:} \quad & \delta u(0) = 0 \text{ and } \delta u(L) = \dot{X} \\ \text{box problem:} \quad & \delta u(0) = \delta u(L) = \dot{X} \end{aligned} \tag{5.9}$$

– a structural equation which writes

$$\begin{aligned} \text{piston problem:} \quad & m\ddot{X} + d\dot{X} + kX = c^2 \delta\rho(L) \\ \text{box problem:} \quad & m\ddot{X} + d\dot{X} + kX = c^2(\delta\rho(L) - \delta\rho(0)) \end{aligned} \tag{5.10}$$

The reader should notice that both linearized problems are set on $[0; L]$. Since W itself is a perturbation, the preceding approximation produces an error of the second order.

We now have to find the different modes of each linear problem. In the following, we shall limit our investigations to the cases where $d = 0$. When $d > 0$, the system is naturally damped. When $d < 0$, the system is naturally undamped and unstable. The importance of the case where $d = 0$ should be emphasized. In that case, the physical system is just stable. Thus, the numerical qualities of the simulation are directly related to numerical properties of the integration methods, particularly in terms of stability.

We first consider the piston problem. A solution of (5.8) with the "left" boundary condition $\delta u(0) = 0$ is given by

$$W = \begin{pmatrix} 1 \\ +c \end{pmatrix} \cos[\omega(t - \frac{x}{c})] + \begin{pmatrix} 1 \\ -c \end{pmatrix} \cos[\omega(t + \frac{x}{c})] \quad (\text{with } \omega \in I\!R). \tag{5.11}$$

If we assume a coupled mode of the preceding form exists, then for this mode we have:

$$\dot{X} = \delta u(L) = \frac{2c}{\rho_0} \sin(\frac{\omega L}{c}) \sin(\omega t) \quad \text{which gives} \tag{5.12}$$

$$\ddot{X} = \frac{2c\omega}{\rho_0} \sin(\frac{\omega L}{c}) \cos(\omega t) = -\omega^2 X \tag{5.13}$$

On the other hand, the density perturbation at the right moving end of the piston is given by

$$\delta\rho(L) = 2\cos(\frac{\omega L}{c}) \cos(\omega t). \tag{5.14}$$

Finally, the structural equation (5.10) for the piston is verified (with $d = 0$) if and only if the following relation is true:

$$\boxed{\text{Piston problem:} \quad \left(\frac{\omega L}{c}\right) \tan\left(\frac{\omega L}{c}\right) \left(1 - \frac{k}{m\omega^2}\right) = \frac{\rho_0 L}{m}.} \tag{5.15}$$

This formula deserves several comments. We see that when the piston is given an infinite mass (i.e. is fixed), we find an infinity of purely acoustic modes in the fluid part of the piston problem. We also see that if the piston is given a fixed structural eigenfrequency, and if its mass is big enough compared to $\rho_0 L$, the coupled eigenfrequencies get closer to this structural eigenfrequency. Finally, we can notice that the structure is not slowed by the fluid and the system undergoes oscillations which are rather acoustic (we assume that the structural pulsation $\omega_s = \sqrt{k/m}$ is smaller than the lowest purely acoustic pulsation).

We now consider the box problem. A solution of (5.8) with the boundary condition for the moving box $\delta u(0) = \delta u(L)$ is given by

$$W = \begin{pmatrix} 1 \\ +c \end{pmatrix} \cos[\omega(t - \frac{x - L}{c})] - \begin{pmatrix} 1 \\ -c \end{pmatrix} \cos[\omega(t + \frac{x}{c})] \quad (\text{with } \omega \in I\!R). \tag{5.16}$$

We assume again a coupled mode of the preceding form exists. We then have:

$$\dot{X} = \delta u(0) = \delta u(L) = \frac{c}{\rho_0}\left(\cos(\omega t) + \cos[\omega(t + \frac{L}{c})]\right) \quad \text{which gives} \tag{5.17}$$

$$\ddot{X} = -\frac{\omega c}{\rho_0}\left(\sin(\omega t) + \sin[\omega(t + \frac{L}{c})]\right) = -\omega^2 X \tag{5.18}$$

On the other hand, the density perturbations at the ends of the box are given by

$$\delta\rho(0) = \cos[\omega(t + \frac{L}{c})] - \cos(\omega t) = -\delta\rho(L) \tag{5.19}$$

Finally, after some short algebraic transformations, we find the structural equation (5.10) for the box problem is verified (with $d = 0$) if and only if the following relation is true:

$$\boxed{\text{Box problem: } \frac{\rho_0 L}{m}\tan\left(\frac{\omega L}{2c}\right) = \left(\frac{\omega L}{2c}\right)\left(\frac{k}{m\omega^2} - 1\right)} \tag{5.20}$$

We should compare this formula to the preceding one. When the box is given an infinite mass, we find an infinity of purely acoustic modes (and their pulsation are doubled, because both ends are now moving). As for the piston case, the coupled eigenfrequency gets close to the structural eigenfrequency if the latter is fixed and the mass of the box tends to infinity. Finally, we notice that, contrary to the piston case, the structure is rather slowed by the fluid and the system undergoes slow oscillations (under the assumption that ω_s is smaller than the lowest purely acoustic pulsation).

5.2.4 Data sets for test cases

In this section, we want to define a set of test cases for both problems. For a test case, the geometry is set with the equilibrium length of the piston/box L; the fluid equilibrium state definition requires the sound speed c and the density ρ_0; the structure is defined by giving the mass m and the stiffness k (and possibly the damping d if it is not taken equal to zero). However, we can derive from a dimensional analysis that, out of these five data, only two induce independant variations of the aspect of the test case. In the following, we shall set $L = 1$m, $\rho_0 = 1.3$kg/m and $c = 330$m/s (this value was deduced from the equation $\rho_0 c^2 = \gamma P_0$ with $\gamma = 1.4$ and $P_0 = 1$atm). A variation of these parameters would be considered as a change in unities of time, length and mass. Test cases will be characterized by the two paramaters m and ω_s (derived from k by $m\omega_s^2 = k$).

In the chapter, we consider the following test cases:

- **case 1**: $m = 0.8$kg and $\omega_s = 100$ s^{-1}
- **case 2**: $m = 2.1$kg and $\omega_s = 100$ s^{-1}
- **case 3**: $m = 40$kg and $\omega_s = 30$ s^{-1}

Cases 1 and 2 are not far from data found in classical aeroelastic problems for a two-dimensional two-degree of freedom NACA airfoil (see [25, 66]). The structure has a mass of the same order of magnitude as the fluid mass involved in the system. The structural pulsation ω_s is rather small compared to the lowest purely acoustic pulsation (which is given by $\pi c/L \simeq 1038$ s^{-1} for the piston problem). Case 3 is of a different type: the mass of the structure is very important, and the structural pulsation is rather small. The system is strongly influenced by the structure and rather weakly coupled. We should obtain greater performances of our numerical methods for time-integration.

5.3 Numerical methods

The numerical simulation of an aeroelastic problem is two-fold: it requires at least the simulations of the fluid dynamics and the structural mechanics and the use of numerical methods in both domains. On the one hand, the structure is generally discretized using a classical finite element method. However, in our problems, the structure has only one degree of freedom (which is the displacement X) as if it was reduced to a material point. This moving structure must be integrated in time. We shall present in the following a well-known family of time-integration methods used for the structure.

On the other hand, the fluid is enclosed in the moving/flexible box. The fluid domain, which will be discretized, is also moving along with the piston or the box. Then, the numerical simulation requires the use of moving grids (at least at fluid domain boundaries). As a consequence, we shall have to produce methods for moving the grid (these methods are rather straightforward for one-dimensional problems). We also have to consider ALE formulations of Euler equations, i.e. formulations with imbedded non physical spatial coordinates. We shall have to use numerical methods for the resolution in time and space of these formulations.

Finally, we present in this section the specific numerical methods used for the coupled integration in time and space of the coupled fluid-structure interaction problem. Actually, the simulation of this coupled aeroelastic problem is not strictly reduced to the integration of structural mechanics and fluid dynamics in a moving domain. The coupling has to be simulated. We shall see it can not be simulated in a totally coupled way, because of the use of implicit schemes, at least for the structure. We shall then introduce staggered schemes, and finally subcycling methods when the stability limits on the time step for the fluid and the structure are very different.

5.3.1 Numerical methods used for the structure

In both the piston and the box problems, which are one-dimensional, the structure has only one degree of freedom. Then, no discretization problem appears. However, a classical **finite element** discretization could be used for more complex structures [61, 45]. Throughout this section, we assume the equation for the structure as presented in (5.5) holds. In the following, we shall present numerical methods that are also

convenient when m, d and k are real symmetric matrices, m and k being definite positive, and d simply positive.

We present here rapidly a general family of methods for the time-integration of structural dynamics: the **generalized-α method** [15]. We suppose the applied force F is known during the integration of the structure. The generalized-α method depends on four coefficients: β and γ (which keep the same role as in Newmark methods [44, 39]), and α_f and α_m (time-shifting coefficients). Superscripts will be reserved for time step ordinals. For any quantity z, for any given parameter θ ($\theta \in I\!R, 0 < \theta < 1$), and for any time step ordinal n, we use the notation

$$z^{n+\theta} \equiv (1-\theta)z^n + \theta z^{n+1}.$$

The generalized-α method can be described as follows:

- assume at time t_n, $X(t_n) \equiv d^n$, $\dot{X}(t_n) \equiv v^n$ and $\ddot{X}(t_n) \equiv a^n$ are known
- assume d^{n+1} and v^{n+1} are given by the following expressions, depending on the unknown quantity a^{n+1} (through $a^{n+2\beta}$ and $a^{n+\gamma}$):

$$d^{n+1} = d^n + \Delta t v^n + \frac{\Delta t^2}{2} a^{n+2\beta} \tag{5.21}$$

$$v^{n+1} = v^n + \Delta t a^{n+\gamma} \tag{5.22}$$

- using the preceding assumptions, find a^{n+1} solution of the structural dynamics equation:

$$m a^{n+1-\alpha_m} + d v^{n+1-\alpha_f} + k x^{n+1-\alpha_f} = F^{n+1-\alpha_f} \tag{5.23}$$

- using (5.21-5.22), compute the next time step computational values d^{n+1} and v^{n+1} and set $X(t_{n+1}) = d^{n+1}$, $\dot{X}(t_{n+1}) = v^{n+1}$ and $\ddot{X}(t_{n+1}) = a^{n+1}$

The family of generalized-α methods contains the Newmark methods (with $\alpha_m = \alpha_f = 0$), the HHT-α methods ($\alpha_m = 0$) [36] and the WBZ-α methods ($\alpha_f = 0$) [76]. The accuracy, the stability, the high-frequency and low-frequency dissipations of the method depends on the parameters β, γ, α_m and α_f.

It can be shown [15] that the method is second-order accurate when $\gamma = 1/2 + \alpha_f - \alpha_m$. The method is unconditionally stable, provided $\alpha_m \leq \alpha_f \leq 1/2$ and $2\beta \geq 1/2 + \alpha_f - \alpha_m$. Finally, Chung and Hulbert describe an optimal choice of parameters for this method, which is unconditionally stable, second-order accurate, and has an optimal combination of high-frequency and low-frequency dissipations. As functions of the user-specified spectral radius in the high-frequency limit ρ_∞, the parameters are:

$$\alpha_m = \frac{2\rho_\infty - 1}{\rho_\infty + 1},\ \alpha_f = \frac{\rho_\infty}{\rho_\infty + 1},\ \gamma = 1/2 + \alpha_f - \alpha_m,\ \beta = \frac{1}{4}(1 + \alpha_f - \alpha_m)^2 \tag{5.24}$$

In this chapter, we shall use this method with different values of $\rho_\infty \in [0, 1]$. We shall also use the classical trapezoidal rule defined by $\gamma = 1/2$, $\beta = 1/4$ and $\alpha_m = \alpha_f = 0$. We would like to put the emphasis on a particular point for more complex simulations: if you consider a linear structure, and you use only linear schemes,

like the trapezoidal rule or the generalized-α method, the time integration of the structure requires the solution of a linear system for each time step. If the structural time step remains fixed during the simulation, all matrices involved remain constant and can be factorized once and for all. This advantage should be conserved when the time-integration of the fluid part in the staggered methodology is performed simultaneously.

5.3.2 Numerical methods used for the fluid

In this section, we deal with the fluid part of the simulation. The influence of the structure on the fluid flow is the result of a two-fold boundary condition. From a physical point of view, the structural boundary of the fluid domain matches exactly the boundary of the structure, and the fluid normal velocity at the fluid-structure interface is equal to the interface normal speed. As a consequence, we shall present in this section numerical methods which can be used for the simulation of fluid dynamics in a moving domain.

The fluid domain is no longer considered as fixed. The spatial discretization will also be moving, at least at the boundaries. Some numerical experiments have been made and presented in previous chapters, on "transpiration" methods, where the grid is fixed everywhere, the fluid-structure interface included, and where transpiration terms were added to compensate for the violation of the matching condition of both fluid and structure interfaces [64]. These methods are efficient for linearized cases, and are of possibly lower interest for non-small displacement. However, they would give good numerical estimates for the coupled linear eigenfrequencies of the physical system.

In this chapter, we shall consider numerical methods with moving fluid grids. The use of this kind of methods is rather simple and general. They are known as Arbitrary Lagrangian-Eulerian formulations. Although they have a general form [20], they can be applied on Euler equations [61]. The latter take the following integral form:

$$\boxed{\frac{d}{dt}\left[\int_{C_x} W\,dx\right] + \int_{C_x} div_x \bar{F}\,dx = 0.} \tag{5.25}$$

where x is the spatial physical position of a point, C_x is the geometric cell of integration. The boundaries of this cell are assumed to move with the mesh local speed w (depending on x). W is the vector of conservative variables $(\rho, \rho u, E)^t$ and $\bar{F}$ is the ALE-modified flux vector given by:

$$\bar{F} = \begin{pmatrix} \rho\bar{u} & \\ \rho u\bar{u} & +P \\ E\bar{u} & +Pu \end{pmatrix} \quad \text{and} \quad \bar{u} = u - w. \tag{5.26}$$

From (5.25), the deduction of a **finite volume explicite scheme** is straightforward. The numerical method will be written:

$$A_i^{n+1}W_i^{n+1} - A_i^n W_i^n + \Delta t\left(\bar{\Phi}(W_i^n, W_{i+1}^n) - \bar{\Phi}(W_{i-1}^n, W_i^n)\right) = 0, \tag{5.27}$$

where C_i^n is the ith cell at time t^n (and $C_i^n = [x_{i-1/2}^n, x_{i+1/2}^n]$), W_i^n is the average of W on cell C_i^n at time t_n, A_i^n is the area of cell C_i^n at time t_n, Δt is the time step (such that $t^{n+1} = t^n + \Delta t$), and $\bar{\Phi}$ is a numerical flux such that

$$\Delta t \bar{\Phi}(W_i^n, W_{i+1}^n) \simeq \int_{t^n}^{t^n+\Delta t} \bar{F}(x_{i+1/2}^n) d\tau \tag{5.28}$$

The evolution of A_i^n with time is given by:

$$A_i^{n+1} - A_i^n + \Delta t \left(-w_{i+1/2}^n + w_{i-1/2}^n \right) = 0, \tag{5.29}$$

Since the grid points are updated according to

$$x_{i+1/2}^{n+1} = x_{i+1/2}^n + \Delta t w_{i+1/2}^n, \tag{5.30}$$

(5.29) is equivalent to

$$A_i^n = x_{i+1/2}^n - x_{i-1/2}^n, \forall i, \forall n \tag{5.31}$$

The complete method will not be fully described till we give our choice for the numerical flux $\bar{\Phi}$ in (5.27). Throughout this chapter, the time integral of (5.28) is approximated using the **flux-vector splitting of Van Leer** [74]. The approximation is only taken as **first-order** accurate for several reasons: it is quite simpler (though spatial second-order accuracy can be achieved with Van Leer fluxes [6] or with the flux-difference splitting of Roe in dynamic meshes [57]), and it allows the use of much lighter first-order time-integration schemes without stability problems. We could also argue that the main goal of the present chapter is the investigation of the coupling simulation, which still is complex, even when it is done with simple uncoupled methods.

This splitting takes the following form on dynamic meshes [6, 3]:

$$\bar{\Phi}(W_i^n, W_{i+1}^n) = \bar{\Phi}^+(W_i^n) + \bar{\Phi}^-(W_{i+1}^n) \tag{5.32}$$

with

$$\bar{\Phi}^{\pm}(W_i^n) = \pm \frac{\rho}{4c}(\bar{u} \pm c)^2 \begin{pmatrix} 1 \\ \dfrac{\pm 2c - \bar{u}}{\gamma} + u \\ \dfrac{-\bar{u}^2 \pm 2\bar{u}c}{\gamma+1} + \dfrac{2c^2}{\gamma^2-1} + \dfrac{u^2}{2} - \dfrac{w(\bar{u} \mp 2c)}{\gamma} \end{pmatrix} \tag{5.33}$$

where we have taken

$$\left| \begin{array}{lcl} \rho & = & \rho_i^n \\ c^2 & = & \frac{\gamma P_i^n}{\rho_i^n} \end{array} \right. \quad \left| \begin{array}{lcl} u & = & u_i^n \\ w & = & w_{i\pm 1/2}^n \end{array} \right. \quad \left| \begin{array}{lcl} \bar{u} & = & u - w \end{array} \right. \tag{5.34}$$

The preceding expressions for the extended Van Leer flux-vector splitting are always valid under the condition $|\bar{u}| < c$ (we limit this study to subsonic cases).

We now describe the treatment of boundary conditions (5.4). For both ends of the chamber, the boundary condition is enforced in the following weak sense: the left end boundary flux is taken equal to $(0, \quad P_1, \quad P_1 w_1)^t$ (we recall 1 is the index of the first left cell in the fluid). As well, the right end boundary flux is given by $(0, \quad P_N, \quad P_N w_N)^t$ (we assume we have N cells in the fluid).

Finally, we must put the emphasis on a peculiar point. We do have a choice on the motion of the mesh. The grid velocity at the fluid-structure interface should be set equal to the structural velocity. However, we can choose any mesh motion consistent with this condition. In general, the mesh can be considered as a third field for the fluid-structure interaction simulation. It can be given any artificial mass and damping matrices, and integrated like a structure [48]. For instance, Batina [5] proposed a method for the smooth motion of the fluid mesh around a deforming airfoil, which was based on a spring model. This method was compared to a simple change of frame of reference in the case of a rigid motion of the structure [45] and gives good results efficiently.

Thoughout the whole chapter, we choose to move the fluid mesh in order to have a uniform cell size at any time. For the box problem, all points are given the same speed (and cells keep the same contant size). Though the box is rigid in that case, we keep the dynamic mesh formulation. Assuming we have N points in the mesh, the mesh motion is given by

$$\forall i, \quad 1 \leq i \leq N, \quad x_i^n = \frac{i-1}{N-1} L + X^n \quad \text{and} \quad w_i^n = \dot{X}^n. \tag{5.35}$$

For the piston problem, all grid speeds vary in proportion with the distance from the fixed left end of the chamber:

$$\forall i, \quad 1 \leq i \leq N, \quad x_i^n = \frac{i-1}{N-1}(L + X^n) \quad \text{and} \quad w_i^n = \frac{i-1}{N-1}\dot{X}^n. \tag{5.36}$$

5.3.3 Coupling numerical methods and subcycling

In this section, we deal with numerical methods which are needed for the simulation of coupled fluid and structural fields. We presented in the two previous sections methods for the simulation of structural dynamics and fluid dynamics on a moving domain, which are not coupled systems. The goal of this section is two-fold: introduce methods directly needed by the coupling phenomenon, and couple both sets of uncoupled methods presented earlier. We also need to consider subcycling.

Coupling numerical methods

We only consider staggered strategies. They consist in the successive decoupled integrations of the structure and the fluid. Each field is frozen during the time integration of the other field. This kind of strategy has many advantages. First, the use of existing schemes, programs and procedures for both separate fields is made possible. It allows

also to imagine intra-field and inter-field parallel implementation of the schemes [63]. Second, the use of implicit schemes in a totally coupled time integration scheme would induce a terrible computational cost, because the grid position and velocity would be a numerical variable as well. On the other hand, this kind of staggered scheme may not be stable, even if both the schemes used for separate fields are used far under stability limits. However, the investigation of staggered schemes for one-dimensional linear model problems has recently produced some results [63].

The basic line of a first family of staggered algorithms could be sketched as follows:

1. assume you dispose of all computational values after the nth time step. They are the structural displacements, speeds and possibly accelerations on all discretization points (or elements), but also the locations and speeds of all fluid grid points, and, of course, the field of conservative variables vector W in the whole fluid mesh. We shall denote respectively these computational values by S^n (all structural informations), M^n (for the fluid mesh) and F^n for the fluid field.

2. compute the distribution of forces and moments exerted by the fluid pressure on the structure (through the fluid-structure interface)

3. assume it is constant during the next time step and compute the state of the structure after the next time step (getting S^{n+1}).

4. compute a possible fluid grid after the current time-step. The future grid M^{n+1} must satisfy the condition that both fluid and structural boudaries are matching along the interface at time t^{n+1}.

5. compute the average speeds of each fluid grid point during the current time step.

6. use this speed field for the time-integration of the fluid, and get F^{n+1}.

This methodology is the most popular. It is volume-continuous in the following sense: even though the fluid and the structure may be discretized in different ways, both continuous boundaries (boundaries before discretization) are spatially matching; near the interface, the whole volume is occupied either by the fluid or by the structure. This kind of methods will be referred to as volume-continuous methods.

For these methods, all steps seem clear and natural. However, we shall see in the next section that important momentum and energy violations are induced, limiting the stability of the global algorithm. The preceding algorithm can be understood as "integrate the structure and then the fluid, and do it again..." But the symmetrical algorithm "integrate the fluid and then the structure, and so on..." is also possible (the reader should note that the following second methodology differs from the first one by more than an index change !):

1. assume you dispose of all computational values after the nth time step S^n, M^n ans W^n.

2. make a prediction for the global state of the structure at time t^{n+1}. This prediction could be made with an actual integration of the structure under a constant pressure equal to P^n. However, it could be done simply with a first-order explicit linear predictor.

3. compute a possible mesh M^{n+1} at time t^{n+1}, the interface of this mesh must be matching the predicted location for the fluid-structure interface at time t^{n+1}.

4. compute the average speeds of all fluid grid points during the current time-step.

5. perform the time-integration of the fluid part of the problem with these mesh speeds (getting F^{n+1}).

6. compute a good approximation of the time integral of the pressure forces and moments around the structure during the current time-step.

7. perform the time-integration of the structure and get S^{n+1}.

The most significative difference between both methodologies is the matching condition on the fluid-structure interface. In the second method, there is no matching requirement for the fluid and the structural boundaries after each time-step. With no consideration of spatial discretizations of the fluid and the structure near their interface, we do not assume that both continuous boundaries are matching any more. We have relaxed the matching hypothesis on the continuous boundaries. This kind of methods will be referred to as volume-discontinuous methods.

Note that the difference between methodologies could be also interpreted in the following way. In continuous methods, the information received by the fluid from the structure is exact (in the sense it is the correct location of the structure at a certain date) but late. On the contrary, in discontinuous methods, this information is only predicted, but at the right time.

The second methodology seems to allow strong numerical errors at the interface. However, if the prediction of the next location of the structure is accurate, the matching of the interfaces will be achieved with a possibly satisfying accuracy. On the one hand, the matching condition is relaxed, and satisfied with a limited accuracy. On the other hand, the time-integration of the structure might be done with more accuracy, because the fluid pressure distribution at the end of the current time-step (at time t^{n+1}) is already known. Advantages and drawbacks of these two methodologies will be further discussed in the following section. We should put the emphasis on the fact that the volume conservation for the fluid will be written on the fluid volume only, so that we can keep the conservation properties of our schemes.

Subcycling

Finally, we introduce here the principle of subcycling. The time integration of the structure will be done with the generalized-α method or the classical trapezoidal rule (Newmark method with $\gamma = 1/2$ and $\beta = 1/4$) which are both unconditionally stable.

However, if the lowest coupled pulsation of the system ω_C can be estimated thanks to (5.15) and (5.20), the use of a time-step greater than $1/\omega_C$ will produce very inaccurate results. The limit $\Delta t_C^{lim} = 1/\omega_C$ corresponds to six points per oscillations, which gives a rather poor representation of a sinusoidal curve. The same is true for the structure alone. No structural time-step should be taken smaller than $\Delta t_S^{lim} = 1/\omega_s$. Also, since we shall use a simple forward-Euler first-order scheme for the time-integration of the fluid, the time step Δt_F will be limited by a CFL-like condition [45]:

$$\Delta t_F^{lim} = \min_i \frac{\Delta x_i^n}{|\bar{u}_i^n| + c_i^n}, \tag{5.37}$$

where c_i^n is the local sound speed (equal to $\sqrt{\gamma P_i^n/\rho_i^n}$). Throughout this chapter, the chamber is given in both problems a length unity. And the fluid grid was made of $N = 50$ points (and fifty cells around these points). The experience proves that, for industrial cases like those discussed in [25, 66], the limit time step for the structure integration Δt_S^{lim} can be very large compared to Δt_F^{lim}.

This gives the idea of subcycling the fluid. Since the integration of both fields is decoupled in staggered schemes, there is no need to integrate them with the same time step. The only constraint is to advance in time both fields with the same quantity, but not necessarily in the same number of steps. Then, the last step of the first methodology and the fifth step of the second can be performed in a subcycled way: only the grid point speeds are needed. For instance, they could be fixed for each group of subcycles without difficulties. The subcycling can enhance the performance of a code, because it (usually) reduces the number of structural integrations. It also enhances the accuracy of the time-integral of the fluid forces and moments on the structure mentionned in the second methodology. This may be an additional advantage. Last but not least, we already have advocated the use of a constant structural time step Δt_S when we use linear schemes for linear structures. Since the fluid equations are not linear, and since the stability conditions for the corresponding schemes are not constant throughout the computation (see (5.37) which is clearly time-dependent), the use of subcycling is necessary: it allows to keep Δt_S constant while Δt_F varies. Another solution would consist in the limitation of the fluid time-step Δt_F uniformly to a smaller value, in order to keep a constant time step and verify (5.37). This would affect the efficiency of the method as well.

In the following sections, we describe and comment the results given by both methodologies. They must be compared in terms of stability for the limit time-step Δt_S^{lim} and the limit number of subcycles for the fluid. We should also compare their accuracy (especially phase errors and numerical damping). Finally, the possibilities of enhancements will be discussed.

5.4 Volume-continuous methods

In this section, we review in detail investigations on the first type of methods presented above. Considering both fluid and structural interfaces as common and constantly

matching (at least, before spatial discretization), we mainly study the effects of subcycling and the influence of numerical schemes for grid speeds on the simulations.

5.4.1 Description of the algorithm

The volume-continuous method is the most direct and natural, and the most popular as well. The basic idea is the following. Assuming we want to use a staggered scheme, and considering we need to know the motion of the mesh for the time integration of fluid dynamics, we should advance the structure, compute a new grid and the average grid speed during the time-step and then advance the fluid in time. The subcycling process can be added to the general idea of the method. We now give a precise sketch of the method:

1. Compute the pressure P_N^n on the piston (and also P_1^n for the box) at time t^n. There is no actual computation for our two one-dimensional model problems. However, the external force distribution should be computed at this step in more complex computations, like three-dimensional computations with approximately matching grids [53],

2. advance the structure using a generalized-α method or a simple trapezoidal rule using a fixed time-step Δt_S for the structure,

3. get the displacement of the structure at time t^{n+1} and compute a new fluid grid location (this can be done directly in one dimension according to (5.35) or (5.36)). However, more complex methods have been reviewed for multi-dimensional cases in [45]),

4. fix a motion law for the fluid grid points during the fluid subcycles: for each grid point, the final location must be equal to the previously computed location,

5. advance the fluid part of the problem with multiple subcycles, using average grid point speeds, depending on the previously defined law of motion. Throughout this chapter, we shall denote by $n_{S/F}$ the approximate number of fluid subcycles. It is given by
$$n_{S/F} = \frac{\Delta t_S}{\Delta t_F}. \tag{5.38}$$
It is not necessarily an integer. However, we shall assume throughout this chapter that $n_{S/F}$ is an integer. In actual numerical simulations, the last subcycle for the fluid is performed with a time step $\widetilde{\Delta t_F}$ that can be smaller than Δt_F, so that we have
$$\Delta t_S = (n_{S/F} - 1)\,\Delta t_F + \widetilde{\Delta t_F} \tag{5.39}$$
We shall also denote by $W^{n,k}$ the fluid state after the kth subcycle. We use the conventions that $W^{n,0} = W^n$ and $W^{n,n_{S/F}} = W^{n+1}$.

5.4.2 Numerical results

For the first numerical tests, we took for steps 4 and 5 the following natural law of motion for the fluid grid points: assuming both displacements x_N^n and x_N^{n+1} are already known, we use:

$$x_N(t) = X_N^n + \frac{X_N^{n+1} - X_N^n}{\Delta t^S}(t - t^n) \quad \text{for} \quad t \in \left[t^n, t^{n+1}\right] \quad (t^{n+1} \equiv t^n + \Delta t_S) \tag{5.40}$$

which gives a constant average speed for the last grid point w_N during the $n_{S/F}$ subcycles Δt_F equal to

$$w_N = \frac{X_N^{n+1} - X_N^n}{\Delta t^S}. \tag{5.41}$$

All remaining fluid grid points locations and speeds were computed according to the simple algorithms (5.35) or (5.36).

We first applied this algorithm to the piston problem (**case 1**). The structural displacement is presented as a function of time on Figure 5.3. The structural time step used was $\Delta t_S = 10^{-4}$ which corresponds to an approximate number of subcycles $n_{S/F}$ equal to 4. The result is quite satisfying. The system, which is genuinely physically stable, is added a light numerical viscosity (due to the first-order accurate upwind scheme used in the fluid part). However, when we use a bigger time step for the

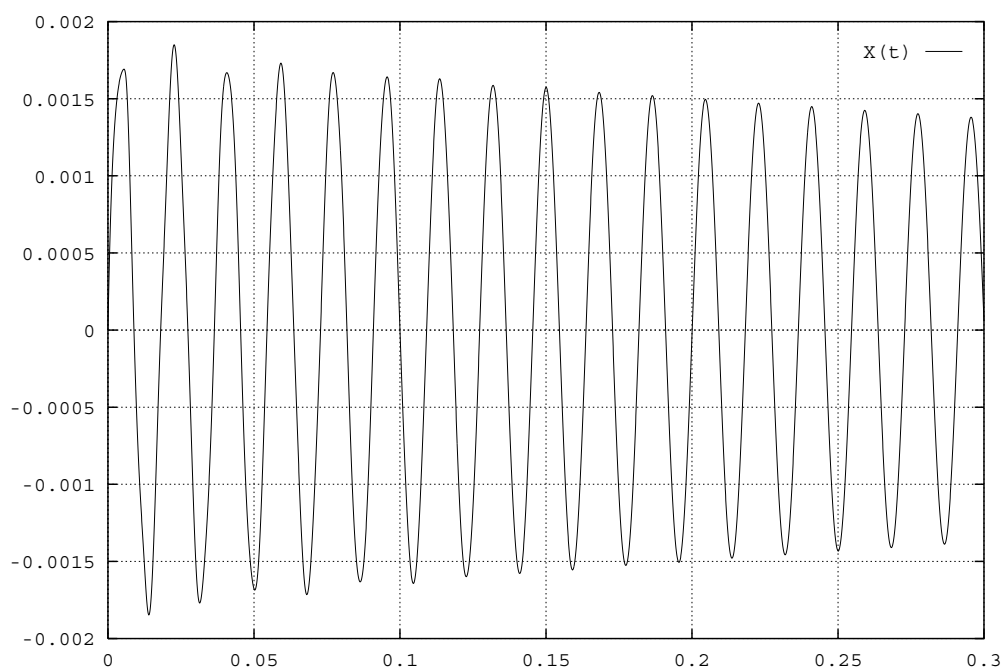

FIG. 5.3 – *$X(t)$ for the piston problem,* **case 1**, *$\Delta t_S = 10^{-4}$ with a volume-continuous method.*

structure, the global scheme becomes unstable. A typical result is showed on Figure 5.4.

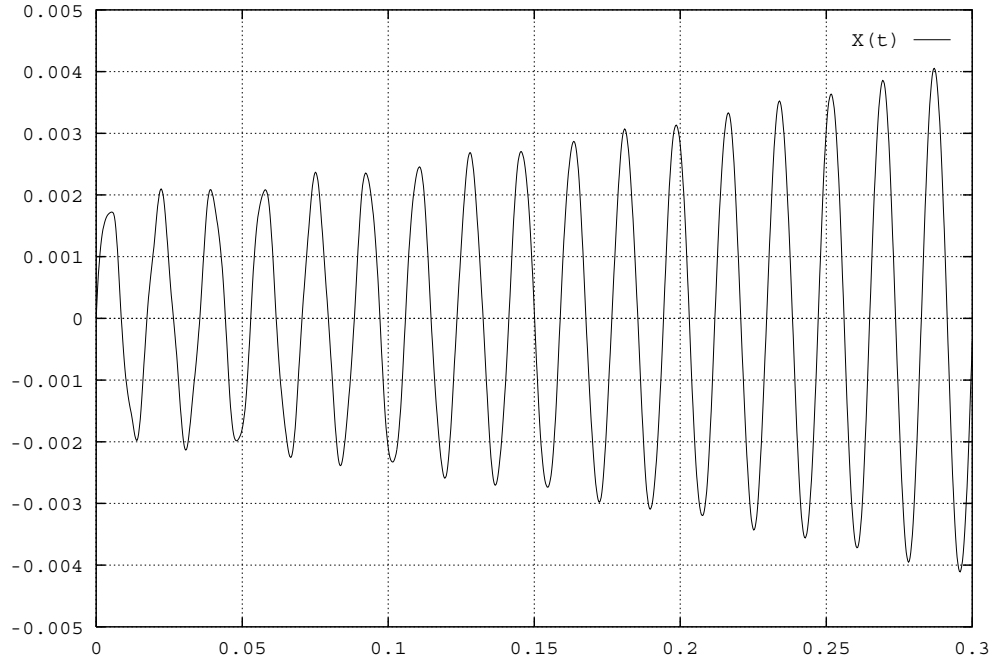

FIG. 5.4 – *$X(t)$ for the piston problem,* **case 1**, $\Delta t_S = 2.6 * 10^{-4}$ *with a volume-continuous method.*

The time step $\Delta t_S = 2.6\,10^{-4}$ corresponds to $n_{S/F} \simeq 10$. The results we obtained for the piston problem are not specific. We have made the same numerical tests with the box problem (with **case 2**). We present on Figure 5.5 (resp. Figure 5.6) the box displacement as a function of time for $\Delta t_S = 2 * 10^{-4}$ (resp. $\Delta t_S = 3 * 10^{-4}$), which corresponds to $n_{S/F} \simeq 8$ (resp. $n_{S/F} \simeq 11$).

Similar results were also described in [63]. We intend to give an simple explanation of the instability induced by the staggered subcycled algorithm we used. We present on Figure 5.7 the relative variation of the total energy of the system for the same numerical test as in Figure 5.6. We can see it increases exponentially.

We shall show in the following that this algorithm does not conserve the global energy, though we use a conservative scheme for the fluid.

5.4.3 Discussion on conservation

For instance, let us consider the box problem. We consider the global energy $\mathbf{E}$ of the system. We also denote by $\mathbf{E_F}$ and $\mathbf{E_S}$ respectively the energy of the fluid and the structure. Before spatial discretization, these energies can be written as:

$$\mathbf{E}(t) = \overbrace{\int_{X(t)}^{L+X(t)} E(t,x)dx}^{\mathbf{E_F}(t)} + \overbrace{\frac{1}{2}m\dot{X}(t)^2 + \frac{1}{2}kX(t)^2}^{\mathbf{E_S}(t)} \tag{5.42}$$

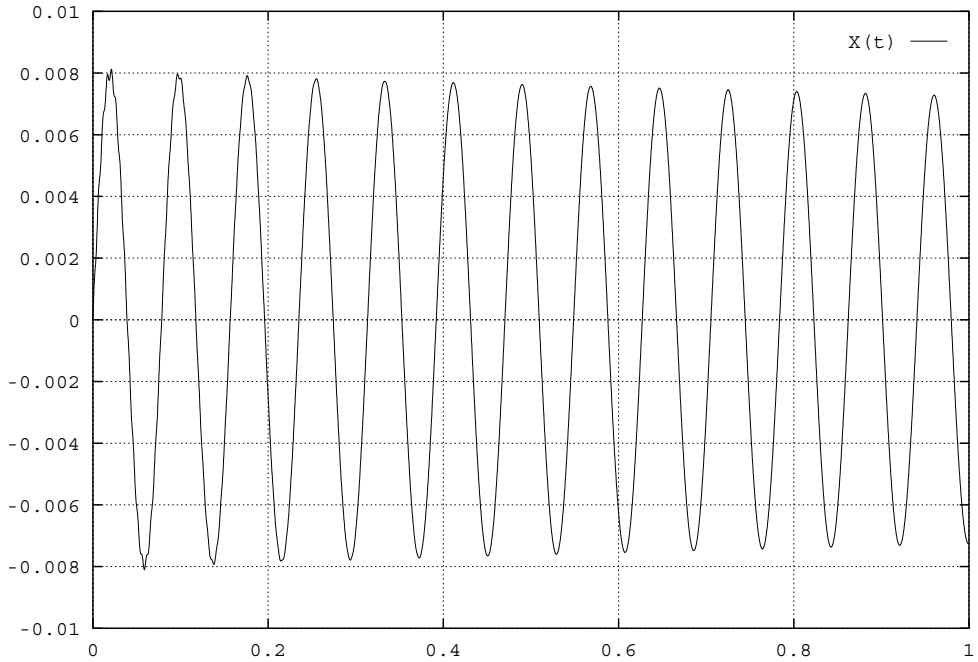

FIG. 5.5 – $X(t)$ *for the box problem,* **case 2**, $\Delta t_S = 2*10^{-4}$ *with a volume-continuous method.*

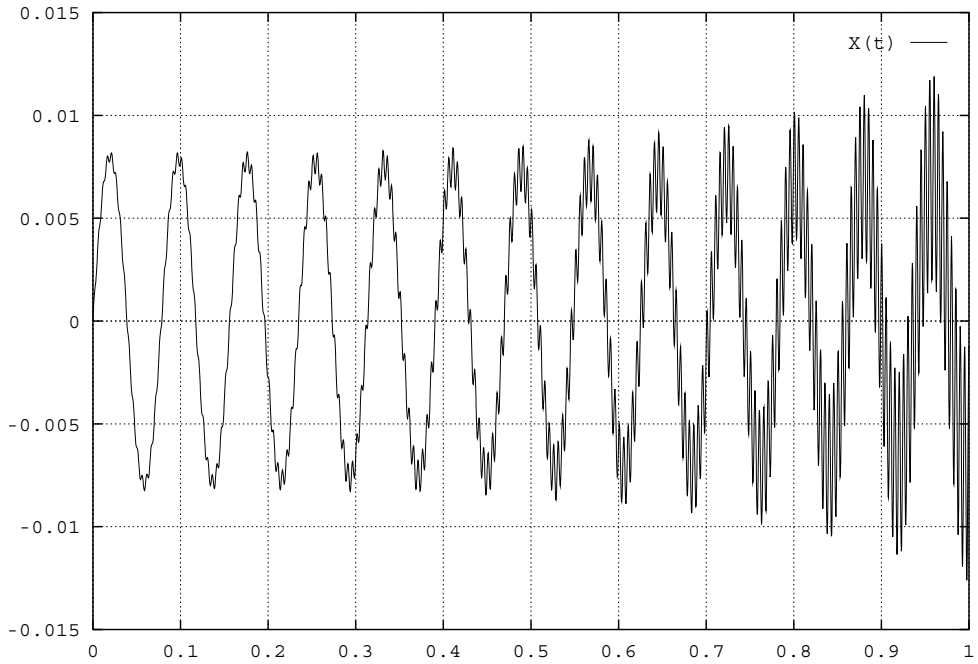

FIG. 5.6 – $X(t)$ *for the box problem,* **case 2**, $\Delta t_S = 3*10^{-4}$ *with a volume-continuous method.*

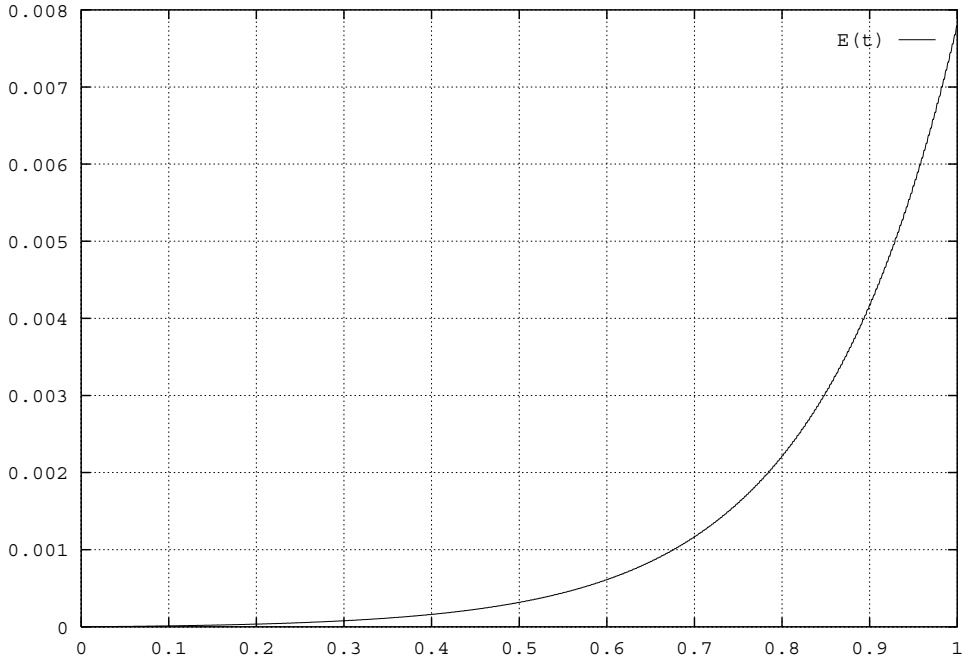

FIG. 5.7 – *$E(t)$ for the box problem,* **case 2**, $\Delta t_S = 3 * 10^{-4}$ *with a volume-continuous method.*

After spatial discretization, we define all corresponding discrete energies by:

$$\mathbf{E}^n = \overbrace{\sum_{i=1}^{N} A_i^n E_i^n}^{\mathbf{E_F}^n} + \overbrace{\frac{1}{2} m \dot{X}^{n^2} + \frac{1}{2} k X^{n^2}}^{\mathbf{E_S}^n} \tag{5.43}$$

We assume we use a trapezoidal rule for the time-integration of the structure. During the time step Δt_S, the fluid exerts a pressure at both ends taken as constant on the structure, and equal to P_1^n and P_N^n. Thus, it is easily showed that the energy variation for the box is given by:

$$\mathbf{E_S}^{n+1} - \mathbf{E_S}^n = \Delta t_S \left(P_N^n - P_1^n\right) \frac{\dot{X}^n + \dot{X}^{n+1}}{2}$$

The trapezoidal rule has the property that the preceding equation reduces to

$$\mathbf{E_S}^{n+1} - \mathbf{E_S}^n = \left(P_N^n - P_1^n\right) \left(X^{n+1} - X^n\right) \tag{5.44}$$

On the other hand, the energy variation for the fluid during each subcycle Δt_F depends only on the boundary fluxes given on page 145, because we use the conservative scheme (5.27). This variation is given by:

$$\mathbf{E_F}^{n,k+1} - \mathbf{E_F}^{n,k} = -\Delta t_F \left(P_N^{n,k} w_N^{n,k} - P_1^{n,k} w_1^{n,k}\right)$$

Since the mesh velocity is constant and equal to $(X^{n+1} - X^n)/\Delta t_S$, we have:

$$\mathbf{E_F}^{n,k+1} - \mathbf{E_F}^{n,k} = -\frac{1}{n_{S/F}} \left(P_N^{n,k} - P_1^{n,k}\right) \left(X^{n+1} - X^n\right). \tag{5.45}$$

Finally, the total energy variation for the fluid through all subcycles is given by:

$$\mathbf{E_F}^{n+1} - \mathbf{E_F}^{n} = -\frac{1}{n_{S/F}} \left[\sum_{k=0}^{n_{S/F}-1} \left(P_N^{n,k} - P_1^{n,k}\right) \right] \left(X^{n+1} - X^n\right). \tag{5.46}$$

Since the pressure distribution varies during the fluid subcycles, we have as a consequence:

$$\mathbf{E}^{n+1} - \mathbf{E}^{n} = \frac{1}{n_{S/F}} \left[\sum_{k=0}^{n_{S/F}-1} \left[\left(P_N^{n} - P_N^{n,k}\right) - \left(P_1^{n} - P_1^{n,k}\right)\right] \right] \left(X^{n+1} - X^n\right) \neq 0 \tag{5.47}$$

The preceding equation should be interpreted the following way. Though the physical system receives no external work (fixed end of the spring, and equal external pressure on both ends of the box, which are moving at the same speed), the total energy is not conserved. It means that the respective works of the force exerted by the fluid on the structure and the force exerted by the structure on the fluid were not computed as opposite. The careful reader should already have noticed that these forces themselves were not computed as opposite but respectively as:

$$Force[\text{Fluid} \rightarrow \text{Box}] \overset{\text{comp. as}}{=\!=\!=} \Delta t_S \left(P_N^n - P_1^n\right) \tag{5.48}$$

and

$$Force[\text{Box} \rightarrow \text{Fluid}] \overset{\text{comp. as}}{=\!=\!=} -\frac{\Delta t_S}{n_{S/F}} \left[\sum_{k=0}^{n_{S/F}-1} \left(P_N^{n,k} - P_1^{n,k}\right) \right]. \tag{5.49}$$

The preceding results hold for a general Newmark method, not necessarily equal to the trapezoidal rule, provided it is unconditionally stable (which is achieved when $2\beta \geq \gamma \geq 1/2$). The difference is a simple numerical dissipation in the structural part of the integration. This remark holds also for the generalized-α method.

The instability of the staggered subcycled scheme can be explained in the following way. The discrepancy between exchanged works or exchanged forces at the fluid-structure interface increases as the number $n_{S/F}$ of subcycles and Δt_S get bigger. This difference induces variations on the eigenvalues of the transformation matrix (matrix operating on numerical values at time t^n to obtain numerical values at time t^{n+1}). When the time step Δt_S is small enough, these eigenvalues have a modulus less than one (because of numerical viscosity, the scheme is stable at least for a small $n_{S/F}$). As $n_{S/F}$ increases, the perturbation increases, and a modulus greater than one appears.

On Figure 5.4 and Figure 5.6, we showed two results of unstable simulations where the subcycle factor $n_{S/F}$ was beyond stability (respectively $n_{S/F} \simeq 10$ and $n_{S/F} \simeq 11$).

But there is no explicit expression for the stability limit on $n_{S/F}$ (such as "$n_{S/F} < 12$" or whatever). The limit is rather put on the dimensionless numbers $\omega_C \Delta t_S$ or $\omega_S \Delta t_S$ which have to be small compared to unity (we write $\omega_S \equiv \sqrt{k/m}$ for the pulsation of the structure and we recall ω_C is the lowest coupled pulsation of the physical system). For example, we show on Figure 5.8 a simulation of the box problem with **case 3** where we obtain a stable simulation with $\Delta t_S = 3 * 10^{-3}$ which corresponds to $n_{S/F} \simeq 109$. Though $n_{S/F}$ is huge, we have $\omega_C \Delta t_S = 0.09 \ll 1$.

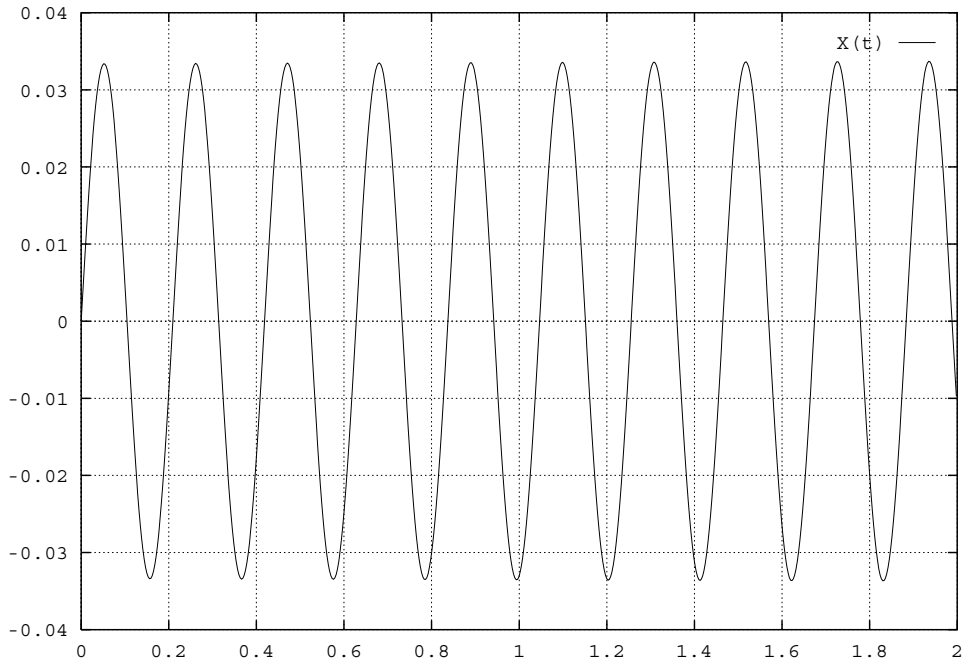

FIG. 5.8 – *$X(t)$ for the box problem,* **case 3**, *$\Delta t_S = 3 * 10^{-3}$ with a volume-continuous method.*

We show on Table 5.1 the set of stability limits we found for both problems in all three cases. We can notice the order of magnitude of the non-dimensionalized time step $\omega_C \Delta t_S$ where the method becomes unstable is 1% (except the box problem in **case 3**) which corresponds to six hundred points per period of oscillation (which is very inefficient). The result is acceptable for the box problem in **case 3**. We have to take fifty time steps per coupled period of oscillations. This is quite bad in deed, since this case is very weakly coupled. The case is strongly governed by the structure and the scheme should therefore be almost unconditionally stable !

As a conclusion, we emphasize the fact that volume-continuous methods have a rather low stability limit, since they require for most cases the use of several hundreds of elementary time-integrations for each period of coupled oscillation. These methods are currently used in all industrial aeroelastic computations. We intend to present in the next section a new type of methods where the matching condition on interfaces

TAB. 5.1 – *Stability limits on Δt_S for both problems in* **cases 1 to 3**.

problem	test case	ω_S (s^{-1})	ω_C (s^{-1})	Δt_S (s)	$n_{S/F}$	$\omega_S \Delta t_S$	$\omega_C \Delta t_S$
piston	**case 1**	100	344	$1.5\ 10^{-4}$	6	$1.5\ 10^{-2}$	$5.20\ 10^{-2}$
piston	**case 2**	100	253	$1.3\ 10^{-4}$	5	$1.3\ 10^{-2}$	$3.29\ 10^{-2}$
box	**case 1**	100	61.7	$1.5\ 10^{-4}$	6	$1.5\ 10^{-2}$	$0.93\ 10^{-2}$
box	**case 2**	100	78.5	$2.6\ 10^{-4}$	10	$2.6\ 10^{-2}$	$2.04\ 10^{-2}$
piston	**case 3**	30	66.3	$2.0\ 10^{-4}$	8	$0.6\ 10^{-2}$	$1.32\ 10^{-2}$
box	**case 3**	30	29.5	$4.0\ 10^{-3}$	160	$12.\ 10^{-2}$	0.12

is relaxed. We shall show that they are not perfect (they are not unconditionally stable), but the drawbacks are dramatically reduced. At this point, the reader should remember that volume-continuous methods produce a violation of the principle of action and reaction (for the contact forces at the fluid-structure interface) in terms of momentum and energy. We show in the next section that the momentum and energy conservations can be better satisfied with the volume-discontinuous methods.

5.5 Volume-discontinuous methods

In this section, we present a new type of methods for the numerical simulation of coupled aeroelastic problems. We show the enhancement proposed and discuss numerical results. We also present some complementary tests based on classical ideas, like predictor-corrector loops and numerical auto-adaptive filters.

5.5.1 Description of the algorithm

The basic idea of these methods is the relaxation of the matching condition on the fluid-structure interface. This idea might seem surprising, since all coupling phenomena take place at this point. However, we intend to relax the matching condition up to a limited point. We shall assume and investigate that the non-matching fluid and structural interfaces remain close during the numerical simulation. We shall see that this method allows us to get rid of the discomfort of staggered schemes, where the integration in time of a first field is done using a very inaccurate information coming from the other field.

The principle of such a method is simple. We do not require that both interfaces match exactly (with no consideration on spatial discretizations of both boundaries), but that they remain close throughout the computation. For each structural time-step (that can be subcycled for the fluid part), we make a prediction of the state of the structure at the end of the time step. We imagine a fluid mesh motion during the current time step which matches the prediction at the end of the time step. Then we advance the fluid (possibly in a subcycled way). We store the fluid pressure forces

on the structure during this integration, and use this pressure distribution for the structural part of the integration. The method is now described in more detail:

1. compute a prediction of the state of the structure at the end of the current time step Δt_S. This prediction can be more or less complex. The more accurate this prediction, the more accurate the coupling. This prediction will be discussed later in this section.

2. from the predicted displacement of the structure at time t^{n+1}, compute a new fluid grid location (again, this can be done very simply in one-dimensional problems according to (5.35) or (5.36)).

3. fix a motion law for the fluid grid points during the fluid subcycles: for each grid point, the final location must be equal to the location previously computed (which matches the predicted location of the structure at the end of the current time step).

4. advance the fluid part of the problem with $n_{S/F}$ subcycles, using average grid point speeds, depending on the previously defined law of motion. $n_{S/F}$ is defined again as in (5.38) and (5.39). We shall again denote by $W^{n,k}$ the fluid state after the kth subcycle. We recall that $W^{n,0} = W^n$ and $W^{n,n_{S/F}} = W^{n+1}$. During each of these fluid time steps, some numerical boundary fluxes are used: $(0, P_1^{n,k}, P_1^{n,k} w_1^{n,k})^t$ and $(0, P_N^{n,k}, P_N^{n,k} w_N^{n,k})^t$ for both problems.

   The momentum terms $P_1^{n,k}$ and $P_N^{n,k}$ appear in the momentum equations (5.5) and (5.6). For the piston problem, these terms can be seen as the actual force exerted on the fluid and the first term is the force exerted by the fluid on the support of the left fixed end of the chamber. For the box problem, both terms can be interpreted as the forces exerted on the fluid.

   Thus, we can compute the sum of all these momentum terms during the $n_{S/F}$ subcycles (for simplicity reasons, we assume here that $\Delta t_S/\Delta t_F$ is an integer; all following equations could be rewritten with a non-integer fraction $\Delta t_S/\Delta t_F$. The force exerted on the fluid by the box per time-step is computed as

$$Force[\text{Box} \to \text{Fluid}] \overset{\text{comp. as}}{=\!=\!=} -\frac{\Delta t_S}{n_{S/F}} \left[\sum_{k=0}^{n_{S/F}-1} \left(P_N^{n,k} - P_1^{n,k} \right) \right] \tag{5.50}$$

   which is simply deduced from (5.49), and the force exerted on the fluid by the piston per time-step is computed as

$$Force[\text{Piston} \to \text{Fluid}] \overset{\text{comp. as}}{=\!=\!=} -\frac{\Delta t_S}{n_{S/F}} \left[\sum_{k=0}^{n_{S/F}-1} P_N^{n,k} \right] \tag{5.51}$$

5. advance the structure using a generalized-α method or a simple trapezoidal rule using the fixed time-step Δt_S and an external force, which is the opposite of the force we just computed. The great advantage of this method clearly appears. We have enforced the "action and reaction" condition

$$Force[\text{Structure} \to \text{Fluid}] + Force[\text{Fluid} \to \text{Structure}] \overset{\text{comp. as}}{=\!=\!=} 0. \tag{5.52}$$

5.5.2 Conservation enhancements

We would like to add a few remarks concerning this volume-discontinuous method. We first notice that the method depends of the prediction used in the first step of the algorithm. We have a wide choice for this prediction. The error in the predictor will certainly be less important than the error on the external pressure in the first method. We understand also that the accuracy, or the possible stabilization properties of this prediction enhance the global accuracy and stability of the method.

Second, we have noticed that the global momentum is conserved concerning the interaction (5.52). We now investigate the conservation of the global energy. Considering the box problem with constant grid points speeds during the subcycles, and using notations defined in (5.42) and (5.43), we have again for each subcycle

$$\mathbf{E_F}^{n,k+1} - \mathbf{E_F}^{n,k} = -\Delta t_F \left(P_N^{n,k} w_N^{n,k} - P_1^{n,k} w_1^{n,k} \right).$$

Since the mesh velocity is constant and equal to $(\widetilde{X^{n+1}} - \widetilde{X^n})/\Delta t_S$, we have:

$$\mathbf{E_F}^{n,k+1} - \mathbf{E_F}^{n,k} = -\frac{1}{n_{S/F}} \left(P_N^{n,k} - P_1^{n,k} \right) \left(\widetilde{X^{n+1}} - \widetilde{X^n} \right). \tag{5.53}$$

where $\widetilde{X^{n+1}}$ is the predicted position of the structure at the beginning of the nth time step (and $\widetilde{X^n}$ is the previous one). Finally, the fluid energy variation through all subcycles is given by:

$$\mathbf{E_F}^{n+1} - \mathbf{E_F}^{n} = -\frac{1}{n_{S/F}} \left[\sum_{k=0}^{n_{S/F}-1} \left(P_N^{n,k} - P_1^{n,k} \right) \right] \left(\widetilde{X^{n+1}} - \widetilde{X^n} \right). \tag{5.54}$$

On the other hand, assuming we use a simple trapezoidal rule for the structure, with an external force satisfying (5.52), the energy variation through one time step writes

$$\mathbf{E_S}^{n+1} - \mathbf{E_S}^{n} = \frac{1}{n_{S/F}} \left[\sum_{k=0}^{n_{S/F}-1} \left(P_N^{n,k} - P_1^{n,k} \right) \right] \left(X^{n+1} - X^n \right). \tag{5.55}$$

If we write ε^n for the mismatching error at time t^n ($\varepsilon^n = X^n - \widetilde{X^n}$), the system total energy variation through one time step of this method is given by

$$\mathbf{E}^{n+1} - \mathbf{E}^{n} = \frac{1}{n_{S/F}} \left[\sum_{k=0}^{n_{S/F}-1} \left(P_N^{n,k} - P_1^{n,k} \right) \right] \left(\varepsilon^{n+1} - \varepsilon^n \right). \tag{5.56}$$

If the matching error remains small, then the global energy of the system will be conserved with a good accuracy. The preceding equation should be compared with (5.47). In the preceding equation, the order of magnitude of the energy error depends on the quality of the prediction. Then the error can be reduced not only with a time step reduction (which is not the aim of this work), but with enhancement of the order of accuracy of the prediction for example. And the availability of two time-derivatives for the structure make all sorts of predictions very easy. This characteristic induces

the great flexibility of the method. On the contrary, (5.47) proves that the energy conservation error of the volume-continuous method could only be reduced with the use of a prediction of the time-averaged fluid pressure force, which is certainly very difficult to perform (it would require an investigation of the fluid state throughout a thick band of cells along the fluid-structure interface). However, the momentum conservation is exactly performed with the second method, and can only be approximately done with the first method coupled with any prediction.

As a second remark, we emphasize here that both interfaces are not matching either at the beginning or at the end of a time step. For our one-dimensional model problems, this characteristic does not make the algorithm more complex. However, the resolution would not be so simple for two- or three-dimensional problems. As a matter of fact, fluid pressure forces on a given fluid interface point should be transmitted to some "corresponding" point of the structural interface [53]. The correspondance could simply be point-to-point, but more complex geometrical methods should be tested.

We also point out the fact that the volume-continuous method described in Section 5.4 can be seen as a volume-discontinuous method with a bad prediction $\widetilde{X^{n+1}} = X^n$. Hence, volume-discontinuous methods should be more accurate and more stable. Reciprocally, volume-discontinuous methods cannot be seen as volume-continuous methods with a better prediction.

5.5.3 Numerical tests

We begin with numerical tests where we have given a constant fluid grid points speed thoughout the subcycles. The mesh locations are given by (5.40). As stated earlier, the volume-discontinuous method is flexible, since several types of predictions can be used. We review in the following some methods of prediction, which could not be coupled with the volume-continuous method in a simple way.

Explicit first-order prediction (constant speed)

We first try to use the most simple and natural prediction for the structure, which writes

$$\widetilde{X^{n+1}} = X^n + \Delta t_S \dot{X}^n \tag{5.57}$$

This prediction is only first-order accurate, but has the advantage of its simplicity (it can be applied to complex multi-dimensional structures with no computational costs). For each numerical test, we may present two curves, which are the structural displacement X and the mesh displacement (its right end) $\widetilde{X}$ as functions of the time. These curves will be compared with those of the preceding section.

We present on Figure 5.9 these curves for the piston problem in **case 1**. The structural response is correct (same as in Figure 5.3) at the beginning, but is quite overdamped. The time step used was $\Delta t_S = 0.9 * 10^{-3}$ which is far beyond the time step used in Figure 5.4 or Figure 5.5. Figure 5.10 shows that the scheme is conditionally stable, and that $\Delta t_S = 1.15 * 10^{-3}$ is beyond the stability limit (which was found to

be close to $\Delta t_S = 1.1 * 10^{-3}$). The volume-discontinuous method made possible the use of a time-step (and a subcycling factor $n_{S/F}$) seven times bigger.

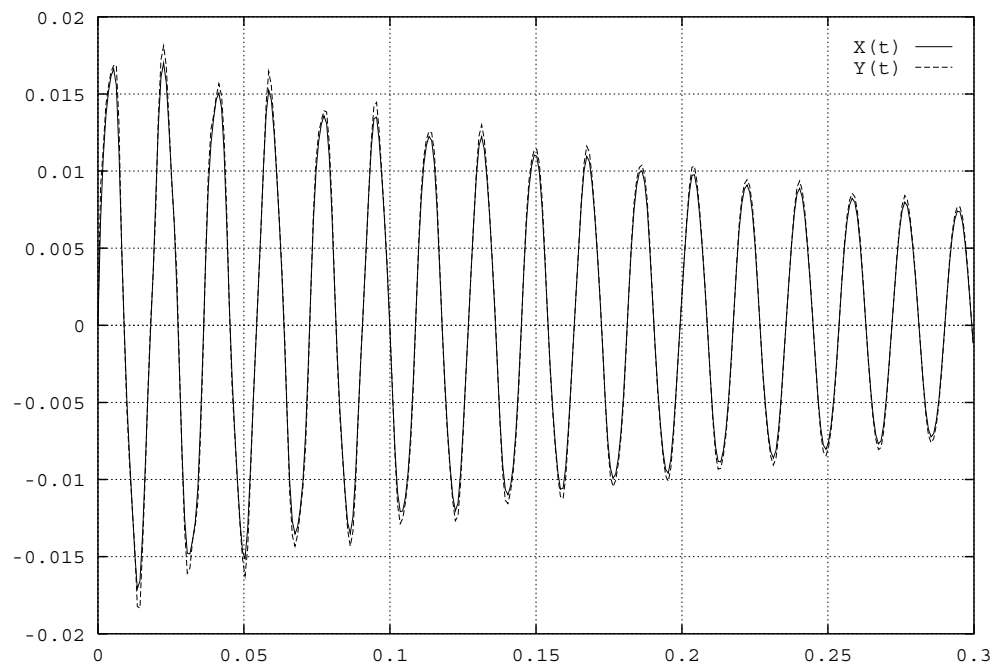

FIG. 5.9 – *$X(t)$ and $Y(t) = \widetilde{X}(t)$ for the piston problem,* **case 1**, $\Delta t_S = 0.9 * 10^{-3}$ *(volume-discontinuous method with an explicit first-order prediction).*

On Figure 5.11 and Figure 5.12 is presented the structural displacement as a function of time for two numerical simulations of the box problem (**case 2**). When $\Delta t_S = 0.8 * 10^{-3}$, the scheme is stable and gives a result close to Figure 5.5. In that case, the signal is not overdamped. For $\Delta t_S = 0.86 * 10^{-3}$, the scheme has reached instability. Spurious mesh oscillations appear.

If we look at Figure 5.13, where the relative variation of the total energy of the system is presented as a function of time, we see the global energy relative error increases exponentially like in Figure 5.7 for the volume-continuous method. However, the stability limit for this case is $\Delta t_S = 0.83 * 10^{-3}$, which is three times bigger than for the first method.

Comparing with the volume-continuous method, we see that this method has an enhanced stability, even when the first one had good results. We present on Figure 5.14 the structural displacement for the box problem in **case 3**. We see the scheme is stable for a bigger time step ($\Delta t_S = 1. * 10^{-2}$ which corresponds to a subcycling factor $n_{S/F} = 357$ and $\omega_C \Delta t_S = 0.01$!).

Finally, we present in Table 5.2 the stability limits we found for both problems in **cases 1** and **2** for the volume-discontinuous method. If we compare this table with Table 5.1, we see a general enhancement for the structural time step Δt_S (and the subcycling factor). The relaxation of the matching condition allowed a better

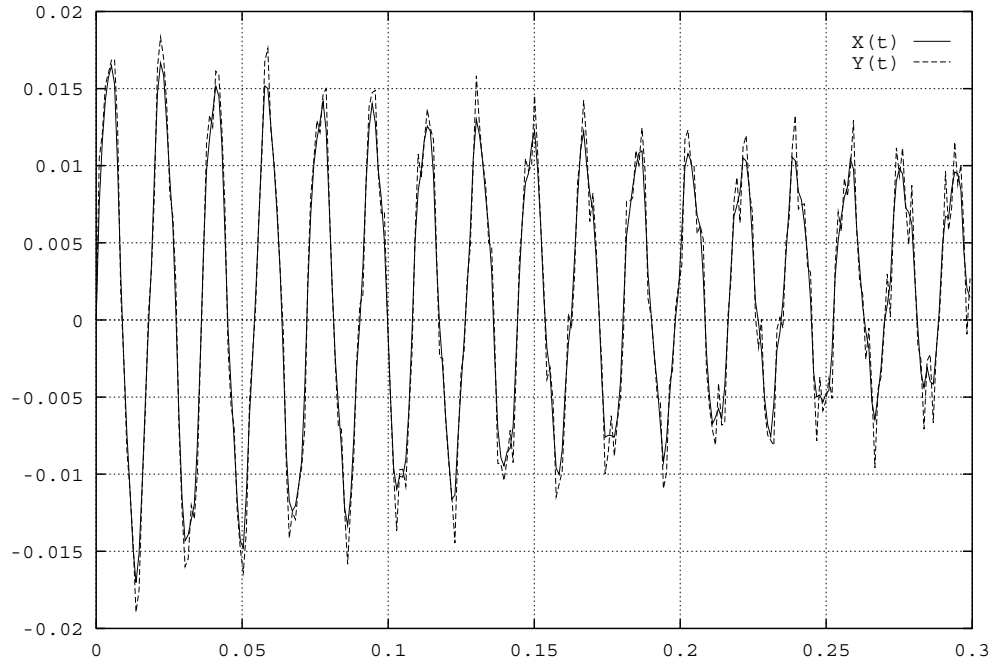

FIG. 5.10 – *$X(t)$ and $Y(t) = \widetilde{X}(t)$ for the piston problem,* **case 1**, $\Delta t_S = 1.15 * 10^{-3}$ *(volume-discontinuous method with an explicit first-order prediction).*

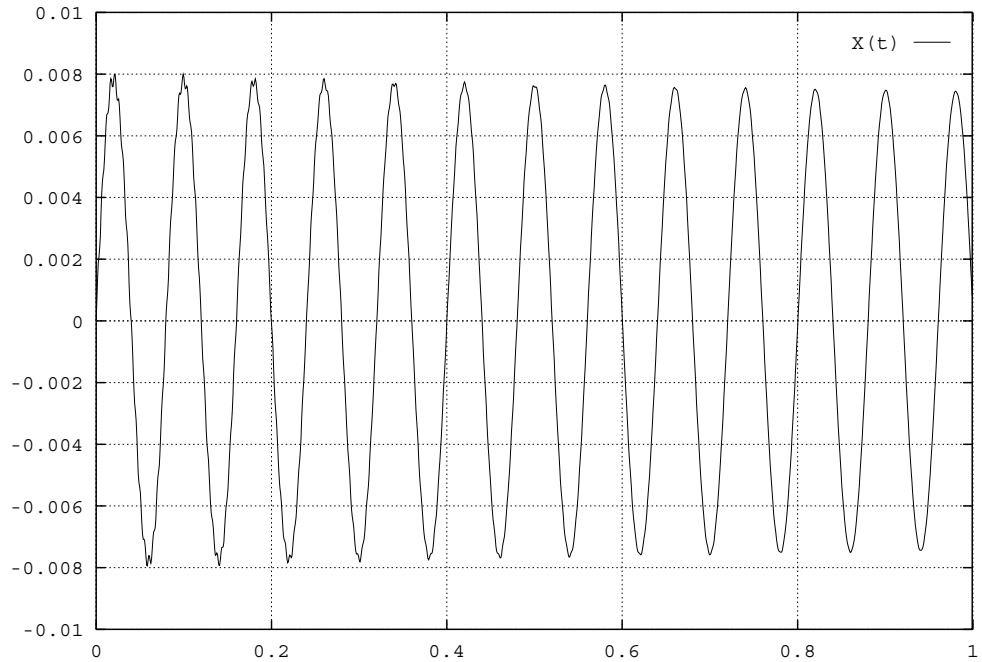

FIG. 5.11 – *$X(t)$ for the box problem,* **case 2**, $\Delta t_S = 0.8 * 10^{-3}$ *(volume-discontinuous method with an explicit first-order prediction).*

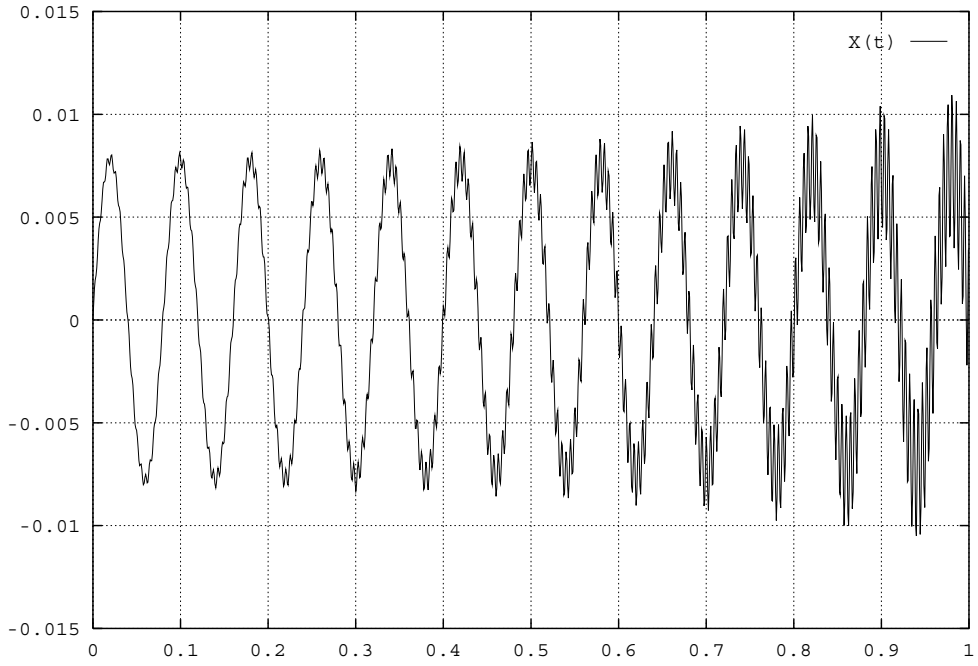

FIG. 5.12 – $X(t)$ *for the box problem,* **case 2**, $\Delta t_S = 0.86*10^{-3}$ *(volume-discontinuous method with an explicit first-order prediction).*

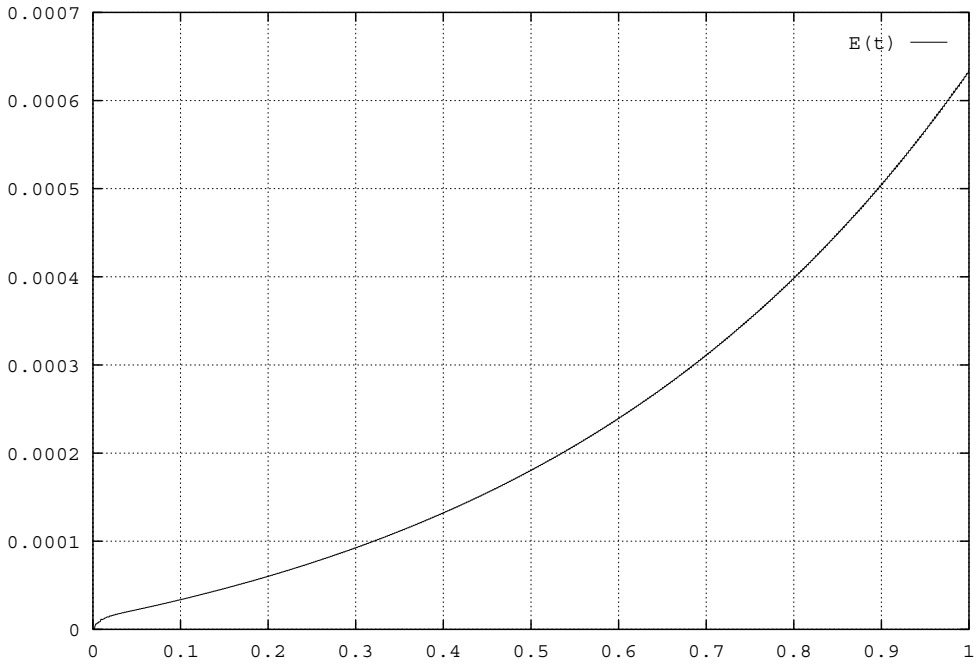

FIG. 5.13 – $E(t)$ *for the box problem,* **case 2**, $\Delta t_S = 0.86*10^{-3}$ *(volume-discontinuous method with an explicit first-order prediction).*

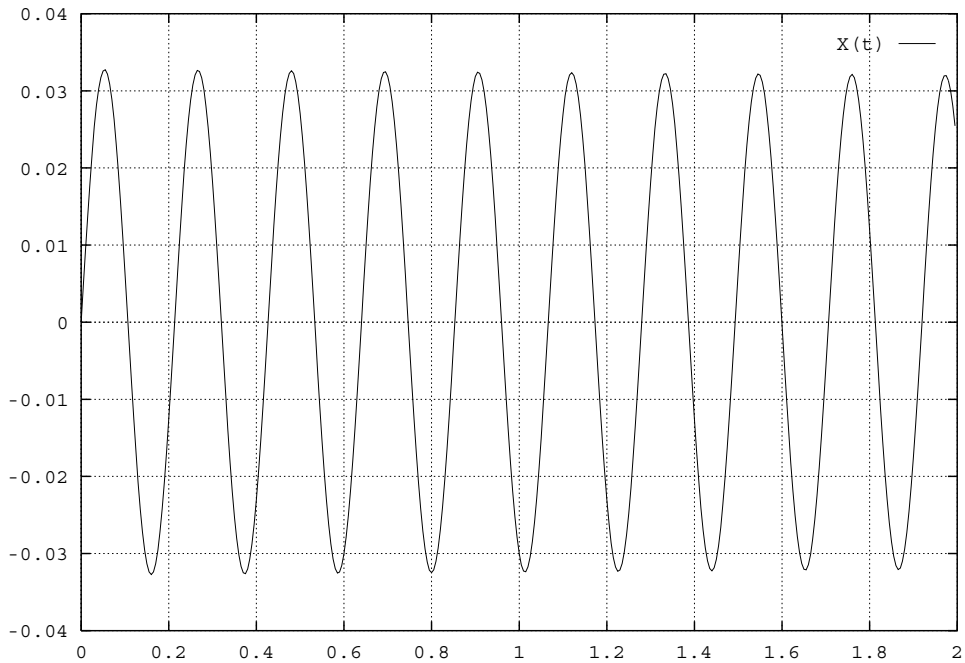

FIG. 5.14 – *$X(t)$ for the box problem,* **case 3**, $\Delta t_S = 1. * 10^{-2}$ *(volume-discontinuous method with an explicit first-order prediction).*

TAB. 5.2 – *Stability limits on Δt_S for both problems in* **cases 1 and 2**.

problem	test case	ω_S (s^{-1})	ω_C (s^{-1})	Δt_S (s)	$n_{S/F}$	$\omega_S \Delta t_S$	$\omega_C \Delta t_S$
piston	**case 1**	100	344	$1.1\ 10^{-3}$	39	$1.1\ 10^{-1}$	$3.78\ 10^{-1}$
piston	**case 2**	100	253	$1.3\ 10^{-3}$	52	$1.3\ 10^{-1}$	$3.29\ 10^{-1}$
box	**case 1**	100	61.7	$7.0\ 10^{-4}$	26	$7.0\ 10^{-2}$	$4.32\ 10^{-2}$
box	**case 2**	100	78.5	$8.3\ 10^{-4}$	32	$8.3\ 10^{-2}$	$6.52\ 10^{-2}$

conservation of the energy through the interaction, and an exact conservation for the momentum. The consequence is the gain in stability, though we used the elementary prediction (5.57).

Explicit second-order prediction (constant acceleration)

In this section, we present a family of prediction method depending of the real parameter θ defined by

$$\widetilde{X^{n+1}} = X^n + \Delta t_S \left[(1+\theta)\dot{X}^n - \theta \dot{X}^{n-1}\right] \tag{5.58}$$

This prediction is at least first-order accurate, and second-order accurate for $\theta = 1/2$. We show on Figure 5.15 the displacement for the box problem in **case 2**. It is similar to the result given on Figure 5.11. However, this new method is less stable: the new stability limit is close to $\Delta t_S = 0.78 * 10^{-3}$. We have clearly observed that the enhancement of the accuracy in the prediction method (when it is done in an uncoupled way, independant of the fluid flow) reduces the stability domain of the method. This remark is also valid for other predictions of the following type:

$$\widetilde{X^{n+1}} = X^n + \Delta t_S \dot{X}^n + \theta' \Delta t_S^2 \ddot{X}^n \tag{5.59}$$

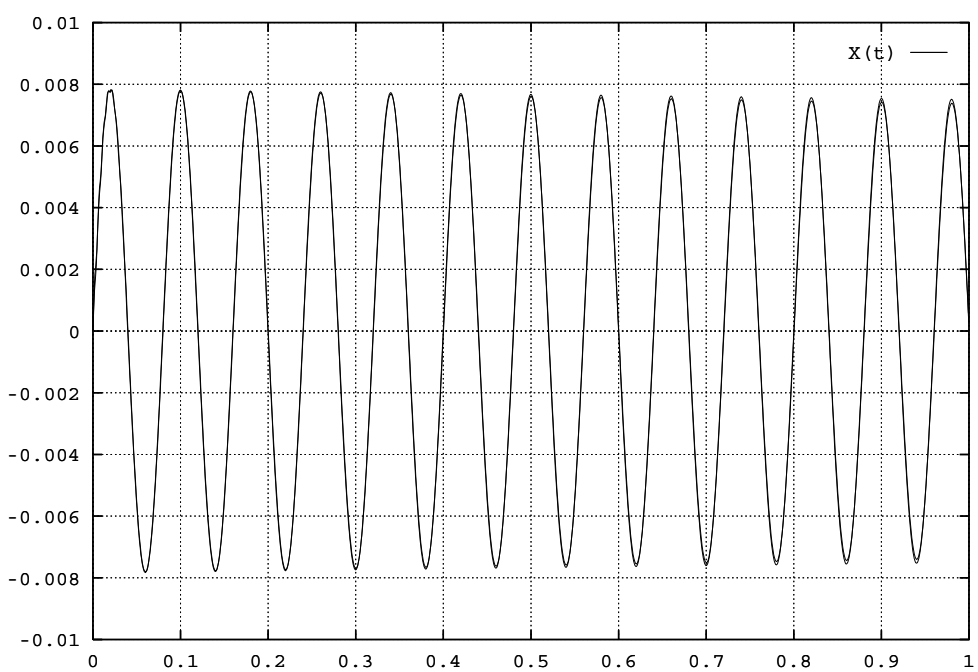

FIG. 5.15 – *$X(t)$ for the box problem,* **case 2**, $\Delta t_S = 0.75 * 10^{-3}$ *(volume-discontinuous method with an explicit second-order prediction).*

The limited stability of these kinds of predictions might be a consequence of their uncoupled nature. For example, the method (5.58) means the average acceleration

during the previous time step has the same value in the current time step. This is equivalent in a certain sense to an assumption on the fluid pressure during the current time step. This aspect could possibly be eliminated with coupled predictions. They will be investigated in the following.

Prediction iterations

We can obtain a coupled method of prediction by iterating the procedure described in 5.5.3. We propose the following algorithm:

-0- at time t^n, store the fluid state, the fluid grid and the structural state. Set $ipc = 0$

-1- compute a prediction of the structural displacement at time t^{n+1} according to (5.57)

-2- using this prediction for the structure, compute a fluid mesh at time t^{n+1} and average mesh speeds for the current time step. Using subcycles, advance the fluid in time and store the time-averaged fluid pressure on the structure according to (5.50-5.51).

-3- advance the structure till t^{n+1} with the preceding external pressure.

-4- If $ipc <$ IPC, use the structural displacement at time t^{n+1} as a prediction, reset all computational values to the values stored at step **0**. Do $ipc = ipc + 1$ and go to step **2**.

We notice that for each time step, the computational cost is IPC times bigger, since IPC steps of the regular volume-discontinuous method are done. The storage for this method is also double, since we have to store all computational values before each prediction cycle. We show on Figure 5.16 the performance of this method for the piston problem in **case 1**. We used IPC $= 2$, with $\Delta t_S = 1.8 * 10^{-3}$, which is the double of the time step used in Figure 5.9. Then computational costs are comparable for the structural part. For the fluid part of the problem, the time step is fixed by a CFL-like condition and in all cases, the computational cost is IPC times bigger. The method is stable. We have increased its stability domain.

We emphasize the fact that the preceding time step corresponds to $\omega_C \Delta t_S = 0.756$ which is a rather poor resolution for each coupled period. This explains why the solution is so much damped. The same test for IPC $= 4$ and $\Delta t_S = 3.6 * 10^{-3}$, (which gives $\omega_C \Delta t_S = 1.51$ and means we have only four points per period) which induces again a comparable computational cost for the structure, produced an even more damped solution.

For the box problem (in **case 2**), the result is more interesting. The present iterated method with IPC $= 2$ does not show instability for $\Delta t_S = 3.2 * 10^{-3}$ (a time step four times bigger than the time step used for the test of Table 5.2). The displacement for this test is shown on Figure 5.17.

The solution is a little more damped, maybe because we have only 25 time steps per coupled period instead of 100 as in Figure 5.15. For this method, with IPC $= 2$,

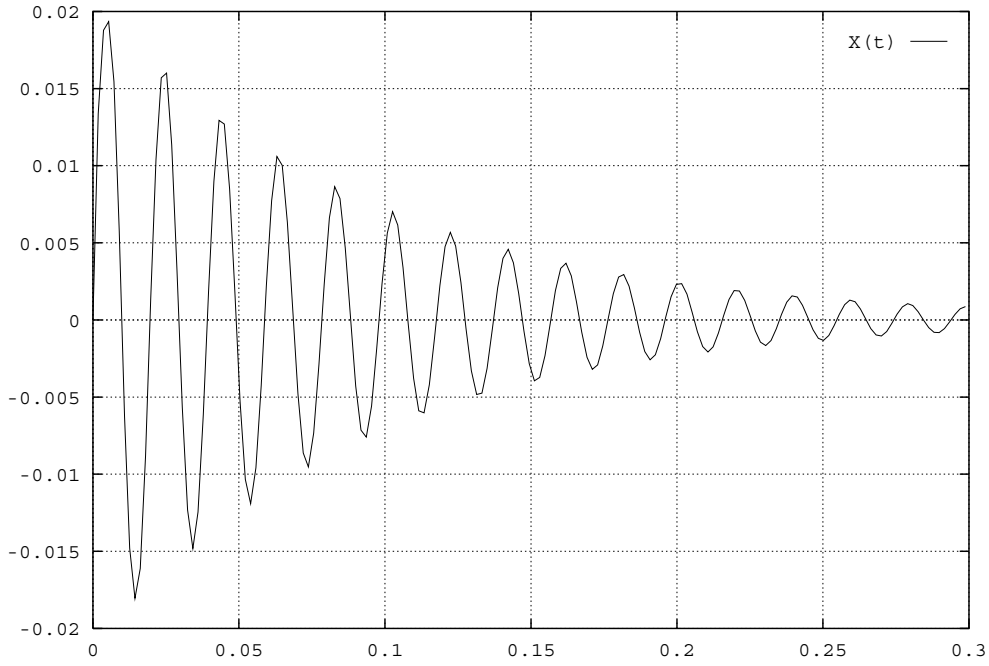

FIG. 5.16 – *$X(t)$ for the piston problem,* **case 1**, *$IPC = 2$ and $\Delta t_S = 1.8 * 10^{-3}$ (volume-discontinuous method with prediction iterations).*

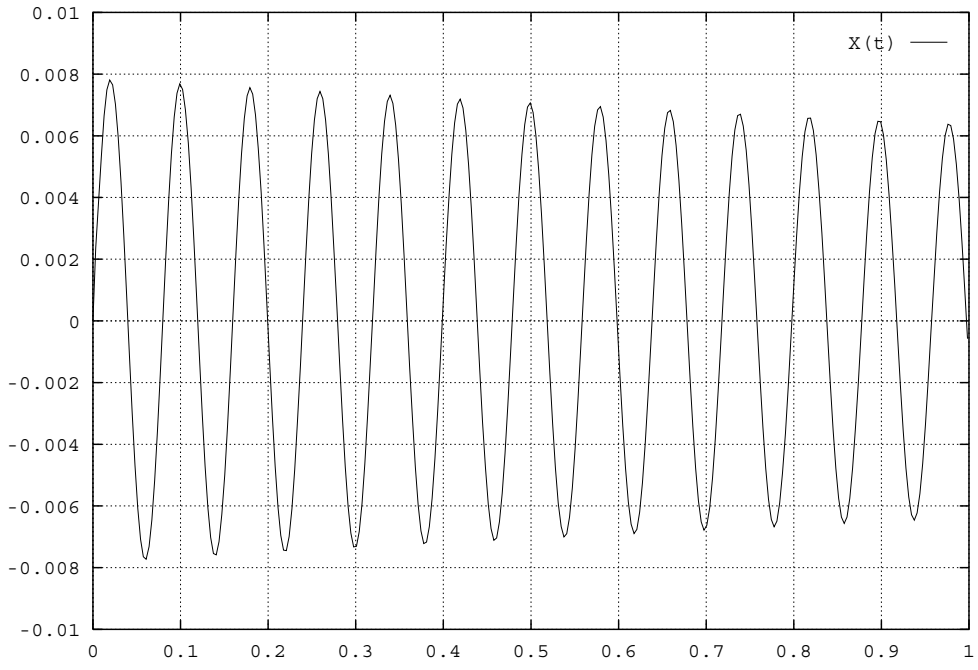

FIG. 5.17 – *$X(t)$ for the box problem,* **case 2**, *$IPC = 2$ and $\Delta t_S = 3.2 * 10^{-3}$ (volume-discontinuous method with prediction iterations).*

instability does not appear before $\Delta t_S = 8. * 10^{-3}$, which corresponds to 10 time steps per period and $n_{S/F} = 285$, as shown on Figure 5.18.

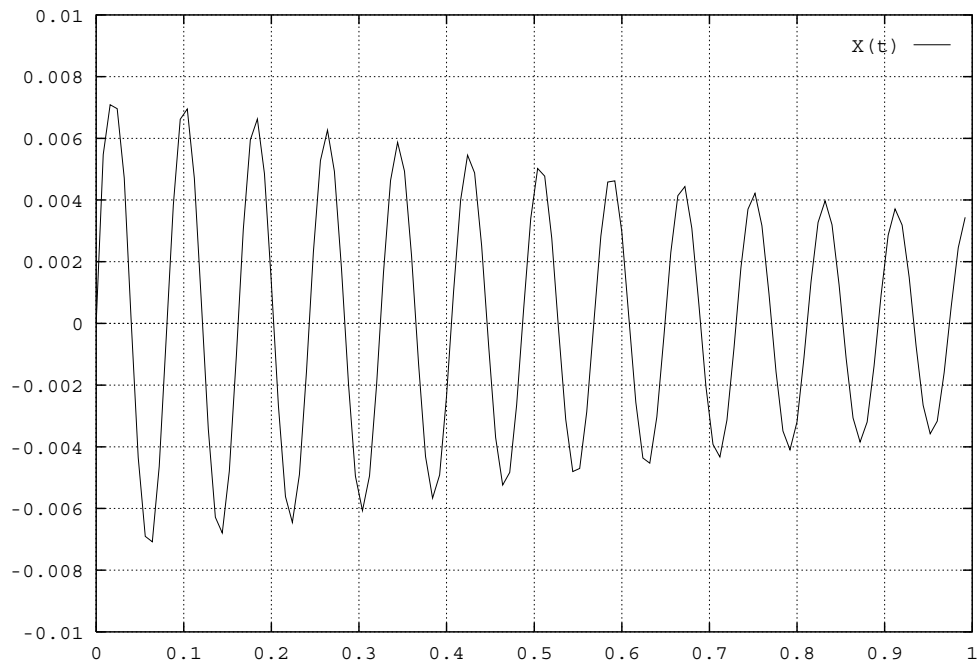

FIG. 5.18 – *$X(t)$ for the box problem,* **case 2**, *IPC = 2 and $\Delta t_S = 8. * 10^{-3}$ (volume-discontinuous method with prediction iterations).*

Our conclusion is the following. We have tried to increase the stability domain of our method by repeated prediction cycles. This was done successfully, but we got some overdamped solutions when we used too few time steps per coupled period of oscillations. However, we noticed that the predictor for the structural displacement at the end of the current time step was depending on the step ordinal *ipc*. More precisely, there is a slow and oscillating convergence towards a limit. This remark is the starting point for our next prediction method.

Assumed convergence of prediction iterations

The basic idea of this method is the same as previously. We intend to perform prediction cycles. We have noticed, that for a number of prediction cycles greater than one, the computational cost for the fluid part is at least doubled, for any time step Δt_S. Our goal is to cut down this computational cost. An efficient way would be the following method: for every other P time steps Δt_S, perform actually two prediction cycles. For other time steps, use some information and perform only one cycle with a more efficient prediction. However, this is a little bit idealistic. Indeed, we first try to perform something easier. We first answer the following question: is there a simple way to enhance the performance of the method with IPC = 2? For each time step,

we lose information, which is the difference between our first prediction, and the final displacement of the structure.

For each prediction cycle, we use a prediction $\widetilde{X^{n+1}}$ for the structural displacement at the end of the current time step in step **2**, and we get a displacement X^{n+1} in step **3**. Then X^{n+1} is a function of $\widetilde{X^{n+1}}$. We make the assumption that this function is linear, i.e.

$$X^{n+1} = -\mathbf{a}^{n+1}\widetilde{X^{n+1}} + \mathbf{b}^{n+1}. \tag{5.60}$$

where $\mathbf{a}^{n+1}$ and $\mathbf{b}^{n+1}$ are some step-dependent coefficients. We know that, for the preceding method, stability increases with the number of prediction cycles. We also know that for an infinite number of prediction cycles, when convergence is achieved, we have $X^{n+1} = \widetilde{X^{n+1}}$, and according to (5.56) the global energy of the system is conserved. We deduce the following method:

- for the first prediction cycle, use the predictor (5.57). We write $\widetilde{X^{n+1}}^1$ for this first prediction. We get the structural displacement $\overline{X^{n+1}}$ after the first prediction cycle.
- for the second cycle: compute the value of $\mathbf{b}^{n+1}$ assuming $\mathbf{a}$ is constant by

$$\mathbf{b}^{n+1} = \overline{X^{n+1}} + \mathbf{a}^n \widetilde{X^{n+1}}^1 \tag{5.61}$$

  and use as the second prediction $\widetilde{X^{n+1}}^2$ the fixed point of the the function defined by coefficients $\mathbf{a}^n$ and $\mathbf{b}^{n+1}$, which writes

$$\widetilde{X^{n+1}}^2 = \frac{\mathbf{b}^{n+1}}{1+\mathbf{a}^n}. \tag{5.62}$$

  Finally, since we have computed two evaluations of our assumed linear function, we can update both coefficients in order to satisfy the system

$$\left\{ \begin{array}{rcl} \overline{X^{n+1}} & = & -\mathbf{a}^{n+1}\widetilde{X^{n+1}}^1 + \mathbf{b}^{n+1} \\ X^{n+1} & = & -\mathbf{a}^{n+1}\widetilde{X^{n+1}}^2 + \mathbf{b}^{n+1} \end{array} \right. \tag{5.63}$$

We present on Figure 5.19 the results of this method for the piston problem in **case 1**. We show the structural displacements for a time step $\Delta t_S = 1.8 * 10^{-3}$ for this assumed convergence method and for the simple prediction iteration method (Figure 5.16). The result is less damped and the coupled pulsation is more accurately approximated ($332s^{-1}$ instead of $317s^{-1}$, the exact value being $344s^{-1}$). We show on Figure 5.20 the corresponding results for $\Delta t_S = 0.9*10^{-3}$. Both results are really close. However, though the coupled pulsation is correctly simulated, both solutions are quite overdamped.

We conclude that the errors of the simple prediction iterations method were not corrected by our assumed convergence approach. The method produces disappointing results, and gives no hope about its ability to reduce computational costs, by reducing the proportion of time steps where actual prediction iterations are made as stated at the beginning of this section. This method is elementary. We investigate in the following section the use of numerical filters, which may be well fitted to the natural flexibility of the volume-discontinuous method.

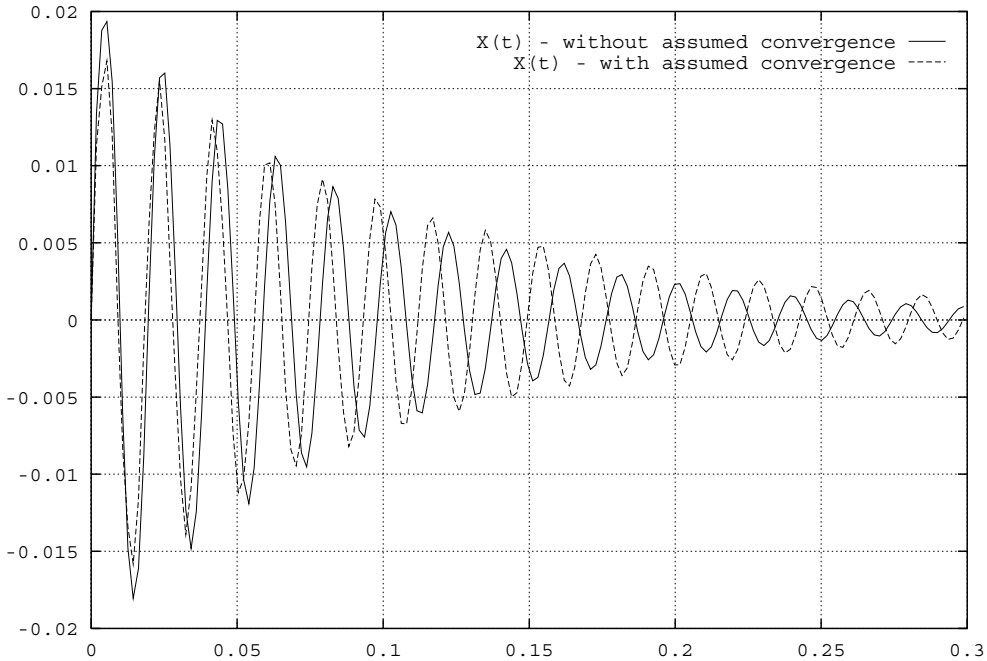

FIG. 5.19 – *$X(t)$ for the piston problem,* **case 1**, *$IPC = 2$ and $\Delta t_s = 1.8 * 10^{-3}$ (volume-discontinuous method with enhanced prediction iterations).*

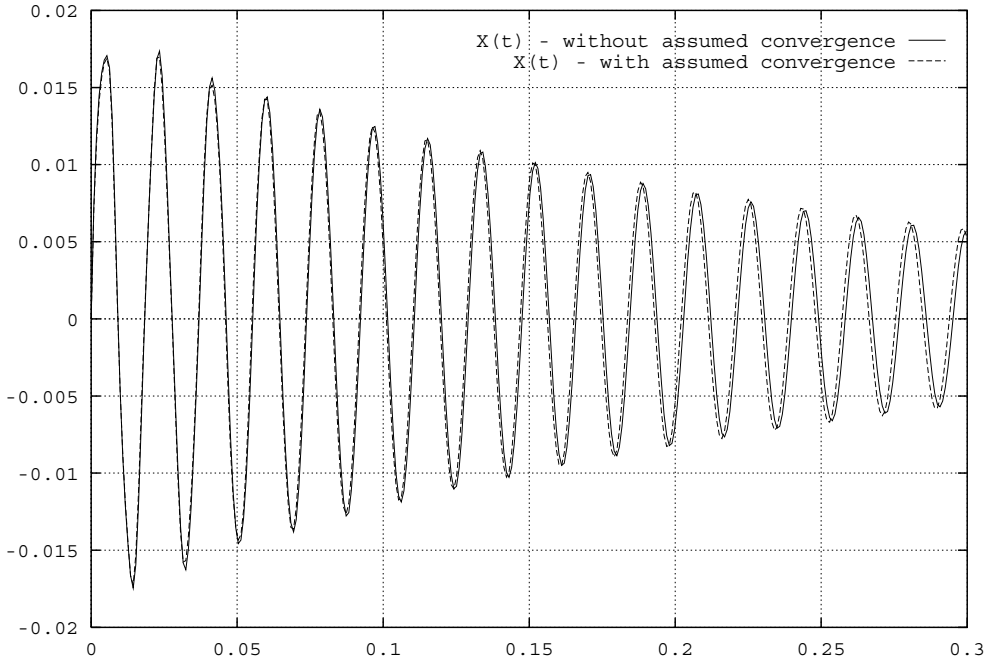

FIG. 5.20 – *$X(t)$ for the piston problem,* **case 1**, *$IPC = 2$ and $\Delta t_s = 0.9 * 10^{-3}$ (volume-discontinuous method with enhanced prediction iterations).*

Predictions using filters

If we observe numerical results presented on Figures 5.6, 5.10 and 5.12, we notice that the instability is first met by some high-frequency mode, that we could call a grid mode. As stated earlier, the volume-discontinuous method has great flexibility. We can use a smoothing prediction for the structural displacement, without applying this smoothing procedure directly to the structure, which could not have been possible with the volume-continuous method.

In order to conserve the generality of the algorithm, we base a new method on adaptive numerical filters, which are able to detect and filter some modes, without defining *a priori* the frequency. In the following, we quickly present adaptive numerical filters, and show their use to provide smooth predictions in our model problems.

Looking at Figure 5.12, we see that our prediction carries an increasing amount of noise. The transformation of this prediction into something smoother is a typical task of signal processing (a nice course on signal processing can be found in [7]). Throughout the computation, the prediction (5.57) gives successive values, which are seen as a signal. We are interested in the suppression of high-frequency modes in our incoming signal, and this can be done with numerical filters [13]. However, though we know the structural eigenfrequency, we do not assume we know the coupled eigenfrequency of the system. Then, we have to use adaptive numerical filters, which are able to detect and filter low-frequency modes [8].

In this work, we have used gradient-type adaptive numerical filters. We present now their very simple principle. Let us assume we dispose of a one-dimensional signal we would like to filter, because we know it is the sum of a sinusoidal signal and a "white" noise (denoted by ϵ), for example

$$x^n = \sin(n\omega_C \Delta t_S) + \epsilon^n \tag{5.64}$$

For a sinusoidal signal, second-order adaptive filters (depending on the two previous data x^n and x^{n-1}) are well fitted because of the following remark:

$$\epsilon^n \equiv 0 \Longrightarrow x^{n+1} - 2\cos(\omega_C \Delta t_S)\, x^n + x^{n-1} \equiv 0 \tag{5.65}$$

The idea of gradient-type adaptive filters is to consider the left term of the preceding equation as an error on the signal, since it only depends on the noise sequence ϵ. The algorithm is the following:

$$\left\{ \begin{array}{rcl} e^{n+1} & = & x^{n+1} - a_1^n x^n - a_2^n x^{n-1} \\ \left[\begin{array}{c} a_1^{n+1} \\ a_2^{n+1} \end{array} \right] & = & \left[\begin{array}{c} a_1^n \\ a_2^n \end{array} \right] + \delta \left[\begin{array}{c} x^n \\ x^{n-1} \end{array} \right] e^{n+1} \end{array} \right. \tag{5.66}$$

The reader should notice that the algorithm depends only on a user-fixed parameter δ. No approximation of the term $\omega_C \Delta t_S$ is used. We shall see in the following how the parameter δ is fixed.

The result sequence e^n is an approximation of the noise sequence ϵ^n. If we dispose of the input sequence x^n, the output filtered sequence will be $x^n - e^n$. The stability

of the algorithm is approximately proved under the assumption that the error e^{n+1} has no correlation with the previous input data (which is fairly true at convergence). Then, stability is achieved when the *a posteriori* error $x^{n+1} - a_1^{n+1}x^n - a_2^{n+1}x^{n-1}$ has a smaller expected value than the *a priori* error $x^{n+1} - a_1^n x^n - a_2^n x^{n-1}$. Thus, we have stability when

$$\delta\sigma^2 < 1 \tag{5.67}$$

where δ is the parameter used in (5.66) and σ^2 is the squared magnitude of the input noise sequence ϵ^n. Usually, the parameter δ is set far below the limit defined by (5.67), because convergence of sequences a_1 and a_2 might be achieved quicker [8]. We show on Figure 5.21 the *a priori* error sequence e^n for a typical numerical test (the noise has a unity squared magnitude and we used $\delta = 0.05$).

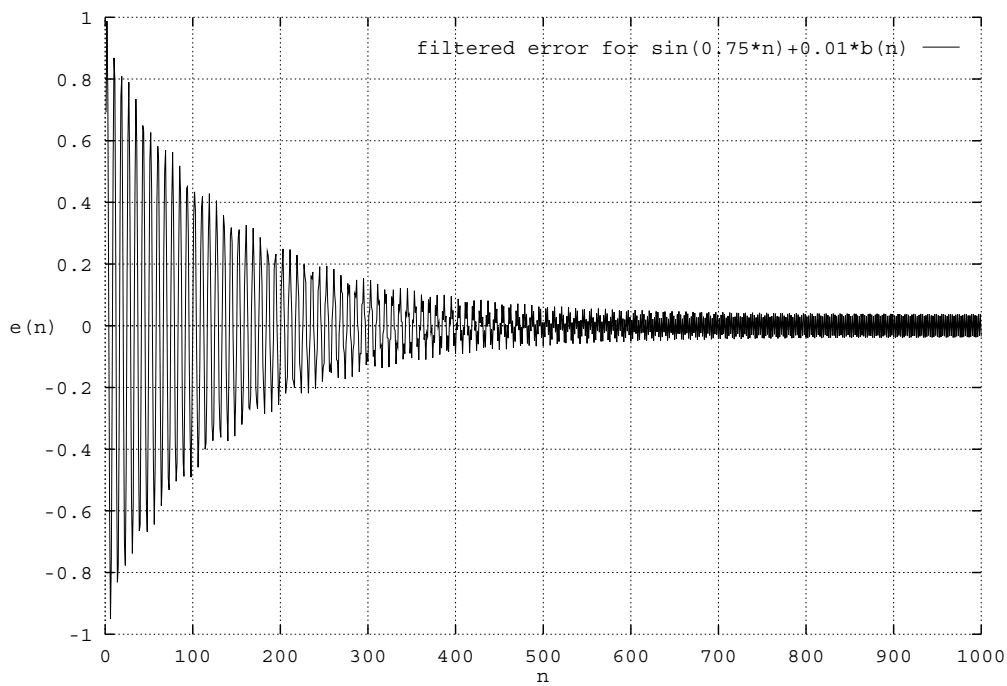

FIG. 5.21 – *a priori error for* $x^n = \sin(0.75 * n) + 0.01 * \epsilon^n$ *(*$\delta = 0.05$*)*

These filtering methods were coupled to our volume-discontinuous method in the prediction part of our algorithm (the first step; see page 157). The multiple steps of the method can be described as follows:

- the input for the method is the sequence of piston displacements X^n. When instability is reached for the simple volume-discontinuous method, we assume some numerical noise increases. We want to get rid of this noise.

- we compute the sequence $Y^{n+1} = X^{n+1} - 2X^n + X^{n-1}$. The high-frequency noise (see for example Figure 5.14) will be smoothed, and the modulus of X^n is

used for the evaluation of the squared magnitude response of Y^n. Actually, the parameter δ is fixed according to $\delta = 1/(12\sigma^2)$ where σ is the sliding maximum of X^n. Coefficients a_1 and a_2 for the sequence Y^n are deduced from the filtering.

- these elements could be sufficient to provide a prediction for the next value of Y, and then for X. However, a general characteristic of the gradient adaptive scheme presented in (5.66) is that it is not efficient for a typical signal (5.64) when the parameter $\omega_C \Delta t_S$ is too small. Thus, we filter a subsequence of Y in order to obtain a greater accuracy on the signal Y, and its parameters ($\omega_C \Delta t_S$ and the possible damping). In that step, we have to give an estimate for the coupled pulsation of the system. We use the structural lowest eigenpulsation, and this is the only problem-dependent parameter in the method.

- finally, a prediction of X^{n+1} is computed using the assumption that it is the real part of a complex exponential function of the time (or equivalently, of n).

We now present some results for the box problems in **case 2**. We show on Figure 5.22 the structural displacement for a time step $\Delta t_S = 10^{-3}$ and $n_{S/F} = 36$ (which is to be compared to Figure 5.12). The method is stable, and produces a very weak numerical damping. A result with $\Delta t_S = 3.2 * 10^{-3}$ and $n_{S/F} = 116$ is presented on Figure 5.23. In comparison with Figure 5.17, the result is very satisfying, since the coupled pulsation and the damping numerically observed are very close to those of Figure 5.17, but the cost of the simulation and the computational storage have been halved.

As a conclusion, we can say that the flexibility of the volume-discontinuous method can be and has been well used. With more or less complex predictions, we have been able to enhance subcycling stability to a satisfying point, since for the case of Figure 5.23, we have used approximately twenty time steps per coupled period of oscillation, which is a reasonable limit.

We would like to put again the emphasis on the fact that the set of predictions presented above could not be used for the volume-continuous method, since it would directly affect the structural displacement.

5.6 Discussion

In this section, we intend to discuss the possibilities of enhancements of the previous methods and their possible extensions to multi-dimensional aeroelastic problems. We first present some time-interpolation aspects for the previous methods. Then we consider the space-interpolation difficulties that may be encountered for multi-dimensional extensions.

As stated earlier, we have considered subcycled schemes in sections 5.4 and 5.5 where the time variation of the fluid mesh was given by (5.40). This method is not

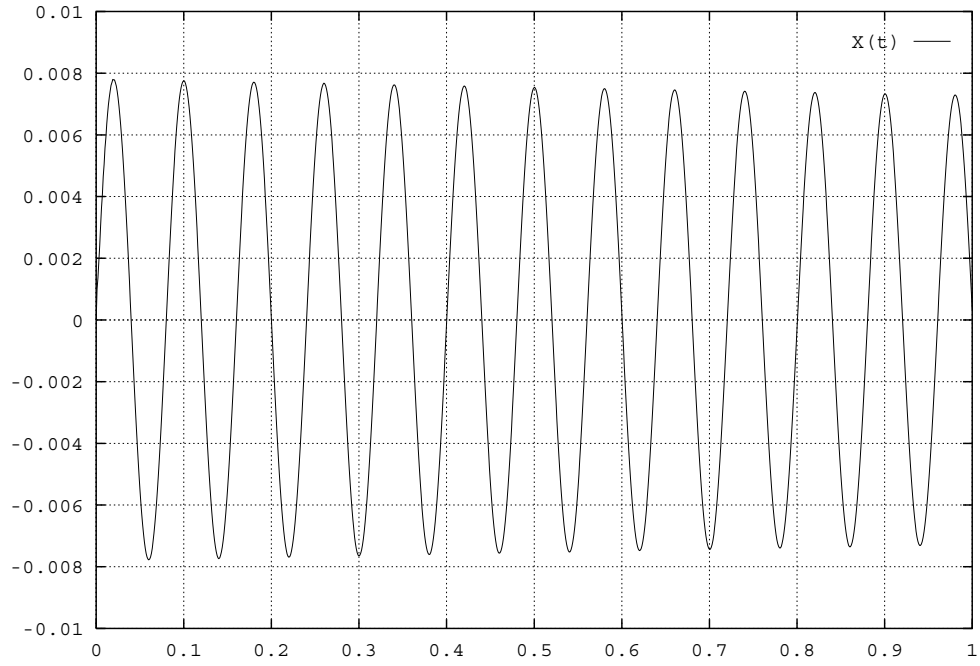

FIG. 5.22 – $X(t)$ *for the box problem,* **case 2**, $\Delta t_S = 1.0 * 10^{-3}$ *(volume-discontinuous method with filtered prediction).*

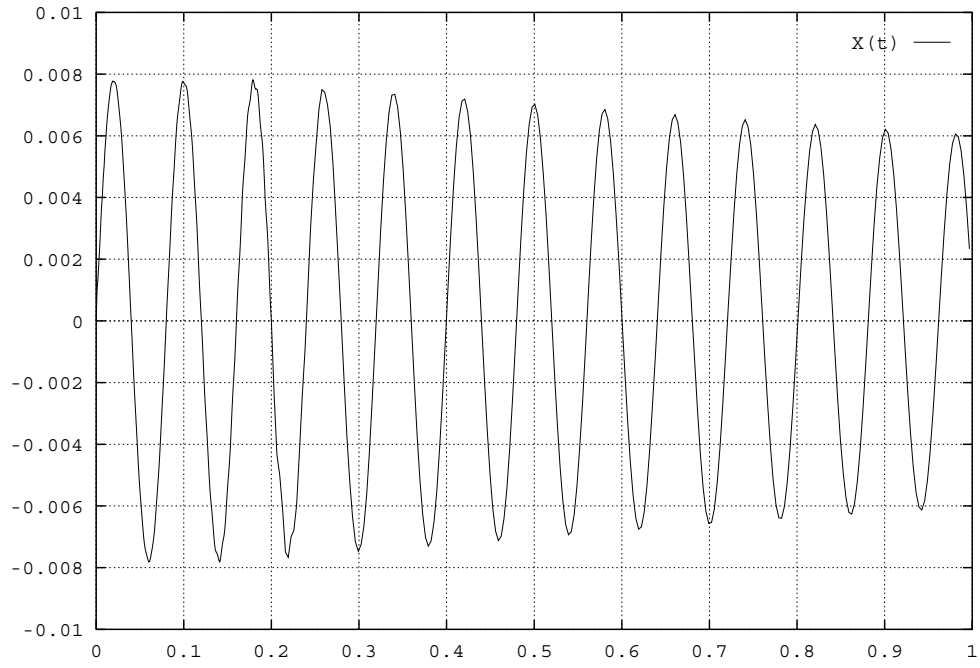

FIG. 5.23 – $X(t)$ *for the box problem,* **case 2**, $\Delta t_S = 3.2 * 10^{-3}$ *(volume-discontinuous method with filtered prediction).*

accurate, particularly when the structural time step Δt_S increases. Thus, we first investigate in the following the influence of the time interpolation of the fluid grid motion on the numerical results. Throughout this chapter, we have used the linear law of motion (5.40) for the fluid mesh during subcycles. This law of motion could be more accurate. However, in most cases, like computations corresponding to Figures 5.18-5.20, we tried with no success to reduce numerical damping. Actually, the numerical damping was caused by the use of a big structural time step Δt_S, which gave us a quite inaccurate prediction for the structural displacement at the end of the step. The inaccuracy of the linear motion of the fluid mesh was covered by the inaccuracy of the prediction.

However, some work has been done on time-interpolation aspects in cases where we disposed of a very accurate prediction of the structural displacement [77]. For example, adaptive numerical filtering produces as an output informations on the pulsation and phase of the processed signal. These informations can be easily used to construct some accurate law of motion for the fluid mesh. This was done successfully, as shown on Figure 5.24, which presents another result for the same test case as Figure 5.23.

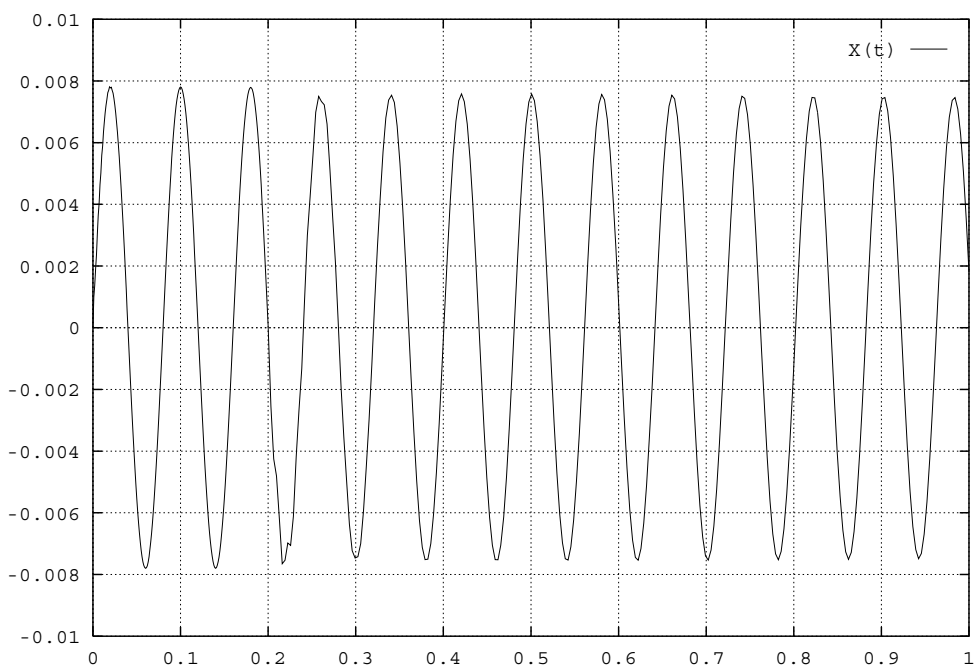

FIG. 5.24 – *$X(t)$ for the box problem,* **case 2**, $\Delta t_S = 3.2 * 10^{-3}$ *(volume-discontinuous method with filtered structural prediction and non-linear fluid mesh motion).*

The structural displacement is very slightly damped. This damping was produced by the numerical viscosity added in the fluid by the explicit first-order numerical scheme. The preceding result is quite optimal, since damping and pulsation are well simulated, and stability is conserved though $\omega_C \Delta t_S = 0.25$ (which corresponds to 25 time steps per coupled period of oscillations).

We also tested the generalized-α method we presented in (5.21-5.23). This method was constructed to control and possibly reduce high-frequency modes with a user-specified high-frequency dissipation. However, the generalized-α method is used for the structure only. In the test cases we considered in this chapter, the structure is reduced to a point and the only eigenfrequency is low. Then the generalized-α method may not have any influence on high-frequency coupled modes. This was numerically confirmed. The generalized-α method will be used in future works for complex structures.

As said before, our structure has only one degree of freedom. We then have not mentionned any spatial interpolation problem at the fluid-structure interface. This might be the least easy part of the extension of these methods to multi-dimensional cases. In the case where the fluid and the structural meshes are conforming (same vertices at the common interface), the extension of the volume-continuous method is easy. For the volume-discontinuous method, and for the volume-continuous method when both grids are not conforming, the extension is a little more complex. Both methods should be added a procedure allowing the transfer of pressure forces and structural displacements between the fluid and the structure. Actually, the most part of industrial test cases are non-conforming (the fluid and structural spatial discretizations are different). This kind of procedure has already been implemented (see [53] for example).

We shall focus the next chapter on the extension of the methods presented in the present chapter to two-dimensional problems: the Euler flutter analysis of a two degree of freedom classical NACA airfoil in transonic regime and the supersonic flutter of a panel with a large number of degrees of freedom. Our aim will be the use of subcycling schemes, which allow a limited number of structural time-integrations (optimal would be twenty-five as in the box problem seen previously) per coupled period of oscillations.

Chapitre 6

Two-dimensional Euler aeroelastic simulations

6.1 Introduction

Fluid-structure interaction and, more particularly, aeroelasticity are such fields, where numerical simulation can be used to improve the physical understanding of coupled instabilities, appearing for instance in aircrafts [31] or suspended-span bridges [68]. However, the direct totally coupled resolution is still out of reach. Actually, we have at our disposal complex, efficient and robust numerical methods for both the simulations of a structure and a fluid flow, and the natural way to predict the aeroelastic behavior of a flexible structure in a fluid flow, would be resulting from the coupling of methods for both decoupled fields [32].

They have to be solved simultaneously. The structure defines a part of the fluid field boundary, while the fluid exerts a pressure force along the fluid-structure interface. The fluid domain varies in time, and the resolution has to be performed on a moving mesh. Among a set of existing methods [61], we have chosen the use of dynamic meshes [5] for an Arbitrary Lagrangian-Eulerian (ALE-[20]) formulation of Euler equations.

Since we intend to simulate coupled phenomena involving Structural Dynamics and Fluid Dynamics, we are genuinely interested in the actual coupling of existing methods. In the previous chapters, we first studied the influence and the control of side-effects of several coupling methods for a simple linear one-dimensional problem [64]. Even if CFD and SD methods are accurate and efficient, we have found that the global coupling scheme is very important. However, new schemes have been elaborated on coupled linear one-dimensional problems [63], that ensure properties often verified by each decoupled fields methods, like for instance stability and conservation. These methods are simply extended to non-linear Euler one-dimensional aeroelastic cases, but with no theoretical proof of their properties. However, the use of techniques issued from signal processing and the formulation of a new type of volume-discontinous methods allowed us to achieve accuracy and robustness [62].

In this chapter, we extend these volume-discontinuous methods to two-dimensional Euler aeroelastic simulations. The first physical problem consists of a NACA airfoil

profile in rigid motion in transonic fluid flow. We deal with a two degree-of-freedom structural model. The second problem is the simulation of the supersonic panel flutter of a plate. We intend to use implicit unconditionally stable methods for the structure. On the contrary, we use an explicit time-integration scheme for the fluid, and we intend to investigate the possibility of subcycling the fluid. This subcycling would allow us to perform much less structural integrations, while the fluid time-step is limited by CFL-like conditions. A successful subcycling mixed with inter-field parallelism can significantly reduce the total solution time [24]. We shall discuss the computational savings in this chapter only for the second problem, since the integration of a two-degree-of-freedom airfoil in rigid motion requires a very small computational time, compared with the fluid. This is not the case in the second problem, and generally in multiple degree-of-freedom structures or three-dimensional cases.

We begin in Section 6.2 with the presentation of the physical problems we consider: first, a rigid, two-degree-of-freedom NACA-0012 airfoil profile in an inviscid 2D Euler fluid flow, and second, a flat panel under a supersonic flow. Structural and fluid equations are set, and the boundary conditions at the far-field fluid boundary and at the fluid-structure interface are detailed. We show that these two-dimensional model problems are important steps on our way to complex, non-linear, three-dimensional aeroelastic configurations.

In Section 6.3, we present the whole set of CFD and CSD methods we use for the resolutions of decoupled fields. For the fluid, we introduce the algorithm for the fluid grid motion, the ALE formulation of Euler equations in this moving grid and the numerical method we use: a Godunov's type finite-volume method based on a MUSCL-type second-order extension of Roe's flux. We reformulate the structural equations into a matricial form in order to use a simple trapezoidal rule.

In Section 6.4, we review the enhancements we made on numerical methods that are necessary for the effective coupling of both fields. We start from the simple subcycled algorithm presented in [46]. We then add time-averaging in aeroelastic forces exerted on the structure and we introduce the version of our volume-discontinuous methods in two dimensions. We discuss the role of the structural prediction we use, and particularly the global energy and momentum conservations. We finally study some precise points of the grid motion and updating methods.

In Section 6.6, we finally present the global coupling algorithm which gave the most accurate results with the best efficiency, which is strictly related to the subcycling factor.

6.2 The physical problems

We present here the two aeroelastic problems we try to simulate. They are clearly more complex than the one-dimensional (linear and non-linear) problems we considered in the previous chapters, which had only a single degree of freedom. They are non-linear (Euler equations for the fluid), two-dimensional and with multiple degrees of freedom.

The rigid NACA airfoil problem is quite simple compared to the flat panel under a transonic flow. In both cases, we are interested in simulating the flutter of the structure (and in giving good predictions of the conditions where instablility is reached).

6.2.1 The rigid NACA airfoil in transonic inviscid flow

We are interested in the numerical simulation of the two-dimensional inviscid flow around a transonic wing profile (a NACA airfoil). This case is a simplification of future three-dimensional test-cases, where the fluid domain surrounds the global body of an aircraft. This kind of simulation allows aircraft designers to know the characteristics of their wings/planes when they are coupled with the fluid flow, at a lower cost.

As we have described it before, the fluid and the structure are interacting, and an occuring phenomenon is necessarily coupled. Anyway, such a simulation requires some knowledges in the fields of both fluid and structural dynamics and their corresponding computational know-hows. In the following, we describe successively the model equations for the fluid and the airfoil. We also review in detail boundary conditions for the flow and source terms for the airfoil.

Structural equations

The structure is a simple NACA airfoil profile, which is assumed rigid. Only two degrees of freedom are given: the vertical displacement h and the rotation θ around the center of rotation. We expect to apply the methods not only to this simple case, but also to multiple degree of freedom problems, like the panel flutter or those considered in [63, 26]. Equations for the evolutions of h and θ are given in [46]. They are written in a dimensionalized form:

$$\left\{ \begin{array}{rcl} m\ddot{h} + S_\theta \ddot{\theta} + c_h \dot{h} + k_h h & = & F_h \\ S_\theta \ddot{h} + I_\theta \ddot{\theta} + c_\theta \dot{\theta} + k_\theta \theta & = & F_\theta \end{array} \right. \tag{6.1}$$

where m, I_θ and S_θ denote respectively the mass of the profile, and the inertial and static moments of the profile around the elastic center; c_h and c_θ are damping coefficients for each degree of freedom, and k_h and k_θ are the corresponding stiffness coefficients. Finally, F_h and F_θ are the lift and moment (around the elastic center located at $a_h b$) exerted on the profile by the fluid. The profile is described on Figure 6.1.

We now give the values for the coefficients defining the structure. First, we make three choices fixing the physical unities for mass, length and time (see Table 6.1-1). Unities can be easily modified by changing these entries.

The structure is then defined through numbers without dimension. They are listed on Table 6.1-2. Finally, all parameters used in (6.1) are given by the following set of equations:

$$\left\{ \begin{array}{rcl} b & = & c/2 \\ \omega_h & = & \lambda \omega_\theta \\ k_h & = & m\omega_h^2 \\ c_h & = & 2\xi_h \omega_h m \end{array} \right. \qquad \left\{ \begin{array}{rcl} S_\theta & = & mbx_\theta \\ I_\theta & = & mb^2\gamma_\theta^2 \\ k_\theta & = & I_\theta \omega_\theta^2 \\ c_\theta & = & 2\xi_\theta \omega_\theta I_\theta \end{array} \right. \tag{6.2}$$

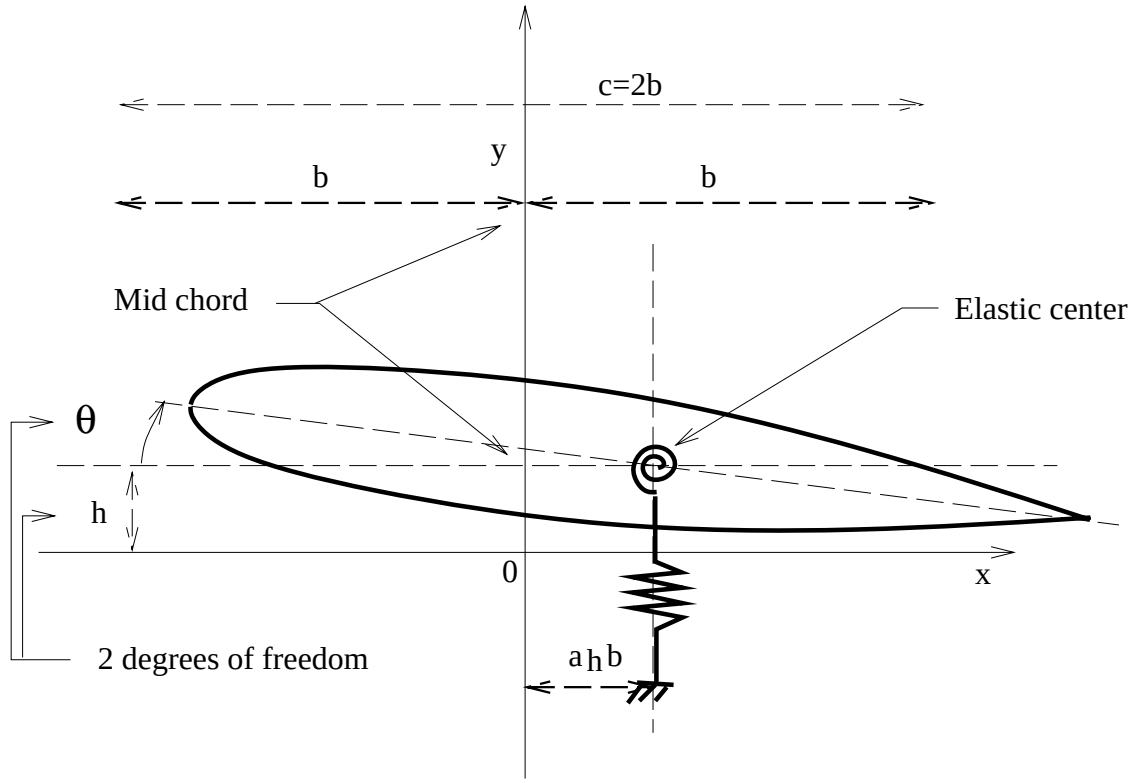

FIG. 6.1 – *The two degree-of-freedom airfoil*

We now come back to the lift and moment coefficients F_h and F_θ. The pressure force of the fluid is exerted along the airfoil profile Γ, which is detailed on Figure 6.2. The coefficients are given by :

$$F_h = \int_\Gamma p\vec{n}.\vec{j}ds \tag{6.3}$$

$$F_\theta = \int_\Gamma p(\vec{r} \times \vec{n})_z ds \tag{6.4}$$

where $\vec{r}$ is the location vector taken from the center of elasticity, as shown on Figure 6.2.

m	1.0 Kg
c	1.0 m
ω_θ	100 s^{-1}

a_h	-1
x_θ	1.8
ξ_θ	0
ξ_h	0
γ_θ	1.865
λ	1

TAB. 6.1 – *Unity fixing assumptions and coefficients without dimension.*

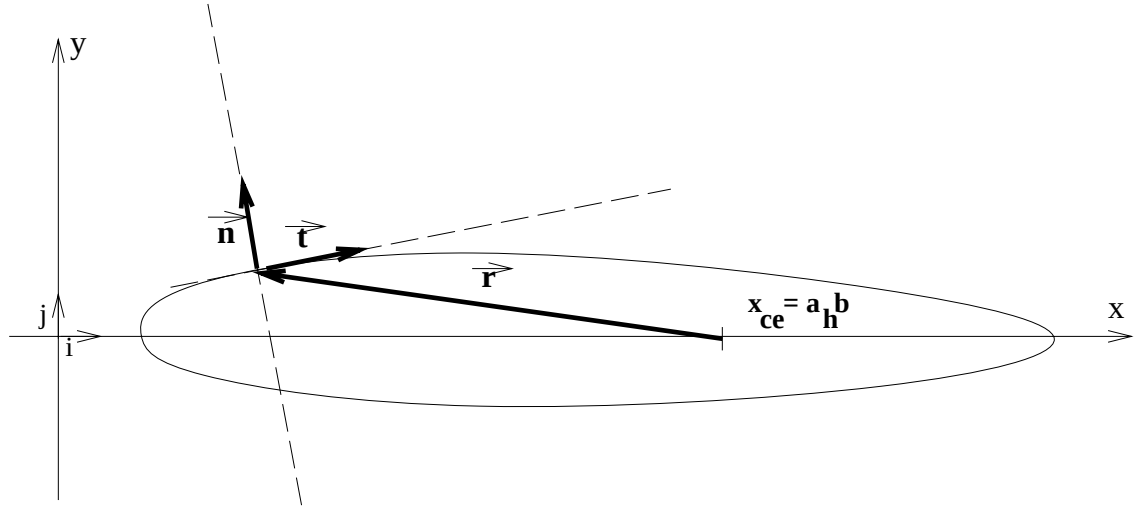

FIG. 6.2 – *Detail of the integration of F_h and F_θ.*

Equations for the fluid

We consider a perfect gas flowing around the airfoil profile. We assume the flow is uniform at infinity in any direction. For computational simplifications, we assume the vector W of conservative variables is constant and equal to W_∞ outside the farfield fluid boundary Γ_∞ (see Figure 6.3). The reader should notice that Γ_∞ is assumed fixed and that the airfoil profile moves. Thus, we should now write $\Gamma(t)$ for the time-dependent location of the airfoil profile. Then, the fluid domain $\Omega(t)$ between Γ_∞ and $\Gamma(t)$ is also time-dependent.

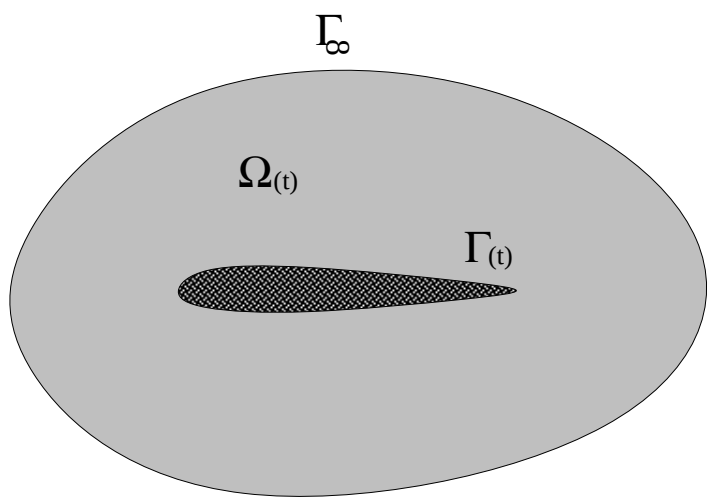

FIG. 6.3 – *The time-dependent fluid domain.*

The fluid is assumed inviscid and satisfies Euler equations. The vector of conserva-

tive variables W is given by :

$$W = \begin{pmatrix} \rho \\ \rho u \\ \rho v \\ E \end{pmatrix} , \tag{6.5}$$

where ρ, u, v and E respectively denote the density, the velocity along the x-axis and the y-axis, and the volumic total energy. Euler equations then write

$$\begin{pmatrix} \rho \\ \rho u \\ \rho v \\ E \end{pmatrix}_t + \begin{pmatrix} \rho u \\ \rho u^2 + P \\ \rho uv \\ (E+P)u \end{pmatrix}_x + \begin{pmatrix} \rho v \\ \rho uv \\ \rho v^2 + P \\ (E+P)v \end{pmatrix}_y = 0 , \tag{6.6}$$

where the pressure P is given by the law of perfect gas

$$P = (\gamma - 1)\left(E - \frac{1}{2}\rho(u^2 + v^2)\right) \text{ with } \gamma = 1.4 . \tag{6.7}$$

The boundary conditions for the fluid are the following:

1. $\underline{W = W_\infty}$ along the farfield boundary Γ_∞
2. $\underline{\vec{u}.\vec{n} = \dot{\vec{r}}.\vec{n}}$ along the moving profile $\Gamma(t)$ (we have written $\vec{u} \equiv (u, v)^t$ for the fluid vectorial velocity, $\vec{r}$ for the location of the generic point on the profile, $\vec{n}$ for the local normal to the profile and the dot stands for a time-derivative).

The whole problem will be completly set if we give the value of W_∞. As functions of the user-specified non-dimensionalized parameters M_∞, $V^\star$ and μ (some typical values are given on Table 6.2), the fluid values at infinity are given by

$$\left\{ \begin{array}{rcl} \rho_\infty & = & \dfrac{m}{\pi \mu b^2} \\ (u_\infty \ v_\infty) & = & (b\omega_\theta V^\star \ 0) \\ P_\infty & = & \dfrac{\rho_\infty u_\infty^2}{\gamma {M_\infty}^2} \\ E_\infty & = & \dfrac{P_\infty}{\gamma - 1} + \dfrac{1}{2}\rho_\infty u_\infty^2 \end{array} \right. \tag{6.8}$$

M_∞	0.8
$V^\star$	5.477
μ	60

TAB. 6.2 – *Coefficients without dimension defining the fluid at infinity.*

The problem is defined by the nine non-dimensionalized parameters given on Table 6.1-2 and Table 6.2, and the three unity fixing dimensionalized values given on Table 6.1-1.

This problem is of interest because flutter can appear when the Mach number increases. We will use a transonic $M_\infty = 0.8$ which is slightly over the instability limit. We present on Figure 6.4 the density contours when flutter is reached. We see two supersonic zones and two shocks under and above the airfoil. The shocks oscillate back and forth with the airfoil. This oscillation produces a negative damping, and finally the instability.

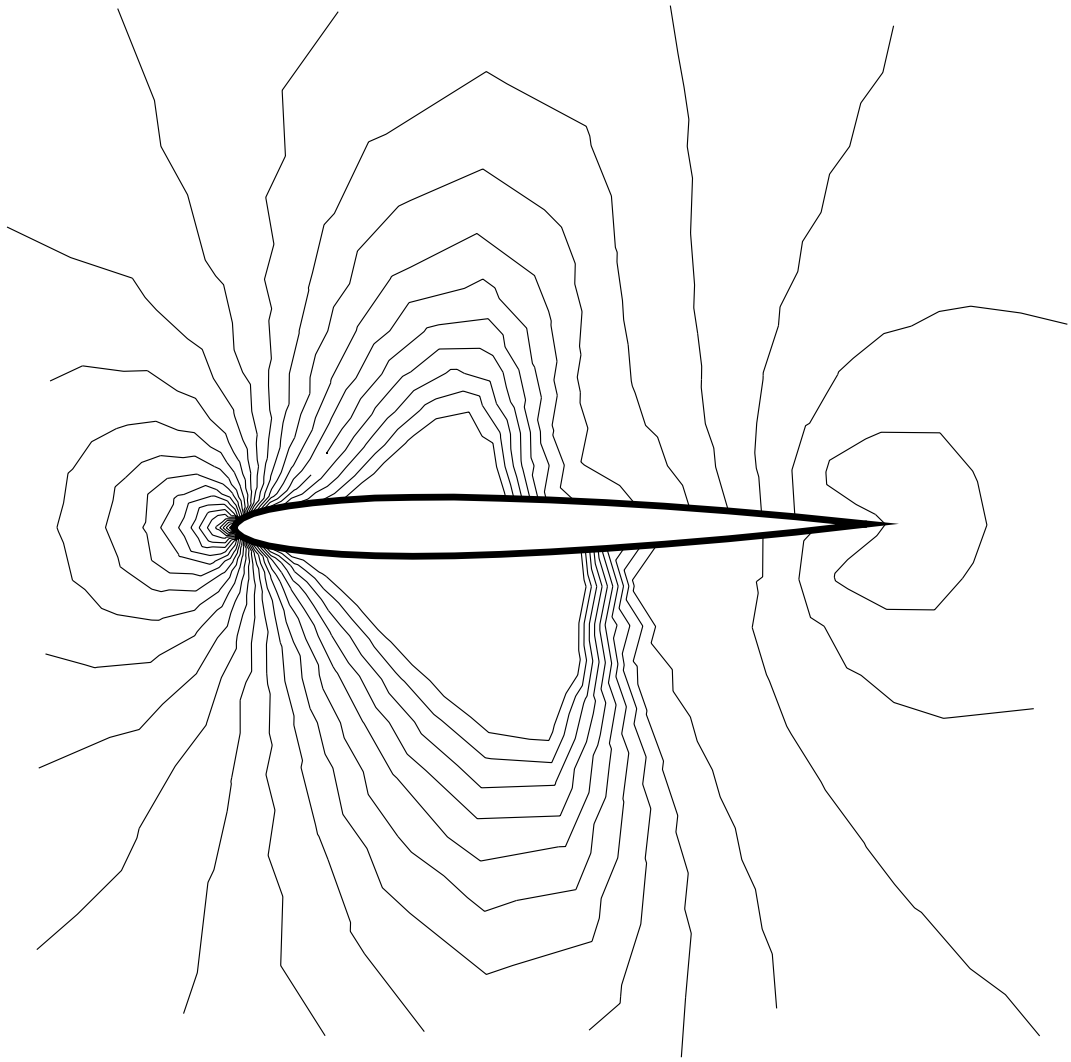

FIG. 6.4 – *Non-dimensionalized density ($Min = 0.7$, $Max = 1.3$) under flutter.*

6.2.2 Flat panel under supersonic inviscid flow

We also test our numerical methods on a more complex problem. We consider a flat panel with infinite aspect ratio in a supersonic airstream. We investigate the instability of such a panel, and we try to simulate the panel flutter described on page 418 and

following of [11]. This case is not far from the case presented in Chapter 4. We deal with the same test case as in [26]. This problem concerns the behavior of a surface skin panel that has one side exposed to an airstream and the other side to still air. We now describe the equations for the fluid and the structure. We also give a short sketch of the linear instability study of flat panels with infinite aspect ratio presented in [11].

Structural equations

The flat panel with infinite aspect ratio suits well with two-dimensional fluid flow simulation. The whole test case can be seen as a degenerated three-dimensional problem. The panel (Figure 6.5) is given a length $L = 0.5\ m$, a uniform thickness $h = 1.35\ 10^{-3}\ m$, a Young modulus $E = 7.728\ 10^{10}\ N/m^2$, a Poisson ratio $\nu = 0.33$ and a density $\rho_S = 2710\ Kg/m^3$ (these default values might be changed in the following). The panel is clamped at both ends (points $x = 0$ and $x = L$).

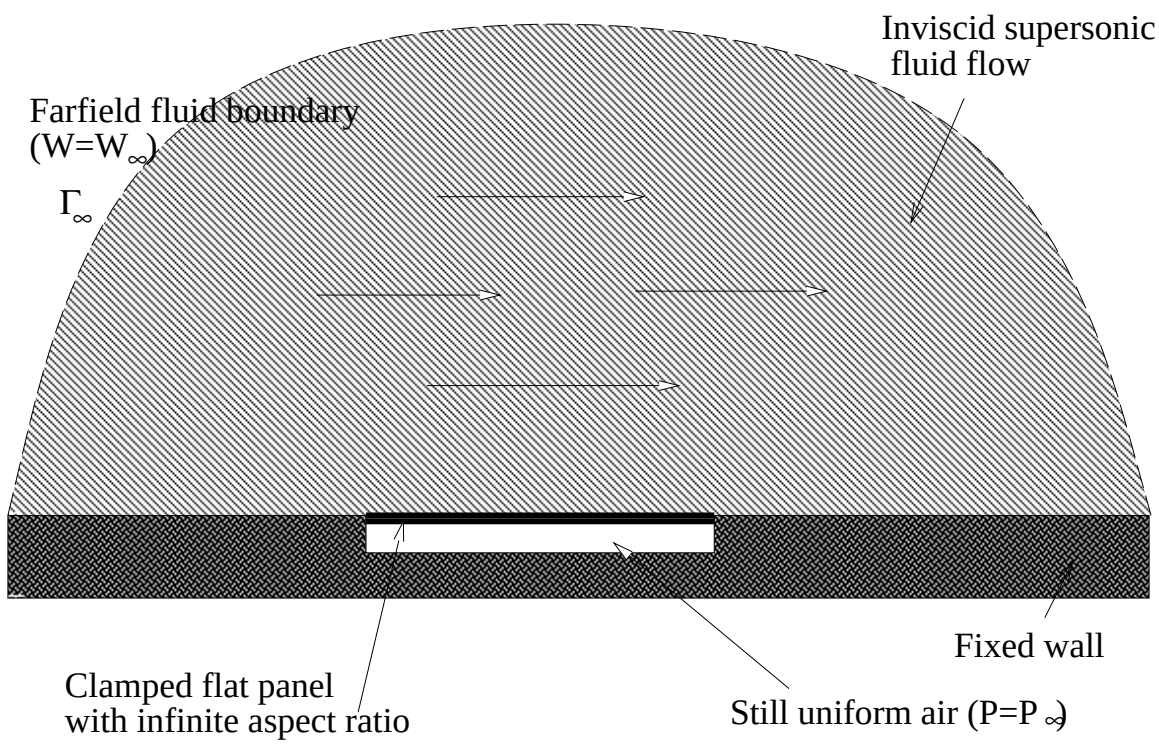

FIG. 6.5 – *The flat panel with infinite aspect ratio.*

The structure is modelized and discretized in several different ways. First, we base our study upon the shallow shell theory. The equation for the initially flat panel fea-

tures the small lateral (vertical) deflection X. We assume that this deflection constitutes the sole dependent variable of the structural part of the problem.

The continuous structural equation for this model writes:

$$m_0 \frac{\partial^2 X}{\partial t^2} + D \frac{\partial^4 X}{\partial x^4} = F, \tag{6.9}$$

where F is the field of vertical forces applied to the panel (it is given by $F(x) = d(P(x) - P_\infty)$, P_∞ being also the still air pressure, and has the dimension of N/m), m_0 is the lineic mass of the panel (the depth of the panel is infinite, but taken equal to $d = 1\ m$ for the simulation). m_0 and D are given by

$$\begin{aligned} m_0 &= \rho_S h d, \\ D &= \frac{E h^3 d}{12(1-\nu^2)}. \end{aligned} \tag{6.10}$$

The structure is discretized regularly into $N_x + 1 = 300$ intervals ($N_x = 299$ degrees of freedom). A finite-difference formulation is used. The mass matrix M is lumped, and the stiffness operator K (bi-laplacian) is obtained via classical finite-differences. There is no structural damping. M and K are given by

$$M = m_0 \Delta x \begin{pmatrix} 1 & & 0 \\ & \ddots & \\ 0 & & 1 \end{pmatrix}, \quad K = \frac{D}{\Delta x^3} \begin{pmatrix} 6 & -4 & 1 & & & 0 \\ -4 & \ddots & \ddots & \ddots & & \\ 1 & \ddots & \ddots & \ddots & \ddots & \\ & \ddots & \ddots & \ddots & \ddots & 1 \\ & & \ddots & \ddots & \ddots & -4 \\ 0 & & & 1 & -4 & 6 \end{pmatrix}, \tag{6.11}$$

where the spatial step Δx is given by $\Delta x = L/N_x$.

We have also tested some different modelizations. For example, we tried a finite-element formulation on two modelizations for our panel based on beams. Each point was given two degrees of freedom (vertical deflection and rotation of the panel) or three degrees of freedom (vertical and horizontal deflections, and rotation). The mass was lumped, and the stiffness matrix of each beam element was respectively given by K^2_{el} and K^3_{el} for two and three degrees of freedom per point:

$$K^2_{el} = \frac{D}{\Delta x^4} \begin{pmatrix} 12 & 6\Delta x & -12 & 6\Delta x \\ 6\Delta x & 4\Delta x^2 & -6\Delta x & 2\Delta x^2 \\ -12 & -6\Delta x & 12 & -6\Delta x \\ 6\Delta x & 2\Delta x^2 & -6\Delta x & 4\Delta x^2 \end{pmatrix}, \tag{6.12}$$

$$K_{el}^3 = \begin{pmatrix} \frac{ES}{\Delta x^2} & 0 & 0 & -\frac{ES}{\Delta x^2} & 0 & 0 \\ 0 & \frac{12D}{\Delta x^4} & \frac{6D}{\Delta x^3} & 0 & -\frac{12D}{\Delta x^4} & \frac{6D}{\Delta x^3} \\ 0 & \frac{6D}{\Delta x^3} & \frac{4D}{\Delta x^2} & 0 & -\frac{6D}{\Delta x^3} & \frac{2D}{\Delta x^2} \\ -\frac{ES}{\Delta x^2} & 0 & 0 & \frac{ES}{\Delta x^2} & 0 & 0 \\ 0 & -\frac{12D}{\Delta x^4} & -\frac{6D}{\Delta x^3} & 0 & \frac{12D}{\Delta x^4} & -\frac{6D}{\Delta x^3} \\ 0 & \frac{6D}{\Delta x^3} & \frac{2D}{\Delta x^2} & 0 & -\frac{6D}{\Delta x^3} & \frac{4D}{\Delta x^2} \end{pmatrix}, \tag{6.13}$$

where the cross section S is simply given by

$$S = hd. \tag{6.14}$$

We verified that these beam models, as well as the shallow shell model of our flat panel gave the same structural eigenfrequencies. We found

$$\begin{aligned} \omega_1 &= 196 s^{-1}, \\ \omega_2 &= 540 s^{-1}, \end{aligned} \tag{6.15}$$

for all three models, with very little differences (actually, the accuracy of each discretization has an influence on the results).

However, all these formulations gave stiffness matrices with a limited number of diagonals, because all models were rather one-dimensional. In order to test our numerical methods in cases where the time integration of the structure is expensive, we finally tried an actual two-dimensional modelization. It was a fine-element formulation based on a plane-stress three-dimensional elastic model. The structure is discretized in N_x horizontal and N_y vertical quadrilateral isoparametric elements (in a structured way). The elements were numbered the cheapest way (vertically and then horizontally). Each point of the mesh was given two degrees of freedom (vertical and horizontal deflections). For example, the stiffness matrix of one quadrilateral isoparametric element (actually, a rectangle $\Delta x \times \Delta y$ with $\Delta x = L/N_x$ and $\Delta y = h/N_y$) writes:

$$\frac{Ed}{1-\nu^2}\begin{pmatrix}
\phi+\frac{\nu'\psi}{2} & \frac{1+\nu}{8} & \frac{\nu'\psi}{4}-\phi & -\frac{1-3\nu}{8} & \frac{\phi-\nu'\psi}{2} & \frac{1-3\nu}{8} & -\frac{2\phi+\nu'\psi}{4} & -\frac{1+\nu}{8} \\
 & \psi+\frac{\nu'\phi}{2} & \frac{1-3\nu}{8} & \frac{\psi-\nu'\phi}{2} & -\frac{1-3\nu}{8} & \frac{\nu'\phi}{4}-\psi & -\frac{1+\nu}{8} & -\frac{2\psi+\nu'\phi}{4} \\
 & & \phi+\frac{\nu'\psi}{2} & -\frac{1+\nu}{8} & -\frac{2\phi+\nu'\psi}{4} & \frac{1+\nu}{8} & \frac{\phi-\nu'\psi}{2} & -\frac{1-3\nu}{8} \\
 & & & \psi+\frac{\nu'\phi}{2} & \frac{1+\nu}{8} & -\frac{2\psi+\nu'\phi}{4} & \frac{1-3\nu}{8} & \frac{\nu'\phi}{4}-\psi \\
 & & & & \phi+\frac{\nu'\psi}{2} & -\frac{1+\nu}{8} & \frac{\nu'\psi}{4}-\phi & \frac{1-3\nu}{8} \\
 & & & & & \psi+\frac{\nu'\phi}{2} & -\frac{1-3\nu}{8} & \frac{\psi-\nu'\phi}{2} \\
 & \text{symmetric part of} & & & & & \phi+\frac{\nu'\psi}{2} & \frac{1+\nu}{8} \\
 & \text{the matrix} & & & & & & \psi+\frac{\nu'\phi}{2}
\end{pmatrix} \tag{6.16}$$

where we have used

$$\begin{aligned}
\nu' &= 1-\nu \\
\phi &= \frac{\Delta y}{3\Delta x} \\
\psi &= \frac{\Delta x}{3\Delta y}.
\end{aligned}$$

The quadrilateral isoparametric elements have well-known defaults. They have a quite poor accuracy (a lot of elements are needed to obtain the eigenfrequencies of the structure with an acceptable accuracy) and are easily subject to "mesh locking" (decline of accuracy with shape distortion) when the aspect ratio of elements is very different from 1.

Anyway, all these modelizations produce mass and stiffness matrices. In all cases, there is no structural damping. The fluid pressure force is simply transferred from the fluid to the structure when both the fluid and structural meshes are matching. The computation of the applied pressure forces will be detailed later in the non-matching cases. Also, the fluid pressure applied from the still air under the panel is constant and equal to P_∞.

Fluid equations

The fluid equations are the same as (6.5)-(6.7). The fluid domain is enclosed between Γ_∞, the fixed wall and the clamped flat panel. This domain has partially moving

boundaries. The boundary conditions are the following:

- $\underline{W = W_\infty}$ along the farfield fluid boundary Γ_∞. The state vector W_∞ is supersonic with an horizontal velocity. It is completely defined by the pressure $P_\infty = 25714\ Pa$, the density $\rho_\infty = 0.4\ Kg\ m^{-3}$ and the Mach number M_∞ (which will be taken greater than 2 - these cases are completely supersonic). We have

$$W_\infty = \begin{pmatrix} \rho_\infty \\ \rho_\infty M_\infty \sqrt{\dfrac{\gamma P_\infty}{\rho_\infty}} \\ 0 \\ P_\infty \left(\dfrac{1}{\gamma - 1} + \dfrac{\gamma M_\infty}{2} \right) \end{pmatrix}. \tag{6.17}$$

- $\underline{v = 0}$ (we recall v is the vertical velocity of the fluid) along the fixed wall (slip condition)

- $\underline{\vec{u}.\vec{n} = \dot{\vec{r}}.\vec{n}}$ (where $\vec{u} = (u\ v)^t$ is the fluid velocity, $\vec{n}$ is the local normal to the panel and $\dot{\vec{r}}$ is the local speed of the interface) along the fluid-panel interface. This is also a slip condition.

Instability of flat panels with infinite aspect ratio

In the next lines, we take the time to give a quick sketch of a simplified analytical study on the linear instability of a flat panel with infinite aspect ratio. This study was found in detail in [11].

For this analysis based upon the shallow shell theory, we use a first-order approximation of the aerodynamic theory. We neglect the influence of three-dimensional aerodynamic effects and limit our results to Mach numbers beyond approximately 1.6.

We assume that the deflection X of the structure is very small, so that we can achieve a linear stability analysis. We make also the additional assumptions that the problem is actually two-dimensional (infinite aspect ratio, no variable depends of the y coordinate perpendicular to the plane of Figure 6.5) and that the clamped panel is free of initial stress. Then, the fluid pressure forces in (6.9) can be simply expressed as a function of the vertical deflection X, and the global aeroelastic equation now writes

$$m_0 \frac{\partial^2 X}{\partial t^2} + D \frac{\partial^4 X}{\partial x^4} = -\frac{d\rho_\infty u_\infty^2}{\sqrt{M_\infty^2 - 1}} \frac{\partial X}{\partial x} - \frac{d\rho_\infty u_\infty (M_\infty^2 - 2)}{(M_\infty^2 - 1)^{3/2}} \frac{\partial X}{\partial t}, \tag{6.18}$$

where $u_\infty \equiv M_\infty \sqrt{\dfrac{\gamma P_\infty}{\rho_\infty}}$ is the gas velocity at infinity. The boundary conditions for the deflection X (clamped panel) are:

$$X(0) = X(L) = \frac{\partial X}{\partial x}(0) = \frac{\partial X}{\partial x}(1) = 0. \tag{6.19}$$

Then we seek a complex solution to (6.18) with the boundary conditions (6.19) of the following form:

$$\forall x \in [0; L],\ \forall t,\ X(x,t) = \overline{X}(x)e^{\alpha t}, \tag{6.20}$$

where α is a complex pulsation and $\overline{X}$ is a complex amplitude (we then have to take the real or the imaginary part of the previous solution). Then $\overline{X}$ is solution of (6.18) if and only if

$$\frac{\partial^4 \overline{X}}{\partial x^4} + \lambda \frac{\partial \overline{X}}{\partial x} + k\ \overline{X} = 0. \tag{6.21}$$

where we have taken

$$\left\{ \begin{array}{rcl} \lambda & = & \dfrac{d\rho_\infty u_\infty^2}{D\sqrt{M_\infty^2 - 1}} \\ \\ k & = & \dfrac{m_0}{D}\ \alpha^2 + \lambda\ \dfrac{M_\infty^2 - 2}{u_\infty\,(M_\infty^2 - 1)}\ \alpha \end{array} \right. \tag{6.22}$$

For example, the previous equations allow us to find the natural pulsations of the simply supported flat panel (in that case, boundary conditions are $X(0) = X(L) = X''(0) = X''(1) = 0$). If the fluid is omitted ($\rho_\infty = 0$), obvious solutions take the form

$$\begin{array}{rcl} \overline{X}(x) & = & \sin\left(\dfrac{n\pi x}{L}\right) \quad \text{and} \quad \alpha = i\omega_n, \\ k & = & -\dfrac{m_0\omega_n^2}{D} \quad \text{from (6.22)}, \\ k & = & -\dfrac{n^4\pi^4}{L^4} \quad \text{(boundary condition at } L) \\ \text{which gives} \quad \omega_n & = & n^2\pi^2\sqrt{\dfrac{D}{m_0 L^4}}. \end{array}$$

We get back to the coupled problem. If we put $\overline{X}(x) = e^{px}$, we obtain the characteristic equation

$$p^4 + \lambda p + k = 0, \tag{6.23}$$

which has four complex roots

$$\left\{ \begin{array}{rcl} p_1 & = & -\epsilon + b \\ p_2 & = & -\epsilon - b \\ p_3 & = & \epsilon + ic \\ p_4 & = & \epsilon - ic \end{array} \right. \tag{6.24}$$

where the complex numbers b, c and ϵ satisfy the system

$$\begin{array}{rcl} b^2 & = & \dfrac{\lambda}{4\epsilon} - \epsilon^2 \\ c^2 & = & \dfrac{\lambda}{4\epsilon} + \epsilon^2 \\ k & = & -2\epsilon^2 + \dfrac{\lambda^2}{16\epsilon^2}. \end{array}$$

In terms of the four roots in (6.24), we take the amplitude equal to

$$\overline{X}(x) = A_1 e^{p_1 x} + A_2 e^{p_2 x} + A_3 e^{p_3 x} + A_4 e^{p_4 x} \tag{6.25}$$

where the A_i's are obtained by applying the boundary conditions. For the case of the clamped panel, there is a non-zero solution $\overline{X}$ of the form (6.25) with the boundary conditions (6.19) if we have

$$\begin{vmatrix} 1 & 1 & 1 & 1 \\ p_1 & p_2 & p_3 & p_4 \\ e^{p_1 L} & e^{p_2 L} & e^{p_3 L} & e^{p_4 L} \\ p_1 e^{p_1 L} & p_2 e^{p_2 L} & p_3 e^{p_3 L} & p_4 e^{p_4 L} \end{vmatrix} = 0,$$

which reduces to

$$bc\,[\cosh(2\epsilon) - \cosh(b)\cos(c)] = 3\epsilon^2 \sinh(b)\sin(c).$$

Finally, the system to be solved by the four complex unknowns α, b, c and ϵ writes the following:

$$\begin{cases} \dfrac{m_0}{D}\,\alpha^2 + \lambda\,\dfrac{M_\infty^2 - 2}{u_\infty\,(M_\infty^2 - 1)}\,\alpha = -2\epsilon^2 + \dfrac{\lambda^2}{16\epsilon^2} \\ b^2 = \dfrac{\lambda}{4\epsilon} - \epsilon^2 \\ c^2 = \dfrac{\lambda}{4\epsilon} + \epsilon^2 \\ bc\,[\cosh(2\epsilon) - \cosh(b)\cos(c)] = 3\epsilon^2 \sinh(b)\sin(c) \end{cases} \tag{6.26}$$

A method of resolution from Houbolt [37] in order to find the flutter boundaries is cited in [11]. For example, it gives for the following data

$$\begin{cases} d &= 1\ m \\ L &= 0.5\ m \\ h &= 1.35\ 10^{-3}\ m \\ \rho_S &= 2710\ Kg/m^3 \\ E &= 7.728\ 10^{10}\ N/m^2 \\ \nu &= 0.33 \end{cases}, \quad \begin{cases} \gamma &= 1.4 \\ P_\infty &= 25714\ Pa \\ \rho_\infty &= 0.4\ Kg/m^3 \\ M_\infty &= 2.2686 \end{cases}, \tag{6.27}$$

the complex values:

$$\begin{cases} \epsilon &= -2.903 - 0.066\ i \\ b^2 &= -63.48 + 0.875\ i \\ c^2 &= -46.64 + 1.646\ i \\ \alpha &= 462.2\ i \end{cases}$$

The complex pulsation α is purely imaginary. The system is at the flutter limit. These data will be used to test our numerical methods, since the exact solution should be a perfect (neither damped nor undamped) oscillatory behaviour. A glance at the results will tell us what amount of numerical damping our algorithms produce, and whether or not they are stable.

6.2.3 Comparison with one-dimensional problems

In this section, we discuss some differences between the two-dimensional model problem we consider in this paper, and some simple one-dimensional aeroelastic problems, essentially those discussed in the previous chapters.

The first, slight difference comes from the boundary conditions. In one dimension, the velocity of the fluid was equal to the speed of the wall. In two dimensions, this condition is only forced on the normal speeds, which is a little weaker. However, the numerical treatments of these boundary conditions are similar.

The second main difference concerns the motion of the fluid mesh. In both cases, the fluid domain is a function of the time, because its boundary varies. Then, the fluid domain has to be remeshed (or the mesh has to be moved) continuously. This task is a little more complex in two dimensions than in one dimension, where we can choose to have a uniform mesh size (this size varying in time).

The third difference appears in the computation of the forces applied on the structure. In one dimension, these forces are applied on single points. So no error is done during the spatial integration. In the airfoil profile case, the generalized forces F_h and F_θ are integrated along the airfoil profile. This spatial integration depends on the spatial approximation used for the fluid. For instance, since we use a finite-volume formulation for the fluid, the fluid pressure will be considered as constant on fluid cells, which will allow us to do this spatial integration in a simple way. We notice here that this method will have to be enhanced for two-dimensional cases with multiple degrees of freedom in the structure, where the fluid and structural meshes may not be matching at their common interface. In the case of the panel flutter simulation, some rematching procedures and spatial integration methods will have to be used [53]. Discussions on energy conservations will also be more complex, because the duality discussed in Chapter 4 will not be preserved.

6.3 Numerical methods

In this part, we present the numerical methods used for the simulation of our model problems. These methods are classical, in the fields of Computational Fluid Dynamics or Computational Structural Dynamics. For the fluid, the main characteristic is the classical finite-volume formulation on a moving mesh. Some interesting points are found in the mesh moving/updating algorithm. For the structure, we only use well-known unconditionally stable methods.

The most important contribution to numerical methods in the field of fluid-structure interaction simulations deals with the coupling of both fields. We shall investigate these coupling methods in the next section, and we only present in this section numerical methods dealing with each field, as if the fluid and the structure were decoupled.

6.3.1 Numerical methods used for the fluid

In this section, we describe the numerical methods used for the time integration of the fluid. Since the fluid domain depends on time, we shall first present the spatial discretization and the moving/updating schemes we used. We shall finish with somewhat classical numerical methods used for the fluid itself, once we have introduced the Arbitrary Lagrangian-Eulerian (ALE) formulation of Euler equations.

Spatial discretization: design and updating scheme

We first describe the initial state of the fluid mesh. We shall use a finite-volume formulation for the fluid. So we need a set of cells. We assume we have an initial triangulation $\Omega^h(0)$ of the fluid domain $\Omega(0)$. The boundary points of this triangulation are located either on the far-field boundary Γ_∞ (and they form the set Γ_∞^h), or on the profile $\Gamma(0)$ (set $\Gamma^h(0)$) .

We assume that we dispose of the fluid mesh at time t_1 and that we know the location of the fluid/structure interface at time t_2. For the airfoil problem, we only need the values $\theta(t_2)$ and $h(t_2)$ of the two structural degrees of freedom at time t_2. For the panel problem, we have to know the whole structural state at time t_2. The updating scheme for the fluid mesh is the following:

1. Like Γ_∞, the far-field points of the discretization Γ_∞^h do not move.

2. $\Gamma^h(t_2)$ is computed from existing data. For the airfoil, it is deduced from $\Gamma^h(0)$ by the following rigid motion: a rotation of $\theta(t_2)$ around the elastic center, followed by a vertical translation of $h(t_2)$. For the panel, a spatial interpolation might be needed to computed the location of the part of the discrete fluid boundary next to the structure.

3. The rest of $\Omega^h(t_2)$ is obtained via a method proposed by Batina [5] and generalized by Lesoinne and Farhat [48]. This method enables us to move the mesh, with no addition or deletion of any vertex. We now describe it shortly. To each edge ij between two vertices (i and j) of the triangulation, we give a stiffness, for example the inverse of its length, i.e.

$$k_{ij} = \frac{1}{\sqrt{(x_i - x_j)^2 + (y_i - y_j)^2}}, \tag{6.28}$$

but another choice could be made (this choice will be discussed later). We want to compute the displacements $\vec{\delta}_i$ of all vertices from $\Omega^h(t_1)$ to $\Omega^h(t_2)$ This will be done with a Jacobi-type iterative method. We assume we can build a prediction $\vec{\delta}_i^{pr}$ for the displacements (for example, a linear extrapolation based on previous displacements; this will also be discussed later). The initialization writes:

$$\left\{ \begin{array}{lcll} \vec{\delta}_i^0 & = & 0, & \text{for } i \in \Gamma_\infty \\ \vec{\delta}_i^0 & = & \vec{x}_i(t_2) - \vec{x}_i(t_1), & \text{for } i \in \Gamma^h \\ \vec{\delta}_i^0 & = & \vec{\delta}_i^{pr}, & \text{for other } i \in \Omega^h. \end{array} \right. \tag{6.29}$$

Jacobi iterations are performed, in the sense that we compute

$$\vec{\delta}_i^{n+1} = \frac{\sum_{j\in N(i)} k_{ij}\vec{\delta}_j^n}{\sum_{j\in N(i)} k_{ij}}, \text{for } i \in \Omega^h/(\Gamma^h \bigcup \Gamma_\infty), \tag{6.30}$$

where $N(i)$ is the set of vertices which neighbour i. When the method has converged after N iterations (i.e. when the difference between successive displacements fields is small enough), we take:

$$\vec{x}_i(t_2) = \vec{x}_i(t_1) + \vec{\delta}_i^N, \text{for } i \in \Omega^h. \tag{6.31}$$

ALE formulation

We present here the Arbitrary Lagrangian-Eulerian formulation of Euler equations (6.6). They allow us to consider classical Euler equations in a moving domain. The principle is the following: we use a moving frame of reference, which is not identically fixed to the laboratory anymore. In some regions of the domain, the frame can move with the fluid, giving locally a Lagrangian approach. The whole method is described for example in [61]. We denote by $\vec{\xi}$ the mixed geometric variable. It takes the role of a moving frame of reference. If the grid was structured and moving, the iso-ξ_i curves would represent the mesh lines. Both variables $\vec{x}$ and $\vec{\xi}$ are time dependent functions of each other, as

$$\vec{\xi} = \vec{\xi}(\vec{x}, t) \qquad \text{and} \qquad \vec{x} = \vec{x}(\vec{\xi}, t). \tag{6.32}$$

Defining the quantities J and $\vec{w}$ by

$$J = \det\left(\left.\frac{\partial \vec{x}}{\partial \vec{\xi}}\right|_t\right) \text{ and } \vec{w} = \left.\frac{\partial \vec{x}}{\partial t}\right|_{\vec{\xi}}, \tag{6.33}$$

the ALE formulation writes:

$$\boxed{\left.\frac{\partial (JW)}{\partial t}\right|_{\vec{\xi}} + J\ div_{\vec{x}}\vec{\bar{F}} = 0} \tag{6.34}$$

where

$$\bar{F}_x = \begin{pmatrix} \rho\bar{u} \\ \rho u\bar{u} + p \\ \rho v\bar{u} \\ e\bar{u} + pu \end{pmatrix}, \quad \bar{F}_y = \begin{pmatrix} \rho\bar{v} \\ \rho u\bar{v} \\ \rho v\bar{v} + p \\ e\bar{v} + pv \end{pmatrix} \quad \text{and} \quad \left| \begin{array}{l} \bar{u} = u - w_x \\ \bar{v} = v - w_y \end{array} \right. . \tag{6.35}$$

If the moving frame of reference is linked to the mesh $\Omega^h(t)$, i.e. if the $\vec{\xi}$ coodinates of vertices do not depend of the time, then we can consider cells $C_{\vec{x}}$ in $\Omega^h(t)$, which

correspond to a constant cell $C_{\vec{\xi}}$ in the $\vec{\xi}$-space. Then an integral form of (6.34) writes:

$$\boxed{\frac{d}{dt}\left[\int_{C_{\vec{x}}} W\, d\vec{x}\right] + \int_{C_{\vec{x}}} div_{\vec{x}}\vec{\bar{F}}\, d\vec{x} = 0.} \tag{6.36}$$

Numerical schemes

As stated earlier, we shall use a finite-volume formulation of ALE-Euler equations (6.35-6.36). In a very classical way, for each vertex i, we shall define the cell C_i as described on Figure 6.6. ∂C_i will denote the boundary of this cell, and, in general, j will denote the generic index of a vertex neighbouring i, and $N(i)$ the set of the neighbours of i. ∂C_{ij} will denote the common part of ∂C_i and ∂C_i.

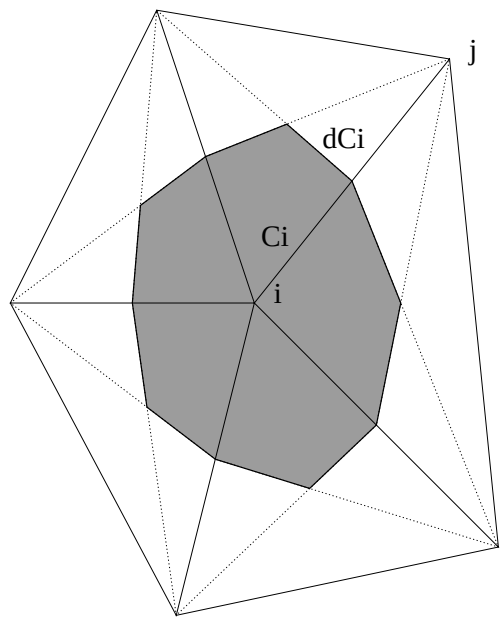

FIG. 6.6 – *Cell and boundary for vertex i*

We assume W_i is the average value of the field W in cell C_i. Our numerical scheme takes the form:

$$(A_i W_i)_t + \sum_{j\in N(i)} \|\widetilde{\partial C_{ij}}\|.\bar{\Phi}(W_i, W_j, \widetilde{\vec{\eta_{ij}}}) = 0, \tag{6.37}$$

where A_i is the area of cell C_i, $\widetilde{\partial C_{ij}}$ is a time-average of ∂C_{ij} (of length $\|\widetilde{\partial C_{ij}}\|$ and normal $\widetilde{\vec{\eta_{ij}}}$ oriented from C_i to C_j), and $\bar{\Phi}$ is a numerical flux such that

$$\Delta t\, \|\widetilde{\partial C_{ij}}\|.\bar{\Phi}(W_i, W_j, \widetilde{\vec{\eta_{ij}}}) \simeq \int_{t^n}^{t^n+\Delta t} \left[\int_{\partial C_{ij}} \vec{\bar{F}}.\vec{\eta_{ij}}\, d\sigma\right] d\tau \tag{6.38}$$

We use a Godunov's method based on a Roe's linearization of the hyperbolic flux $\vec{\bar{F}}$. The numerical flux $\bar{\Phi}$ of (6.38) depending of the two vectors of conservative variables

W_i and W_j, and a time-average normal $\widetilde{\vec{\eta_{ij}}}$ to the moving interface ∂C_{ij} will be taken as:

$$\bar{\Phi}(W_i, W_j, \widetilde{\vec{\eta_{ij}}}) = \frac{\vec{\vec{F}}(W_i) + \vec{\vec{F}}(W_j)}{2}.\widetilde{\vec{\eta_{ij}}} - \left|\widetilde{\mathcal{A}}(W_i, W_j, \widetilde{\vec{\eta_{ij}}}) - \left(\widetilde{\vec{w_{ij}}}.\widetilde{\vec{\eta_{ij}}}\right) I\right|.\frac{W_j - W_i}{2}, \tag{6.39}$$

where the matrix $\widetilde{\mathcal{A}}(W_i, W_j, \widetilde{\vec{\eta_{ij}}})$ is the Jacobian of the flux $\vec{\vec{F}}.\widetilde{\vec{\eta_{ij}}}$ taken at Roe's average W_{ij} of both states W_i and W_j classically defined by

$$W_i = \begin{pmatrix} \rho_i \\ \rho_i u_i \\ \rho_i v_i \\ E_i \end{pmatrix}, \quad W_j = \begin{pmatrix} \rho_j \\ \rho_j u_j \\ \rho_j v_j \\ E_j \end{pmatrix}, \quad W_{ij} = \begin{pmatrix} \rho_{ij} \\ \rho_{ij} u_{ij} \\ \rho_{ij} v_{ij} \\ E_{ij} \end{pmatrix}, \quad \text{with}$$

$$\begin{aligned}
\rho_{ij} &= \frac{\sqrt{\rho_i}\rho_i + \sqrt{\rho_j}\rho_j}{\sqrt{\rho_i} + \sqrt{\rho_j}} \\
u_{ij} &= \frac{\sqrt{\rho_i}u_i + \sqrt{\rho_j}u_j}{\sqrt{\rho_i} + \sqrt{\rho_j}} \\
v_{ij} &= \frac{\sqrt{\rho_i}v_i + \sqrt{\rho_j}v_j}{\sqrt{\rho_i} + \sqrt{\rho_j}} \\
H_{ij} &= \frac{\sqrt{\rho_i}H_i + \sqrt{\rho_j}H_j}{\sqrt{\rho_i} + \sqrt{\rho_j}},
\end{aligned}$$

where H is the total volumic enthalpy (given by $\rho H = E + P$). The absolute value signs in (6.39) mean we first diagonalize the matrix, and then take the absolute values of the eigenvalues (this notation is common to all Roe-type methods).

The whole method will be completely defined as soon as we precisely give the choices for $\widetilde{\vec{w_{ij}}}$ and $\widetilde{\vec{\eta_{ij}}}$. Considering two connected vertices S_i and S_j, the part of cell interface $\partial C_{ij} = \partial C_i \bigcap \partial C_j$ is made of two segments, defined using cells gravity centers $G_{1,ij}$ and $G_{2,ij}$ as described on Figure 6.7.

Before each time-step, we give to all mesh points a velocity. This velocity is assumed constant throughout the time-step. Hence, the velocity $\vec{w}_i^{n+1/2}$ will denote the speed of the vertex i during the nth time-step. N'Konga and Guillard have discussed a choice for $\widetilde{\vec{w_{ij}}}$ and $\widetilde{\vec{\eta_{ij}}}$ [57]. $\widetilde{\vec{w_{ij}}}$ will be taken as the average of the velocities of both gravity centers $G_{1,ij}$ and $G_{2,ij}$ of Figure 6.7.

The normal $\widetilde{\vec{\eta_{ij}}}$ will be taken as the average of the two normals you get as described on Figure 6.7, based on the locations of all five points (S_i, S_j, I_{ij}, $G_{1,ij}$ and $G_{2,ij}$) at the beginning and the end of the time-step (trapezoidal rule). This choice was advocated because it gives to the Jacobian $\widetilde{\mathcal{A}}(W_i, W_j, \widetilde{\vec{\eta_{ij}}})$ a propriety similar to Roe's linearization in the standard case (see [45] for more details). It was also advocated by Farhat et *al*

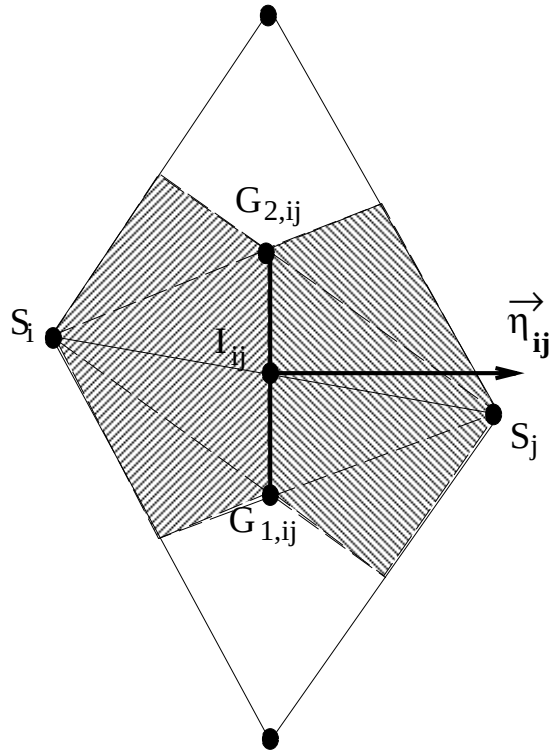

FIG. 6.7 – *Definition of* $\widetilde{\vec{w_{ij}}}$ *and* $\widetilde{\vec{\eta_{ij}}}$.

[26] for conservation reasons. Indeed, if the locations of the vertices are updated with the scheme

$$S_i^{n+1} = S_i^n + \Delta t \vec{w}_i^{n+1/2}, \tag{6.40}$$

where Δt is the current time-step, then a uniform field $W \equiv W_0$ is conserved thoughout the computation (i.e. the volume is also conserved) if the cell areas are updated with the following scheme:

$$(A_i)_t + \sum_{j \in N(i)} \|\widetilde{\partial C_{ij}}\|. \left(-\widetilde{\vec{w_{ij}}}.\widetilde{\vec{\eta_{ij}}}\right) = 0, \tag{6.41}$$

where the time scheme is the same as in (6.37).

The extension to second-order accuracy follows the general idea of the MUSCL scheme, initially devlopped by Van Leer [73], and adapted to unstructured finite elements by Fezoui [29]. The general ideas are applied to the new hyperbolic system, deriving from the ALE formulation of standard Euler equations, involved in (6.34). We have chosen half-centered half-upwind gradient for the second-order extension. We send back the reader to [45] for more details on this second-order extension and on the treatment of boundary conditions (this treatment is standard, since the vertices on Γ_∞ are not moving).

The temporal part of (6.37) will be treated by the following three-step Runge-Kutta method with low storage (we denote by W the field of conservative variables and by

$\Psi(W)$ the second term of (6.37)):

$$\begin{cases} W^{(0)} &= W^n \\ W_i^{(k)} &= \dfrac{A_i^n}{A_i^{n+1}} W_i^{(0)} - \dfrac{1}{A_i^{n+1}} \dfrac{\Delta t}{4-k} \Psi\left(W^{(k-1)}\right), \quad k = 1, 2, 3 \\ W^{n+1} &= W^{(3)} \end{cases} \tag{6.42}$$

Remark: this scheme is third-order time-accurate in the linear case. However, the low storage algorithm limits the accuracy to second-order in such a non-linear case [43]. In (6.42), the cell areas are constantly taken as their value at the end of the time-step, which forbids an actual second-order accuracy for the temporal scheme. However, some tests were made, and reveal this is not a source of significant inaccuracy.

6.3.2 Numerical methods used for the structure

In the case of the airfoil profile in transonic airstream, the structure has only two degrees of freedom and the numerical integration is fast and simple. However, we shall reformulate (6.1) to the same more general form as for the panel problem, where the mass and stiffness matrices have already been defined in (6.9). Then we present the schemes we used. We shall end this section with some discussion on the choices made in the computations of the generalized forces we used (for instance, F_h and F_θ of (6.1) and (6.3-6.4) for the airfoil problem, and F in (6.9) for the panel problem).

Reformulation of the structural equations.

We shall rewrite (6.1) in a matricial way. It is equivalent to

$$M\ddot{X} + D\dot{X} + KX = F, \tag{6.43}$$

where we have taken

$$M = \begin{pmatrix} m & S_\theta \\ S_\theta & I_\theta \end{pmatrix}, \quad D = \begin{pmatrix} c_h & 0 \\ 0 & c_\theta \end{pmatrix}, \quad K = \begin{pmatrix} k_h & 0 \\ 0 & k_\theta \end{pmatrix},$$
$$X = \begin{pmatrix} h \\ \theta \end{pmatrix}, \quad F = \begin{pmatrix} F_h \\ F_\theta \end{pmatrix}. \tag{6.44}$$

The structural equations for the panel in supersonic airstream take also the preceding form with the matrices defined in (6.11), with no damping ($D = 0$) and X still denotes the field of structural displacements. Note that the mass matrix M, the diffusion matrix D, and the stiffness matrix K are symmetric. M and K are definite positive (since $k_h > 0$, $k_\theta > 0$ and $\gamma_\theta > x_\theta > 0$ in the airfoil case). The trapezoidal rule (as a member of the Newmark family of methods) which we shall present in the following, can be used on an equation of the form of (6.43) in any dimension.

Trapezoidal rule.

The trapezoidal rule is a particular example of Newmark's method. This method depends more generally on two parameters [36]. The choice $\beta = 0.25$ and $\alpha = 0.5$ reduces to the trapezoidal rule. In the following, A^n, V^n and X^n will respectively denote approximations of $\ddot{X}(t^n)$, $\dot{X}(t^n)$ and $X(t^n)$. Using the time step $\Delta t = t^{n+1} - t^n$, the scheme reads:

$$\begin{cases} X^{n+1} & = & X^n + \Delta t \dfrac{V^n + V^{n+1}}{2} \\ V^{n+1} & = & V^n + \Delta t \dfrac{A^n + A^{n+1}}{2} \\ A^{n+1} & \text{such that} & MA^{n+1} + DV^{n+1} + KX^{n+1} = F \end{cases} \tag{6.45}$$

where F is an estimate of the generalized force at time t^{n+1}. This scheme is second-order accurate. If the mass and stiffness matrices are definite positive, and if the dissipation matrix D is positive (i.e. if the system (6.43) with no external force has only stable solutions) then the scheme (6.45) is unconditionally stable, since we have the property:

$$E^{n+1} \leq E^n, \left(E = \frac{1}{2}{}^tVMV + \frac{1}{2}{}^tXKX\right) \tag{6.46}$$

if $F = 0$. Then the quadratic form E (the structural energy) on X and V is bounded. Since M and K are definite positive, X and V are bounded. And so is A. The scheme is then unconditionally stable. Furthermore, it does not add numerical dissipation.

Pressure choices in time and space.

In this section, we would like to discuss shortly some choices which can be made concerning the generalized force F. If the pressure force on the structure at time t^{n+1} is not known, we have to use an estimate. If we use a subcycled coupling scheme (for example, we choose to advance the structure ten times less often, but with ten times larger time steps), then we have to choose the pressure force we shall use (since we have computed these forces at ten different times).

In short, the integration of the structure depends a lot on the general coupling scheme: the energetic exchange at the fluid/structure interface depends of the time interpolations that are used.

Geometrically, some choices have to be made. In the case of the airfoil profile, there are only two degrees of freedom. The generalized forces detailed in (6.3-6.4) are discretized straightforwardly: we use a discrete integration along Γ^h. But we may have had interpolations if the airfoil was flexible, and if the airfoil and the fluid meshes were not conforming at the interface. This is the case for the panel flutter simulation. We used several discretizations, and structural meshes were not matching the fluid grid at the interface. We chose a very simple interpolation algorithm. It is presented on Figure 6.8. Each structural point is given two fluid neighbouring points, which enclose it along the interface. Also, corresponding barycentric coordinates are stored. Then, the pressure applied to this structural point $P_{F\to S}$ is the average of the neighbouring fluid pressures with these barycentric coordinates. Reciprocally, the displacement of a

fluid grid point at the interface $X_{F\to S}$ is computed the same way, from neighbouring structural displacements.

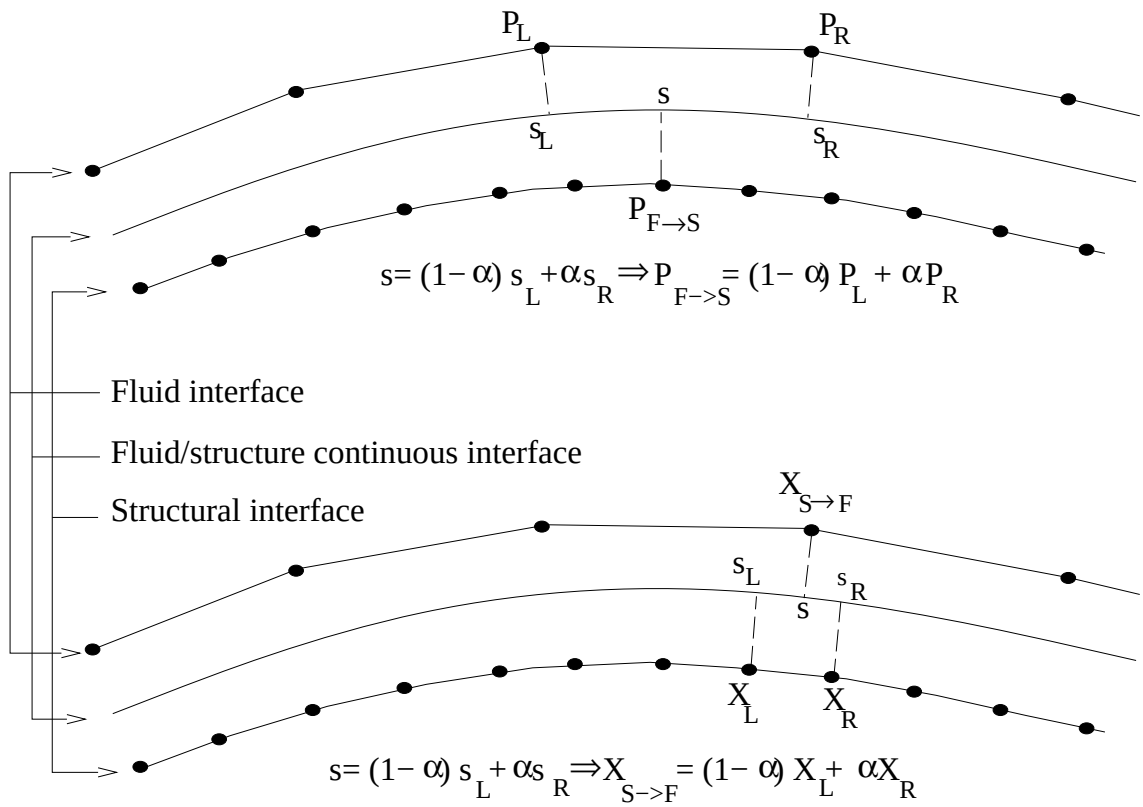

FIG. 6.8 – *Interpolations at the interface if the grids are not matching.*

6.4 Enhancements of the general coupling scheme

In this section, we review several methods used for the actual coupling of the fluid and the structure. Some of these methods have been introduced in [62]. However, they are extended to multiple dimensions. The reader will find in the following a rough list of numerical methods, which, in general, introduce some enhancements in the global algorithm. Though some methods will be let aside, they were reported for information.

We consider in this section the **airfoil profile simulation**. Since it is very simple, we can try a lot of particular choices. In the next section, we will deal with the panel flutter simulation, which is quite more complex. Finally, in the last section, we shall discuss and sum up the advantages and discomforts of these enhancements, and make a step towards a global algorithm, a little closer to an "ultimate aeroelastic coupling scheme".

Throughout this section, we assume we are interested in subcycling the fluid (which is the case indeed). We would like to perform less structural time integrations (with a larger time-step) than fluid time integrations. Therefore, we shall always keep in mind

that we would like the maximum subcycling factor $n_{F/S}$ with the same computational performances.

6.4.1 Structural time-interpolation

We start from the most popular general staggered algorithm, which was named "volume-continuous method" in [62]. The time integration corresponding to one structural time step Δt_S is performed as follows:

- compute the generalized forces F of (6.1)
- perform a time integration of the structure (6.45) with these generalized forces with the time step Δt_S
- update the mesh displacements on Γ and construct the new mesh grid at the end of this time step as described in Section 6.3.1
- compute the grid velocities as in (6.40)
- perform as many fluid time steps (6.42) as necessary to complete the time step Δt_S.

If we choose this algorithm, we can use some time interpolation of extrapolation of the pressure forces of the first step. We present on Figure 6.9 the rotation θ (in degrees) of our wing profile (test case defined by Table 6.1 and Table 6.2; fluid scheme: Runge-Kutta 1 with $CFL = 0.9$) with two different choices, compared with a reference curve obtained with no subcycling (method "0"). The method "1" corresponds to the algorithm presented. The method "2"corresponds to the following choice for F:

$$F = \bar{F}^{n-1/2} \equiv \frac{1}{\Delta t_S} \sum_{k=1}^{n_{F/S}} \Delta t_{F_k} F_k^{n-1}, \tag{6.47}$$

where the summation is extended over all subcycles, and F_k^{n-1} denotes the pressure forces computed after the kth subcycle in the preceding time integration. For methods "1" and "2", the subcycling factor was $n_{F/S} = 60$. We see that the choice has a visible influence on the numerical results. We know why the second method is worse than the first one: the computed value for F is roughly close to $F(t^{n-1/2})$ (and in the case of method 1, it would be $F(t^n)$). We just presented this first elementary result to show the importance of **any** time-interpolation method. By the way, we notice that both schemes give results different from the reference curve.

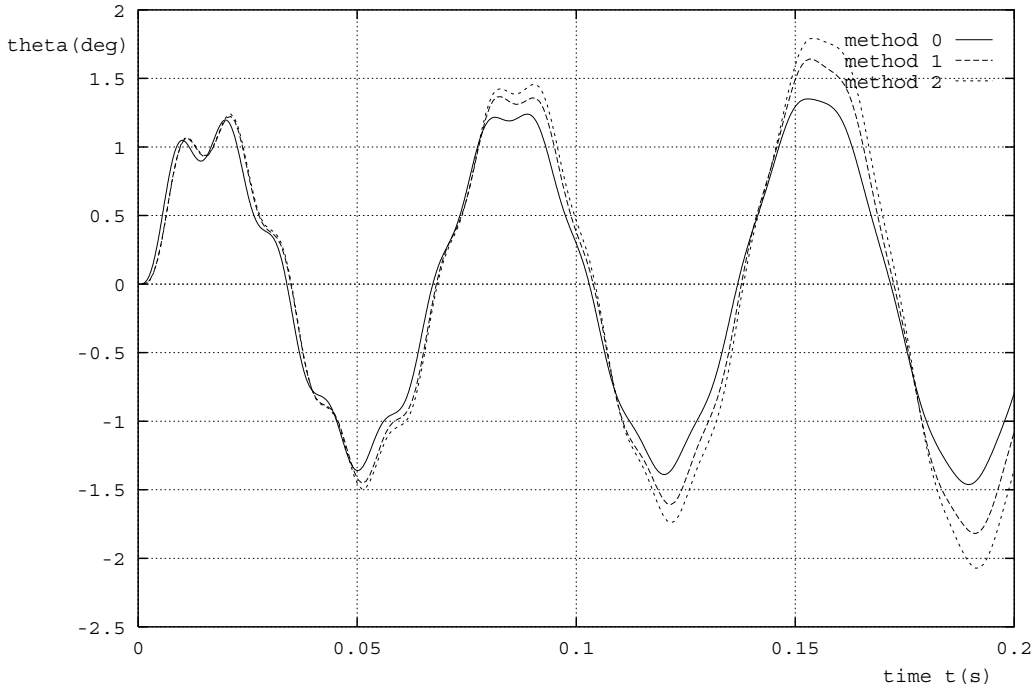

FIG. 6.9 – *Airfoil rotation with different interpolation methods.*

6.4.2 Volume-continuous or volume-discontinuous methods

In the previous chapter, the use of some"volume discontinuous" method was advocated. In short, this kind of methods allows to reduce considerably the energy conservation errors. The principle is simple: assume you can construct with good accuracy a prediction of the state of the structure at the end of the *next* time step, then you should perform the three last steps of Section 6.4.1, and finish with the actual time-integration of the structure. In that case, if your prediction was exact, the global energy could be exchanged exactly between the fluid and the structure. Moreover, even if your prediction is not exact, you are still able to conserve exactly the momentum equations.

The global coupling algorithm is the following:

- compute a prediction for the location of the structure at the end of the current time step (say $\widetilde{X^{n+1}}$)
- update the mesh displacements on Γ and construct the new mesh grid at the end of this time step as described in Section 6.3.1
- compute the grid velocities as in (6.40)
- perform as many fluid time steps (6.42) as necessary to complete the time step Δt_S.
- compute some generalized forces F of (6.1)

– perform a time integration of the structure (6.45) with these generalized forces with the time step Δt_S.

The reader should notice that at the end of a time-step, both sides of the fluid-structure interface are *a priori* not conforming, since the fluid mesh is conforming with the prediction of the location of the structure.

As a beginning, we used a simple first-order prediction of the structural location of the first step:

$$\widetilde{X^{n+1}} = X^n + \Delta t_S V^n, \tag{6.48}$$

and the generalized forces of the fifth step is the simple time average $\bar{F}^{n+1/2}$ (note the index change) given in (6.47).

On Figure 6.10, we present the rotation of the airfoil as a function of time for different tests. The method "0" is still the reference curve. The method "2" curve is the same as previously (we use the time-average generalized force of (6.47)). Finally, the method "3" curve represents a simulation with the volume-discontinuous method, based on the same time average generalized force. We see that the result is much closer to the reference curve.

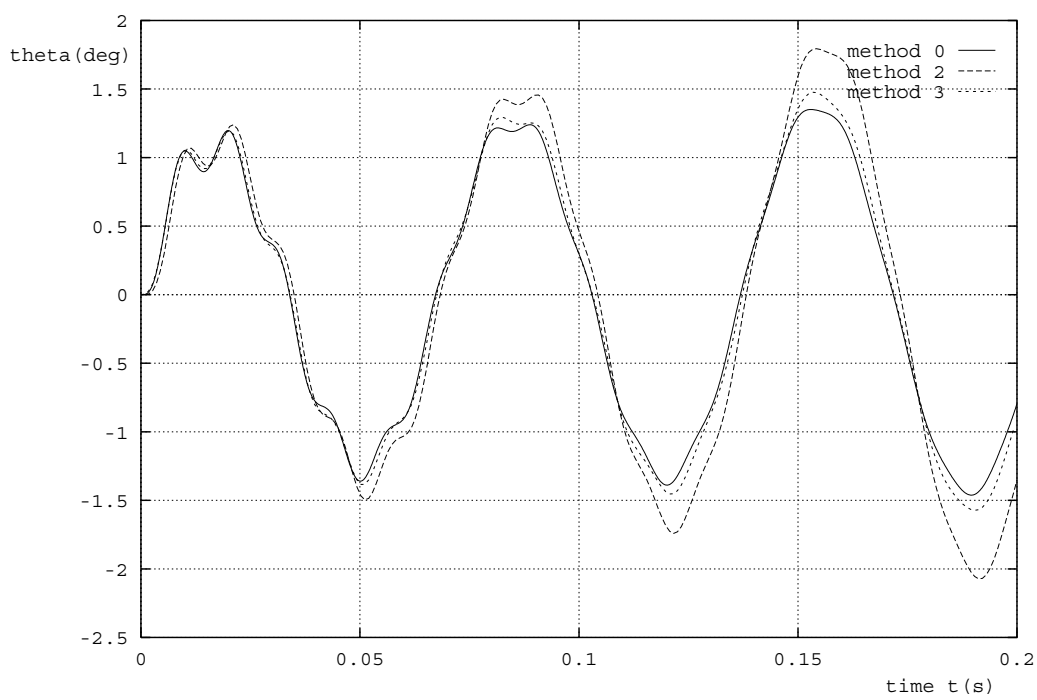

FIG. 6.10 – *Airfoil rotation with volume continuous/discontinuous methods.*

6.4.3 Role of the prediction in volume-discontinuous methods

In the preceding section, we gave a short outline of a volume-discontinuous method. We can wonder what influence has the prediction we make on the structural state at the end of the time step. In this section, we compare the results of the volume-discontinuous method with different predictions (with different orders of accuracy).

On Figure 6.11, we present the rotations of the airfoil as functions of time for the same test case as previously. We compare the simple "first-order" accurate prediction of (6.48), with three other simple predictions: first, the following "second-order" accurate prediction:

$$\widetilde{X^{n+1}} = X^n + \Delta t_S V^n + \frac{\Delta t_S^2}{2} A^n, \tag{6.49}$$

then the result $\widetilde{X^{n+1}}$ of a numerical integration of the structure with the trapezoidal rule, with the previous value for the generalized force F, i.e.

$$\left\{ \begin{array}{lll} \widetilde{X^{n+1}} & = & X^n + \Delta t_S \dfrac{V^n + \widetilde{V^{n+1}}}{2}, \\ \widetilde{V^{n+1}} & = & V^n + \Delta t_S \dfrac{A^n + \widetilde{A^{n+1}}}{2}, \\ \widetilde{A^{n+1}} & \text{such that} & M\widetilde{A^{n+1}} + D\widetilde{V^{n+1}} + K\widetilde{X^{n+1}} = \bar{F}^{n-1/2}, \end{array} \right. \tag{6.50}$$

and finally a prediction based only on displacements (which is first-order accurate):

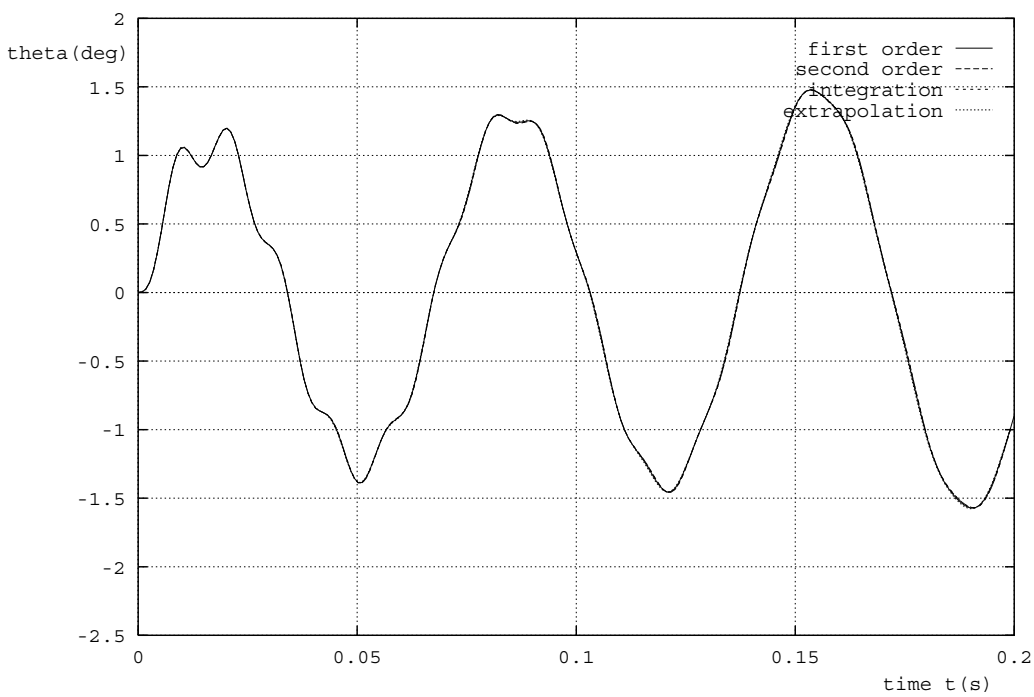

FIG. 6.11 – *Volume-discontinuous method with different predictions.*

$$\widetilde{X^{n+1}} = 2X^n - X^{n-1}. \tag{6.51}$$

We see that all four curves are identical. Then, we can deduce that the first-order prediction is sufficient. For these curves, we used approximatively 76 structural time steps per coupled oscillation and the time step Δt_S is rather small, but not negligible (compared to the coupled period of oscillation). However, we have found that second-order prediction can be less stable in some cases. These results were already found in [62], where predictions of higher orders of accuracy were found less stable. We have also noticed, that the first-order prediction based only on displacements induces more high-frequency dissipation, which might be useful in the cases where high-frequency modes are present and make the structural speed oscillate (for example, in cases with multiple degrees of freedom for the structure). This will be discussed for the panel case.

6.4.4 Energy conservation

In this section, we study a possible enhancement of the global algorithm based on energetic considerations. We assume we use a volume-discontinuous method with the trapezoidal rule for the structural time-integration. Then, we have to make a choice for the pressure force F applied to the structure and used in (6.45). We already considered the use of a time average of the pressure force in Section 6.4.1. We concluded that this choice was not interesting *when used with* the volume-continuous method. We then have to test some new choices, coupled with the volume-discontinuous method.

We shall now show some elements of demonstration "with the hands". As a matter of fact, we shall consider only energetic exchanges at an interface element (anyway, we do not discuss here some fine points on the spatial scheme, but on the temporal scheme). If the fluid is subcycled, then (the reader can check that) the energy received by the fluid through the structural boundary element is roughly given by:

$$E_F = -\sum_{k=1}^{n_{F/S}} \Delta t_{Fk} F_k^n w_k^n,$$

where w_k^n is the boundary velocity during the kth subcycle. We assume we take w constant through all subcycles. Then, we have

$$E_F = -\bar{F}^{n+1/2} \Delta t_S \; w^{n+1/2}. \tag{6.52}$$

where $\bar{F}^{n+1/2}$ is defined as in (6.47). On the other hand, the energy received by the structure, thanks to the properties of the trapezoidal rule, is given by:

$$E_S = \frac{F_I^n + F_I^{n+1}}{2} \Delta t_S V^{n+1/2},$$

where F_I^{n+1} is the input of the trapezoidal rule for the step $t^n \to t^{n+1}$, and $V^{n+1/2}$ is given in (6.45). Then, if the prediction for the structure is good enough (i. e. if the

fluid and structural interfaces remain close), then we shall have

$$E_S \simeq \frac{F_I^n + F_I^{n+1}}{2} \Delta t_S \; w^{n+1/2}.$$

Finally, the total amount of energy *created* is given by:

$$\Delta E \simeq \left[\frac{F_I^n + F_I^{n+1}}{2} - \bar{F}^{n+1/2} \right] \Delta t_S \; w^{n+1/2}. \tag{6.53}$$

We now can discuss different numerical choices for the input F_I^n of the trapezoidal rule. We show on Figure 6.12 the rotation of the airfoil as a function of time with different inputs. The *method 0* curve is showed for comparison.

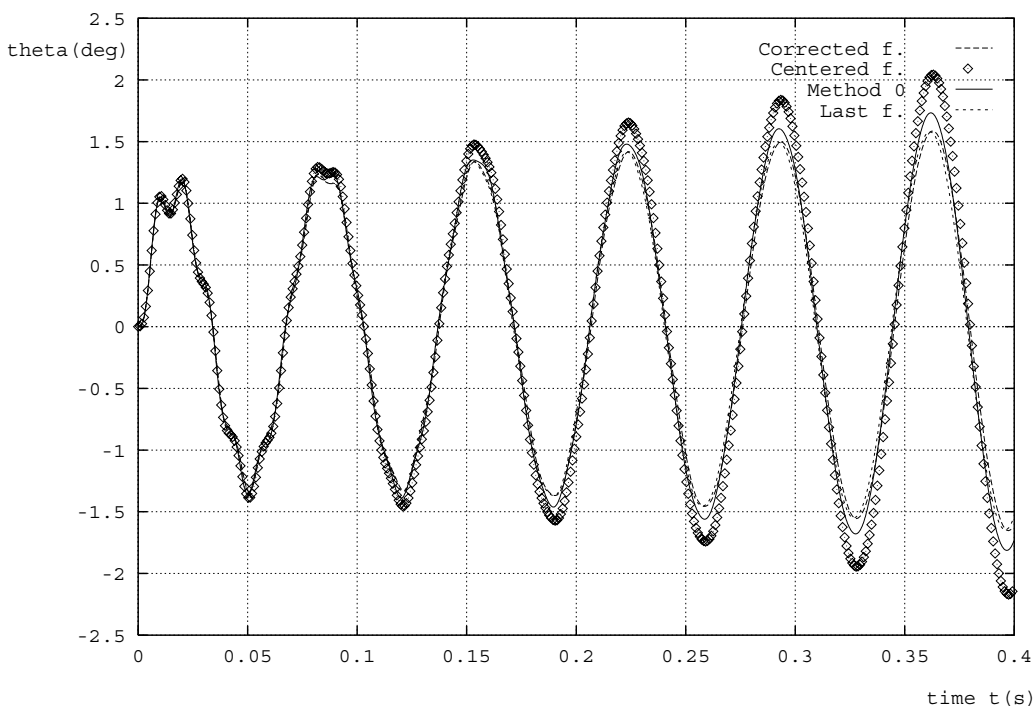

FIG. 6.12 – *Newmark method and energy conservation.*

The *centered forces* curve corresponds to the choice:

$$\textit{centered forces method:} \quad F_I^{n+1} = \bar{F}^{n+1/2}. \tag{6.54}$$

We see that the result is not really good. The amplification of the flutter has changed. This was predictable, since this choice generates energetic errors, as showed by (6.53). The *last forces* curve corresponds to the choice:

$$\textit{last forces method:} \quad F_I^{n+1} = F^n_{n_{F/S}} \equiv F^{n+1} \tag{6.55}$$

(we only use the last pressure forces, computed after the $n^{th}_{F/S}$ and last subcycle). We see that the result is much better. We deduce from (6.53) that the energetic error is close to

$$\Delta E \simeq \left[\frac{F^n + F^{n+1}}{2} - \bar{F}^{n+1/2}\right] \Delta t_S \; w^{n+1/2},$$

which should be small (if the time step Δt_S is small enough compared to the coupled period of oscillation). Finally, the *corrected forces* curve corresponds to the choice:

$$\textit{corrected forces method:} \quad F_I^{n+1} = 2 * \bar{F}^{n+1/2} - F_I^n. \tag{6.56}$$

We see that the result is really close to the preceding one, though the above definition was chosen to annihilate the predicted energetic error (actually, the only term remaining is now $\Delta E = \Delta t_S \bar{F}^{n+1/2}[V^{n+1/2} - w^{n+1/2}]$, which can be reduced as desired with the choice of an appropriate accurate prediction). In many cases, these two methods behave identically. But the *corrected forces method* might be more stable and accurate for large time-steps Δt_S.

6.4.5 Grid motion and subcycling

In the preceding sections, we have only considered a constant speed motion of the mesh during each structural time-step. The choice is very simple: for each structural time-step, we compute once and for all subcycles the mesh speeds. This would not have been the case if we had chosen some more accurate interpolation of the grid point locations. However, C. Farhat and N. Maman (see also [26]) confirm that the use of a parabolic or linear path for the fluid mesh during subcycles give no significantly different results.

This might be different for cases where very few time steps are used for each coupled period of oscillation: the structural speed could vary a lot from one time-step to the next one, and the use of a linear path for the fluid mesh could induce some extra numerical diffusion (due to the difference between the fluid velocity and the mesh speed at the fluid/structure interface during the first fluid subcycles of a global time step.)

6.4.6 Mesh updating equation

In this section, we consider the equation defining the mesh updating process. In Equations (6.28-6.31), we solve an elastic equation for the mesh displacement. The stiffness of each edge of the mesh, defined in (6.28) is computed after each structural integration.

We have observed that this process may not be optimal, even in cases where all mesh displacements seem small. In some cases, some triangles in the mesh tend to

collapse. It is easy to understand, that, if a triangle has a bad ratio, the elastic model of the process presented does not really pull the triangle the other way. Actually, when a triangle collapses, the lengths of its edges do not vary considerably in all cases.

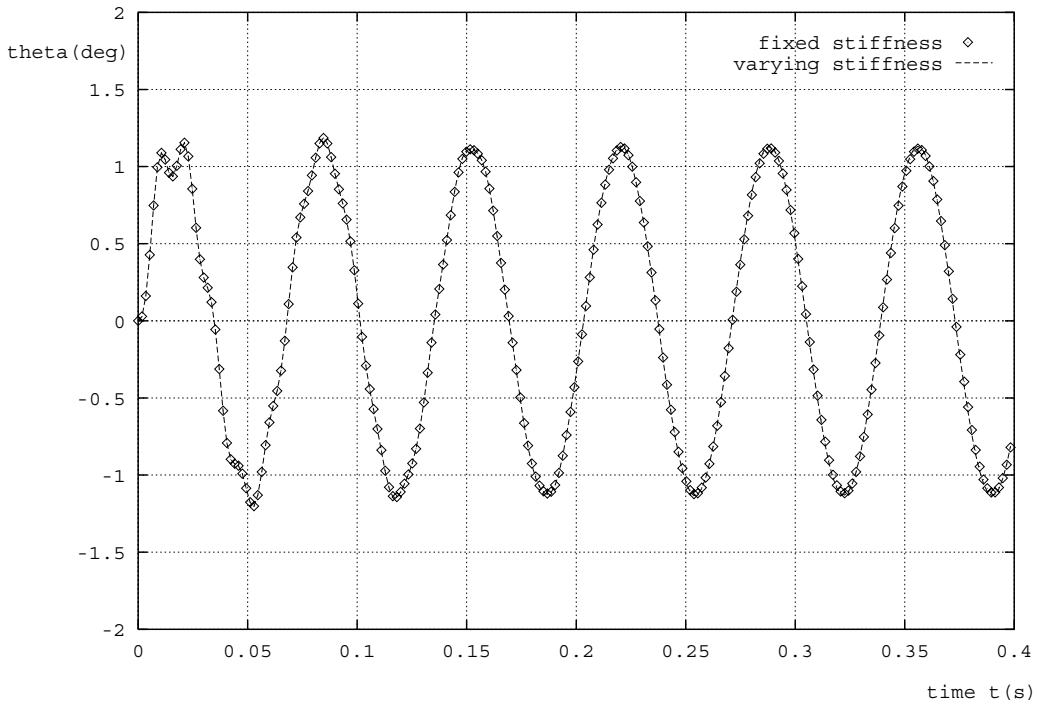

FIG. 6.13 – *Fixed and variable stiffness of the edges.*

We present on Figure 6.13 the rotation θ of the airfoil for two different methods. Both computations are made on a 2280 point, 4320 element fluid mesh, with all same parameters as before, but a structural time-step such that we have 38 time-steps per coupled period of oscillation. In both computations, the subcycling factor is approximately (at the beginning) $n_{F/S} = 560$. Also, 300 Jacobi iterations (6.30) were performed in order to have a good convergence at each mesh update. We see that both results are really close.

The *varying stiffness* curve was obtained with the algorithm (6.28-6.31). In that computation, some triangles have slightly collapsed, which produces a important reduction of the fluid time step (evaluated via the CFL-condition for our explicite scheme). Since the structural time-step was fixed, the subcycling factor $n_{F/S}$ increased up to 918!

The *fixed stiffness* curve was obtained with a slightly different algorithm: the stiffness of each edge is not recalculated after each time-step. Then the lengths of the edges tend to stay near their initial value. The final subcycling factor was $n_{F/S} = 590$ with this trick. Note that an extra 24% CPU time was necessary to get the *varying stiffness* curve. We have plotted on Figure 6.14 the fluid time steps during the computations (as a function of the time). There is an oscillation of the fluid time step due to the structural oscillation itself. However, we see a significant reduction of the fluid time

steps for the *varying stiffness* computation, where some triangles collapse regularly in the *varying stiffness* method. This probably comes from the fact that nothing helps the mesh to get back to its initial quality. On the contrary, in the *fixed stiffness* curve, we can observe that the oscillations are centered around the same average.

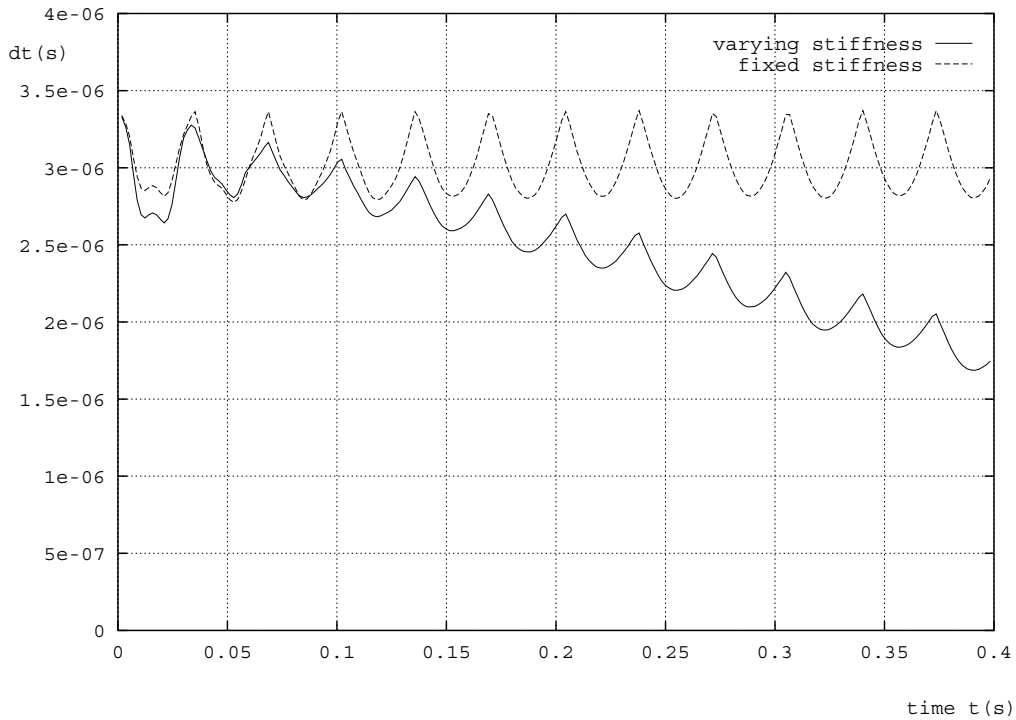

FIG. 6.14 – *Fluid time steps for computations with fixed and variable stiffness.*

We can also point out the fact that, when the stiffness of edges is fixed throughout the simulation, some computational time is spared, since the stiffnesses of edges are not recalculated.

We have tried other formulas for the stiffness of each edge in the spring analogy we presented in (6.28): for example, a stiffness linked to the square of the length or on the areas of neighbouring triangles. But these methods did not give better results than the "fixed stiffness" method.

C. Farhat advocated the use of torsion springs at each angle of a triangle, which could avoid the collapsing of the triangles. Some other tricks deriving from mesh optimization might be useful to prevent mesh collapsing in more complex cases. For example, Dervieux and Palmerio [18] have advocated different methods relying on physical analogies. However, the fixed stiffness method was sufficient for our problem, where the displacements are small.

6.4.7 Mesh updating algorithm.

In this section, we discuss some points on the mesh updating algorithm presented in (6.28-6.31). We have not precisely defined the prediction $\vec{\delta}_i^{pr}$ for the mesh displacements in (6.29). Let us assume we want to compute the mesh displacements between times t^n and t^{n+1}, then we use the following prediction (the first time step excepted):

$$\vec{\delta}_i^{pr}(t^n \to t^{n+1}) = 2 * \vec{\delta}_i(t^{n-1} \to t^n) - \vec{\delta}_i(t^{n-2} \to t^{n-1}). \tag{6.57}$$

This prediction is very efficient. Since the structural time step (and then the time gap between each mesh computation) is constant throughout the computation, this prediction is second-order accurate (for the mesh location). We have noticed that the prediction may have an influence on the divergence noticed in the previous section. However, when the mesh does not collapse, this prediction is quite optimal (and the prediction has less influence as the number of Jacobi iterations (6.30) increases).

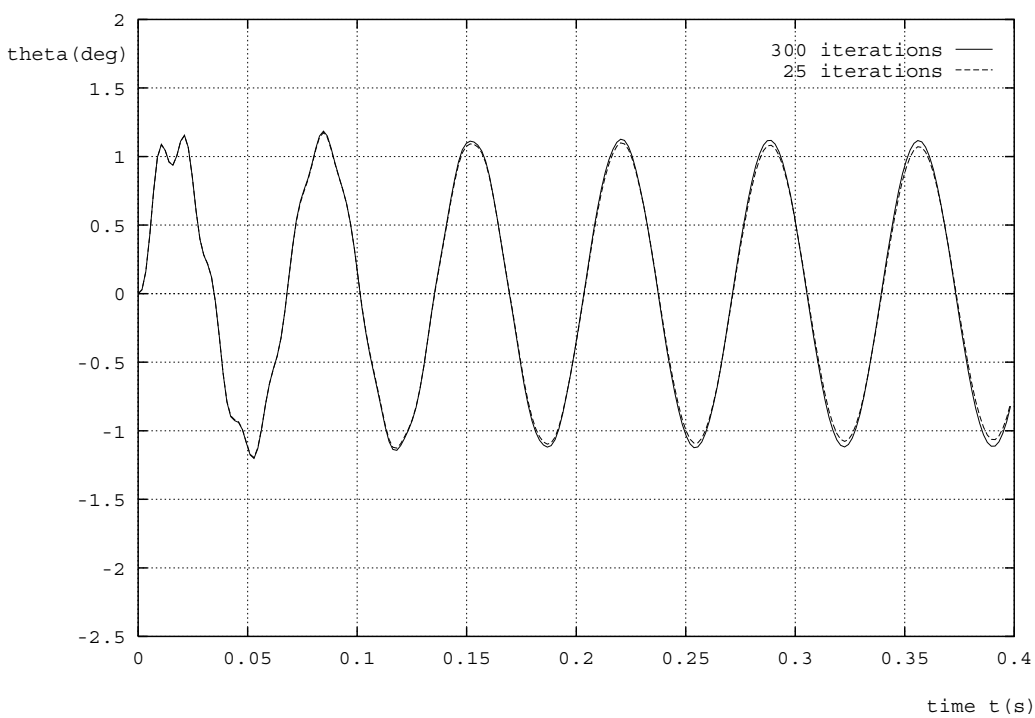

FIG. 6.15 – *Rotation with different numbers of Jacobi iterations.*

We now discuss the influence of the number of Jacobi iterations on the numerical results. On Figure 6.15, we present the rotation of the airfoil resulting from to simulations differing by the number of Jacobi iterations in the mesh updating algorithm (other enhancements are added): 25 and 300 Jacobi iterations. We see that the results are quite identical. The "25" curve is a little more damped. If we check the fluid time steps during the computations, we see that the mesh has not a sufficient number of Jacobi iterations to follow the structure (see Figure 6.16).

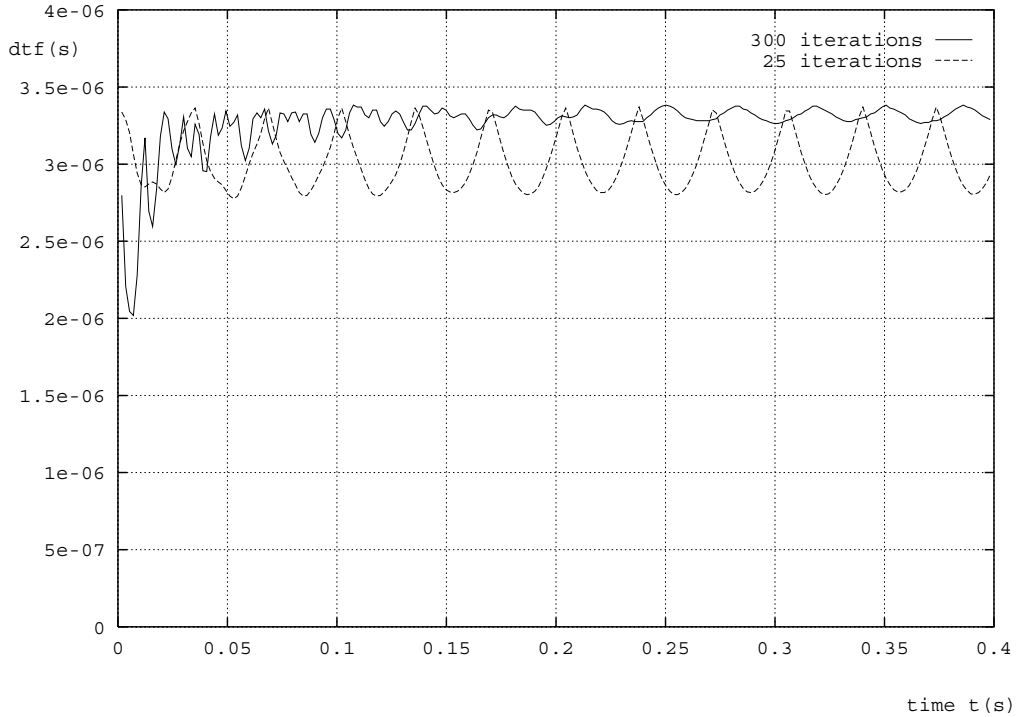

FIG. 6.16 – *Fluid time steps with different numbers of Jacobi iterations.*

We have also noticed that, when the displacements are not negligible, a too small number of Jacobi iterations might induce a mesh divergence (some triangles are inverted). This is due to the fact that Jacobi iterations do not converge very quickly when the displacements vary a lot.

6.5 Application to the panel flutter simulation

In this section, we apply the previous enhancements to the numerical simulation of the panel flutter described in Section 6.2.2. An analysis given in [11] allowed us to find the theoretical Mach number where the panel flutter appears. For the following data:

$$\left\{\begin{array}{rcl} d & = & 1\ m \\ L & = & 0.5\ m \\ h & = & 1.35\ 10^{-3}\ m \\ \rho_S & = & 2710\ Kg/m^3 \\ E & = & 7.728\ 10^{10}\ N/m^2 \\ \nu & = & 0.33 \end{array}\right. , \quad \left\{\begin{array}{rcl} \gamma & = & 1.4 \\ P_\infty & = & 25714\ Pa \\ \rho_\infty & = & 0.4\ Kg/m^3 \\ M_\infty & = & 2.2686 \end{array}\right. ,$$

the instability appears, with a pulsation equal to $\bar{\omega} = 462\ rad/s$. Moreover, the flutter mode is shown on Figure 6.17. We check that the panel seems clamped, and we notice

that this coupled mode is unsymmetrical, because of the action of the supersonic airstream. The point with the maximal amplitude in the flutter mode is located at $x = 0.35\ m$.

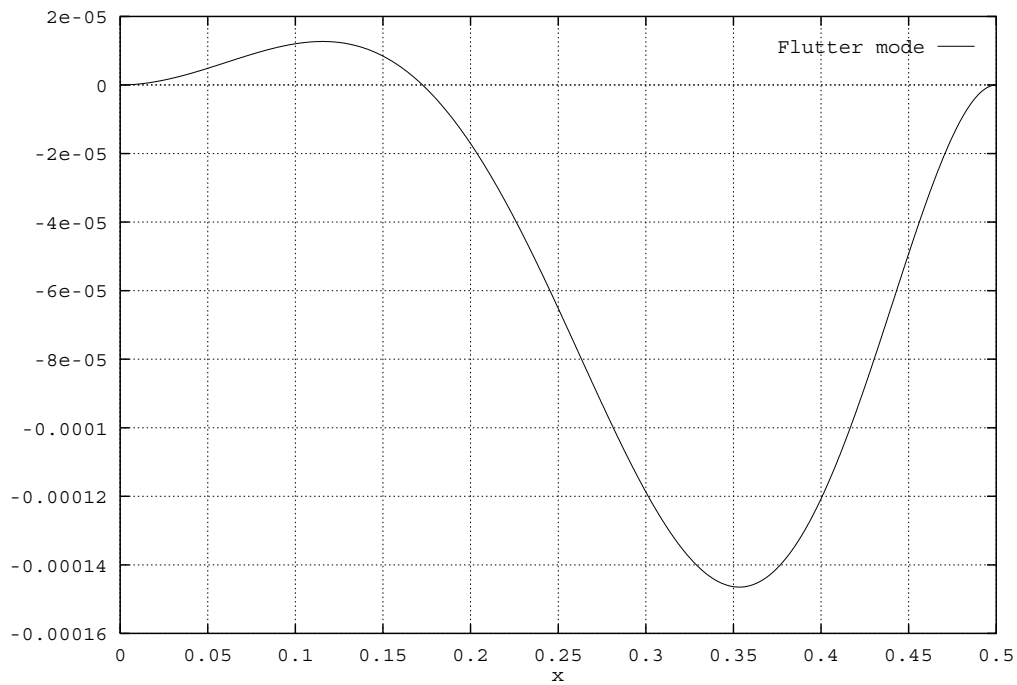

FIG. 6.17 – *Vertical deflection for the flutter mode.*

6.5.1 Simulations with few degrees of freedom (< 300)

We first perform some simulations based upon the shallow shell theory. The panel is discretized as a shell, with 299 points which have only one degree of freedom. The mass matrix is lumped, and the mass and stiffness matrices are presented in (6.10-6.11). The fluid mesh is matching at the interface. The total fluid unstructured grid is made of 1654 vertices and 2936 triangles. For all these simulations, we use second-order fluxes for the resolution of Euler equations, along with the explicit Runge-Kutta time-integrator described in (6.42). We use a Courant number equal to 1.4, which is inside the stability domain of the fluid uncoupled simulator.

Reference computation

As a reference computation, we first use a structural time-step equal to $\Delta t_S = 1.23\ 10^{-6} s$, which induces **no subcycling** in the fluid. Compared to the first period of the panel, this time step is very small (remember $\omega_1 = 197\ rad/s$ which gives

$\omega_1 \Delta t_S = 2.42\ 10^{-3}$). Since this time-step is very small, all methods give back the same results. We then use only two Jacobi iterations for each mesh computation.

The initial condition for the problem is the following: we compute a steady-state flow around the structure, which is perturbed along its second mode (as in [63]). We show on Figure 6.18 the first two uncoupled modes of the panel. The reader can check that these modes are symmetric and that they correspond to the clamped boundary conditions.

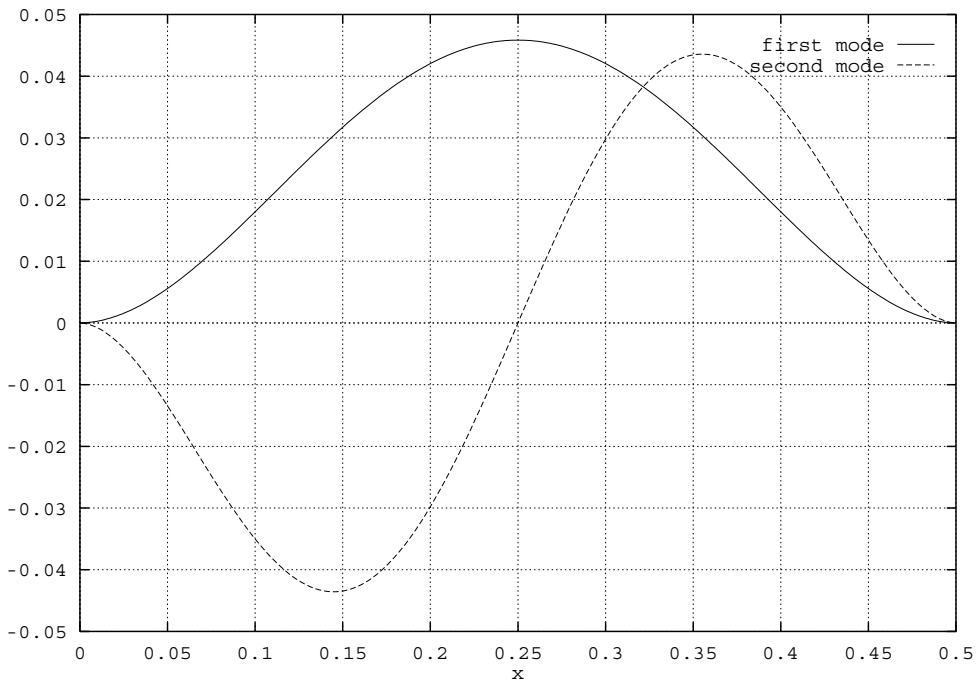

FIG. 6.18 – *Vertical deflection for the first two natural modes of the panel.*

We also show on Figure 6.19 the non-dimensionalized density contours (such that it is equal to 1 at infinity) of the steady-state solution around the perturbed structure. We see that the stream is also perturbed, and a new pressure distribution is exerted on the structure. As predicted by the aerodynamic theory giving (6.18), the steady-state flow is sensitive to the derivative $\partial X/\partial x$. This explains why the density seems to have three extrema.

Finally, the structure is given back the ability to move, and the simulation starts. We present on Figure 6.20 the displacement of the point of abscissa $x = 0.35\ m$ for a flow with a Mach number equal to $M_\infty = 2.23$. We see that, after a transient time, the oscillations go on with no amplification or damping. Instability is just reached. The non-dimensionalized density contours around the fluttering structure are shown on Figure 6.21.

Numerically, we found the limit Mach number $\bar{M}_\infty = 2.23$ which is in good agreement with the theoretical $\bar{M}_\infty = 2.2686$. We also find numerically that the flutter pulsation is $\bar{\omega} = 452\ rad/s$ which is also in good agreement. This discrepancies might

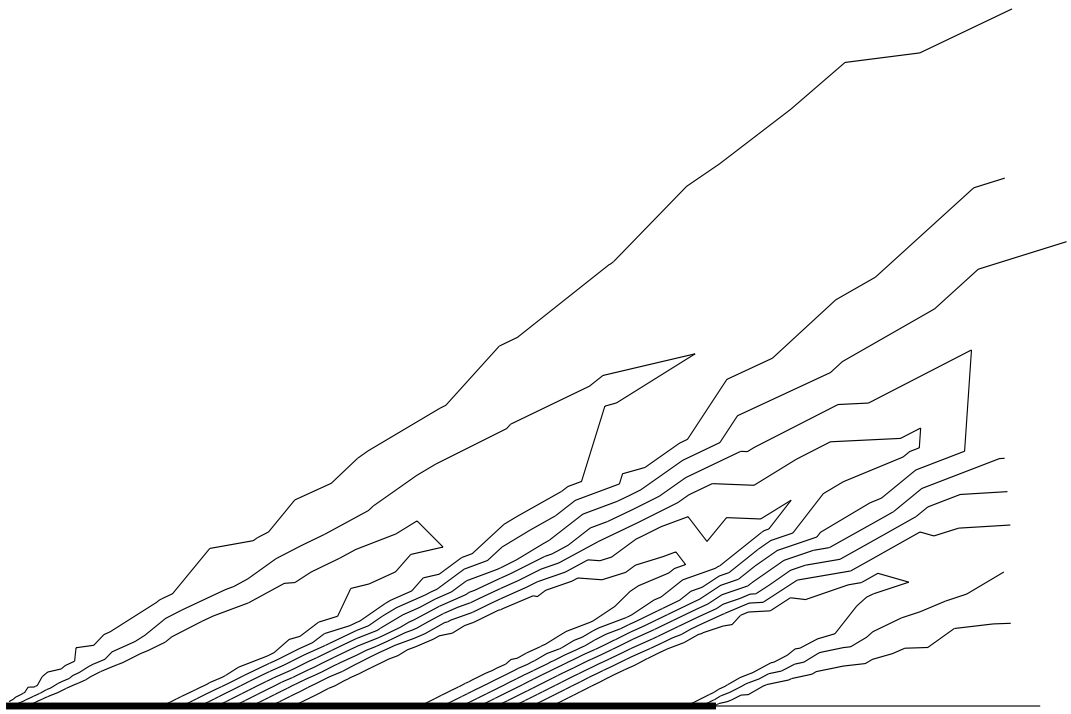

FIG. 6.19 – *Non-dimensionalized density ($Min = 0.997$, $Max = 1.0005$, $N_{step} = 7$). Initial steady-state flow around the perturbed panel (located by the thick line).*

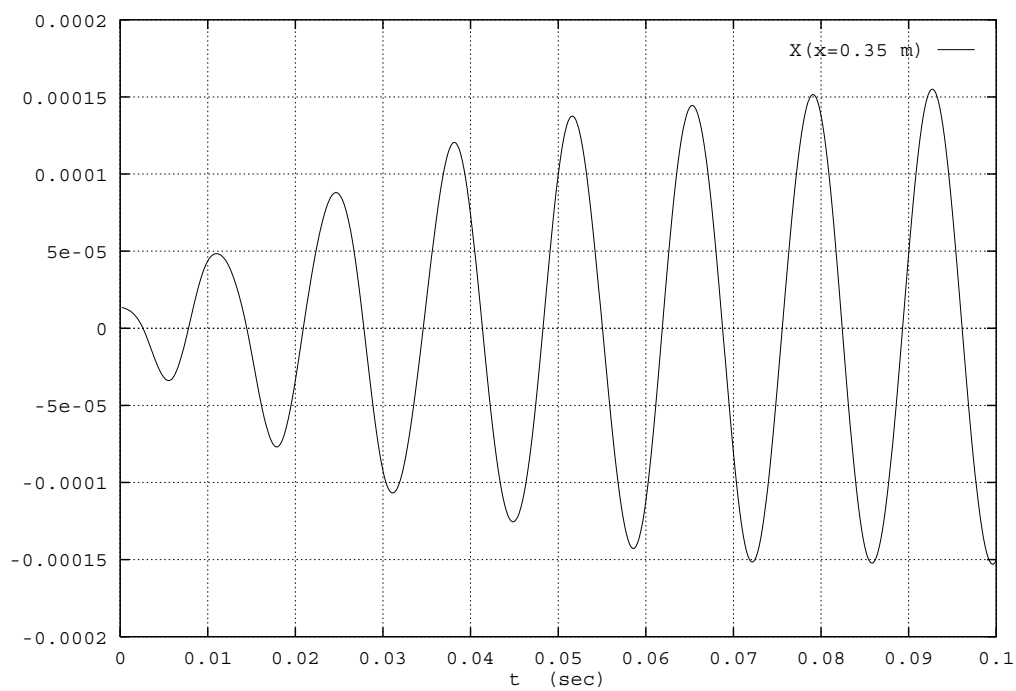

FIG. 6.20 – *Vertical deflection of the point located at $x = 0.35$ m – reference test with no subcycling and $\Delta t_S = 1.23\ 10^{-6} s$.*

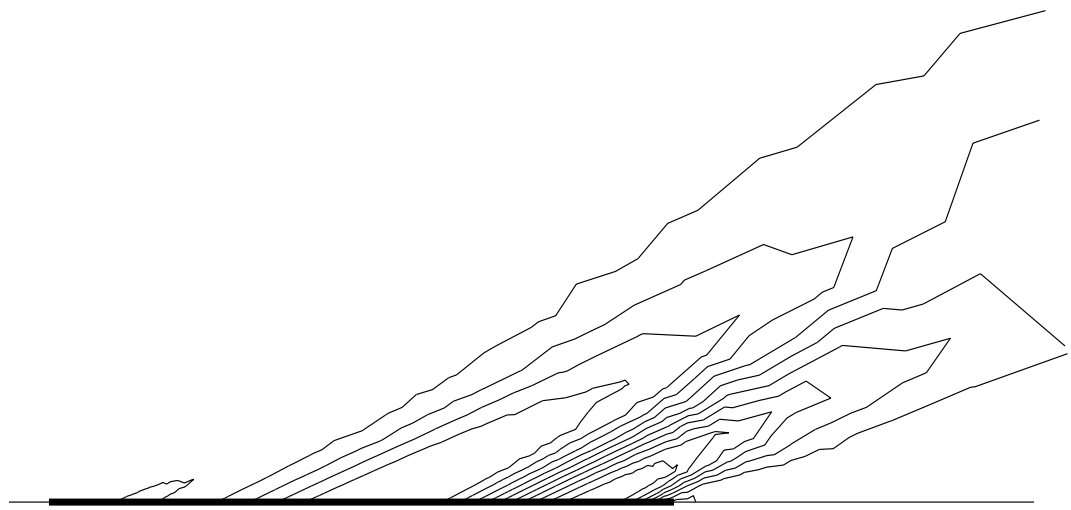

FIG. 6.21 – *Non-dimensionalized density ($Min = 0.997$, $Max = 1.0005$, $N_{step} = 7$). Flow around the fluttering panel (located by the thick line).*

be consequences of the small amount of structural degrees of freedom we have. This first computation will stand as a reference in the following.

Influence on the prediction in volume-discontinuous methods

We now test the volume-discontinuous method described in Section 6.4. We add the major improvements we reviewed: we used the corrected forces method (6.56), a constant mesh speed during subcycles, a mesh updating algorithm with fixed egde stiffnesses, fifty Jacobi iterations per structural time step and the second-order accurate prediction (6.57). We choose a structural time-step equal to $\Delta t_S = 2\ 10^{-4} s$, which corresponds to 70 time-steps per coupled period of oscillations. This gives a subcycling factor equal to $n_{S/F} = 161$.

We first test three simple first-order predictions: those given in (6.48) and (6.51), and the following "advanced" prediction

$$\widetilde{X^{n+1}} = X^n + \Delta t_S \left(2\ V^n - V^{n-1} \right).$$

We have plotted on Figure 6.22 the vertical deflection at $x = 0.35m$ for these three predictions and we compare with the reference curve. We see that the advanced prediction produces a high amount of numerical damping and that the others do not combine well with subcycling, since slight numerical instability appears. Note that no phase error is present.

The preceding curves might seem unsignificant, because the amplification in the displacement of a single point does not mean that instability is reached or that numerical damping is in excess. Therefore we have plotted on Figure 6.23 the mass product

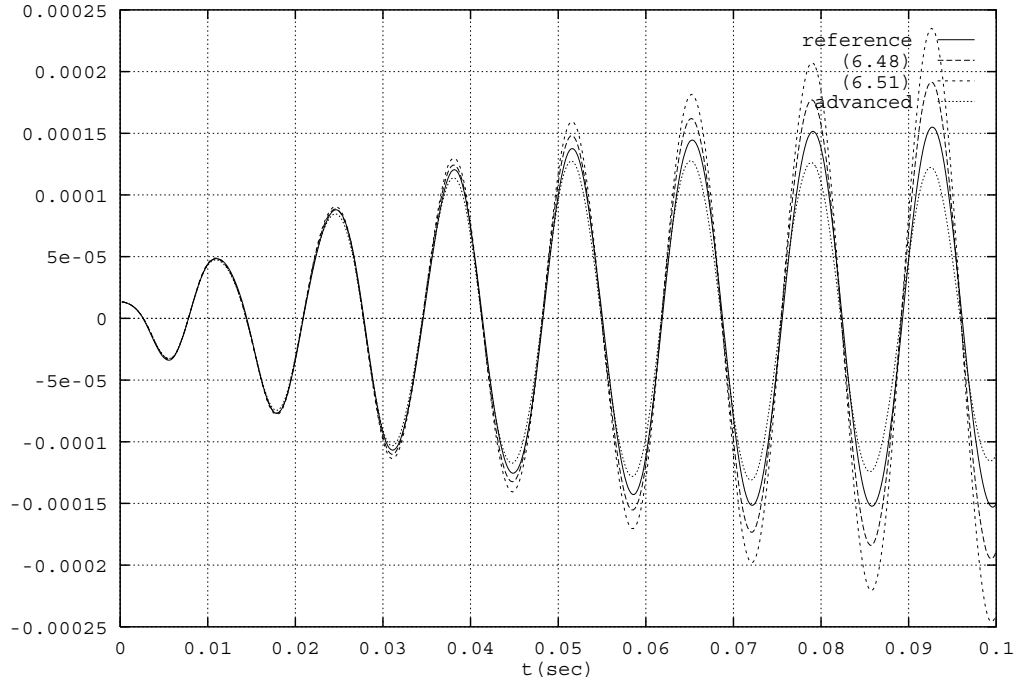

FIG. 6.22 – *Vertical deflection at $x = 0.35\ m$ with different first-order predictions and subcycling ($n_{S/F} = 161$).*

of the displacement field X with the second structural mode (i.e. $X_2^t M X$) for the same simulations. We see that the curves have the same characteristics. In the following, we will present curves concerning the mass product. If not otherwise mentionned, it will also mean that curves for the displacement at $x = 0.35\ m$ have the same shapes. Note on Figure 6.23 that the mass product oscillates without damping or amplification at the end of the simulation, which shows clearly that we are very close to the instability limit.

We then test two simple second-order predictions. One is using the Taylor series up to second order:

$$\widetilde{X^{n+1}} = X^n + \Delta t_S\ V^n + \frac{\Delta t_S^2}{2}\ A^n, \tag{6.58}$$

and the other one which does not use any acceleration:

$$\widetilde{X^{n+1}} = X^n + \Delta t_S \left(1.5\ V^n - 0.5\ V^{n-1}\right). \tag{6.59}$$

The mass product with the second mode is plotted on Figure 6.24 for the corresponding computations. We see that the prediction (6.58) is unstable with this time step. On the contrary, the prediction (6.59) is stable, and in very good agreement with the reference curve, even with this subcycling factor $n_{F/S} = 161$.

On Figure 6.25, we present the same results for the prediction (6.59) with bigger subcycling factors and structural time steps. The method is perfectly acceptable for

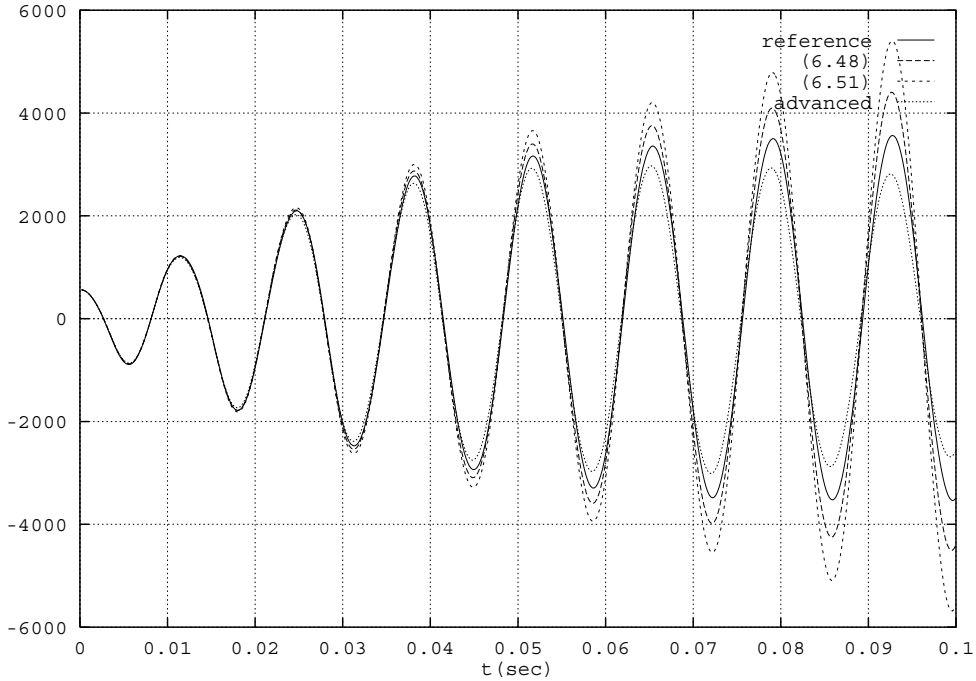

FIG. 6.23 – *Mass product $X_2^t MX$ with different first-order predictions and subcycling ($n_{S/F} = 161$).*

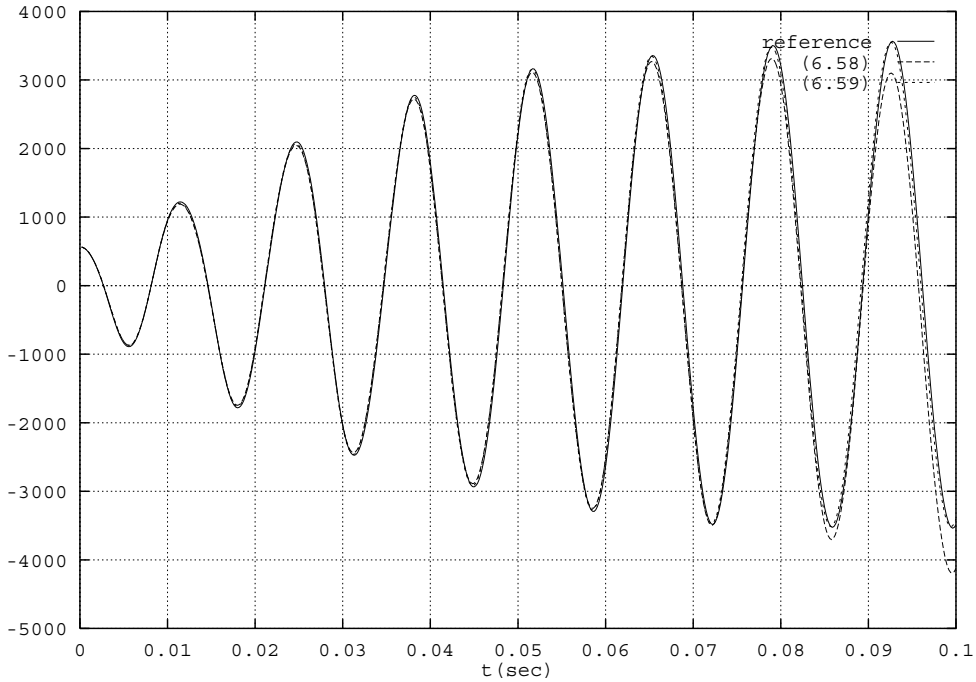

FIG. 6.24 – *Mass product $X_2^t MX$ with different second-order predictions and subcycling ($n_{S/F} = 161$).*

$\Delta t_S = 4\ 10^{-4} s$ which corresponds to 35 time steps per coupled period of oscillation. For $n_{F/S} = 483$ ($\Delta t_S = 6\ 10^{-4} s$), we only have 23 time steps per oscillation, which gives a rather poor definition. Then the scheme appears to be slightly inaccurate and unstable as could be predicted.

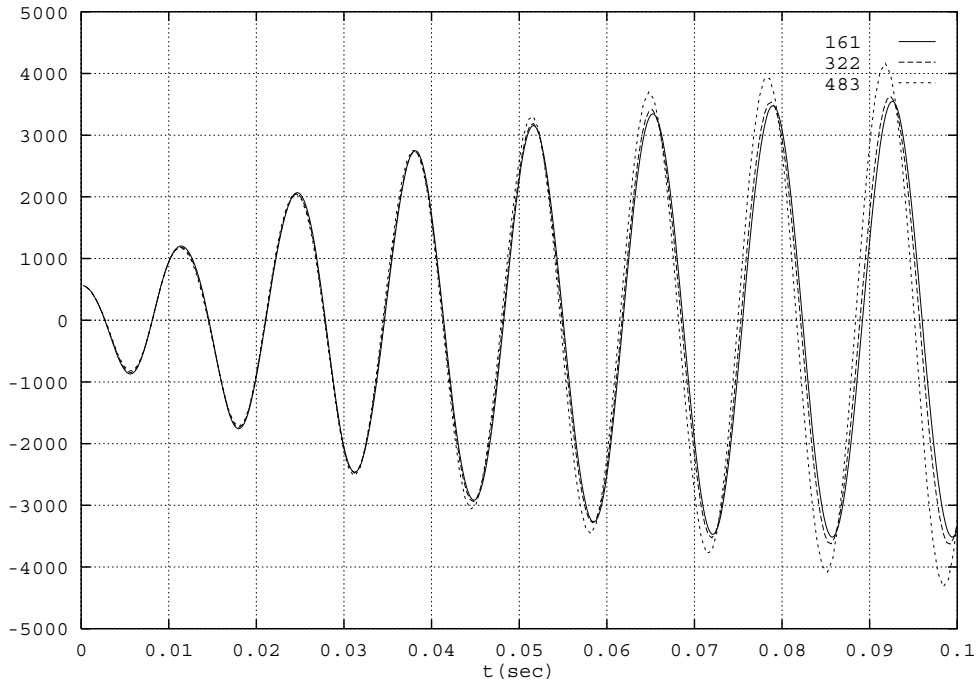

FIG. 6.25 – *Mass product $X_2^t M X$ with the prediction (6.59) and different subcycling factors $n_{S/F}$.*

6.5.2 Computations with thousands of degrees of freedom

In order to check if our algorithm goes on well with a lot of degrees of freedom, we get back to the finite-element method on quadrilateral isoparametric elements based upon the plane-stress three-dimensional elastic model of Section 6.2.2 (page 186).

The whole computation is the same as previously, but the panel is discretized as an elastic volume (actually surface, since the problem is two-dimensional). We put 790 points on the length and three points on the height. Each point is given two degrees of freedom (vertical and horizontal displacements). This makes 4740 degrees of freedom. The aspect ratio for the quadrilateral elements is 1.07. So mesh locking is avoided. We find again that the flutter appears at $M = 2.23$. We show on Figure 6.26 the mass product with the second mode for the volume-discontinuous method with the prediction (6.59) for $\Delta t_S = 2\ 10^{-4} s$ and $n_{F/S} = 161$.

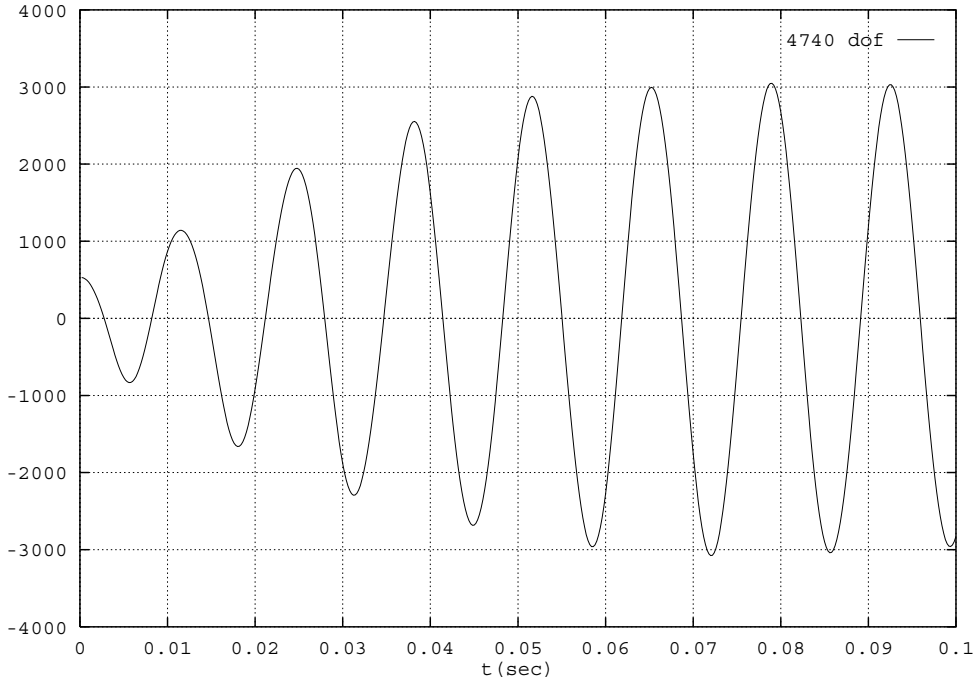

FIG. 6.26 – *Mass product* $X_2^t MX$ *with the prediction (6.59) and* $n_{S/F} = 161$ *for the panel with* 4740 *dof.*

This computation was made on a Cray Y-MP2E/232[1]. With a 1654 vertex and 2936 element fluid mesh, it required 59 *min* with a performance of 156 Mflops. The savings due to subcycling have been estimated to 101 *min* (mesh recalculations and structural integrations). The result is satisfying, since the case is just at the stability limit.

The initial aim of an industrial simulation would have been the determination of the flutter limit for a given structure. In order to do this, we test our method on a huge structure for different Mach numbers. We use the previous elastic model with quadrilateral isoparametric elements. This time, we have 2221 on the length and 7 points on the height of the panel. This makes 31094 degrees of freedom in the structure. We use a sky-line storage for the matrices, which reduces to a million terms. With these data, the aspect ratio for the elements is perfect, so no mesh locking appears. However, the change in models (compared to the shallow shell theory) gives an instability limit around $M_\infty = 2.24$.

We first perform computations with $M_\infty = 2.24$. We show on Figure 6.27 the mass product with the second mode for our method with no subcycling ($\Delta t_S = 1.23\ 10^{-6} s$) and with a subcycling of $n_{F/S} = 162$ ($\Delta t_S = 2.\ 10^{-4} s$). The results are in perfect agreement. The first simulation tells us that at $M_\infty = 2.24$, we are beyond the stability

1. We would like to thank the Conseil Régional of Provence-Alpes-Côte d'Azur which provided computational time on the computer Cray Y-MP2E/232 of the Institut Méditérranéen de Technologie.

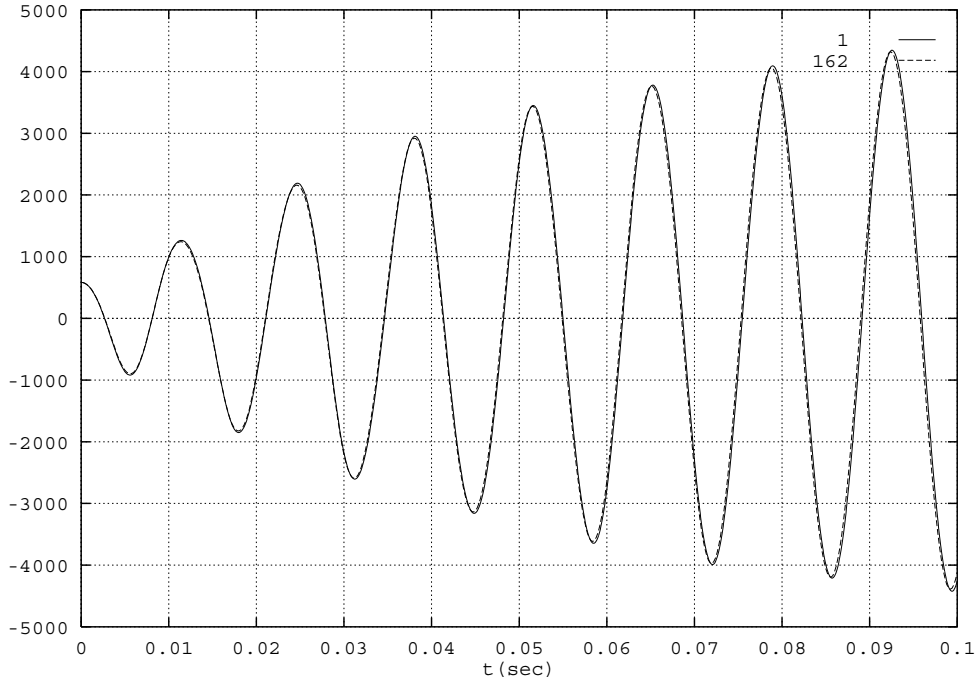

FIG. 6.27 – *Mass product* $X_2^t MX$ *with* $n_{S/F} = 1$ *and* $n_{S/F} = 162$ *for the panel with* 31094 *dof at* $M_\infty = 2.24$.

limit. The second one tells us our method is very accurate, and that the structural integration is sufficient only once in 162 times. The displacements of the point at $x = 0.35m$ for the same tests are shown on Figure 6.28. They also are really close.

As previously, we have tested the method with bigger time steps. We find again that $\Delta t_S = 4\ 10^{-4}s$ (35 time steps per coupled period of oscillation) gives good results, and that $\Delta t_S = 6\ 10^{-4}s$ (23 time steps per oscillation) gives a poor resolution (see Figure 6.29). The costs of the previous computations (also made on the Cray Y-MP2E/232) are given on Table 6.3. We see that subcycling can allow dramatic sparings in computational costs when the structure is complex. This can easily be explained: the vectorized version of the fluid procedures[2] are notably more efficient than structural procedures where sky-line storage prevents an efficient vectorization.

Finally, we make again the same computations with $M_\infty = 2.23$. Our point is to prove that our method with subcycling allows a accurate determination of the limit Mach number. This would prove that the stability of the method is not a consequence of the production of excessive numerical damping. We show on Figure 6.30 the mass product with the second mode for our method with several large subcycling factors $n_{F/S}$. The results are not surprising. From previous computations, we deduced that $n_{F/S} = 484$ (23 time steps per coupled period of oscillation) gives numerical instability,

2. We thank SINUS of INRIA and particularly A. Dervieux and S. Lantéri for providing us all necessary unvectorized procedures needed for the fluid.

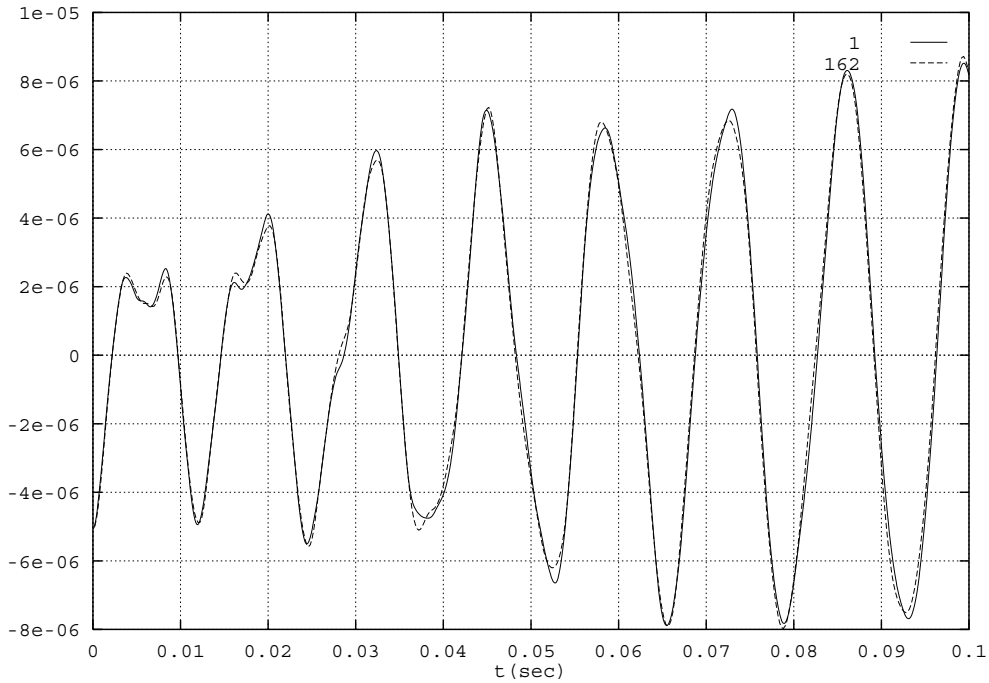

FIG. 6.28 – *Vertical deflection at* $x = 0.35m$ *with* $n_{S/F} = 1$ *and* $n_{S/F} = 162$ *for the panel with* 31094 *dof at* $M_\infty = 2.24$.

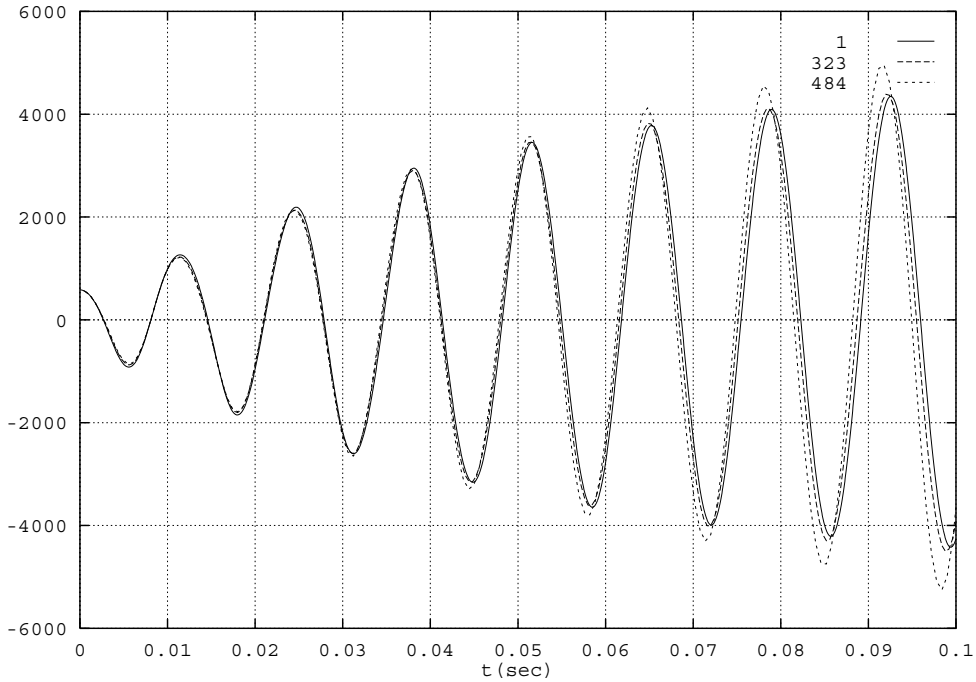

FIG. 6.29 – *Mass product* $X_2^t MX$ *with several subcycling factors* $n_{S/F}$ *for the panel with* 31094 *dof at* $M_\infty = 2.24$.

$n_{S/F}$	CPU time (hours)	Mflops
1	5.48	136
4	2.54	143
41	1.60	153
81	1.54	154
162	1.51	155
323	1.49	156

TAB. 6.3 – *Computational costs and performance for several subcycling factors.*

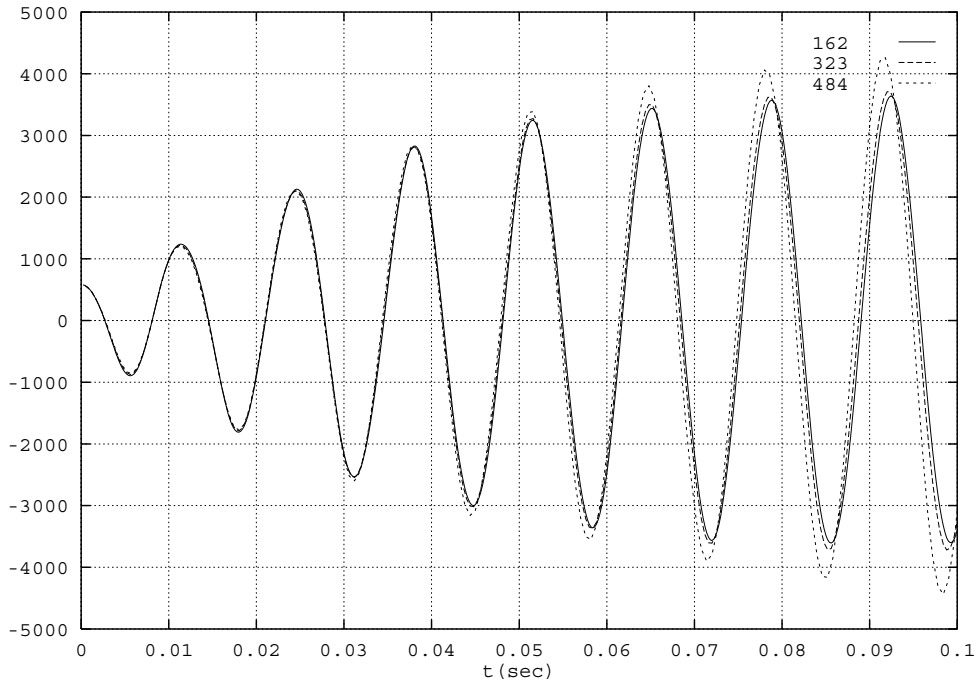

FIG. 6.30 – *Mass product* $X_2^t MX$ *with several subcycling factors* $n_{S/F}$ *for the panel with* 31094 *dof at* $M_\infty = 2.23$.

while $n_{F/S} = 162$ and $n_{F/S} = 323$ do not. Since the mass products with the second mode for $n_{F/S} = 162$ and $n_{F/S} = 323$ are slightly damped at $M_\infty = 2.23$ and undamped at $M_\infty = 2.24$, we conclude that our method, **with subcycling up to $\mathbf{n_{F/S} = 323}$**, allows us to detect that the flutter limit is such that $2.23 < M_\infty^{flutter} < 2.24$.

As a conclusion, we put the emphasis on some important points. We were able to perform computations with heavy subcycling. This can reduce dramatically the computational time. The method is stable, accurate and produces no numerical damping if the number of structural time steps per coupled period of oscillation is at least 35, which is the weakest condition that could be imagined for this kind of staggered method.

6.6 Conclusion

In this section, we sum up all enhancements reviewed in this paper, and we present the global optimal algorithm for the numerical simulations we are interested in. We recall we use an explicit time scheme for the fluid, and the trapezoidal rule for the structure (implicit, unconditionally stable). We then want to subcycle the fluid, and to spare computational cost on the structural part.

We assume we dispose of all computational quantites at time t^n. We intend to advance in time towards $t^{n+1} = t^n + \Delta t_S$. The global algorithm is the following:

1. **compute a prediction $\widetilde{X^{n+1}}$ for the structure at time t^{n+1}**. Use the second-order accurate prediction (6.59) (in some cases, a first-order accurate prediction, either (6.48) or (6.51), might be more stable).

2. **move the mesh**. The location of the mesh at time t^{n+1} is obtained with the algorithm presented on (6.28-6.31).

   (a) The stiffness of the edges are computed once and for all at the beginning of the simulation, as the inverse of their initial length.

   (b) The prediction for the mesh displacement during the current time-step is given by (6.57).

   (c) We can choose the number of Jacobi iterations between 25 and 50 (as shown on Figure 6.16, more iterations can prevent spurious oscillation of the mesh: with 25 iterations, the average time-step is smaller and the number of fluid iterations needed is bigger than with 300 iterations).

3. **compute the grid velocities**. They are simply computed as in (6.40).

4. **advance the fluid in time with as many time steps Δt_F as necessary**.

During all subcycles, the grid velocities are constant. Each fluid time-step requires:

(a) the computation of all geometric time-dependent variables (for example, the cell areas and the grid normals $\widetilde{\vec{\eta}_{ij}}$ in (6.39).

(b) the use of the pressures on the fluid/structure interface to compute $\bar{F}^{n+1/2}$ the time-averaged generalized force on the structure during the subcycles defined in (6.47).

(c) the time-integration of the fluid over Δt_F with the three step Runge-Kutta scheme presented on (6.42). This equation was issued from the resolution of the ALE-formulation of Euler equations by a Godunov's type finite volume method based on a second-order accurate version of Roe's numerical flux.

5. **compute the applied force on the structure** F_I^{n+1}. We advise to use the last forces method (6.55) or the corrected forces method (6.56). The first one is cheaper, since it does not require the computation of the time-averaged force described in 4.b. However, the corrected forces method gives an exact conservation of the momentum, and an error on the energy conservation which only depends on the structural prediction accuracy.

6. **advance the structure of** Δt_S. This can be done with the simple trapezoidal rule, which is unconditionally stable, second-order time-accurate, and with no numerical dissipation. Use the source term previously computed F_I^{n+1}.

This algorithm is quite general. It is under test with more complex configurations (other panels, two-dimensional and three-dimensional wing/body geometries).

Quatrième partie

Conclusion

Dans cette thèse, nous nous sommes intéressés à la simulation numérique de phénomènes d'interaction fluide-structure. Plus précisément, nous avons mis au point des méthodes d'intégration décalée pour des problèmes aéroélastiques bidimensionnels non-linéaires.

Nous avons tout d'abord détaillé les méthodes disponibles pour ce genre de problème. Elles concernent chacun des trois aspects de la simulation numérique de phénomènes d'interaction fluide-structure.

L'écoulement peut être régi par plusieurs systèmes d'équations. Nous nous sommes limités aux équations d'Euler bidimensionnelles (fluide compressible non-visqueux). Cependant, une caractéristique constante de toutes les interactions est que le domaine fluide est déformable. Le traitement de cette nouvelle difficulté fait appel à des changements de variables ou de référentiels astucieux pour certains cas particuliers, ou à de nouvelles formulations, de type ALE ou à maillage dynamique. Ces dernières comportent des aspects Lagrangiens près de l'interface fluide-structure, et Eulériens dans l'écoulement. Les méthodes à maillage dynamique s'adaptent particulièrement bien aux formulations en volumes-finis sur tous les types de maillage, et restent proches des méthodes classiquement utilisées en mécanique des fluides.

Nous avons ensuite présenté les algorithmes couramment utilisés pour simuler le couplage effectif entre le fluide et la structure. Nous avons montré pourquoi l'intégration globale du système complet est irréalisable. Nous avons présenté les méthodes d'intégration décalée. Très populaires, elles permettent une simulation en boîte noire des deux sous-systèmes. Cependant, ces méthodes sont élémentaires. Leur précision faible et leur stabilité inconnue limitent considérablement les pas de temps utilisés et entrainent de gros coûts de calcul.

Quant à elles, l'intégration en temps et la discrétisation de la structure ne présentent pas de difficulté propre aux phénomènes d'interaction fluide-structure. La structure reçoit simplement une distribution surfacique de forces de pression exercées par le fluide.

Nous avons ensuite étudié quelles propriétés numériques (stabilité, précision, efficacité, etc...) sont transmises à une méthode d'intégration décalée par chacune des méthodes utilisées pour le fluide et la structure.

Nous avons montré, pour un cas mono-dimensionnel linéaire très simple, que ces propriétés dépendent très fortement de la manière dont le couplage est effectivement pris en compte au niveau duscret. Nous avons pu observer que la stabilité ne se transmet pas en général à l'algorithme global. Nous avons pu même prédire avec précision la stabilité et l'amortissement numérique introduit spécifiquement par le traitement du couplage. Ces prédictions nous ont aussi permis de mettre au point des schémas originaux, mais dépendant du problème, plus précis et plus stables. Ainsi, l'étude d'un problème modèle simple nous a fait entrevoir la nécessité d'une étude plus théorique sur les propriétés numériques des schémas d'intégration décalée.

Cette étude a porté sur le même problème linéaire acoustique mono-dimensionnel. Nous avons utilisé des formulations énergétiques (fonctions de Lyapunov du système couplé). Nous avons ainsi pu établir l'inconditionnelle stabilité de nouveaux schémas

implicites décalés, dans leur version simple ou sous-cyclée. Nous avons également recherché des implémentations parallèles et efficaces de ces algorithmes. De plus, ces nouveaux résultats nous ont permis d'établir des critères généraux pour construire des schémas plus précis et plus stables.

Enfin, nous avons appliqué ces critères à des problémes non-linéaires monodimensionnels et bidimensionnels.

Dans un premier temps, nous nous sommes intéressés à deux problèmes aéroélastiques où la structure linéaire comporte un seul degré de liberté, et où le fluide est régi par les équations d'Euler mono-dimensionnelles. Les considérations énergétiques, si précieuses pour les problèmes linéaires, nous ont mis sur la voie d'un traitement original du couplage à l'interface fluide-structure. Une nouvelle méthode a été mise au point, où l'interface fluide-structure est dédoublée. Cette méthode permet d'intégrer le fluide en premier, à l'aide d'une prédiction de la position de la structure à la fin du pas de temps courant. Ainsi, la méthode est plus souple : sa précision et sa stabilité dépendent fortement de la prédiction utilisée et le sous-cyclage ne pose pas de difficulté particulière.

De nombreuses prédictions ont été testés sur ces problèmes mono-dimensionnels. Nous avons fait appel à un éventail assez large de méthodes numériques, allant des moyennes temporelles simples aux filtres numériques auto-adaptatifs. Nous avons obtenus des résultats très satisfaisants, où la précision et la stabilité de l'algorithme global ne sont plus limitées que par celles des méthodes utilisées dans chaque sous-système.

Nous avons vérifié que ces conclusions restent valides pour différents problèmes bidimensionnels complexes. Nous avons étudié numériquement le flottement d'un profil d'aile en mouvement rigide dans un écoulement transsonique et celui d'un panneau linéairement élastique sous un écoulement supersonique. Dans ces deux problèmes, des effets non-linéaires prépondérants empêchent toute approche linéarisée ou fréquentielle. Seule une approche véritablement instationnaire permet de simuler précisément l'apparition du flottement. Nous avons donc utilisé nos algorithmes de couplage appliqués à des schémas d'ordre élevé en temps et en espace pour le fluide et la structure. Dans les deux cas, nous avons obtenu les résultats espérés. D'une part, la limite de stabilité de l'algorithme global se situe au moins au-delà des limites de stabilité des schémas utilisés pour chaque sous-système (implicite pour la structure, explicite pour le fluide). D'autre part, l'algorithme de couplage n'introduit ni amortissement numérique ni dispersion supplémentaires.

Après ce travail, de nombreuses perspectives sont ouvertes. Du point de vue théorique, certaines questions sont restées sans réponse. Par exemple, on ne sait rien démontrer de la stabilité d'un schéma explicite sous-cyclé, même dans un cas linéaire. On peut également envisager d'appliquer les considérations énergétiques présentées ici à d'autres problèmes linéaires, comme, par exemple, celui de l'interaction entre un ensemble de particules chargées et les champs électromagnétiques qu'elles induisent.

D'un point de vue plus numérique, on peut chercher à tester l'ensemble des méthodes de couplage présentées sur des problèmes proches et plus complexes (écoulements non-visqueux ou visqueux, bidimensionnels ou tridimensionnels, autour de

configurations réelles, pourvues éventuellement de dispositifs de contrôle actif) ou complètement différents (problèmes aéroélastiques et hydroélastiques où le fluide est incompressible et visqueux).

Bibliographie

[1] D.A. Anderson, J.C. Tannehill, and R.H. Pletcher. *Computational fluid mechanics and heat transfer*. Hemisphere. Mac Graw-Hill, 1984.

[2] W.K. Anderson, J.L. Thomas, and C.L. Rumsey. Extension and Application to Unsteady Calculations on Dynamic Meshes. In *AIAA Eighth Computational Fluid Dynamics Conference, Honolulu, Hawaii*, June 9-11 1987. AIAA paper 87-1152.

[3] W.K. Anderson, J.L. Thomas, and C.L. Rumsey. Extension and Application to Unsteady Calculations on Dynamic Meshes. *AIAA Journal*, 27(6):673–674, June 1989.

[4] E. Barszcz. Intercube communication on the iPSC/860. In *Scalable High Performance Computing Conference, Williamsburg*, April 26-29 1992.

[5] J.T. Batina. Unsteady Euler Airfoil Solutions Using Unstructured Dynamic Meshes. *AIAA Journal*, 28:1381–1388, Aug 1990.

[6] J.T. Batina. Implicit Flux-Split Euler Schemes for Unsteady Aerodynamic Analysis Involving Unstructured Dynamic Meshes. *AAIA Journal*, 29:1836–1843, Nov 1991.

[7] M. Bellanger. *Traitement numérique du signal*. CNET-ENST, Collection technique et scientifique des télécommunications. Masson, 1987.

[8] M. Bellanger. *Analyse des signaux et filtrage numérique adaptatif*. CNET-ENST, Collection technique et scientifique des télécommunications. Masson, 1989.

[9] T. Belytschko and J. M. Kennedy. Computer models for subassembly simulation. *Nuclear Engineering Design*, 4(49):17–38, 1978.

[10] T. Belytschko, P. Smolinski, and W.K. Liu. Stability of multi-time step partitioned integrators for first-order finite element systems. *Computer Methods in Applied Mechanics and Engineering*, 49:281–297, 1985.

[11] R.L. Bisplinghoff, H. Ashley, and R.L. Halfman. *Aeroelasticity*. Addison-Wesley, Reading, MA, Nov 1957.

[12] M. Blair, M. H. Williams, and T. A. Weisshaar. Time domain simulations of a flexible wing in subsonic compressible flow. In *AIAA 8th Applied Aerodynamics Conference*, Portland, Oregon, August 20-22 1990. AIAA paper 90-1153.

[13] R. Boite and H. Leich. *Les filtres numériques*. CNET-ENST, Collection technique et scientifique des télécommunications. Masson, 1990.

[14] C.J. Borland and D.P. Rizzetta. Nonlinear Transonic Flutter Analysis. *AIAA Journal*, 20:1606–1615, Nov 1982.

[15] J. Chung and G.M. Hulbert. A time integration algorithm for structural dynamics with improved numerical dissipation: the generalized-α method. *Transctions of ASME, Journal of Applied Mechanics*, 60:371–375, June 1993.

[16] L. Crivelli and C. Farhat. Implicit transient finite element structural computations on MIMD systems: FETI v.s. direct solvers. In *AIAA 34th Structural Dynamics Meeting, La Jolla, California*, April 19-21 1993. AIAA paper No. 93-1310.

[17] R. Dat. *Vibrations aéroélastiques*. Cours de l'Ecole Nationale Supérieure de l'Aéronautique et de l'espace. ENSAE Département des Structures-Matériaux--Technologie, 1978.

[18] A. Dervieux and B. Palmerio. 2D and 3D unstructured mesh adaption relying on physical analogy. Pré-publication en Mathématiques N-207, Sept 1988.

[19] J. Donea, P. Fasoli-Stella, and S. Giuliani. Finite element solution of transient fluid-structure problems in Lagrangian coordinates. In *International Meeting on Fast Reactor Safety and Related Physics*, pages 1427–1435, Chicago, 1976.

[20] J. Donea, S. Giuliani, and J.P. Halleux. An Arbitrary Lagrangian Eulerian Finite Element Method for Transient Dynamic Fluid-Structure Interactions. *Computer Methods in Applied Mechanics and Engineering*, 33:689–723, 1982.

[21] C. Farhat, L. Crivelli, and F.-X. Roux. Extending substructure based iterative solvers to multiple load and repeated analyses. Computer Methods in Applied Mechanics and Engineering (in press).

[22] C. Farhat, L. Fezoui, and Lantéri. Two-dimensional viscous flow computations on the Connection Machine: unstructured meshes, upwind schemes and massively parallel computations. *Computer methods in Applied Mechanics and Engineering*, 102:61–88, 1991.

[23] C. Farhat, S. Lantéri, N. Maman, and P. S. Chen. Parallel and heterogeneous solution of three-dimensional transient coupled aeroelastic problems. submitted for publication.

[24] C. Farhat, M. Lesoinne, P. Stern, and S. Lantéri. High performance Solution of 3D Nonlinear Aeroelastic Problems via Parallel Partitioned Algorithms: Methodology and Preliminary Results. Center for Aerospace Structures - 94-20, University of Colorado, Boulder, Colorado, September 1994.

[25] C. Farhat and T.Y. Lin. Transient Aeroelastic Computations Using Multiple Moving Frames of Reference. AIAA paper 90-3053-CP, 1990.

[26] C. Farhat, N. Maman, and M. Lesoinne. Mixed eplicit/implicit time integration of coupled aeroelastic problems: three filed formulation, geometric conservation and distributed solution. Center for Aerospace Structures - 94-17, University of Colorado, Boulder, Colorado, August 1994.

[27] C. Farhat, K. C. Park, and Y. D. Pelerin. An unconditionnally stable staggered algorithm for transient finite element analysis of coupled thermoelastic problems. *Computer Methods in Applied Mechanics and Engineering*, 85:349–365, 1991.

[28] C. Farhat and N. Sobh. A consistency analysis of a class of concurrent transient implicit/explicit algorithms. *Computer Methods in Applied Mechanics and Engineering*, 8(84):147–162, 1990.

[29] L. Fezoui. Résolution des équations d'Euler par un schéma de Van Leer en éléments finis. INRIA RR-358, INRIA Sophia-Antipolis, January 1985.

[30] Y.C. Fung. *An introduction to the theory of aeroelasticity.* Dover Publications, Inc., New York, second edition edition, 1969.

[31] G.P. Guruswamy. Interaction of Fluids and Structures for Aircraft Applications. *Computers & Structures*, 30(1/2): 1–13 , 1988.

[32] G.P. Guruswamy. Integrated Approach for Active Coupling of Structures and Fluids. *AIAA Journal*, 27 : 788–793, June 1989.

[33] G.P. Guruswamy. Unsteady Aerodynamic and Aeroelastic Calculations for Wings Using Euler Equations. *AIAA Journal*, 28:461–469, Mar 1990.

[34] G.P. Guruswamy. Vortical Flow Computations on Swept Flexible Wings Using Navier-Stockes Equations. *AIAA Journal*, 28:2077–2084, Dec 1990.

[35] A. Harten and J.M. Hyman. Self Adjusting Grid Methods for One-Dimensional Hyperbolic Conservation Laws. *Journal of Computational Physics*, 50:235–269, 1983.

[36] H.M. Hilber, T.J.R. Hughes, and R.L. Taylor. Improved numerical dissipation for time integration algorithms in structural dynamics. *Earthquake Engineering and Structural Dynamics*, 5:283–292, 1977.

[37] J. C. Houbolt. A study of several aerothermoelastic problems of aircraft structures. Mitteilung aus dem Institut für Flugzeugstatik und Leichtbau 5, E.T.H., Zurich, 1958.

[38] T. J. R. Hughes. Analysis of transient algorithms with particular reference to stability behavior. In T. Belytschko and T. J. R. Hughes, editors, *Computational Methods for Transient Analysis* , pages 67–155. North-Holland Pub. Co., 1983.

[39] T.J.R. Hughes and W.K. Liu. Implicit-explicit finite elements in transient analysis: stability theory. *Transactions of the ASME, Journal of Applied Mechanics*, 45:371–374, June 1978.

[40] T.J.R. Hughes, W.K. Liu, and T. K. Zimmermann. Lagrangian-Eulerian finite element formulation for incompressible viscous flows. In *U.S.-Japan Seminar on Interdisciplinary Finite Element Analysis, Cornell University, Ithaca, NY*, August 7-11 1978.

[41] K. Isogai and K. Suetsugu. Numerical Calculation of Unsteady Transonic Potential Flow over Three-Dimensional Wings with Oscillating Control Surfaces. *AIAA Journal*, 22:478–485, Apr 1984.

[42] O.A. Kandil and H.A. Chuang. Unsteady Transonic Airfoil Computation using Implicit Euler Scheme on Body-fixed Grid. *AIAA Journal*, 27:1031–1038, Aug 1989.

[43] S. Lanteri. *Simulation d'Ecoulements Aérodynamiques Instationnaires sur une Architecture S.I.M.D. Massivement Parallèle.* Thèse de doctorat en sciences de l'ingénieur, Université de Nice-Sophia-Antipolis, France, 1991.

[44] S. Lanteri and C. Farhat. Rapport de recherche Aéroélasticité. 1ère partie : étude bibliographique. Contrat DRET/AMDBA/PGSoft/INRIA, 1992.

[45] S. Lanteri and C. Farhat. Rapport de recherche Aéroélasticité. 2ème partie : étude bibliographique et analyse des méthodes. Contrat DRET/AMDBA/PGSoft/-INRIA, 1992.

[46] S. Lanteri and C. Farhat. Rapport de recherche Aéroélasticité. 3ème partie : mouvements de maillages et étude numérique sur des écoulements non visqueux. Contrat DRET/AMDBA/PGSoft/INRIA, 1993.

[47] M. Lesoinne. *Mathematical analysis of three-field numerical methods for aeroelastic problems.* PhD thesis, Department of Aerospace Engineering Sciences, University of Colorado, University of Colorado, Boulder, Colorado, 1994.

[48] M. Lesoinne and C. Farhat. Stability analysis of dynamic meshes for transient aeroelastic computations. In *11th AIAA Computational Fluid Dynamics Conference, Orlando, Florida*, July 6-9 1993. AIAA paper 93-3325.

[49] K.J. Lin, P.J. Lu, and J.Q. Tarn. Flutter Analysis of Cantilever Composite Plates in Subsonic Flow. *AIAA Journal*, 27:1102–1109, Aug 1989.

[50] T.Y. Lin. *A multiple frames of reference approach to aeroelastic computations : application to airfoil flutter analysis.* PhD thesis, Department of Aerospace Engineering Sciences, University of Colorado, University of Colorado, Boulder, Colorado, 1990.

[51] R. Lohner. An Adaptive Finite Element Solver for Transient Problems with Moving Bodies. *Computers & Structures*, 30(1/2):303–317, 1988.

[52] I. Lottati. The Role of Structural and Aerodynamic Damping on the Aeroelastic Behavior of Wings. *Journal of Aircraft*, 23:606–608, Jul 1986. Engineering notes.

[53] N. Maman and C. Farhat. Matching fluid and structure meshes for aeroelastic computations: a parallel approach. Center for Aerospace Structures - 93-12, University of Colorado, Boulder, Colorado, June 1993.

[54] D.J. Mavriplis. Multigrid Solution of the Two-Dimensional Euler Equations on Unstructured Triangular Meshes. *AIAA Journal*, 26:824–831, Jul 1988.

[55] K. Nakahashi and G.S. Deiwert. Self-adaptive Grid Method with Application to Airfoil Flows. *AIAA Journal*, 25:513–520, Apr 1987.

[56] B. N'Konga and H. Guillard. A Roe Scheme on Non-Structured Meshes for Moving Boundaries Problems. In *Proceedings of the 13th IMACS World Congress on Computational and Applied Mathematics*, pages 1.447–1.449, Trinity College, Dublin, Ireland, July 22-26 1991.

[57] B. N'Konga and H. Guillard. Godunov type method on non-structured meshes for three-dimensional moving boundary problems. INRIA RR-1883, INRIA Sophia-Antipolis, Avril 1993.

[58] S. Obayashi, G.P. Guruswamy, and P.M. Goorjian. Streamwise Upwind Algorithm for Computing Unsteady Transonic Flows Past Oscillating Wings. *AIAA Journal*, 29:1668–1677, Oct 1991.

[59] K. C. Park and C. A. Felippa. Computational Methods for Transient Analysis. In T. Belytschko and T. J. R. Hughes, editors, *Partitioned analysis of coupled systems*, pages 157–219. North-Holland Pub. Co., 1983.

[60] K.C. Park, C.A. Felippa, and J.A. De Runtz. Stabilization of Staggered Solution Procedures for Fluid-Structure Interaction analysis. In T. Belytschko and T.L. Geers, editors, *Computational methods for fluid-structure interaction problems*, pages 26.94–26.124. ASME Applied Mechanics Symposia Series, 1977.

[61] S. Piperno. Numerical methods used in aeroelasticity simulations. *Rapport de Recherche CERMICS*, 92-5, 1992.

[62] S. Piperno. Staggered time-integration methods for a one-dimensional Euler aeroelastic problem. *Rapport de Recherche CERMICS*, 94-33, 1994.

[63] S. Piperno, C. Farhat, and B. Larrouturou. Partitioned procedures for the transient solution of coupled aeroelastic problems. Center for Aerospace Structures - 94-06, University of Colorado, Boulder, Colorado, January 1994.

[64] S. Piperno, B. Larrouturou, and M. Lesoinne. Analysis and compensation of numerical damping in a one-dimensional aeroelastic problem. *Rapport de Recherche CERMICS*, 93-17, 1993.

[65] E. Pramono and S. K. Weeratunga. Aeroelastic computations for wings through direct coupling on distributed-memory MIMD parallel computers. In *32nd Aerospace Sciences Meeting and Exhibit*, Reno, Nevada, January 10-13 1994. AIAA paper No. 94-0095.

[66] R.D. Rausch, J.T. Batina, and H.T.Y. Yang. Euler flutter analysis of airfoils using unstructured dynamic meshes. AIAA paper 89-1384, April 3-5 1989. AIAA/-ASME/ASCE/AHS/ASC 30th Structures, Structural Dynamics and Materials Conference, Mobile, Alabama.

[67] B.S. Sarma and T.K. Varadan. Nonlinear Panel Flutter by Finite-Element Method. *AIAA Journal*, 26:566–574, May 1988.

[68] R.H. Scanlan. On the State of Stability Considerations for suspended-span bridges under Wind. In *Proceedings IUTAM-IAHR Symposium*, pages 595–618, Karlsruhe, Germany, 1979.

[69] H. Schlichting. *Boundary layer theory.* McGraw-Hill, New-York, fourth edition edition, 1960.

[70] V. Shankar and H. Ide. Aeroelastic computations of flexible configurations. *Computers & Structures*, 30(1/2):15–28, 1988.

[71] T. W. Strganac and D. T. Mook. Numerical model of unsteady subsonic aeroelastic behavior. *AIAA Journal*, 28:903–909, 1990.

[72] P.D. Thomas and C.K. Lombard. Geometric Conservation Law and Its Application to Flow Computations on Moving Grids. *AIAA Journal*, 17:1030–1037, Oct 1979.

[73] B. Van Leer. Towards the Ultimate Conservative Difference Scheme V: a Second-Order Sequel to Godunov's Method. *Journal of Computational Physics*, 32:pp 361–370, 1979.

[74] B. Van Leer. Flux-vector Splitting for the Euler Equations. *Lecture Notes in Physics*, 170:pp 507–512, 1982.

[75] R.F. Warming and F. Hyett. The modified equation approach to the stability and accuracy analysis of finite-difference methods. *Journal of Computational Physics*, 14(2):159–179, 1974.

[76] W.L. Wood, M. Bossak, and O.C. Zienkiewicz. An alpha modification of Newmark's method. *International Journal for Numerical Methods in Engineering*, 15:1562–1566, 1981.

[77] C. Youssfi. Simulation numérique des phénomènes de couplage fluide-structure. Rapport de stage d'option, Ecole Polytechnique, 1994.

RESUME

Dans cette thèse, nous nous sommes intéressés à la simulation numérique de phénomènes d'interaction fluide-structure. Plus précisément, nous avons mis au point des méthodes générales d'intégration décalée, que nous avons ensuite appliquées à des problèmes aéroélastiques bidimensionnels non-linéaires. Les méthodes couramment utilisées pour ce genre de simulations ont été détaillées. Parmi celles-ci, les méthodes décalées permettent l'utilisation modulaire d'algorithmes classiques en dynamique des structures et en dynamique des fluides (en domaine déformable). Sur un problème modèle linéaire et mono-dimensionnel, nous avons mis en évidence l'importance de l'algorithme de couplage utilisé. Nous avons démontré que des considérations énergétiques permettent d'assurer non seulement la stabilité d'un système couplé linéaire, mais aussi l'inconditionnelle stabilité de nouveaux schémas décalés implicites. Cette stabilité s'étend également aux schémas où le fluide est sous-cyclé, qui permettent une simulation plus rapide, surtout sur machines parallèles. Les idées générales dégagées de ces modèles ont ensuite été appliquées à des problèmes mono-dimensionnels non-linéaires. Elles ont permis d'élaborer une nouvelle méthode à interface double, plus souple, précise et stable, où le principe d'action et réaction est mieux vérifié. Nous avons enfin appliqué ces méthodes à des problèmes bidimensionnels instationnaires d'écoulements non-visqueux autour de structures linéaires mobiles et/ou déformables (flottements transsonique et supersonique): des résultats d'une grande précision ont été obtenu avec des gains de temps de calcul considérables.

Mots clés : interaction fluide-structure – équations d'Euler – maillage mobile non structuré – dynamique des structures – algorithme de couplage – sous-cyclage

ABSTRACT

The aim of this work is the numerical simulation of fluid-structure interactions. More precisely, we have built new general staggered algorithms and applied them to non-linear two-dimensional aeroelastic phenomena. A survey of existant methods showed that staggered algorithms allow a modular use of classical procedures of Structural Dynamics and Computational Fluid Dynamics (with moving boundaries). Using a simple linear one-dimensional model problem, we first showed the influence of the global coupling scheme chosen. Energetic considerations allowed us to prove the physical stability of a coupled system and the numerical unconditional stability of new implicit staggered schemes. Fluid subcycled versions of these schemes were built and implementations on parallel machines were also considered. General principles derived from these linear models were applied to one-dimenional non-linear problems and allowed the construction of a new volume-discontinuous method, which is more flexible, accurate and stable, because the action and reaction principle is verified with more accuracy. Finally, we applied this new method to unsteady two-dimensional inviscid flutter simulations (transonic flutter of a wing profile and supersonic panel flutter). We obtained very accurate results with a dramatic reduction of the computational cost.

Key words: fluid-structure interaction – Euler equations – unstructured dynamic meshes – Structural Dynamics – coupling algorithm – subcycling